



THÈSE DE DOCTORAT
DE L'UNIVERSITÉ PSL

Préparée à Chimie ParisTech / Ecole Nationale Supérieure de
Chimie de Paris (ENSCP)

**Nouveaux Contacts Sélectifs pour des Cellules à
Pérovskites hybrides très efficaces
(Development of New Selective Contacts for Efficient
Hybrid Perovskite Solar Cells)**

Soutenue par

Maria ULFA

Le 3 Avril 2019

Ecole doctorale n° 388

**Chimie Physique et Chimie
Analytique de Paris Centre**

Spécialité

Chimie Physique

Composition du jury :

| | |
|--|---------------------------|
| Pr. Corinne, CHANEAC Professeure, Sorbonne Université | <i>Présidente</i> |
| Pr. Yvan, BONNASSIEUX Professeur, Ecole Polytechnique | <i>Rapporteur</i> |
| Dr. Bruno, SCHMALTZ Maitre de Conférences, Université de Tours | <i>Rapporteur</i> |
| Pr. Fabrice, GOUBARD Professeur, Université Cergy-Pontoise | <i>Examineur</i> |
| Dr. Thierry, PAUPORTÉ Directeur de Recherche CNRS, ENSCP-Paris | <i>Directeur de thèse</i> |



ParisTech



*In the name of Allah SWT
I dedicate this manuscript to all my family, teachers, friends
for their unquestionable support, love, and encouragement
May Allah bless you all ☺*

ACKNOWLEDGMENTS

Bismillahirrahmanirrahim

Alhamdulillah, all praises to Allah SWT for the strengths and His blessing in completing this thesis. It would also not be possible for me to finish my PhD and to write this doctoral thesis properly without the help and support of many kind people around me. In this occasion, I would like to acknowledge and thank in particular the following people.

A very special acknowledge goes out to the Indonesia Endowment Fund for Education (LPDP) scholarship for the opportunity and for the financial support during this PhD program.

I would like to express my deepest appreciation to my thesis director, Dr. Thierry Pauporté for his guidance and patientless for the last three and half years of my PhD. I am grateful for his endless support and patience in research investigation, writing articles, and correcting my manuscripts.

I am also grateful to the following people: Patrick Aschehoug, Sébastien Peralta, Jiawen Liu for their kind help in doing some measurement during my PhD.

I would like to thank Pr. Yvan Bonnassieux and Dr. Bruno Schmaltz for accepting to be my reviewers as well as Pr. Fabrice Goubard and Pr. Corinne Chanéac for being my examiners.

I am deeply grateful for all my colleagues and friends for their help, their support, and for all the great times we shared in the laboratory, and the many scientific discussions. I would like to thank in particular Dr. Yuly Kusumawati, Dr. Jie Zang, Dr. Alexandra Szemjonov, Dr. Sana Koussi, Dr. Pengjiu Wang, Tao Zhu, Daming Zheng, Mariem El Efrif, Maryem, Sana, and many others.

And finally, last but by no means least, I am so grateful for my parents (Hasmi and Ermailis) who raised me with endless love and support, with their unconditional praying for me. For my whole family who always believes in my capability to reach as high as possible in education with all the limitation that I have. And to my husband Yahdi Bin Rus who always courage and accompany me in the whole condition during this PhD. Thanks to all teachers that taught me since I was a child which now bring me to this achievement.

Thanks for all your encouragement!!!

RÉSUMÉ

La cellule solaire pérovskite est l'un des sujets de recherche les plus importants dans le monde depuis sa première publication en 2009. Depuis cette date, l'intérêt de la recherche sur les matériaux pérovskites a été étendu à de nombreux types d'applications. Grâce à des études et des recherches intensives, le rendement de conversion de la cellule solaire à pérovskite a été considérablement amélioré jusqu'à 23% dans une courte durée (10 ans). C'est un résultat incroyable par rapport aux cellules solaires au silicium qui ont mis plusieurs décennies à atteindre un rendement aussi élevé. Les recherches portent maintenant sur tous les composants solaires de la pérovskite: le matériau de pérovskite lui-même, la couche de transport d'électrons et de trous ainsi que la structure et les contacts de l'appareil.

Ce travail de thèse visait à réaliser des cellules solaires pérovskites efficaces, stables et reproductibles et à bien comprendre le fonctionnement des cellules. Nous avons commencé par comparer deux techniques différentes de dépôt de MAPI, appelées une étape et deux étapes. En adoptant les deux techniques, nous pourrions atteindre plus de 17% de performance pour $\text{CH}_3\text{NH}_3\text{PbI}_3$ PSC. Les deux techniques ont ensuite été utilisées pour étudier plusieurs matériaux de transport de trous. Nous avons étudié le rôle de chaque matériau de transport de trous dans plusieurs structures de pérovskite et les réponses électriques des cellules en réalisant des mesures de spectroscopie d'impédance. Enfin, nous avons concentré notre étude sur la structure plane en utilisant un semi-conducteur à large bande interdite, le SnO_2 . Une étude complète a été réalisée, telle que l'épaisseur de la couche de SnO_2 , le temps et la température de recuit et la pérovskite pour obtenir un rendement élevé. Enfin, l'étude comparative avec une cellule de TiO_2 plane et une cellule de TiO_2 mésoporeuse a été réalisée afin de bien comprendre le fonctionnement des cellules.

Au chapitre 1, nous avons présenté le contexte de la recherche sur les cellules solaires. Tout d'abord, nous avons détaillé le mécanisme de travail des cellules solaires au silicium en expliquant la formation d'une jonction p-n, la formation d'un champ électrique intégré et les processus de séparation de charges dans le dispositif. En outre, nous avons également présenté les nouvelles cellules solaires de pérovskite, en décrivant leur développement et leur évolution au cours des dernières années, y compris les différentes couches fonctionnelles utilisées, la structure des cellules, les techniques de dépôt et d'autres paramètres importants. Nous avons également expliqué le mécanisme de fonctionnement des cellules solaires à pérovskite et enfin,

nous avons détaillé les techniques de caractérisation qui sont actuellement utilisées pour le matériau lui-même et le dispositif complet.

Au chapitre 2, nous avons présenté une étude comparative de deux techniques différentes de dépôt de $\text{CH}_3\text{NH}_3\text{PbI}_3$ (1 étape et 2 étapes). Nous avons entièrement caractérisé la couche et les cellules préparées par les deux techniques. Il était clair que les deux conviennent à la préparation de PSC, qui donne plus de 17% de PCE. Nous avons également profondément caractérisé les réponses électriques de la cellule en mesurant l'impédance et la durée de vie de l'électron par spectroscopie à photoluminescence résolue dans le temps. Nous avons observé que les cellules préparées par 2 étapes n'étaient pas très stables pendant les mesures d'impédance, ce qui rendait leur étude complète difficile.

Au chapitre 3, nous avons étudié en détail les deux principaux types de matériaux de transport de trous: moléculaire et polymère. Nous avons entièrement caractérisé et comparé la réponse électrique des PSC préparés avec la molécule de référence Spiro-OMeTAD HTM et le polymère conducteur poly (3-hexylthiophène-2,5-diyl) (P3HT) choisi pour son coût faible et son efficacité. Nous avons également étudié l'effet dopant sur ces HTM. Grâce à la spectroscopie d'impédance, nous avons pu voir clairement que le dopage est vraiment important pour obtenir une efficacité élevée dans la cellule Spiro-OMeTAD alors que l'amélioration était moins significative dans le cas de la cellule P3HT. Nous avons montré que l'oxydation Spiro-OMeTAD par l'additif est importante pour augmenter la conductivité de la couche HTM et diminuer la résistivité interne. De plus, pour les deux HTM, les additifs améliorent l'interface pérovskite / HTM et empêchent la recombinaison des charges. Les dopages ont amélioré l'interface du matériau de transport pérovskite / trou pour la cellule P3HT, tout en aidant de manière significative l'oxydation de Spiro-OMeTAD à augmenter sa conductivité et améliorer de la qualité de l'interface pérovskite / Spiro-OMeTAD.

Au chapitre 4, nous avons étudié plusieurs nouveaux dérivés du carbazole en tant que matériaux de transport de trous. Ces molécules allaient du grand noyau dendritique B186 aux séries DM et iDM ayant un poids moléculaire inférieur. Premièrement, nous avons incorporé tous ces nouveaux HTM moléculaires dans les PSC en utilisant plusieurs types de structures de pérovskite. Parmi eux, B186 et iDM1 ont montré la plus grande efficacité à 14,59% et 15,04%, respectivement. Nous avons étudié la stabilité des cellules B186 en suivant l'efficacité du dispositif ainsi que le diagramme de réduction des rayons X. Nous avons constaté que le B186 avait une meilleure stabilité que Spiro-OMeTAD. Il est intéressant de noter que les DM1 et

DM2 de la série de matériaux de transport de trous DMs ont montré une augmentation significative de l'efficacité en immersion par irradiation lumineuse.

Au chapitre 5, nous avons étudié une structure planaire simple de PSC en incorporant un SnO_2 semi-conducteur SnO_2 avec une large bande interdite en tant que couche de blocage de trous. Au début, nous avons complètement étudié l'épaisseur optimale de SnO_2 , la bonne température et le temps de recuit, ainsi que le substrat utilisé et sa combinaison avec diverses pérovskites. La condition optimale a été trouvée lorsqu'elle a été préparée en revêtant deux fois une solution aqueuse à 2,35% de colloïdal de SnO_2 recuite à basse température (123°C). La couche était exempte de fissures et recouvrait complètement le substrat FTO. Les cellules planaires ont ensuite été préparées en utilisant cette couche combinée avec les pérovskites MAPI (1) -SOF et FAMA. Avec FAMA absorbeur, les dispositifs étaient très efficaces avec un PCE maximum de 18,2% et absence d'hystérésis (6,7% HI) alors qu'avec MAPI (1) -SOF l'efficacité obtenue était de 15,2% avec une hystérésis plus élevée. À des fins de comparaison, nous avons également préparé une cellule solaire plane en pérovskite utilisant une couche de TiO_2 pulvérisée en tant que couche de transport d'électrons ainsi que la structure de référence combinant la couche de blocage pulvérisée et la couche mésoporeuse de TiO_2 . Cela nous a permis d'obtenir des informations complètes sur le fonctionnement de la cellule.

D'après nos études, il est maintenant clair que la couche de transport d'électrons ou la couche de transport de trous sont très importantes pour obtenir des cellules solaires avec efficacité élevée et stables. Les propriétés de ces couches affectent leur capacité à transporter ou à stocker des supports dans l'ensemble du dispositif. De plus, nous avons illustré la grande importance des interfaces dans les appareils. Une condition optimale pour chaque couche, telle que l'épaisseur et la morphologie, donnait un rendement élevé et des cellules solaires pérovskites stables. Cependant, la préparation de la couche de pérovskite elle-même est également cruciale pour obtenir un rendement élevé. La couche doit contenir le moins de défauts et avoir une cristallinité élevée afin de réduire la possibilité que les processus de recombinaison augmentent l'efficacité. Grâce à notre étude de différents matériaux de transport de trous, nous pouvons affirmer que le Spiro-OMeTAD classique n'est peut-être pas le meilleur matériau de transport de trous pour obtenir une stabilité élevée et une protection contre l'humidité. Nous avons montré qu'il existe plusieurs possibilités de trouver de nouveaux matériaux de transport de trous, qu'ils soient moléculaires, polymères ou inorganiques. Dans des études récentes, nous avons constaté qu'un polymère à base de carbazole présentait une efficacité prometteuse, proche de 17% dans notre groupe. D'ailleurs, l'efficacité de la cellule a augmenté de 18% après 7 semaines de

stockage. Cependant, l'objectif de la HTM sans additifs efficaces n'est pas facile à atteindre puisque nous avons montré le rôle clé des additifs dans l'amélioration de l'interface pérovskite / HTM.

En ce qui concerne la couche de transport d'électrons, nous avons montré que la couche d'oxyde de TiO_2 présentait certains inconvénients. Récemment, d'autres oxydes, en particulier SnO_2 , ont également montré un transfert d'électrons rapide depuis l'absorbeur de pérovskite. Maintenant, il est étudié de manière intensive dans de nombreux groupes. Les avantages du SnO_2 ETL incluent une préparation à basse température, une structure cellulaire simplifiée et une faible hystérésis. Cependant, les performances des cellules SnO_2 préparées sont restées inférieures à aux cellules TiO_2 préparées dans le groupe de Pauporté. De plus, nous avons également observé la qualité de l'interface entre chaque couche afin d'obtenir moins de recombinaison dans les cellules, soit par modification de l'interface avec dépôt de couche mince, soit par examen attentif de chaque couche au cours de la préparation de la cellule.

Nous avons commencé notre étude en utilisant de la pérovskite MAPI, qui est moins stable que la pérovskite FAMA. Maintenant, dans notre groupe, nous étudions une pérovskite à cations multiples additionnée de Cs dans la pérovskite FAMA pouvant atteindre 21% de la PCE et ayant une meilleure stabilité. De plus, une pérovskite sans plomb est également une grande opportunité pour les études futures afin de faire face au problème de la toxicité de l'environnement.

Dans le contact métallique, il est possible de changer l'utilisation de l'or avec un autre contact métallique, tel que le noir de carbone, qui peut réduire le coût de fabrication de la cellule.

Sur la base de tous nos résultats et en suivant la tendance des résultats des cellules solaires à la pérovskite, nous croyons que l'efficacité des cellules solaires à pérovskite augmentera continuellement dans l'avenir et il est probable qu'un jour, elles seront commercialisées à grande échelle dans le monde entier.

Table of Contents

| | |
|--|-----------|
| Table of Contents | xii |
| List of Figures | xv |
| List of Tables..... | xxiii |
| List of the abbreviations and symbols..... | xxvi |
| General Introduction | 1 |
| Chapter I :Context | 3 |
| I.1. Solar Energy | 3 |
| I.2. Photovoltaics for solar renewable energy conversion | 4 |
| I.2.1. Silicon solar cells..... | 5 |
| I.2.2. Perovskite solar cells | 8 |
| I.3. Brief description of the perovskite solar cells evolution | 12 |
| I.4. The working principle of perovskite solar cells | 19 |
| I.5. Components of perovskite solar cells..... | 20 |
| I.5.1. The electron transporting layer..... | 20 |
| I.5.2. The perovskite layer | 21 |
| I.5.3. The hole transporting layer..... | 22 |
| I.5.4. The back contact layer..... | 24 |
| I.6. The characterizations of perovskite solar cells and of their components..... | 25 |
| I.6.1. Material characterizations..... | 25 |
| I.6.2. Standard solar spectral irradiance..... | 25 |
| I.6.3. Current-voltage characteristics | 27 |
| I.6.4. Quantum efficiency measurement | 29 |
| I.6.5. Impedance spectroscopy..... | 30 |
| Chapter II :Preparation of CH₃NH₃PbI₃ layers and cell performances | 45 |
| II.1. Introduction..... | 45 |
| II.2. Preparation methods of MAPI-based solar cells..... | 47 |
| II.2.1. Preparation of the blocking layer (<i>bl</i> -TiO ₂) | 47 |
| II.2.2. Preparation of the mesoporous layer (<i>meso</i> - TiO ₂)..... | 49 |
| II.2.3. Preparation of MAPI layers | 49 |
| II.2.4. Preparation of the hole transporting material layer (HTM) | 51 |
| II.2.5. Preparation of the back contact | 51 |
| II.3. Characterization of the MAPI layers prepared by the one-step and the two step methods..... | 51 |

| | |
|--|-----------|
| II.3.1. Morphology properties | 51 |
| II.3.2. XRD | 52 |
| II.3.3. Optical characterizations | 53 |
| II.4. Devices performances | 54 |
| II.5. Aging study of MAPI layers | 56 |
| II.6. PL spectrum and PL decay study | 59 |
| II.7. Impedance study of the MAPI solar cells | 61 |
| II.8. Conclusion | 67 |
| Chapter III :Molecular and polymeric hole transporting material for high performance perovskite solar cells | 71 |
| III.1. Introduction..... | 71 |
| III.2. Experimental..... | 75 |
| III.2.1. Spiro-OMeTAD layer preparation..... | 75 |
| III.2.2. P3HT layer preparation..... | 76 |
| III.2.3. P3HT spin-coating technique | 76 |
| III.3. Optical characterizations | 77 |
| III.4. Perovskite solar cells results..... | 78 |
| III.5. Impedance spectroscopy study of perovskite solar cells | 79 |
| III.6. Photoluminescence (PL) spectrum and decay studies | 86 |
| III.7. Conclusion | 88 |
| Chapter IV :New hole transporting materials for perovskite solar cells | 91 |
| IV.1. Introduction | 91 |
| IV.2. Experimental..... | 93 |
| IV.3. Dendritic carbazole B186 and B74 based HTM..... | 93 |
| IV.3.1. Molecular structure and physico-chemical properties of B186 and B74 | 94 |
| IV.3.2. Solar cells performances..... | 95 |
| IV.3.3. Stability tracking of B186- and B74-caped MAPI(1)-SO layers and solar cells.. | 98 |
| IV.3.4. Impedance study of B186 and the doping effect | 100 |
| IV.3.5. Conclusion | 104 |
| IV.4. DM-based HTM for perovskite solar cells | 105 |
| IV.4.1. The physico-chemical properties of the DM molecules | 106 |
| IV.4.2. Performances of solar cells..... | 107 |
| IV.4.3. Light soaking effect on perovskite solar cells performances..... | 109 |
| IV.4.4. Conclusion | 113 |
| IV.5. iDM HTM-based perovskite solar cells | 114 |

| | |
|---|------------|
| IV.5.1. The physico-chemical properties of the iDM molecules | 114 |
| IV.5.2. Performances of solar cells | 115 |
| IV.5.3. Conclusion | 117 |
| IV.6. General conclusion | 118 |
| Chapter V :Impact of the oxide layer on the performances of perovskite solar cells | 121 |
| V.1. Introduction..... | 121 |
| V.2. Experimental section..... | 123 |
| V.2.1. Preparation of the oxide layers | 123 |
| V.2.2. Preparation of the perovskite layers..... | 123 |
| V.3. Effect of the mesoporous TiO ₂ layer thickness | 124 |
| V.4. Optimization of the SnO ₂ solar cells..... | 127 |
| V.4.1. The TCO | 127 |
| V.4.2. The perovskite..... | 130 |
| (a). Comparison of MAPI and FAMA | 130 |
| (b). Optimization of FAMA in SnO ₂ cells..... | 131 |
| V.4.3. The SnO ₂ preparation..... | 132 |
| (a). The concentration of the SnO ₂ colloidal solution | 133 |
| (b). Annealing temperature and time | 133 |
| (c). Number of coatings | 135 |
| V.5. Study of planar perovskite solar cells: a comparative study of SnO ₂ and TiO ₂ | 142 |
| V.5.1. Optical characterization | 142 |
| V.5.2. Structural characterization | 144 |
| V.5.3. Morphological characterization | 145 |
| V.5.4. Solar cells..... | 146 |
| V.5.5. PL and decay lifetime study..... | 148 |
| V.5.6. Impedance study of various perovskite..... | 151 |
| V.6. Conclusion | 156 |
| General conclusion and some future perspectives | 160 |
| Annex-I..... | 164 |
| Annex-II..... | 166 |
| List of publications and presentations | 169 |

List of Figures

| | |
|---|----|
| Figure 1.1. World energy reserves according to the International Energy Agency (IEA)..... | 3 |
| Figure 1.2. Electricity generation by source in the New Policies Scenario, 2000-2040..... | 4 |
| Figure 1.3. Silicon solar cells operating mechanism. (a) Silicon materials doping to form p-type and n-type semiconductor. (b) p-n junction formation. (c) Formation of the built-in electric field. (d) A pair of electron-hole formation after sunlight irradiation. (e) Charge carriers separation and current generation | 7 |
| Figure 1.4. Schematic of allotropic forms of different types silicon solar cells and their related solar panel module | 8 |
| Figure 1.5. Perovskite crystal structure | 9 |
| Figure 1.6. Perovskite solar cell structure | 10 |
| Figure 1.7. Number of papers on perovskite solar cells published from 2009 to May 15 th , 2018 | 11 |
| Figure 1.8. Chart of the best-cell efficiency of photovoltaic devices recorded by NREL | 12 |
| Figure 1.9. (a) Schematic drawings for power generation in dye-sensitized solar cells. (b) Schematic drawing for perovskite-sensitized solar cell. (c) Energy diagram for power generation. C.B and V.B are the conduction band and the valence band, respectively. C.E is the counter electrode. QD is quantum dot. (d) Illustration of the incorporating the 2-3 nm sized of perovskite $\text{CH}_3\text{NH}_3\text{PbI}_3$ nanocrystal to the TiO_2 surface. (e) Solar cell J - V curve and EQE of (d) | 14 |
| Figure 1.10. Schematic illustration of the charge transfer and charge transport in perovskite-sensitized TiO_2 solar cell and a non-injecting Al_2O_3 -based solar cell with the band energy alignment below (solid circle is electron and open circle is hole) | 15 |
| Figure 1.11. Schematic drawings for the perovskite preparation with the sequential deposition method | 16 |
| Figure 1.12. The architecture evolution of PSCs | 16 |
| Figure 1.13. Fast deposition crystallization (FDC) (left), SEM top-view images from FDC and conventional deposition (right) | 17 |

| | |
|---|----|
| Figure 1.14. Illustration of intramolecular change introduced by Seok et al | 18 |
| Figure 1.15. (a) Illustration of a method for fabricating a continuous graded perovskite film by further spin-coating FABr solution in isopropanol on the (FAPbI ₃) _{0.85} (MAPbBr ₃) _{0.15} perovskite film. SEM top-view images of an as-prepared film (b) and a passivated film (c), respectively. Proposed change of cross sectional structures from the as-prepared perovskite film (d) to the passivated film (e) | 19 |
| Figure 1.16. Schematic representation of the energy levels and electron transfer processes in perovskite solar cells | 20 |
| Figure 1.17. Molecular structure of (a) Spiro-OMeTAD, (b) P3HT, (c) PTAA, and (d) PEDOT:PSS | 24 |
| Figure 1.18. Air mass (AM) calculation | 26 |
| Figure 1.19. Reference solar irradiation spectra according to the standards by American Society for Testing and Materials (ASTM)..... | 27 |
| Figure 1.20. Example of current density-voltage (J-V) characteristic curve illuminated by AM1.5G filter spectrum with a power density of 100 mW.cm ⁻² | 28 |
| Figure 1.21. Example of EQE spectra and J_{ph} integration curve of high efficiency PSCs | 30 |
| Figure 1.22. (a) Sinusoidal Current Response in a linear system. (b) Steady-state and ac I versus E curves upon impedance measurement | 31 |
| Figure 1.23. Nyquist impedance plot | 32 |
| Figure 1.24. (a) Equivalent circuit. (b) Nyquist plot of the spectrum (imaginary as a function of real component). The maximum of the RC-arc takes place at the characteristics angular frequency ω_0 as indicated. (c, d) Bode representations of the impedance spectrum: (c) Magnitude versus the frequency and (d) phase versus the frequency. The simulation was conducted from 1 MHz to 1 mHz..... | 34 |
| Figure 1.25. (a) Equivalent circuit. (b) Nyquist plot. Bode (c) Magnitude and (d) Phase plot versus the frequency from simulation using the presented values for R_1 , R_2 and CPE. The exponent of CPE was changed from the ideal case between 1 and 0.5. The red points in the Nyquist plot correspond to the 10000 Hz frequency. The simulation was conducted from 10 MHz to 1 mHz..... | 36 |

| | |
|---|----|
| Figure 1.26. Equivalent circuit employed for fitting the impedance spectra of perovskite solar cells..... | 36 |
| Figure 2.1. Schematic illustration of spray pyrolysis deposition technique..... | 48 |
| Figure 2.2. (a-c) SEM top views of the blocking TiO ₂ layer: (c) SEM zoom view of (a). (d) Cross-sectional view of the sprayed TiO ₂ blocking layer | 48 |
| Figure 2.3. Schematic of the two-step sequential deposition method of MAPI layer..... | 50 |
| Figure 2.4. Schematic of the one-step deposition method of MAPI layer | 50 |
| Figure 2.5. Top-view of (a) PbI ₂ layer and (b,c) MAPI(2) layer. (d) MAPI(1)-SO layer deposited on TiO ₂ oxide layer. (e) Cross-sectional view of a complete perovskite solar cell by integrating a MAPI(1)-SO layer | 52 |
| Figure 2.6. XRD patterns of CH ₃ NH ₃ PbI ₃ perovskite deposited on the TiO ₂ oxide layer through one-step and two-step deposition methods..... | 53 |
| Figure 2.7. (a) Absorbance and PL spectra of MAPI(1)-SO on glass (red curves) and on FTO/TiO ₂ (dark blue curves). (c) Absorbance and PL spectra of one-step MAPI. Tauc plots of (b) MAPI(2) and (d) MAPI(1)-SO deposited on FTO/TiO ₂ layers..... | 54 |
| Figure 2.8. <i>J-V</i> curves of the best cells in reverse and forward scan direction (under light) and in dark of: (a) MAPI(1)-SO; (b) MAPI(2). (c) Effect of reverse (full line) and forward (dashed line) scan rate variation on <i>J-V</i> curves measurement of a TiO ₂ /MAPI(1)-SO/Spiro-OMeTAD solar cell | 56 |
| Figure 2.9. XRD pattern of; (a,c) MAPI(1)-SO and (b,d) MAPI(2) with and without Spiro-OMeTAD layer deposited on TiO ₂ layer | 58 |
| Figure 2.10. (a,b) Photoluminescence spectra of MAPI(1)-SO (a) and MAPI(2) (b) deposited on glass and on TiO ₂ layers (excitation at 470 nm by a diode laser). (c) Time-correlated single-photon counting curves of the photoluminescence of the (a) and (b) MAPI samples | 60 |
| Figure 2.11. Nyquist plots of impedance spectra of PSCs prepared with MAPI(1)-SO perovskite measured under light (a-f) at 0.2V (a,b) and 0.6V (c,d) applied voltages. Zoom view at (e) 0.2V and (f) 0.5V. (g) Three relaxations and (h) two relaxations equivalent electrical circuits..... | 62 |
| Figure 2.12. Nyquist plots of impedance spectra of MAPI(1)-SO PSCs measured in the dark at 0.2V (a) and 0.6V (b) applied voltages | 63 |

| | |
|--|----|
| Figure 2.13. Effects of batch and of light shining on the C_2 parameter of MAPI(1)-SO cells under various applied potentials (Under light: full symbols; in the dark: cross symbol) | 64 |
| Figure 2.14. (a) Variation of R_2 with V_{appl} for various perovskite (MAPI(2) is a cell prepared with a two-step perovskite); (b) The high frequency relaxation time for MAPI(1)-SO cell as a function of the applied voltage | 65 |
| Figure 2.15. (a) Effect of perovskite and light shining on the low frequency C_4 parameter. (b) Low frequency C_4 parameter of MAPI(1)-SO cells for hysteresis indexes (HI) of 11%, 22% and 30% | 66 |
| Figure 2.16. MAPI(1)-SO cell at various voltage (a) low frequency resistance R_4 in the dark (red square) and under light (dark red square). (b) low frequency relaxation time, τ_{LF} , of the PSCs measured under light | 67 |
| Figure 3.1. (a) Molecular structure of Spiro-OMeTAD, (b) P3HT, (c) 4-tert-butylpyridine (tBP) and (d) bis(trifluoromethane)sulfoimide (LiTFSI) | 75 |
| Figure 3.2. Absorbance curves. (a) Doped and undoped P3HT on glass. Inset: layer picture. (b) Normalized absorbance spectra of doped and undoped P3HT layers on glass. (c) Spiro-OMeTAD undoped on glass and Spiro-OMeTAD doped on FTO/Glass (No layer could be deposited directly on glass in this case and the substrate change explain the observed waves above 420 nm) | 77 |
| Figure 3.3. (a) Exploded schematic view of the perovskite solar cells. (b) Typical J-V curve of solar cells prepared with various doped and undoped P3HT and Spiro-OMeTAD HTM layers (reverse scan) | 78 |
| Figure 3.4. Impedance spectra Nyquist plots of (a,b) Spiro-based PCS at 0.0V, (c,d) Spiro-based PCS at 0.6V, (e,f) P3HT-based PSC at 0.0V and (g,h) P3HT-based PSC at 0.6V. (b), (d), (f) and (h) are zoom views at high frequencies of (a), (c), (e) and (g) respectively | 80 |
| Figure 3.5. (a) General equivalent electrical circuits used to fit the impedance spectra. (b-d) Electrical equivalent circuits used to fit the Spiro-OMeTAD and P3HT impedance spectra | 81 |
| Figure 3.6. (a) High frequency C_1 and R_1 at various V_{appl} measured on Spiro-Un cells. (b) R_s measured at various V_{appl} for PSCs prepared with Doped Spiro-OMeTAD and P3HT HTMs. (c) SEM Cross-sectional view of the Spiro-OMeTAD layer | 82 |

| | |
|--|-----|
| Figure 3.7. Effects of HTM and doping on the variation of C_2 (a) and R_2 (b) parameters with V_{appl} | 83 |
| Figure 3.8. Effects of HTM and doping on the variation with V_{appl} of R_4 (a) and C_4 (b) parameters. Effect of V_{appl} on C_4 of (c) pristine and doped Spiro-OMeTAD solar cells and on L_3 of (d) P3HT-Un and P3HT-Co solar cells | 84 |
| Figure 3.9. PL spectra of (a) Glass/MAPI(1)-SO/Spiro-OMeTAD and (b) Glass/MAPI(1)-SO/P3HT samples. Time-correlated single-photon counting curves of (c) Glass/MAPI(1)-SO/Spiro-OMeTAD and (d) Glass/MAPI(1)-SO/P3HT samples with and without additives..... | 87 |
| Figure 4.1. Molecular structure of B74 (left) and B186 (right) HTMs | 94 |
| Figure 4.2. (a) Device structure and (b) energy level alignment of different device components | 96 |
| Figure 4.3. (a) J - V curves of the best photovoltaic PSCs measured under AM1.5G filtered 100 mW.cm^{-2} illuminations. (b) EQE curves of PSCs prepared with various HTM. (a) and (b) are MAPI(1)-SO cells | 97 |
| Figure 4.4. Evolution of XRD patterns of Glass/FTO/TiO ₂ /MAPI(1)-SO/HTM assemblies stored under ambient conditions (a) Spiro-OMeTAD, (b) B186, and (c) B74 | 99 |
| Figure 4.5. Evolution of device performances and J - V curve parameters with storage time for B186 and Spiro-OMeTAD unencapsulated device cells. (a) Normalized V_{OC} ; (b) Normalized J_{SC} ; (c) Normalized FF and (d) Normalized PCE..... | 100 |
| Figure 4.6. Nyquist plots of impedance spectra of (a,b) of doped and undoped B186 based PSCs. (b) is a zoom view at high frequencies of (a). (c) General equivalent electrical circuit used to fit the impedance spectra. (d,e) Simplified EECs used to fit the impedance spectra of (d) doped B186 and (e) undoped B186 based PSCs..... | 102 |
| Figure 4.7. C_1 (a) and R_1 (b) versus the applied voltage of undoped MAPI(1)-SO/B186 PSCs. (c) C_2 versus the applied voltage of PSCs prepared with B186 in combination of two different hybrid perovskite absorbers, MAPI(1)-SO and FAMA. (d) SEM cross-sectional view of a B186 based PSC..... | 107 |
| Figure 4.8. (a) C_4 of doped B186 cells versus applied potential of two different hybrid perovskite, MAPI(1)-SO and FAMA. (b) R_4 of doped B186 cell measured at various potential | 104 |

| | |
|---|-----|
| Figure 4.9. Molecular structure of DM1, DM2, and DM1P HTMs | 106 |
| Figure 4.10. Energy level alignment of different device components | 107 |
| Figure 4.11. <i>J-V</i> curves of the best PSCs measured under AM1.5G filtered 100 mW.cm ⁻² illuminations at reverse scan direction | 109 |
| Figure 4.12. Light soaking effect on <i>J-V</i> curve of perovskite solar cells prepared with (a) DM1 and (b) DM2 as hole transport material | 110 |
| Figure 4.13. Effect of scan rate of (a) DM1-based and (b) DM1P-based perovskite solar cells | 112 |
| Figure 4.14. Molecular structure of iDM1, iDM2, and iDM4 hole transport materials | 114 |
| Figure 4.15. Best <i>J-V</i> reverse scan curves of the cells combining iDM1 HTM with perovskite absorber | 116 |
| Figure 4.16. <i>J-V</i> curves of iDM1 measured on both directions (reverse and forward) on (a) MAPI(2), (b) MAPI(1)-SOF, and (c) FAMA | 117 |
| Figure 5.1. SEM views of TiO ₂ mesoporous layer prepared using 1:10 (a-b), 1:8 (c-d) and 1:6 (e-f) paste dilutions..... | 125 |
| Figure 5.2. <i>J-V</i> curves of 1-step MAPI solar cells prepared with various TiO ₂ paste dilutions measured at various scan rates in the reverse direction. (a) 1:10 ; (b) 1:8 and (c) 1:6 paste dilutions. The dash lines are the dark currents. (d) Absorbance curve of various TiO ₂ dilutions | 126 |
| Figure 5.3. SEM views of FTO (left) and ITO (right) | 128 |
| Figure 5.4. AFM views of FTO (left) and ITO (right) | 128 |
| Figure 5.5. Absorbance curves of SnO ₂ deposited on two different substrates | 130 |
| Figure 5.6. Perovskite solar cells devices with various perovskite molarities | 132 |
| Figure 5.7. SEM-top view of various coating number of SnO ₂ layer deposited on the glass/ITO substrate..... | 136 |
| Figure 5.8. AFM images of various coating number of SnO ₂ layer deposited on the glass/ITO substrate..... | 137 |

| | |
|---|-----|
| Figure 5.9. SEM-top view of various coating number of SnO ₂ layer deposited on the glass/FTO substrate..... | 137 |
| Figure 5.10. AFM images of various coating number of SnO ₂ layer deposited on the glass/FTO substrate..... | 138 |
| Figure 5.11. (a-d) SEM top view of the bare FTO substrate (a) and after 1 (b), 2 (c) and 4 (d) SnO ₂ spin-coating step (4.5μm x 3.5μm). (e-h) AFM images of the bare FTO substrate (e) and after 1 (f), 2 (g) and 4 (h) SnO ₂ spin-coating steps. (top) : 2μm x 2μm image; (bottom): 800 nm x 800 nm image (the vertical scale was 300nm for all images). (i) SEM top view of the sprayed TiO ₂ layer (<i>spr</i> -TiO ₂) | 139 |
| Figure 5.12. (a) Absorbance curves of different oxides layer deposited on FTO substrates and (b) Tauc's plot of <i>spr</i> -TiO ₂ and <i>spr</i> -TiO ₂ / <i>meso</i> -TiO ₂ absorbance curves..... | 142 |
| Figure 5.13. (a) Absorbance spectra, (b) absorption edge zoom-view and (c) Tauc's plot of FAMA and MAPI(1)-SOF prepared on various oxide layers | 143 |
| Figure 5.14. XRD patterns of FAMA deposited on various oxides layer and MAPI on SnO ₂ layer..... | 144 |
| Figure 5.15. 800 nm x 800 nm AFM images of the perovskite layers deposited on the various oxide layers | 145 |
| Figure 5.16. (a) Planar and (b) mesoscopic PSCs architectures. (c) Cross-sectional SEM view of a planar SnO ₂ /FAMA solar cell. (d) <i>J-V</i> curves under simulated AM 1.5 G illumination of the best cells with various assemblies. (e) <i>J-V</i> curve of a record SnO ₂ /FAMA solar cell measured in the reverse (full line) and forward (dashed line) voltage scan directions | 147 |
| Figure 5.17. (a) Emission spectra of the FAMA layer on glass and supported on various oxide substrates. (b) Time-correlated single-photon counting curves of the photoluminescence of samples (a). (c) PL spectra of MAPI-SOF on glass and on SnO ₂ . (d) Time-correlated single-photon counting curves of the photoluminescence for MAPI-SOF on glass and on SnO ₂ contact layer | 150 |
| Figure 5.18. (a,b) Nyquist plots of the impedance spectra of cells with various ETL and HP assemblies. (c,d) High frequency zoom views of the spectra. (e,f) Real part of the complex impedance plotted versus the frequency. (g,h) Real part of the complex capacitance plotted | |

| | |
|--|-----|
| versus the frequency. (a,c,e,g) Applied potential: 0.0V; (b,d,f,h) Applied potential: 0.6V. (i) Full equivalent electrical circuit used to fit the impedance spectra | 153 |
| Figure 5.19. Variation of the solar cell resistance measured under light at various applied potentials. (a) R_2 ; (b) R_3+R_4 ; (c) Variation of the R_3 parameter with the applied voltage.... | 155 |
| Figure 5.20. Variation of the solar cell capacitances measured under light at various applied potentials. (a) C_2 ; (b) C_3 ; (c) C_4 . Note that C_4 (green open symbol) for SnO_2/FAMA is underestimated due to a very low relaxation frequency IS feature | 156 |
| Figure AI-1. SEM-view of FAMA on various oxides layer and MAPI(1)-SOF on SnO_2 layer | 164 |
| Figure AII-1. Cyclic voltammogram curves of various coating time of SnO_2 layer in an aqueous solution containing the $\text{Fe}(\text{CN})_6^{3-/4-}$ deposited on (a) ITO substrate- 30 min layer annealing time ; (b) FTO substrate-30 min layer annealing time; (c) FTO substrate-3h layer annealing time; (d) Curve of (c) with the CV of <i>spr</i> - TiO_2 sample | 166 |
| Figure AII-2. CV-curve characteristics for the FTO/glass substrate before and after different numbers of SnO_2 coatings | 168 |

List of Tables

| | |
|--|-----|
| Table 1.1. Relationship and impedance corresponding to bulk electrical elements. Furthermore, the corresponding electrical equivalent circuit symbols are presented. The graphical representation of the impedance is displayed in the Nyquist plots where Z' and Z'' are the real and imaginary components respectively | 33 |
| Table 2.1. J - V curve parameters of cells with MAPI(1)-SO and MAPI(2) perovskites | 55 |
| Table 2.2. Parameters of TCSPC of 1-step and 2-step MAPI deposited on glass and TiO_2 . Curves fitted by a bi-exponential decay equation | 61 |
| Table 3.1. Averaged photovoltaic J - V curve parameters and power conversion efficiencies of PSCs prepared by Drop-Spin and Spin-Drop the P3HT precursor solution. (AM1.5G filtered 100 mW cm^{-2} illumination) | 76 |
| Table 3.2. Effect of HTM and additives on the J - V curve parameters (AM1.5 filtered 100 mW.cm^{-2}). Avg: averaged values; Rev: reverse scan direction; For: forward scan direction.. | 79 |
| Table 3.3. Parameters of TCSPC of Spiro-OMeTAD and P3HT deposited on MAPI/glass. Curves fitted by a bi-exponential decay equation | 87 |
| Table 4.1. Comparative thermal, optical and optoelectrochemical properties of carbazole HTMs (B74, B186) and Spiro-OMeTAD | 94 |
| Table 4.2. Best and average J - V curve parameters of the solar cells prepared with Spiro-OMeTAD, B74 and B186 HTM. The standard deviations are given in brackets | 97 |
| Table 4.3. Thermal, optical and optoelectrochemical properties of DM1, DM2, and DM1P HTMs | 106 |
| Table 4.4. Best and averaged J - V curve parameters and PCE for cells prepared with MAPI(2) | 108 |
| Table 4.5a. Light soaking effect on the J - V curve parameters and PCE for cells prepared with DM1/MAPI(2)..... | 110 |
| Table 4.5b. Light soaking effect on the J - V curve parameters and PCE for cells prepared with DM2/MAPI(2)..... | 111 |

| | |
|---|-----|
| Table 4.6. Best and averaged <i>J-V</i> curve parameters and PCE for cells prepared with MAPI(1)-SO..... | 113 |
| Table 4.7. Thermal, optical and optoelectrochemical properties of iDM1, iDM2, and iDM4 HTMs | 115 |
| Table 4.8. Best and averaged <i>J-V</i> curve parameters and PCE for iDM1 cells prepared with MAPI(2), MAPI(1)-SOF, and FAMA..... | 115 |
| Table 5.1. Effect of mesoporous TiO ₂ layer thickness on the average <i>J-V</i> curve parameters (2-step MAPI, AM 1.5 100 mW.cm ⁻² illumination) | 126 |
| Table 5.2. Opto-electronic properties of various n-type wide bandgap oxides used in PSCs | 127 |
| Table 5.3. Summary of <i>J-V</i> parameters of two different TCO substrates | 129 |
| Table 5.4. <i>J-V</i> parameters of SnO ₂ solar cells with MAPI(1)-SO and MAPI(1)-SOF..... | 131 |
| Table 5.5. <i>J-V</i> parameters of SnO ₂ PSC for various FAMA precursor solution concentrations | 131 |
| Table 5.6. Summary of <i>J-V</i> parameters of various SnO ₂ solution | 133 |
| Table 5.7. Effect of annealing temperature and time of the SnO ₂ layer on the <i>J-V</i> curve parameters | 134 |
| Table 5.8. Roughness parameters measured by AFM for the FTO/glass substrate before and after different numbers of SnO ₂ coatings | 140 |
| Table 5.9. Effect of the SnO ₂ coating numbers on the PSC of <i>J-V</i> parameters | 140 |
| Table 5.10. Roughness, RMS roughness, grain size and standard deviation (in brackets) of perovskite layers deposited on the various oxides layer | 145 |
| Table 5.11. Photovoltaic parameters of SnO ₂ -based, TiO ₂ -based planar solar cells and of meso-TiO ₂ based solar cells under 100 mW.cm ⁻² AM 1.5G illumination. The numbers in brackets are the standard deviations | 147 |
| Table 5.12. Parameters of PL decays determined from the bi-exponential TCSP curve fitting. Fast and slow lifetimes and relative contributions of the fast and slow components | 150 |

| | |
|--|-----|
| Table AII-1. CV-curve characteristics for the FTO/glass and ITO/glass substrates before and after different numbers of SnO ₂ coatings | 167 |
|--|-----|

List of the abbreviations and symbols

| | |
|-----------------------|---|
| DSSC | Dye-sensitized solar cell |
| PSC | Perovskite solar cell |
| PCE | Power conversion efficiency |
| P_{inc} | Incident power density |
| P_{max} | Maximum output electrical power |
| V_{oc} | Open circuit voltage |
| J_{sc} | Short circuit photocurrent |
| FF | Fill factor |
| IPCE | Incident photon-to-electron conversion efficiency |
| EQE | External quantum efficiency |
| IS | Impedance spectroscopy |
| Z | Impedance |
| R | Resistance |
| C | Capacitance |
| bl-TiO ₂ | TiO ₂ blocking layer |
| meso-TiO ₂ | TiO ₂ mesoporous layer |
| PbI ₂ | Lead iodide |
| MAI | Methylammonium iodide |
| DMF | Dimethylformamide |
| DMSO | Dimethyl sulfoxide |
| AFM | Atomic force microscopy |
| RMS | Root mean square |
| ETL | Electron transport layer |
| HTM | Hole transport layer |
| TTIP | Titanium isopropoxide |
| LiTFSI | Bis(trifluoromethylsulfonyl)imide lithium salt |
| TBP | Tert-butylpyridine |

| | |
|---|--|
| Spiro-OMeTAD spirobifluorene | [2,2',7,7'-tetrakis(<i>N,N</i> -di- <i>p</i> -methoxyphenyl-amine)9,9'- spirobifluorene] |
| Co(III) _{complex} (bis (trifluoromethylsulfonyl) imide) | tris (2-1H-pyrazol-1-yl) - 4-tert-butylpyridine) – cobalt (III) -tris |
| CB | Chlorobenzene |
| XRD | X-ray diffraction |
| ACN | Acetone nitrile |
| PL | Photoluminescence |
| TCSPC | Time-correlated single-photon counting |
| RC | Relative contribution |
| τ_{fast} | Fast decay time |
| τ_{slow} | Slow decay time |
| EEC | Equivalent electrical circuit |
| P3HT | Poly(3-hexylthiophene) |
| FTO | Fluorine tin oxide |
| SEM | Scanning electron microscopy |
| HOMO | Highest occupied molecular orbital |
| LUMO | Lowest unoccupied molecular orbital |
| CB | Conduction band |
| VB | Valence band |
| ITO | Indium tin oxide |
| TCO | Transparent conduction oxide |
| CV | Cyclic voltammetry |

General introduction

Energy is one of the primary needs in modern human life. Fossil fuels, including coals, petroleum and natural gas, have been the main sources of energy since the industrial revolution began in the XVIII^e century. Due to their limitation and the pollution to the environment that they produce, the use of clean and renewable energy sources is essential. Sun is the most abundant source of energy that is renewable and clean. Through a simple photovoltaic device, the energy of the sunlight can be easily converted into the electricity.

Photovoltaic technologies have been developed since long time ago, starting from a silicon solar cell to more recent dye-sensitized solar cells (DSSCs). Surprisingly, a new family of solar cells based on organo-halide perovskite materials, has been found ten years ago. It has shown amazing results in solar cells technology reaching more than 23% of power conversion efficiency lately. Hybrid perovskite materials have a general formula ABX_3 , contain organic and inorganic elements and show a suitable bandgap to fully absorb the visible region as well as a small part of the infra-red one. The bandgap of this material can be easily modified by simply changing in their elemental composition.

In this thesis, we have investigated several hole transporting materials (HTM) and we have developed PSC with a planar structure. Chapter 1 is a bibliographic review which describes solar cells from the most popular silicon solar cells to the most recent generation, perovskite solar cells (PSCs). More specifically, we introduce the PSCs evolution in the past few years, including the achievement through the years of various functional layers and cells structure. We also detail the preparation of each layer, the working mechanism of PSCs, as well as the various techniques used in the thesis to characterize the PSCs.

In Chapter 2, we will provide a comparative study of two different MAPI layers prepared by a 1-step and a 2-step deposition technique, as well as the characterization of each layer. Cells performances, PL decay, and impedance study will be used to verify the cells functioning. Both deposition techniques were used to get high efficiency of $CH_3NH_3PbI_3$ perovskite solar cells.

In Chapter 3, we compare the integration in the cells of the molecular Spiro-OMeTAD and the conducting polymeric P3HT as HTMs. The effect of the HTM doping on the cell functioning is evaluated through several characterizations. Through PL and PL decay study and impedance spectroscopy (IS) measurements, we deeply analyzed cell parameters that contribute to the cell performances.

In Chapter 4, we investigate a group of new carbazole-based HTMs provided by the LPPI laboratory at Cergy-Pontoise. Several kinds of perovskite structure namely, MAPI(1)-SO, MAPI(1)-SOF, MAPI(2), and FAMA have been used to test their performances in PSCs. Moreover, further study such stability and light soaking of several HTMs will also be provide.

In Chapter 5, we have studied a simple planar structure in PSC. These structures are simpler to prepared compared to the mesoscopic ones. SnO_2 is a wide bandgap n-type semiconductor investigated as an electron transport layer. We have studied and optimize several parameters such as the SnO_2 layer thickness, the substrate used, the annealing temperature and time, and the perovskite. In order to fully understand the characteristic of the SnO_2 layer in PSC, a comparative study with TiO_2 and a $\text{TiO}_2/\text{meso-TiO}_2$ has been carried out.

A general conclusion is provided at the end of this dissertation.

Chapter I

Context

I.1. Solar energy

Energy is one of the primary needs in modern human life. Fossil fuels, including coals, petroleum and natural gas, have been the main resources of energy since industrial revolution began in the XVIII^e century. The disadvantages of burning fossil fuels have been largely pointed out. First and foremost, it increases the CO₂ concentration and is the major reason of environmental damages due to the increase of global warming. Secondly the burning of low quality of coals releases pollutant to the air such as SO₂. These damages will continue due to population growth which will need more energy in their life. Another fact is that fossil fuels are non-renewable sources of energy which will exhaust in the next decades due to limited resources. According to the International Energy Agency (IEA), the end of the fossil fuel resources is forecasted in less than ten decades. Figure 1.1 shows the prediction limit of these fossil fuels. Oil will run out at about 2052, followed by natural gas in 2061 and coals will be the last resources to be run out in 2088.

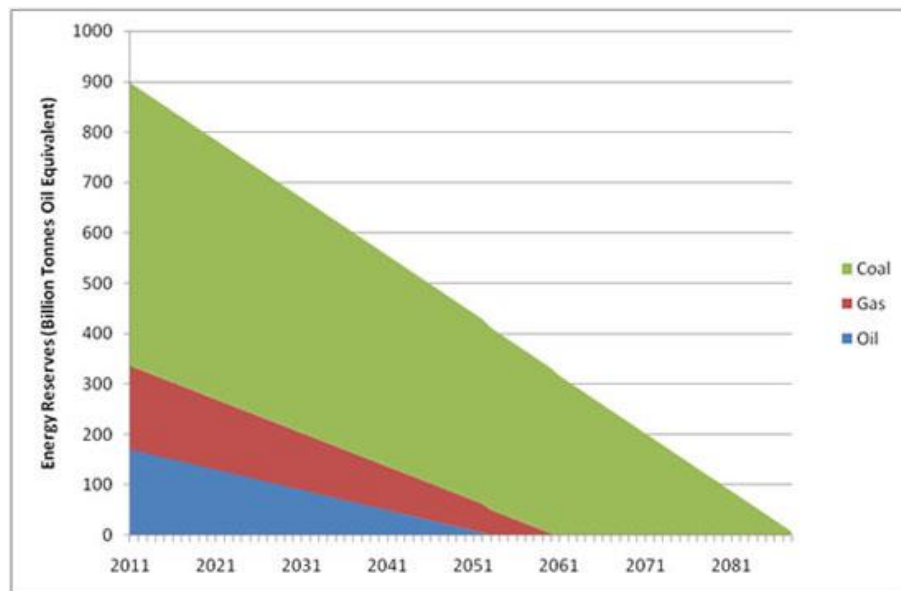


Figure 1.1. World energy reserves according to the International Energy Agency (IEA).

Because of their limitation and pollution issues, people try to find new resources of the energy alternative to fossil fuels that have less or no harmful effects to the environment. Possible green and renewable energies to face those issues are hydroelectric, wind, wave, biomass, geothermal,

and photovoltaics. The projection graph can be seen in Figure 1.2. Solar energy is the most abundant resource of energy amongst others with a potential to provide 23.000 TW if it is efficiently harvested.

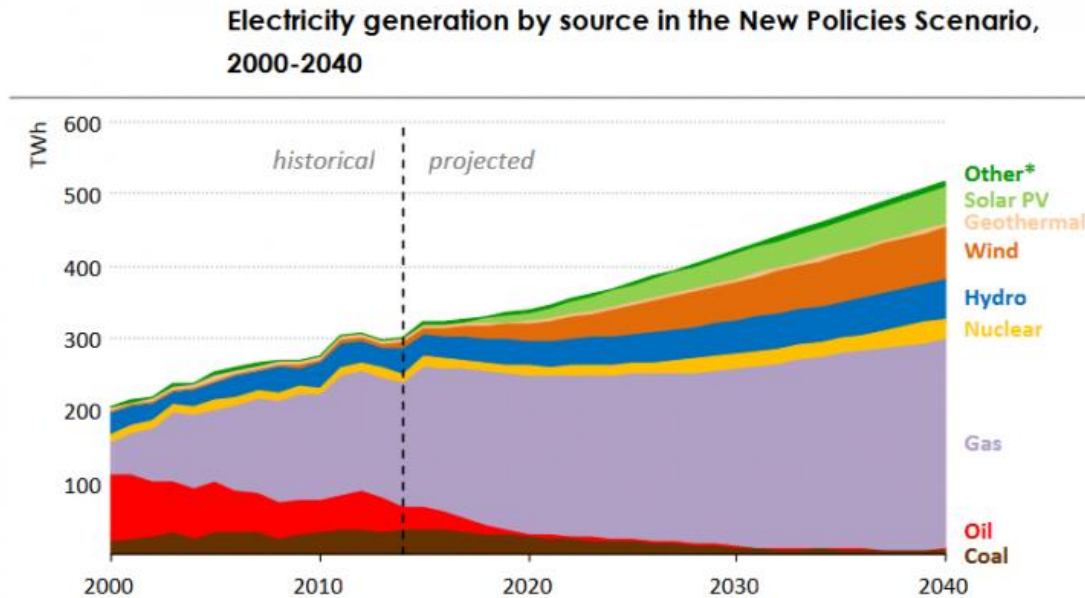


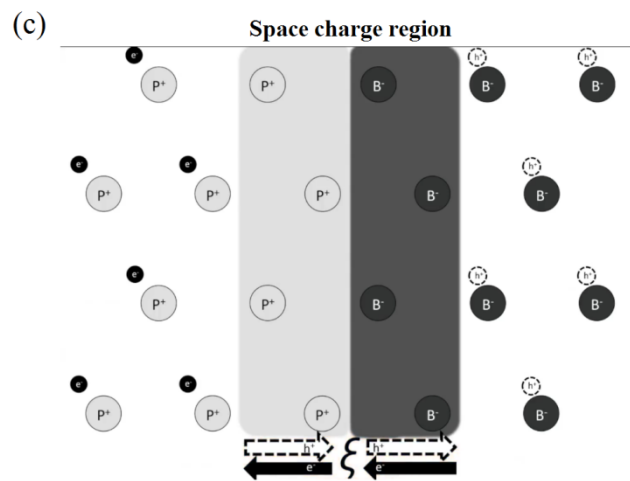
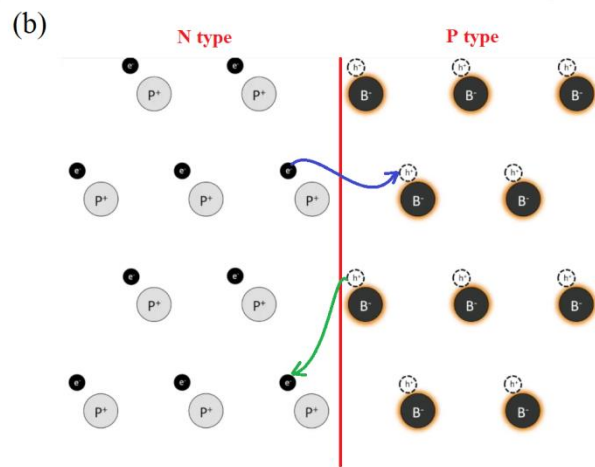
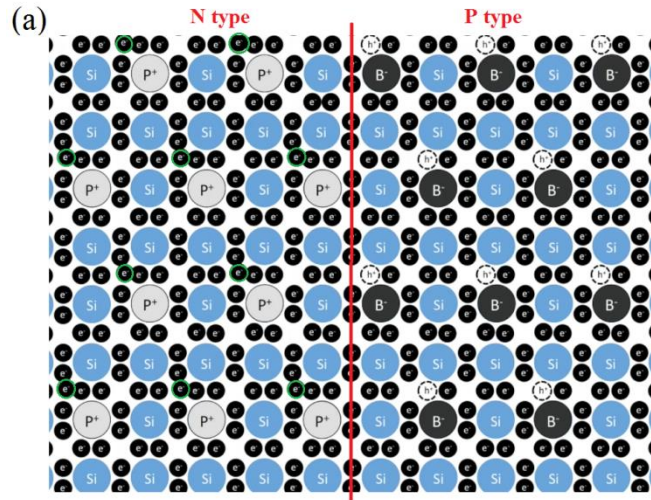
Figure 1.2. Electricity generation by source in the New Policies Scenario, 2000-2040.

I.2. Photovoltaics for solar renewable energy conversion

Photovoltaic (PV) solar cells are devices that convert light directly into electricity. These devices are one of the most promising alternative to harvest and convert the solar renewable energy nowadays due to its abundance on earth and photoelectric effect [1]. Through a simple combination of n-type and p-type semiconductor (SC) materials, the sunlight radiation can be converted into electricity. Many researchers have developed solar cells technologies in order to fulfil the energy demand. The solar cells are usually classified into three generations. Crystallized silicon-based solar cell is categorized as the first generation, while the thin film solar cells (amorphous silicon, CIGS, CdTe) are categorized as the second generation has and have an average efficiency of 10-15%. Others photovoltaic technologies such as dye-sensitized solar cells (DSSCs), organic photovoltaics (OPVs), quantum dot solar cells (QDSCs), multijunction solar cells and the new emerging perovskite solar cells are categorized as the third generation solar cells. The latter one have demonstrated a power conversion efficiency (PCE) as high as 23.3% within just 9 years of research. Some of these solar cells are briefly explained in the next sections.

I.2.1. Silicon solar cells

Among these solar cells technologies, crystallized silicon-based solar cells still dominate the commercial market (about 90%) due to their high efficiency and the high stability with a lifetime that can be as high as 40 years. Silicon solar cells are based on a p-n homojunction. p-type silicon semiconductor is formed when the silicon lattice is doped by boron atom or by another element of the group III of the periodic table. This element traps the free electrons and release free holes leading to an excess of mobile holes. Similarly, by introducing phosphorus or another element of the group V to the silicon lattice, the dopant tends to traps free holes and to release free electrons. It results in a higher concentration of mobile electrons and the SC is n-type doped (Figure 1a). All the charge excesses are free to move randomly. When these two semiconductors are contacted together, a p-n junction is formed. Due to the opposite charges of this junction, the free electrons in n-type semiconductor flow to the p-type to recombine with the free holes. Similarly, holes also flow from the p-type to the n-type (Figure 1b and 1c) and recombine with the electrons. This process continuously occurs until the mobile free carriers exhausted at the p-n junction. It results in a strong built-in electric field (i.e. a space charge region). Under sunlight irradiation, electrons of silicon excited near the space charge region, produce holes and start to move randomly (Figure 1d). The electrons randomly diffuse in the n-type zone while, due to the presence of a strong electric field at the space charge region, the holes drift at the space charge region (Figure 1e) resulting in a separation of the carriers. In the closed-circuit condition, the electrons will travel to the external wire reaching the p-type, where they recombine with the holes, and finally generate a continuous current in the external circuit.



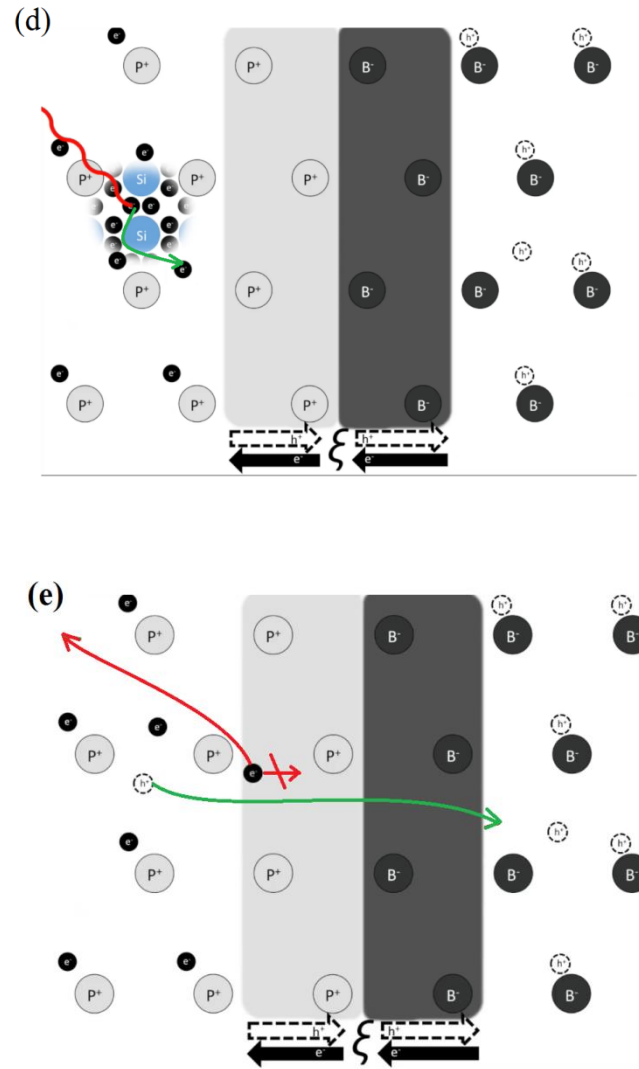


Figure 1.3. Silicon solar cells operating mechanism. (a) Silicon materials doping to form p-type and n-type semiconductor. (b) p-n junction formation. (c) Formation of the built-in electric field. (d) Electron-hole pair formation after sunlight irradiation. (e) Charge carriers separation and current generation.

There are three types of silicon-based solar cells: monocrystalline or single crystalline, polycrystalline, and amorphous silicon (Figure 1.4). The single crystalline silicon solar cells are fabricated from very pure single crystalline wafers of silicon. They have a black dark color. They also have been found to be the most robust technology with a lifetime up to 40 years and with most often 25 years warranty (less than 10% of efficiency loss within 25 years). For these reasons, the price of this type silicon solar cells quite high. The polycrystalline silicon solar cells have a better affordable price due to the less difficulties in fabrication process. However, they also have disadvantages such as the need of more installation space due to a less PCE and an efficiency which decreases significantly with the temperature. We can note that the cost of the

silicon solar cells has significantly decreased during the last years. Finally, amorphous silicon is used in thin film technology solar cells. It can be deposited on various substrates such as glass, metal, and plastic. Amorphous silicon is a more absorbing SC than crystallized silicon due to a direct bandgap transition while the latter is an indirect bandgap sSC.

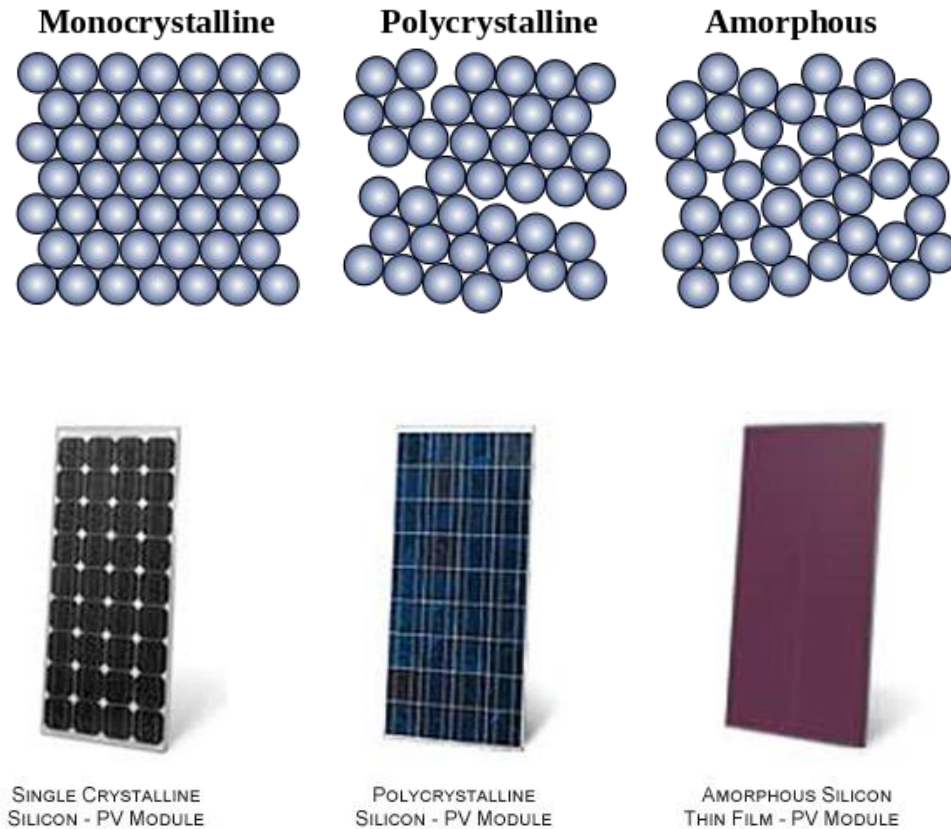


Figure 1.4. Schematic of allotropic forms of different types silicon solar cells and their related solar panel module.

I.2.2. Perovskite solar cells

Historically, the first natural perovskite was discovered by the German mineralogist Gustav Rose in 1839 in the Ural mountain. It was named perovskite in honor of the Russian mineralogist Lev Alexeïevich Perovsky.

Three-dimensional (3D) perovskites have the general formula ABX_3 that adopt the same crystal structure as $CaTiO_3$ where A and B are cations of different atomic radii (A larger than B) and X is a monovalent anion. The ideal structure of the 3D perovskite is cubic. It consists of corner

sharing BX_6 octahedra and the A-cation is located at the interstitial space in the three-dimensional structure formed by the eight adjacent octahedra (Figure 1.5).

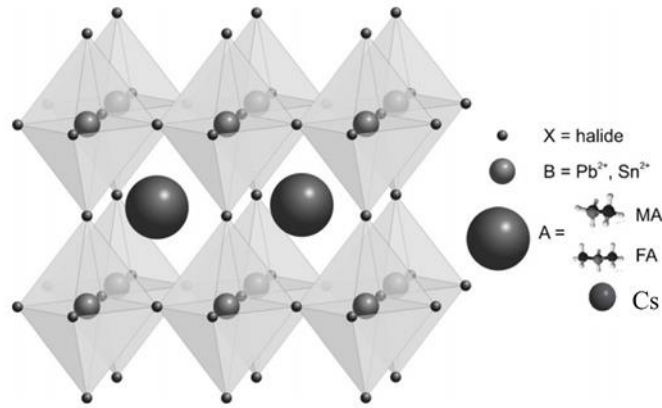


Figure 1.5. Perovskite crystal structure.

In organic-inorganic hybrid perovskite (HP) solar cells, the A cation is typically an organic aliphatic amine such as methylammonium (CH_3NH_3^+) and formamidinium ($(\text{NH}_2)_2\text{CH}^+$) or a monovalent alkali (Li^+ , Na^+ , K^+ , Rb^+ , Cs^+). B is a metallic cation such as Pb^{2+} , Sn^{2+} or Ge^{2+} from group IV and X is a halogen anion which can be Cl^- , Br^- , or I^- . Since a perovskite formed by three main elements, the limits on ionic sizes of each component then so-called the Goldschmidt tolerance factor for a particular perovskite has been defined as:

$$t = \frac{r_A + r_X}{\sqrt{2}(r_B + r_X)} \quad (1.1)$$

Where r_A , r_B , and r_X are the ionic radii of the A, B, and X components of the perovskite lattice. $t = 1$ correspond to a perfectly packed structure, and it can be varied only in a restricted range (0.8 to 1) [2]. For most perovskites it has been stated to lie between 0.8 and 0.9 [3].

The organic-inorganic hybrid perovskite materials have amazing electrical and optical properties. First, it has larger Bohr radius [4], a high dielectric constant, and a weak exciton binding energy (<10 meV) [5]–[7] that permit a fast dissociation of the exciton at room temperature, secondly, it has a long carrier diffusion length (up to 1 μm for thin films) [8] and high carrier diffusion velocity that prevent a quick recombination. Thirdly, the iodide compounds have an appropriate band-gap of about 1.5-1.6 eV that can absorb efficiently the UV-Vis spectral range[4]. These

properties can be tuned by varying the A, B, and X ions [9] and the appropriate selection of different cations and organic anions will change the band-gap of the material [10].

In PSCs, the absorber is typically sandwiched between an electron transporting layer and a hole transporting layer. The photo-generated charge carriers diffuse to the selective contacts. The electrons are then injected into the electron transporting layer and the holes into the hole transporting layer. Due to the charge separation and collection a current is generated. Classically, Au (or Ag) acts as the back contact while FTO (or ITO) is the front contact of the device. Figure 1.6 shows the typical direct structure of a PSC.

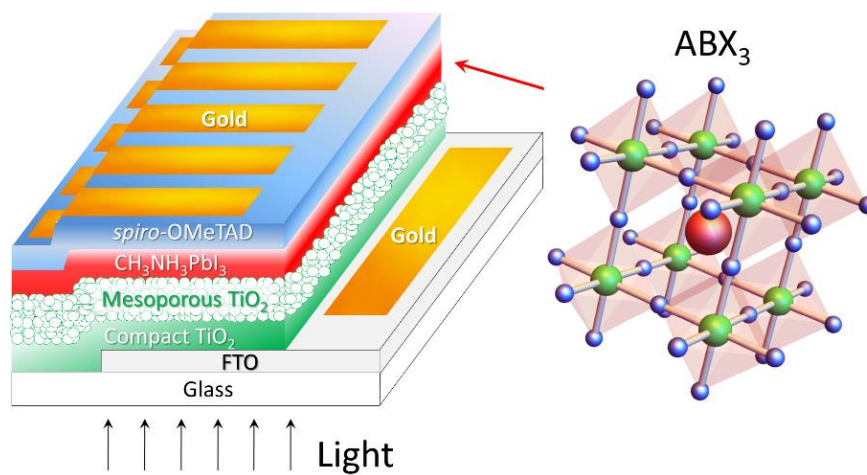


Figure 1.6. Perovskite solar cell structure.

Due to the unique properties of the perovskite materials, they have become the most promising candidates for high-efficiency and low-cost solar cells. From the finding of Kojima et al. in 2009 who first used the CH₃NH₃PbI₃ and CH₃NH₃PbBr₃ perovskites as a sensitizer in dye-sensitized solar cells [11], this subject has attracted a large attention of the solar cells research community and has become one a very hot research topic these last years. This is illustrated by the number of papers annually published on the topic (Figure 1.7) and it has resulted in an amazing efficiency of 23.3 % reached within a short time as shown in the NREL chart (Figure 1.8).

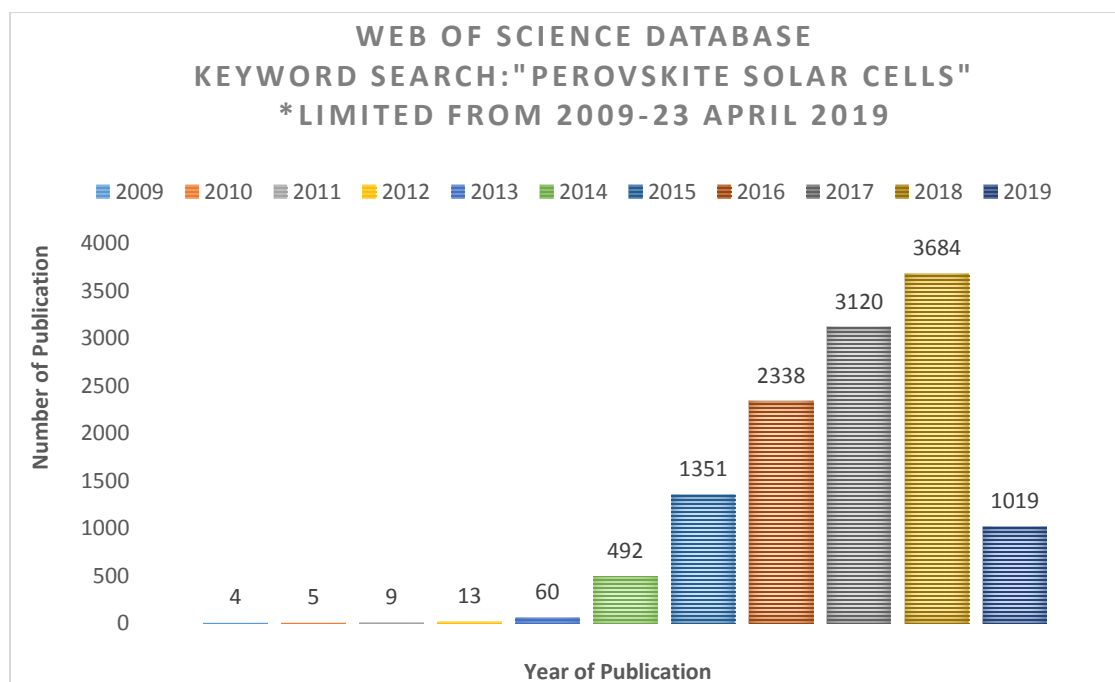


Figure 1.7. Number of papers on perovskite solar cells published from 2009 to April 23th, 2019 (source: Web of Science Database, accessed in 23 April 2019).

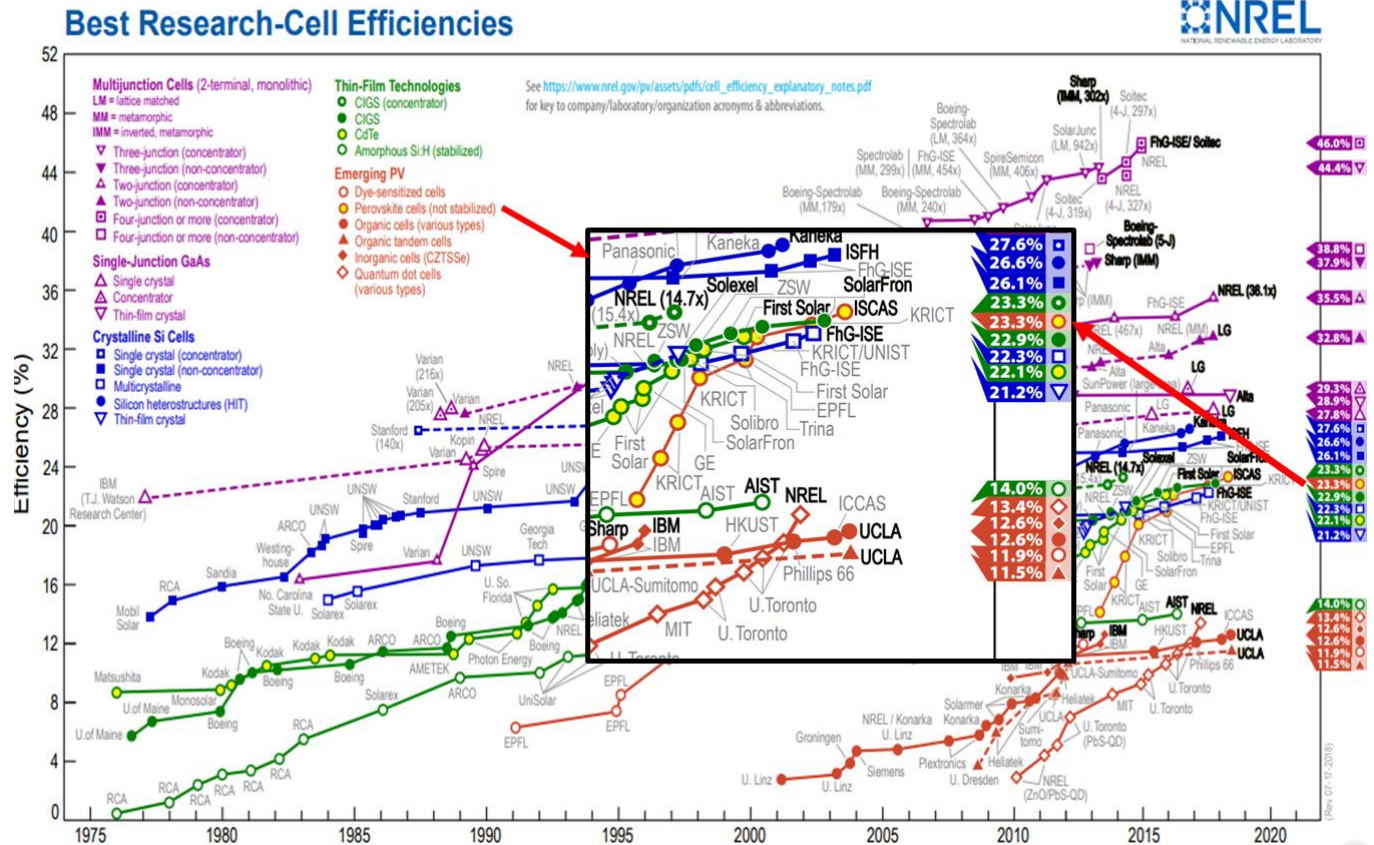


Figure 1.8. Chart of the best-cell efficiency of photovoltaic devices recorded by NREL [NREL chart: <https://www.nrel.gov/pv/cell-efficiency.html>].

The classical methylammonium lead triiodide ($\text{CH}_3\text{NH}_3\text{PbI}_3$) is the most used compound in perovskite solar cells (PSCs) studies. However, recently, multiple cation perovskite containing a mixed organic and inorganic cation ($\text{CH}_3\text{NH}_3^+ + (\text{NH}_2)_2\text{CH}^+ + \text{Cs}^+$) and mixed anions (Cl^- and Br^-) showed better performances as well as better stability.

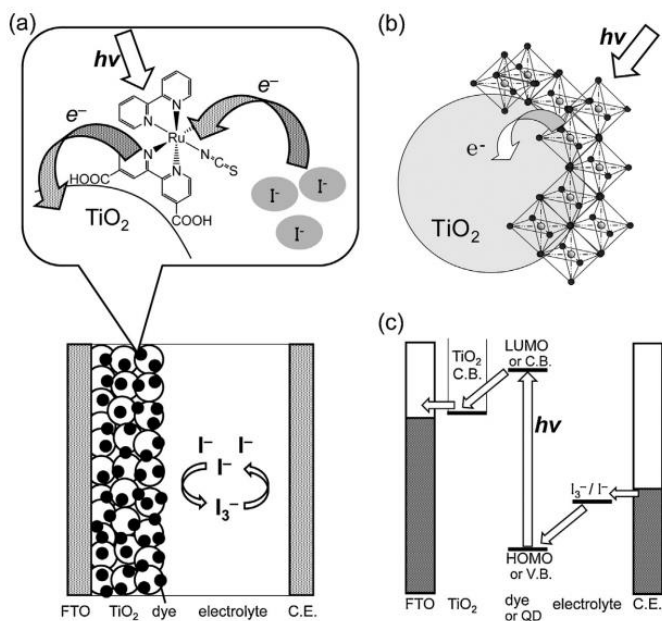
I.3. Brief description of the perovskite solar cells evolution

The perovskite solar cells (PSCs) originated from the dye-sensitized solar cells (DSSCs). The organometal halide perovskites (HPs) was firstly used as sensitizers in a photo-electrochemical cells where $\text{CH}_3\text{NH}_3\text{PbBr}_3$ and $\text{CH}_3\text{NH}_3\text{PbI}_3$ were tested as quantum dots in replacement of a dye [11].

In DSSCs, a mesoporous thick layer of a wide bandgap semiconductor (typically TiO_2 anatase) is sensitized to solar light by the adsorption of a monolayer of a dye (D). Excitons are generated in the dyes by the transition of electrons from the HOMO level to the HUMO levels (D^*). The

electrons are then quickly injected from the photo-excited dye to TiO_2 and the dye cation is produced (D^+). This is followed by the regeneration (reduction) of the oxidized dye by iodide in solution which is oxidized in tri-iodide (I_3^-). I_3^- is finally regenerated at the cell counter-electrode by reduction and the current flow in the external circuit. The general functioning mechanism is summarized in Figure 1.9a. One can note that the liquid electrolyte that contains the redox couple can be replaced by a molecular p-type semiconductor but the PCE is less in this case.

The initial PCE was 3.81% for the first perovskite sensitized solar cells published by Kojima et al., prepared by spin-coating the perovskite precursor solution on top of a mesoporous TiO_2 film on FTO glass substrate. In these cells, like in DSSCs the holes were transported by a redox couple dissolved in an organic liquid electrolyte. The power generation mechanism was described as similar to that in a DSSC as shown in Figure 1.9b and 1.9c. Park et al. followed this finding by a significant improvement of PCE to 6.5% by incorporating the 2-3 nm sized of perovskite $\text{CH}_3\text{NH}_3\text{PbI}_3$ nanocrystal to the TiO_2 surface [12]. However, the cells were not stable due to the dissolution of the perovskite by the acetonitrile solvent.



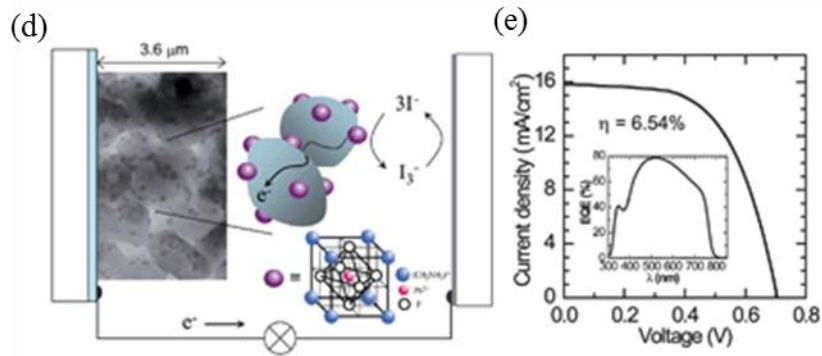


Figure 1.9. (a) Schematic drawings for power generation in dye-sensitized solar cells. (b) Schematic drawing for perovskite-sensitized solar cell. (c) Energy diagram for power generation. C.B and V.B are the conduction band and the valence band, respectively. C.E is the counter electrode. QD is quantum dot [11]. (d) Illustration of the incorporating the 2-3 nm sized of perovskite $\text{CH}_3\text{NH}_3\text{PbI}_3$ nanocrystal to the TiO_2 surface. (e) Solar cell J - V curve and EQE of (d) [12, p. 5].

Liquid-based PSCs have durability problem due to the liquid electrolyte in the device. On May 2012, Snaith et al. submitted a paper in which an all-solid-state perovskite-sensitized solar cells was presented which was based on meso-superstructured HPs and Spiro-OMeTAD as the hole transporting material instead of an iodine/iodide-based electrolyte [13]. The active layer was $\text{CH}_3\text{NH}_3\text{PbI}_2\text{Cl}$ that originated from dissolving PbCl_2 and $\text{CH}_3\text{NH}_3\text{I}$ in DMF solvent. It resulted in a PCE of 7.6% using mesoporous TiO_2 and 10.9% for Al_2O_3 -based devices (Figure 1.2). Park et al. also submitted the solid-state PSCs two months later, which exhibited 9.7% of PCE by using $\text{CH}_3\text{NH}_3\text{PbI}_3$ as the absorber [14]. They assumed a power generation mechanism similar to that in DSSCs, the electrons being injected from perovskite to the conduction band of TiO_2 . The chloride-containing perovskite proposed by Snaith et al. did not rely on the sensitization mechanism while the latter one reported by Park et al. assumed opposite. These two main ideas became the sources of PSC studies [15].

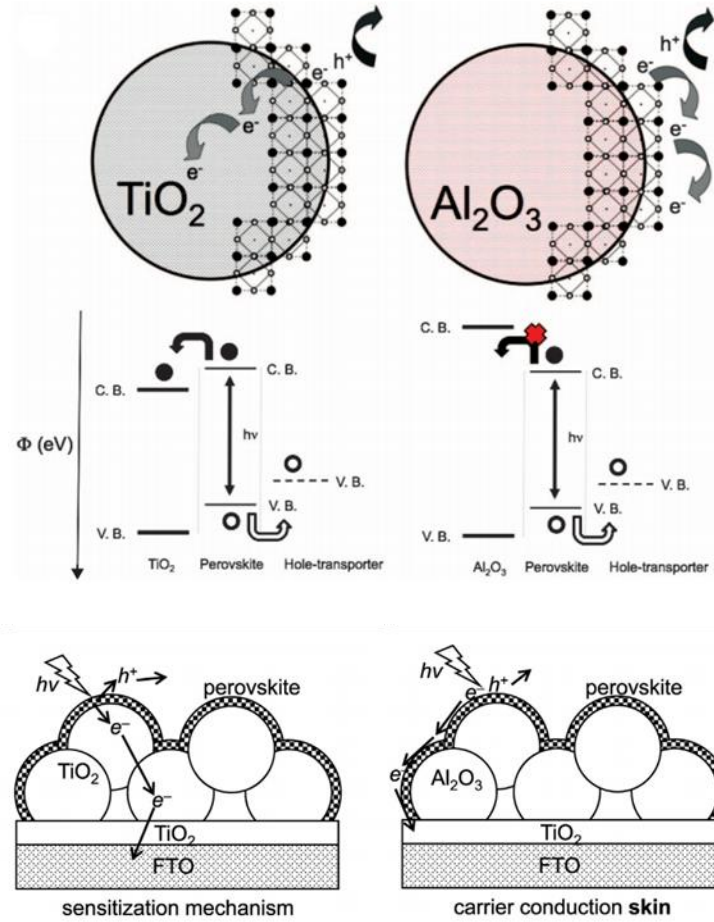


Figure 1.10. Schematic illustration of the charge transfer and charge transport in perovskite-sensitized TiO_2 solar cells and in non-injecting Al_2O_3 -based solar cells with the band energy alignment (the solid circle is an electron and the open circle is a hole) [13].

Grätzel et al. [16] reported a 15% of PCE in 2013 for a perovskite layer prepared by a sequential deposition technique reported previously by Mitzi et al [17]. The PbI_2 layer was first deposited on the TiO_2 layer and then immersed into a $\text{CH}_3\text{NH}_3\text{I}$ solution in order to be converted into perovskite within the nanoporous host (see Figure 1.11). This deposition technique was claimed to permit a better control of the perovskite morphology and to increase the reproducibility.

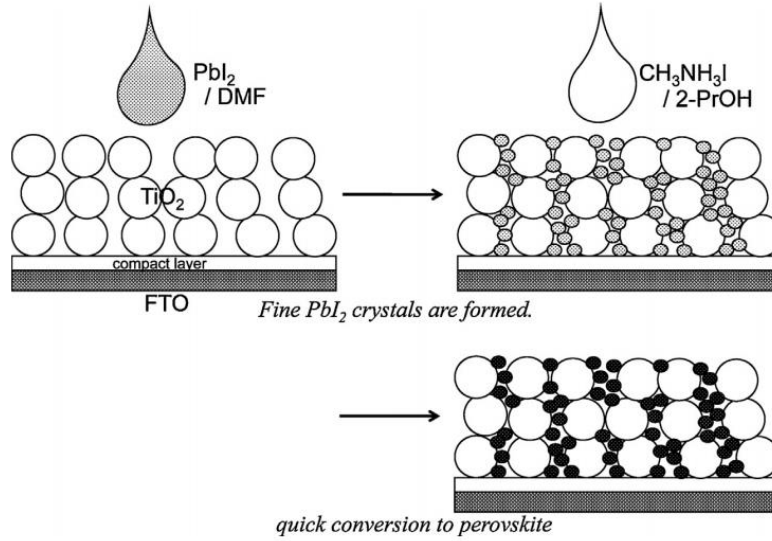


Figure 1.11. Schematic drawings for the perovskite preparation with the sequential deposition method [16].

The researchers also considered the use of a mesoporous oxide layer. On June 2013, Snaith et al. submitted two papers without incorporating the mesoporous layer (planar hetero-junction) PSCs which showed 11.4% [18] of PCE when the perovskite was prepared by a solution process (the mesoporous-based cells procedure) and 15.4% [19] of PCE for the perovskite prepared by dual-source vapour deposition process. These results showed that the mesoporous oxide layer is not necessary to produce efficient devices. Finally, the architecture evolution of perovskite solar cells is summarized in Figure 1.12.

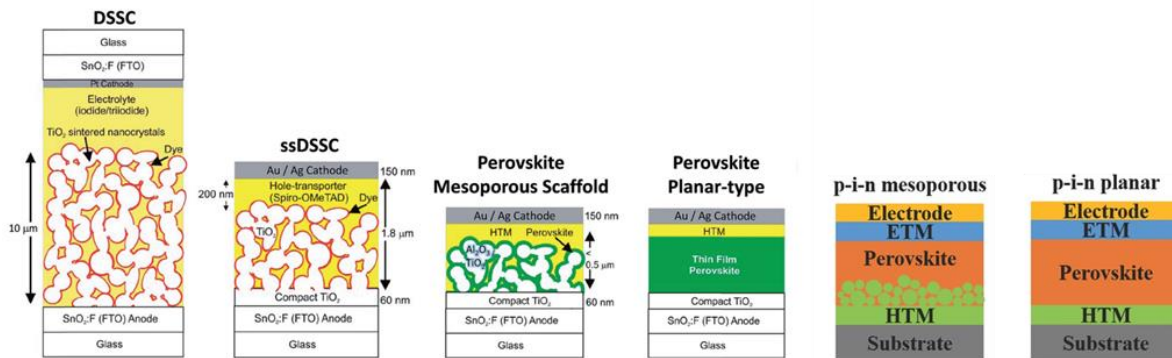


Figure 1.12. The architecture evolution of PSCs [20], [21].

Inverted architecture of PSCs has also been studied. The PCE was only 3.9% PCE in the first publication [22]. However, later, their PCE was significantly improved with four papers which

reported efficiencies of 16.3% [23], 16.5% [24], 17.1% [25] and 17.7% [26]. Mostly, the common architecture used in PSCs are the mesoporous-based and planar-based PSCs.

A significant improvement in the efficiency (19.3%) was reported by Yang et al. and published online in August 2014 by adapting the planar-heterojunction architecture [27]. They carried out the delicate control of the carrier dynamics throughout the device by incorporating yttrium-doped TiO_2 as the electron transport layer. The experiment was conducted by solution-based at low temperature and in the air. In May 2014, Cheng et al. published a dripping anti-solvent method to promote fast-crystallization of the perovskite layer. By using chlorobenzene, a densely packed crystalline perovskite was obtained and led to a 16.2% PCE [28]. This preparation method became one of the most used in the studies on PSCs then. The solvent engineering was also introduced by Han et al. [29] in 2014. DMSO used as a solvent instead of DMF showed smaller distribution of particle sizes and resulted in less deviation in the cells efficiency.

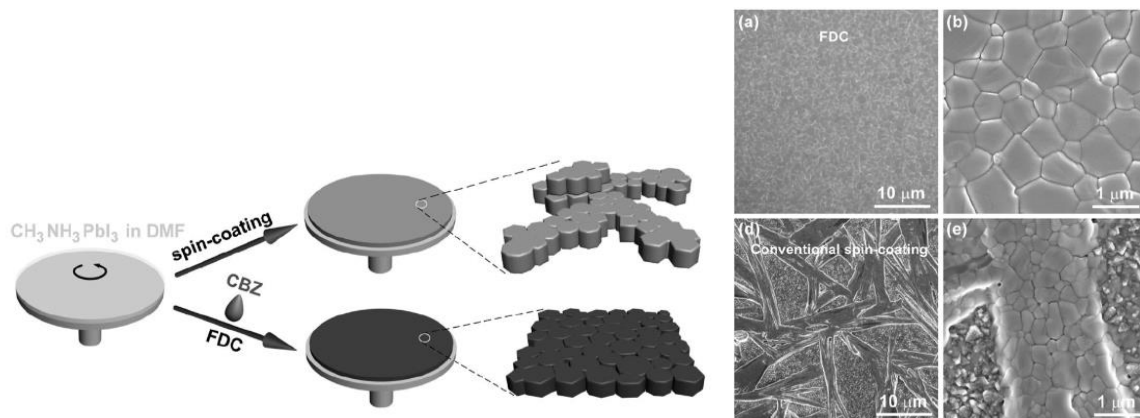


Figure 1.13. Fast deposition crystallization (FDC) (left), SEM top-view images from FDC and conventional deposition (right) [28].

Another remarkable progress was the appearance of the mixed cation perovskite reported by Seok et al. in 2015 [30]. Mixing formamidinium (FA) and methylammonium (MA) formed $(\text{FAPbI}_3)_{0.85}(\text{MAPbBr}_3)_{0.15}$ perovskite structure exhibited 18.4% of the efficiency. Since then, many PSCs papers have adopted this new perovskite structure and it resulted in an efficiency of more than 20%, also in our group (Pengjiu Wang, “Design of oxide contacts and mixed cation hybrid perovskite for highly efficient solar cells”, PhD thesis, 2018). Salida et al. then showed that the solar cell efficiency could be increased by adding small amounts of Cs^+ [31] and/or Rb^+ ions [32].

On February 2015, Seok et al. [33] reported the intramolecular change during the preparation of perovskite layers by replacing the DMSO molecules intercalated in PbI_2 by external FAIs to form highly efficient FAPbI_3 -based PSCs with a certified PCEs exceeding 20%. Park et al. reported the use of DMSO adducts in preparation of MAPbI_3 perovskite's precursor that lead to a 19.7% PCE [34].

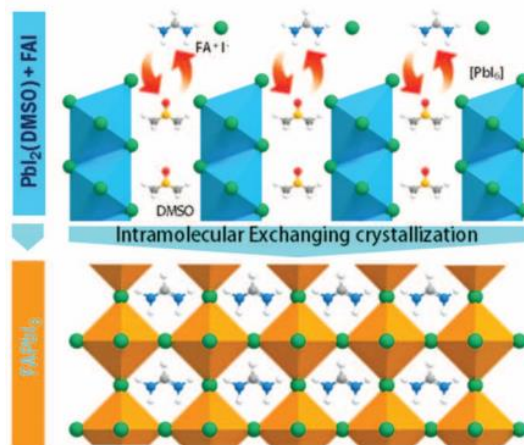


Figure 1.14. Illustration of intramolecular change introduced by Seok et al [33].

On August 2015, Nazeeruddin et al. reported the advantage of using a PbI_2 -rich precursor solution which cells exhibited better performances compared to the stoichiometric case with a PCE at 19.09% [35]. Interestingly, Park's group found the opposite result, they reported the better performances for an excess of MAI [36]. The investigation of the un-stoichiometric case was also studied for mixed cation $(\text{FAPbI}_3)_{1-x}(\text{MAPbBr}_3)_x$. Several papers such as Nazeeruddin, Grätzel, and Hagfeldt et al. reported that changing the PbI_2/FAI ratio resulted 20.8% of PCE for 1.05:1 PbI_2/FAI ratio [37], Seok et al. added 5.7 mol % of PbI_2 to $(\text{FAPbI}_3)_{0.85}(\text{MAPbBr}_3)_{0.15}$ and the cells exhibited a 20.1% PCE [38]. The Grätzel group reported the treatment of the samples with vacuum after the spin-coating process and it resulted in a 20.5% PCE for a 0.16 cm^2 mask and 20.3% for a 1.00 cm^2 mask [28]. An improvement was observed by modifying the perovskite surface using a FABr solution spin-coated on top of $(\text{FAPbI}_3)_{0.85}(\text{MAPbBr}_3)_{0.15}$ perovskite layer. This technique showed 21.31% PCE [39].

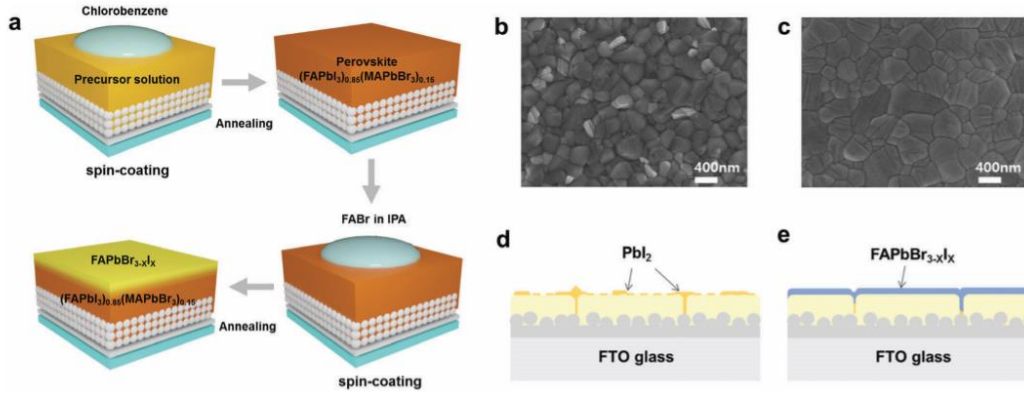


Figure 1.15. (a) Illustration of a method for fabricating a continuous graded perovskite film by further spin-coating FABr solution in isopropanol on the $(\text{FAPbI}_3)_{0.85}(\text{MAPbBr}_3)_{0.15}$ perovskite film. SEM top-view images of an as-prepared film (b) and a passivated film (c), respectively. Proposed change of cross sectional structures from the as-prepared perovskite film (d) to the passivated film (e) [39].

The iodide-management was proposed by Seok et al., in mixed cation perovskite for performance improvement. They prepared the perovskite layer by using the 2-step deposition technique. The PbI_2 and PbBr_2 mixed solution in DMF/DMSO was first spin-coated on TiO_2 layer, then the mixture FAI and MABr dissolved in isopropyl alcohol was spin coated. By using this technique they could report a 22.6% PCE and a NREL certified 22.1% PCE [40]. Adding 5% cesium into mixed cation perovskite resulted a 21.1% PCE [31] and by incorporating Rb^+ to the perovskites, Saliba et al. showed the 21.8% PCE for RbCsFAMA system [32]. Using the latter composition, they also reported in 2016 the used of CuSCN inorganic hole transporting material which exhibited a 20.4% PCE while the Spiro-OMeTAD-based cells resulted in 20.8% PCE [41]. Incorporating Rb and Cselements made a reproducible perovskite layer. Segawa et al. also reported recently a potassium-doped perovskite which showed over 20% of PCE without hysteresis [42]. Finally, the highest record PCE for perovskite solar cells until today is 23.3% (shown by NREL chart in Figure 1.8) which is superior to other thin film solar cell technologies.

I.4. The working principle of perovskite solar cells

Figure 1.16 shows the energy levels and mechanism of charge-transfer processes in a TiO_2 /perovskite/HTM cell. The process started by (1) the photo-excitation of the perovskite absorber and creation of electron-hole pairs after sunlight irradiation. Charge separation then occurred through two possible primary reactions: (2) photo-generated electrons in the perovskite are injected to the TiO_2 , and (3) the holes transfer to the HTM layer. Finally, both electrons and

holes are collected to the front and back contact, respectively, in order to generate the photocurrent. However, there several undesirable processes happen in PSC such as; (4) recombination of the photo-generated charge carriers either radiative or non-radiative as a result of exciton annihilation, as well as recombination of the charge carriers at the three interfaces: (5) TiO_2 /perovskite, (6) perovskite/HTM, and (7) TiO_2 /HTM. The latter may occur only when the perovskite layer is not fully covering. Based on these processes, it is clear that the charge recombination processes (4-7) should occur at a slower time scale than charge generation, separation, and extraction processes (1-3) to get high PCE of PSCs.

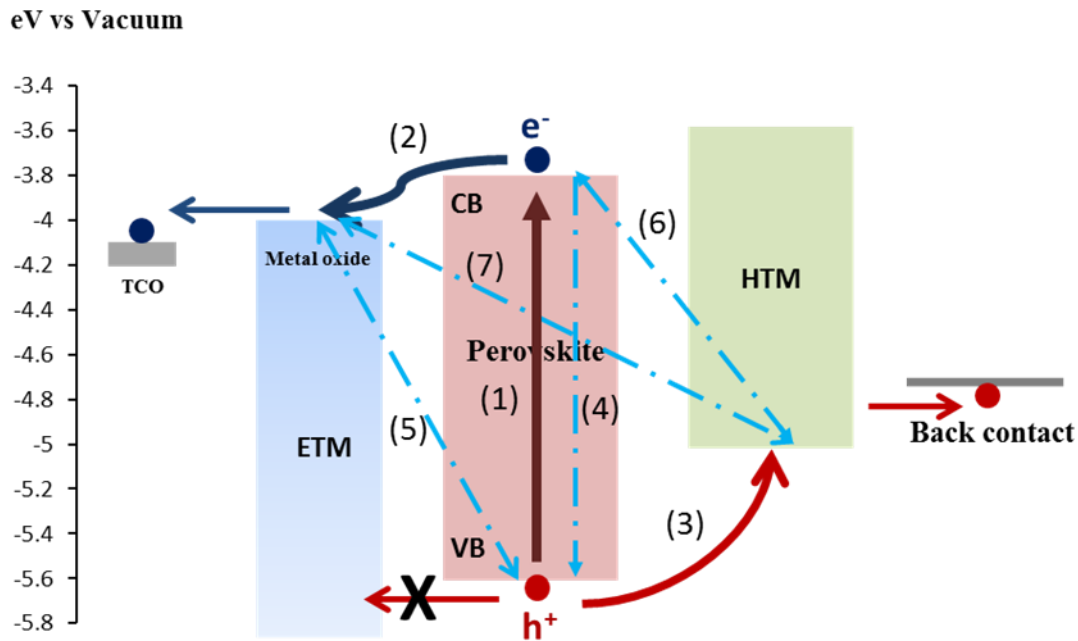


Figure 1.16. Schematic representation of the energy levels and electron transfer processes in perovskite solar cells [43].

I.5. Components of perovskite solar cells

I.5.1. The electron transporting layer

The role of the electron transporting layer (ETL) is to extract electron carrier from the perovskite and ensures its transport to the front contact of the cell. This layer is typically made of an oxide semiconductor with a wide band gap. This layer prevents the direct contact between the transparent conducting oxide (TCO) and the perovskite by well covering the TCO surface. In order to get high performance perovskite solar cells, the ETL must meet several criteria: (a) a good optical transmittance in the visible range; (b) proper band energy levels compared to the

perovskite to promote the efficient electron transfer and well-blocking of the holes; (c) good electron mobility; (d) easy fabrication of high quality of the ETL. This layer is mostly prepared by a simple deposition technique, either spin-coating or spray pyrolysis. It typically needs a 20-100 nm of thickness in optimized cell. Its thickness can be easily controlled by varying the precursor concentration and speed in the case of spin-coating [44]. Mostly used in PSCs as ETL is a compact TiO_2 that deposit directly on top of TCO substrate. TiO_2 is the most widely used ETL material in PSCs due to its matching bandgap/energy levels and high transmittance. Recently, the used of SnO_2 ETL has been reported in many papers to be one of the promising thin layer especially for planar structure of PSCs [45]–[56]. An extensive study of SnO_2 will be provided in Chapter V.

In meso-structured PSCs, a mesoporous layer is used combined with the compact layer. Both these layers (a compact TiO_2 and a mesoporous- TiO_2 layer on its top) are called ETL and is the configuration the most used now. Besides the mesoporous TiO_2 , a porous ZnO is also popular in PSCs study because of its similar energy band position and physical properties to TiO_2 with a higher electron mobility. The latter property is important for the fast electron transport and recombination reduction that potentially improve the performance of the PSCs [57]–[59]. Other structure such as fullerene and its derivatives have also been used as a ETL in PSCs [13], [60]–[64].

I.5.2. The perovskite layer

The absorber material for the solar cells must have a broad range of absorbance between the UV-visible to the near infrared spectral range in order to harvest light efficiently while generating a sufficient voltage. Therefore, the optimum band gap for solar cells is around 1.4 eV-1.5 eV [65]. The organic-inorganic hybrid perovskite material has some amazing properties for solar cells. HPs have a band gap energy that can be varied between 1.2 eV and 2.2 eV by changing their composition. They also exhibit a long carrier diffusion length (up to 1 μm) [8] and high carriers mobility that range from $7.5 \text{ cm}^2\text{V}^{-1}\text{s}^{-1}$ for electrons [66] to $12.5 \text{ cm}^2\text{V}^{-1}\text{s}^{-1}$ - $66 \text{ cm}^2\text{V}^{-1}\text{s}^{-1}$ for holes. [67] These properties are very important for reducing the recombination and producing high performance solar cells. A large Bohr radius (4.6 nm for $\text{CH}_3\text{NH}_3\text{PbI}_3$ bulk single crystal [68]), a high dielectric constant, and weak exciton binding energy ($< 10 \text{ meV}$) [5] that allows the carriers to dissociate quickly at room temperature [69].

$\text{CH}_3\text{NH}_3\text{PbX}_3$ (X is a halogen atom such iodine, bromine, and chlorine) is the most popular composition and was used in the early studies on PSCs. Its optical bandgap varies between 1.5 eV and 2.3 eV depending on the halide element. The bandgap for $\text{CH}_3\text{NH}_3\text{PbI}_3$ and $\text{CH}_3\text{NH}_3\text{PbI}_{3-x}\text{Cl}_x$ found in the literature is 1.58 eV [65], [70] and 1.55 eV [13], respectively. It was also found later that the bandgap can be tuned by varying the A cation (methylammonium (MA: CH_3NH_3^+), formamidinium (FA: $\text{HC}(\text{NH}_2)_2^+$), cesium (Cs^+), rubidium (Rb^+), potassium (K^+)) in the perovskite structure (see Figure 1.6). Due to the difference in the cation size (ionic radius) of MA^+ (2.70 Å [71]), FA^+ (2.79 Å [71]), and Cs^+ (1.81 Å [69], [72]), the bandgap can be tuned accordingly. Eperon et al. found that the bandgap is smaller when the cation sizes is increased [65]. Therefore, the variation of the bandgap followed the sequence Cs^+ (1.73 eV) > MA^+ (1.57 eV) > FA^+ (1.48 eV) [65]. By incorporating FAPbI_3 as the absorber in PSC, a PCE of 14.2% can be achieved [65]. Combining FA and Br is expected to increase the current and the voltage, respectively, since Br has smaller bandgap than iodide. Seok et al, reported a PCE as high as 18.4% by mixing FAPbI_3 and MAPbBr_3 with 85:15 ratio making the $(\text{FAPbI}_3)_{0.85}(\text{MAPbBr}_3)_{0.15}$ perovskite [30]. This perovskite is one of the most used for high efficiency PSCs.

This layer is commonly prepared by a simple and low-cost solution technique such as one-step deposition [14], [73]–[77] and two-step sequential deposition method [16], [17], [78]. Vapor-based deposition technique have also been developed such as dual-source vapor deposition [19], [20], [79]–[81] and vapor-assisted solution process [82]–[85]. More detail about the solution preparation techniques will be explained in Chapter II.

1.5.3. The hole transporting layer

The hole transporting material (HTM) is the third important component in PSCs. It permits the holes transfer from the perovskite to the HTM and its transport to the back contact of the device. This HTM must have proper energy levels alignment to the perovskite for effective charge transport, high conductivity, thermal, morphological, and photochemical stability. Moreover, it must have hydrophobic property to protect the device and avoid its fast degradation.

There are three main categories of solid-state hole transporters: inorganic, polymeric, and molecular. The interests of the inorganic HTMs are their high hole mobility, high-stability, large bandgap and low-cost fabrication process [86]–[94]. Inorganic compounds such as CuI , NiO , and CuSCN have been investigated in PSCs by several groups with a noticeable device performances

increase over the last years [15], [16]. Incorporating CuI in perovskite solar cells has led to a promising result, with 16.8% for the highest PCE in an inverted structure (p-type layer at the bottom) [89]. NiO-based HTM with good optical transparency and appropriate energy levels showed comparable performances when incorporated in inverted structure [97]–[101]. Surprisingly, Grätzel et al. successfully realize in 2017 a high efficiency over 20% PSC based on CuSCN HTM [41].

The polymeric-based HTMs are also explored in a large extent for PSCs due to their high hole mobility and good environmental stability. Poly(3,4-ethylene dioxythiophene) polystyrene sulfonate polymer (PEDOT:PSS), poly (3-hexylthiophene) (P3HT), and poly tri-arylamine (PTAA) are some of the polymeric HTMs that have been studied in PSCs. PTAA was the first polymer incorporated in PSCs [33] and led to the highest PCE (>20%) reported amongst polymeric HTMs [33]. P3HT and PEDOT:PSS were studied intensively with very low efficiency at the beginning (below 1% for P3HT) [76]. Since then a lot of improvements have been implemented such as varying the molecular weight of P3HT [102], F4TCNQ doping [103], and Co(II)-TFSI doping which lead to a promising PCE as high as 16.28% [104]. On the other hand, with appropriate energy levels, PEDOT:PSS can also facilitate an effective hole extraction from the perovskite and a 17% of PCE has been reported [105]. However, this type of HTM has limited chemical stability due to its acidity and hygroscopic nature [95], [106], [107].

The most common HTM materials used in PSC since the beginning is the organic 2,2',7,7'-tetrakis-N, N-di(4-methoxyphenyl)amine-9,9'-spirobifluorene (Spiro-OMeTAD). As detailed in Chapter III, this compounds must be first oxidized and must be prepared combined with several additives such as LiTFSI salt [16], t-BP [108], [109], and Co-complex [30], [110] for optimum conductivity and operation. Spiro-OMeTAD is an organic p-type semiconductor with a large bandgap of about 3.0 eV and is almost transparent when deposited as a thin film on a substrate. Several desirable properties such as good solubility, high glass transition temperature due to a large molecular weight, transparency over the visible wavelength region and solid-state morphology are the reason for the wide use of Spiro-OMeTAD in PSCs [111]. Doped Spiro-OMeTAD has a hole mobility in the range of 1×10^{-5} to $1 \times 10^{-4} \text{ cm}^2\text{V}^{-1}\text{s}^{-1}$ as reported in the literatures [112]–[115]. Incorporating this HTM has permitted the fabrication of PCSs with a high PCE >22%. Other organic molecule HTMs based on pyrene, thiophene, porphyrins, carbazoles,

etc, have also been tested in PSC due to their easily high purity synthesis process, low-cost of starting materials, versatility and good chemical and environmental stability. High PCEs have been reported by many paper with these molecules such as Yang et al. [116] with a 18.8% PCE by introducing a 4,4'-cyclohexylidenebis[*N,N*-bis(4-methylphenyl) benzenamine] (TAPC) small molecule, Lee et al. [117] used porphyrin derivatives HTMs which yielded to a 18% PCE for the best result. Malinauskas et al. [118] and Gratia et al. [119] also reported 19.96% for carbazoles substituted to methoxy diphenylamine HTMs. And surprisingly, a 20.2% PCE was achieved by Nazeeruddin et al. using a thiophene-based HTM [120].

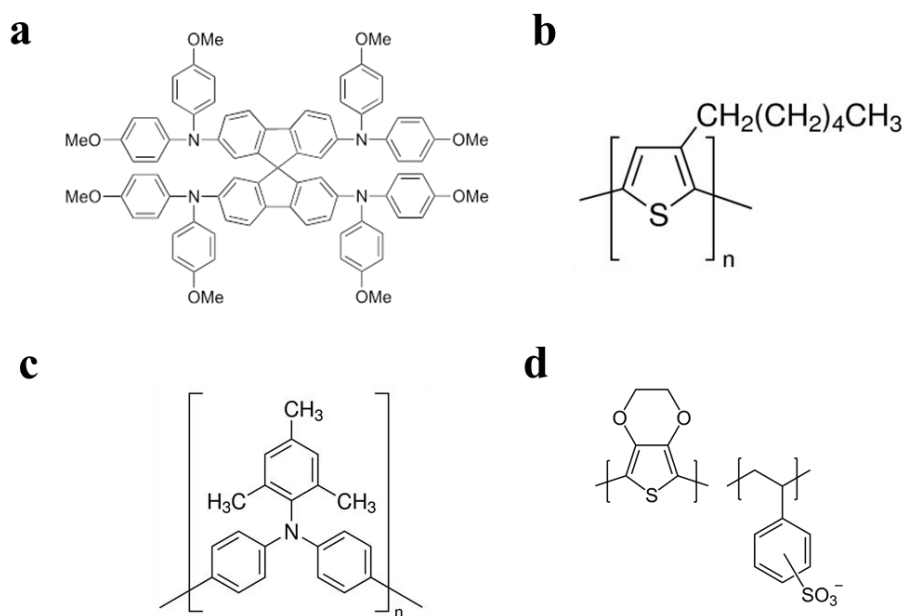


Figure 1.17. Molecular structure of (a) Spiro-OMeTAD, (b) P3HT, (c) PTAA, and (d) PEDOT:PSS.

I.5.4. The back contact layer

The back contacts commonly used in PSCs are a silver or gold layers which are usually prepared by thermal evaporation. They have a low R_{sq} of less than $1 \, \Omega.\text{sq}^{-1}$ and high light reflectivity. Both Au and Ag can react with the halide (iodide) ions in the hybrid perovskite due to the effect of perovskite decomposition and metal migration. Due to the expensive cost of gold and silver, there have been efforts to replace it by low-cost back contact such as carbon-based contact in HTM-free PSC [121]–[124], Al, Cu, etc. Among them, carbon is the cheapest material and showed much longer stability, over 10,000 h with zero lost in PCE tested at ambient air humidity and stabilized temperature of 55°C (continuous illumination) [125], [126].

I.6. The characterizations of perovskite solar cells and of their components

I.6.1. Material characterizations

Perovskite layer

The as-prepared perovskite layer were characterized by using x-ray diffraction (XRD) in order to know the formed crystal structure of the perovskite. This technique allowed us to detect the impurities, and phase of the perovskite layer. We have also measured the optical absorbance properties of layers and calculated their optical bandgap from the absorbance curves. The morphology of the samples were imaged by the scanning electron microscopy (SEM) technique. This technique allowed us to see the distribution and the size of the grains of the perovskite layer. These techniques were very important to get basic information on our perovskite layers. The thickness of the perovskite layers was evaluated from cross-sectional views obtained by SEM.

Electron transport layer (ETL)

The compact layers (blocking layers) were characterized by using the cyclic voltammetry (CV) in order to see their blocking property. This property is important for realizing a good perovskite solar cell. The thickness of the blocking layer and the mesoporous layer can be evaluated by a profilometer and from SEM cross-sectional views.

I.6.2. Standard solar spectral irradiance

The purpose of the solar cell research is to develop photovoltaic devices that can efficiently convert the energy coming from sun into the easy usable electrical energy. However, the conversion properties of a PV device depend on various parameters, mainly the irradiation spectrum, the total power density and the temperature. Because the actual solar spectrum received by a device will vary with the weather, season, time of the day, and location, a standard spectrum has been defined for the determination of the solar cell characteristics and to permit the comparison of devices prepared in various laboratories.

The spectra are standardized by the American Society for Testing and Materials (ASTM). An important parameter in photovoltaics is the AM that is related to the incident angle of light coming from the sun and crossing the terrestrial atmosphere. θ is the angle between the zenith and the sun light incidence, AM is defined from θ as :

$$AM = \frac{1}{\cos \theta} \quad (1.2)$$

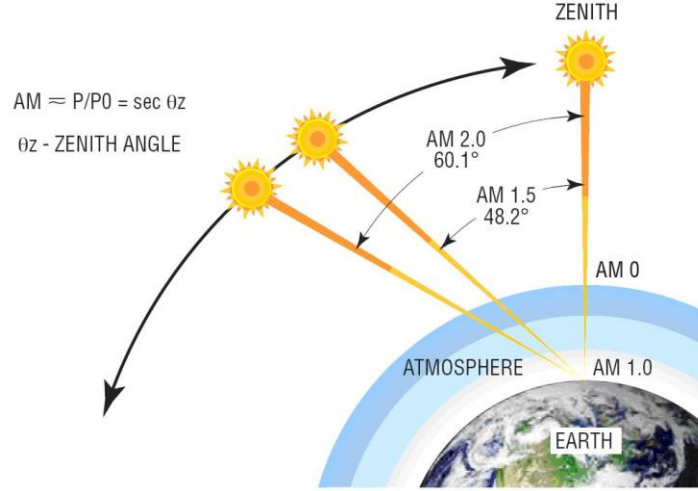


Figure 1.18. Air mass (AM) calculation.

In the Figure 1.18 the solar spectrum used for extraterrestrial application is denoted as Air Mass zero (AM0) based on ASTM standard E 490, and the integrated power of AM0 is 1366.1 W m^{-2} . The shape of this curve is close to the blackbody emission spectrum at 5762 K, the average temperature at the sun surface.

Due to the light absorption and scattering when passing through the atmosphere, the solar spectral irradiance is decreased. Moreover, absorption bands due to O_3 (in the UV), O_2 and H_2O present in the atmosphere appear (Figure 1.18). In the case a θ angle of 48.2° , this solar spectrum is denoted as the AM1.5G (global) standard by ASTM G173, and used for terrestrial applications including direct and diffuse light. The integrated spectral power density of the AM1.5G is standardized at 1000 W m^{-2} or 100 mW.cm^{-2} . The AM1.5D spectrum, also based on ASTM G173, is for terrestrial applications but only includes the direct solar light. It integrates to 888 W m^{-2} . [127] For the sake of comparison, in the literature and in our work, the solar simulators are calibrated with the AM1.5G 1000 W m^{-2} illumination standard and the measurement temperature must be 25°C .

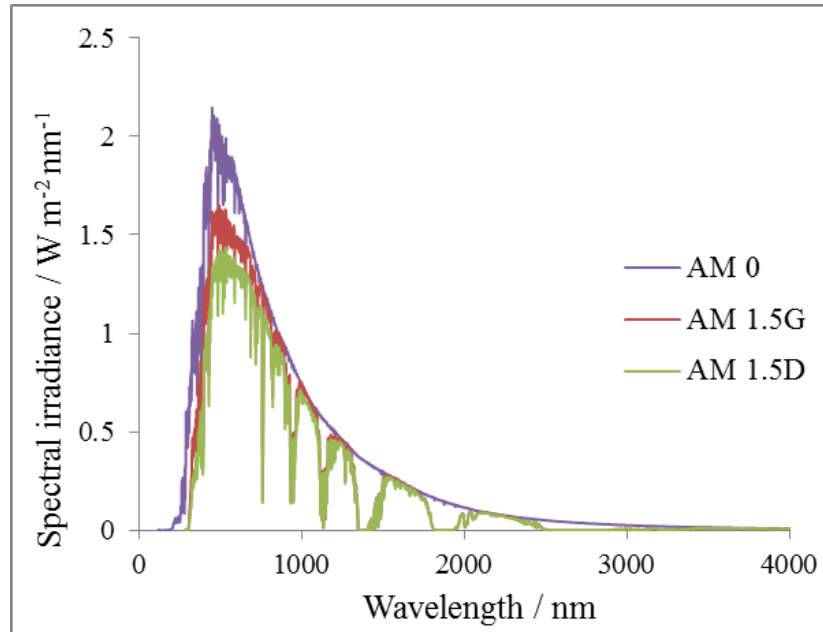
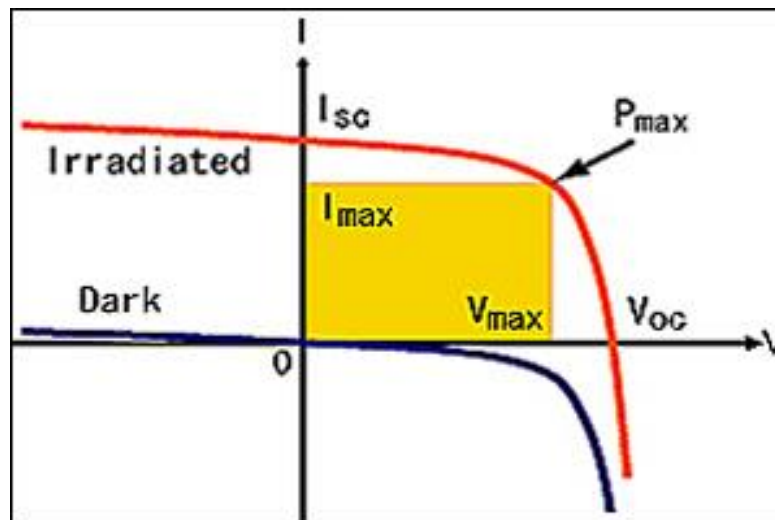


Figure 1.19. Reference solar irradiation spectra according to the standards by American Society for Testing and Materials (ASTM).

I.6.3. Current-voltage characteristics

The standard way to characterize a solar cell device is to measure its current-voltage curve both in the dark and under illumination. The measurement consists in scanning an applied voltage across the solar cell and to record its current response. The cell is illuminated by the AM1.5G filtered spectrum with a power density of 100 mW.cm^{-2} . Examples of curves are shown in Figure 1.20.



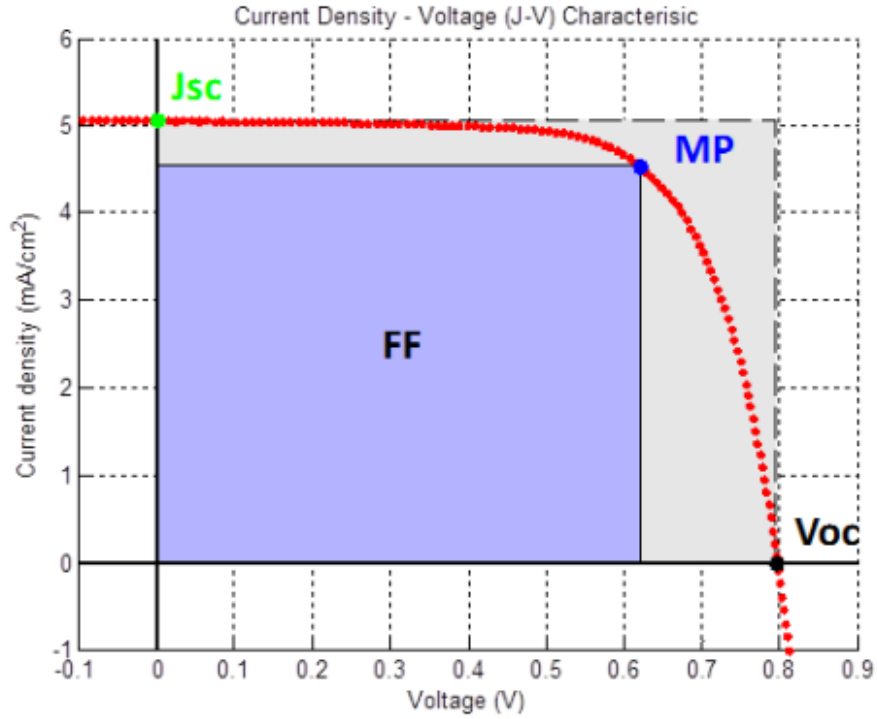


Figure 1.20. Example of current density-voltage (J-V) characteristic curves in the dark and under illumination. MP and P_{\max} are the maximum power point.

The total current density ($J(V)$) is the sum of three terms: the photocurrent density (J_{ph}), the dark diode current density and the shunt current density. $J(V)$ as the function of the applied potential is given by:

$$J(V) = J_{ph} - J_0 \left[\exp\left(\frac{q(V - R_s J)}{nkT}\right) - 1 \right] + \frac{V - R_s J}{R_{sh}} \quad (1.3)$$

with J_0 the saturation current density and J_{ph} the photocurrent density. R_{sh} is the shunt resistance, R_s is the series resistance, n the ideality factor of the diode (equal to 1 if the diode is ideal), T the absolute temperature, k the Boltzmann constant and q the elementary charge. R_s is determined as the inverse of the J-V curve slope at the V_{oc} . It includes the contact resistance at interfaces, the bulk resistance and the sheet resistance of the transparent electrode. R_{sh} is measured as the inverse of the J-V curve slope at zero applied voltage. It comes from non-idealities in the p-n junction, recombination at short circuit and the presence of electronic defects leading to a leakage current.

The power conversion efficiency PCE (%) is defined as the ratio between the maximum power density (at MP point in Figure 1.20) provided by the cell (P_{\max}) and the incident power density (P_{inc}):

$$\text{PCE}(\%) = \frac{P_{\max}}{P_{\text{inc}}} = \frac{V_{\text{oc}} * J_{\text{sc}} * \text{FF}}{P_{\text{inc}}} \quad (1.4)$$

with V_{oc} the open circuit voltage, J_{sc} the short circuit current and FF the fill factor. The FF parameter decreases with the R_s increase and the R_{sh} reduction. The maximum flux of the photogenerated carriers per unit area that are extracted from the solar cell gives J_{sc} . The maximum voltage that can be generated from the solar cell is called the open-circuit voltage, V_{oc} . The J_{sc} depends on several parameters such as sunlight illumination, the total absorbance of the solar cell, the corresponding of the absorber material bandgap to the radiation spectrum, and the recombination loss prior to the extraction. The Fill factor (FF) measures the deviation from ideality. It can range between 0 and 1 and the higher the better for the device performance.

Another important parameter for PSCs is the hysteresis of the J - V curves. These cells present a special feature where the J - V curves measured in the direct and indirect scan direction do not overlap. The difference between both is called the hysteresis and for good cells a not too large hysteresis will be sought for. In the thesis an hysteresis index is defined to quantify this hysteresis effect (see Chapter II, section II.7, the equation number is 2.1).

I.6.4. Quantum efficiency measurement

To investigate the spectral response of the cells, IPCE (Incident photon-to-Electron- conversion efficiency) (also named EQE (External quantum efficiency)) measurements are done. they consist in measuring the quantum efficiency of the solar cells at various light wavelengths:

$$\text{EQE}(\lambda) = \frac{\text{Flux of photoemitted electrons}}{\text{Flux of indident photons}} = \frac{(J_{\text{ph}}(\lambda)/q)}{(\Phi/(h\nu))} \quad (1.5)$$

With:

- λ the wavelength in nm,
- $J_{\text{ph}}(\lambda)$ the photocurrent density (A.cm^{-2}),
- q the elementary charge ($1.602 \cdot 10^{-19} \text{ C}$ or A.s^{-2}),
- Φ the photon flux ($\text{J.s}^{-1}.\text{cm}^{-2}$),

- h the Plank constant ($6.626 \cdot 10^{-34}$ J.s)
- ν the light frequency = c/λ with c the light velocity.

And then :

$$EQE(\lambda) = 1240 \cdot J_{ph}[\text{mA.cm}^{-2}] / (\lambda[\text{nm}] \cdot \Phi [\text{mW.cm}^{-2}]) \quad (1.6)$$

By integrating the $EQE(\lambda)$ curve measured at short circuit over the all solar light wavelength range, the J_{sc} can be found back as shown in Figure 1.21.

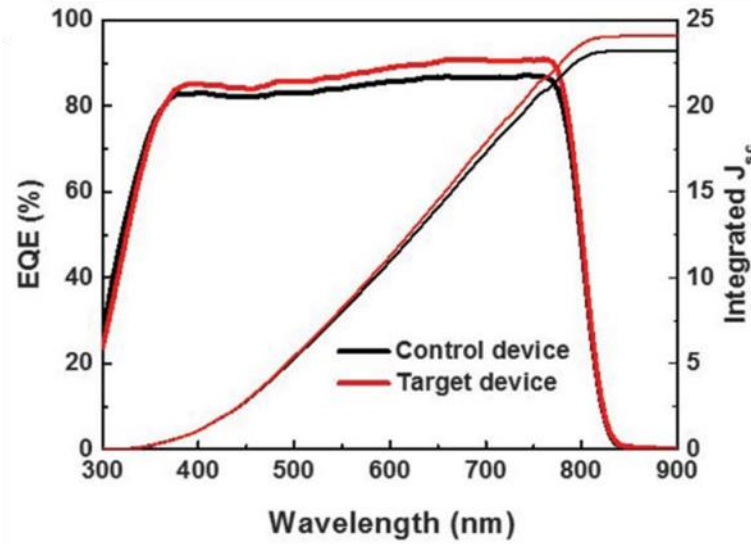


Figure 1.21. Example of EQE spectra and J_{ph} integration curve of high efficiency PSCs. (after : [40]).

I.6.5. Impedance spectroscopy

Impedance spectroscopy (IS) has become a major tool for investigating the properties, functioning and quality of solar cell devices. In this technique, a constant dc voltage (E_s) is applied to the cell with a superimposed ac voltage signal of E_0 amplitude. The cell current response is then measured. This response consists in a dc component (I_s) and an ac one with a I_0 amplitude and a phase shift ϕ (Figure 1.22a).

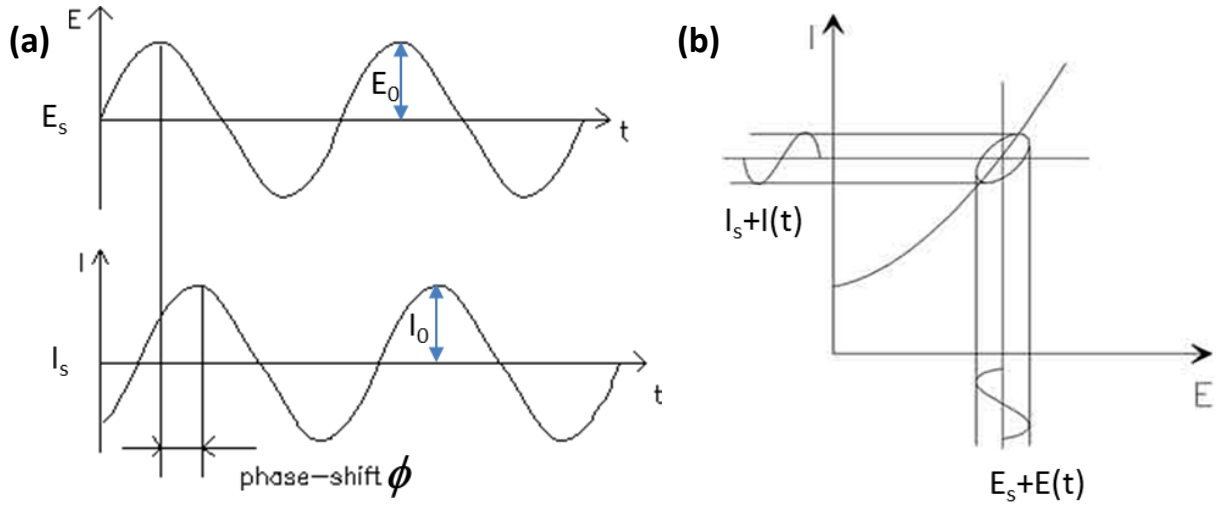


Figure 1.22. (a) Sinusoidal Current Response in a linear system. (b) Steady-state and ac I versus E curves upon impedance measurement.

$$E(t) = E_0 \sin(\omega t) \quad (1.7)$$

$$I(t) = I_0 \sin(\omega t + \phi) \quad (1.8)$$

$$\omega = 2\pi f \quad (1.9)$$

With ω the radial frequency and f the normal frequency.

The impedance $Z(\omega)$ is defined as:

$$Z(\omega) = \frac{E_0 \sin(\omega t)}{I_0 \sin(\omega t + \phi)} = |Z| \frac{\sin(\omega t)}{\sin(\omega t + \phi)} \quad (1.10)$$

With $|Z|$ the impedance magnitude.

For a small signal ($E_0 = 10\text{-}30$ mV), the system becomes pseudo-linear (see Figure 1.22b).

With the Euler's theorem:

$$\exp(i\phi) = \cos \phi + i \sin \phi \quad (1.11)$$

It is possible to express the impedance as a complex function. The potential is described as,

$$E(t) = E_0 \exp(i\omega t) \quad (1.12)$$

and the current response as: $I(t) = I_0 \exp(i(\omega t - \phi))$ (1.13)

Then the impedance is represented as a complex number:

$$Z(\omega) = \frac{E(t)}{I(t)} = |Z| \exp(i\phi) = |Z| (\cos \phi + i \sin \phi) = \text{Re}(Z) + i \text{Im}(Z) \quad (1.14)$$

$$\text{With } |Z| = \frac{E_0}{I_0} \quad (1.15)$$

A Nyquist plot is the presentation of the imaginary part of Z ($-\text{Im}(Z)$) versus the real part of Z ($\text{Re}(Z)$) (Figure 1.23).

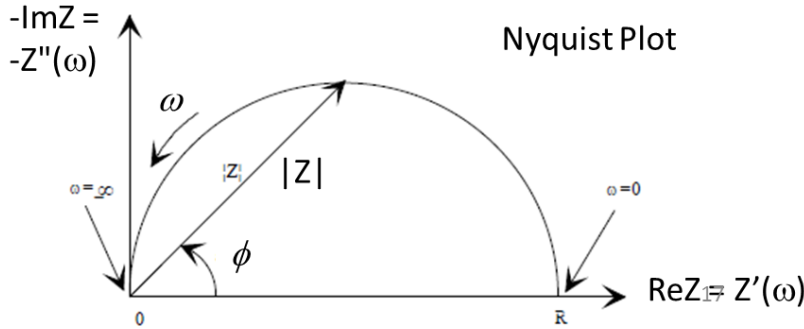


Figure 1.23. Nyquist impedance plot.


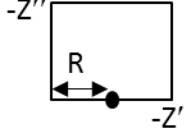
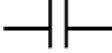
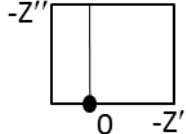
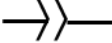
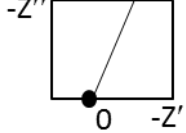

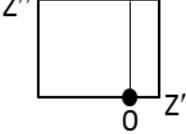
For their analysis, the spectra are fitted with equivalent electrical circuits composed of various electrical elements: resistances, inductances by which voltage are induced in conductor by the magnetic field generated by current and capacitances that correspond to the electrostatic storage of charges induced by an applied voltage between conductors. Collectively, the inductance and the capacitance form the imaginary part of the complex impedance Z'' in Equation 1.14, which is referred to as the reactance while the resistance forms the real part Z' .

The capacitance can be determined from the measurement of the change in the electrical charge, which is described by the equation 1.16.

$$C(\omega) = \frac{I(\omega)}{i\omega E(\omega)} = \frac{1}{i\omega Z(\omega)} \quad (1.16)$$

Many measures of IS can be described by equivalent circuits composed of combinations of a few elements that are indicated in Table 1.1.

Table 1.1. Relationship and impedance corresponding to bulk electrical elements. Furthermore, the corresponding electrical equivalent circuit symbols are presented. The graphical representation of the impedance is displayed in the Nyquist plots where Z' and Z'' are the real and imaginary components respectively.

| Element | Relation | Impedance | Symbol | Nyquist |
|----------------------------|-----------------------|--|--|---|
| Resistor R | $E = IR$ | $Z_R = R$ |  |  |
| Capacitor C | $I = C \frac{dV}{dt}$ | $Z_C = \frac{1}{i\omega C} = -\frac{i}{\omega C}$ |  |  |
| Constant Phase Element Q | | $Z_{CPE} = \frac{1}{(i\omega)^n Q}$ $Q = \frac{1}{ Z }$ |  |  |
| Inductor L | $V = L \frac{dI}{dt}$ | $Z_L = i\omega L$ |  |  |

Equivalent circuits are formed by connecting these elements by wires, representing low resistance paths in the system. When connected in series, the current passing through components is the same, while, when in parallel they experience the same voltage. The impedance of element in series is additive, and for parallel elements the total impedance is the inverse of the sum of the inverse impedance of the individual components. The impedance for the parallel combination of a resistor and a capacitor is described in Equation 1.17. Its Nyquist plot is presented in Figure 1.23.

$$Z(\omega) = \left(\frac{1}{R} + i\omega C \right)^{-1} = \frac{R}{1 + i\omega RC} = \frac{R}{1 + i\omega\tau}$$

$$\tau = RC = \frac{1}{\omega_0}$$
(1.17)

An equivalent circuit consisting of the parallel combination of a R and a C element in addition to a simple series resistance R_1 is shown in the Figure 1.24a. Figure 1.24b-d displays the perspective of the individual planes. The complex Nyquist plot (Figure 1.4c) of the imaginary impedance component as a function of the real component manifests as an arc, often called RC-arc. The top of the arc occurs at the characteristic frequency ω_0 corresponding to a relaxation time τ (Equation 1.17).

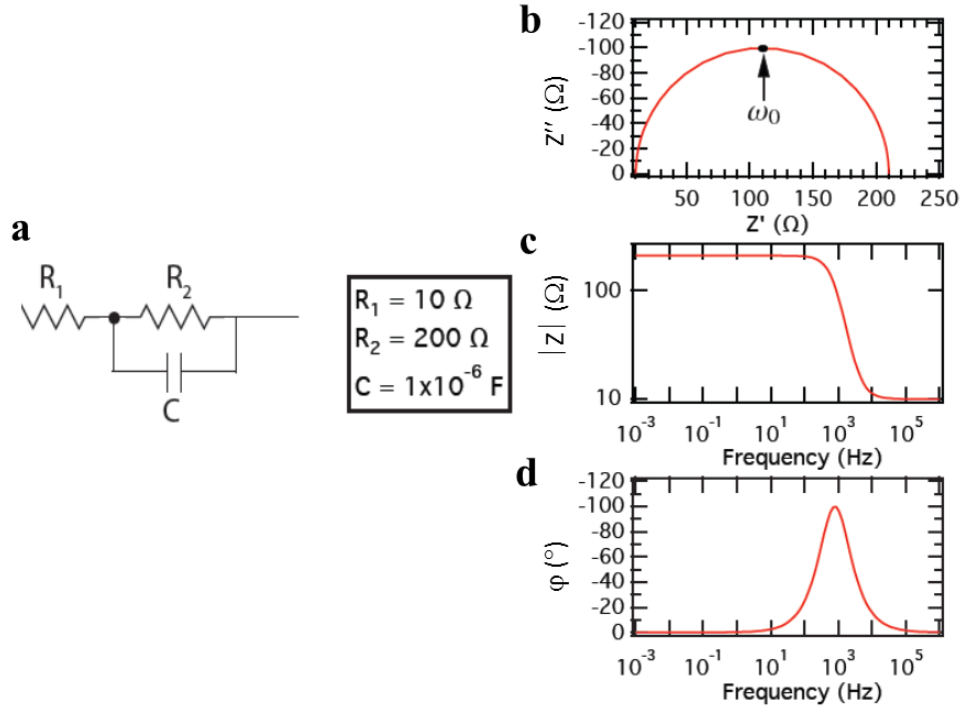


Figure 1.24. (a) Equivalent circuit. (b) Nyquist plot of the spectrum (imaginary as a function of real component). The maximum of the RC-arc takes place at the characteristics angular frequency ω_0 as indicated. (c, d) Bode representations of the impedance spectrum: (c) Magnitude versus the frequency and (d) phase versus the frequency. The simulation was conducted from 1 MHz to 1 mHz.

The high frequency intercept of the arc on the real axis provides a measure of the magnitude of the resistance R_1 associated with the system and the low frequency intercept is equal to $R_1 + R_2$. The addition of a series resistance, R_1 results in the shift of the RC-arc along the real axis. Consequently the dc resistance of this system is the sum of the individual resistors, $Z(0) = R_{dc} = R_1 + R_2$, which in this case is 210 Ω . Hence the data representation in the Nyquist plot is crucial to discern information about the contributions of various resistances within a system. The frequency dependence of the real and imaginary components presented in Figure 1.24 gives a first indication of the behavior of the magnitude $|Z|$ and phase shift ϕ of the impedance as a

function of the frequency. This is useful in the identification of relaxation processes with different time constants, which therefore manifest at different frequencies.

The definitions discussed above correspond to the ideal case. To take into account the deviation from ideality, constant phase elements (CPEs) are employed in place of ideal capacitors. The electrical symbol and impedance expression for a CPE are given in the Table 1.1 and Figure 1.25a. A CPE is typically used to describe a capacitive process which is accompanied by frequency dispersion. The exponent, n accounts for the deviation from the ideal case where $n = 1$ describes an ideal capacitor while $n = 0$ corresponds to a pure resistor.

In the fitting procedure of IS measurements the CPE exponent is typically fixed or left non-restricted, constraining it between 0.5 and 1. The deviation from ideality manifests in a suppression in the RC-arc in the Nyquist plot as depicted in Figure 1.25b. Furthermore, a decrease in the exponent of the CPE results in slower response times of the capacitor as evident by the shift in the position of the 10000 Hz mark in the Nyquist plot. This is reflected in a decrease in the characteristic frequency with increased deviation from ideality. Q is the uncorrected capacitance associated to the CPE (also denoted as CPE_T) and becomes equal to the real capacitance when the exponent n (also denoted CPE_p) is equal to 1. To determine the correct capacitance C of the system the CPE capacitance needs to be corrected to take into account the associated resistance R :

$$C = \left[Q \left(R_1^{-1} + R_2^{-1} \right)^{n-1} \right]^{1/n} \quad (1.18)$$

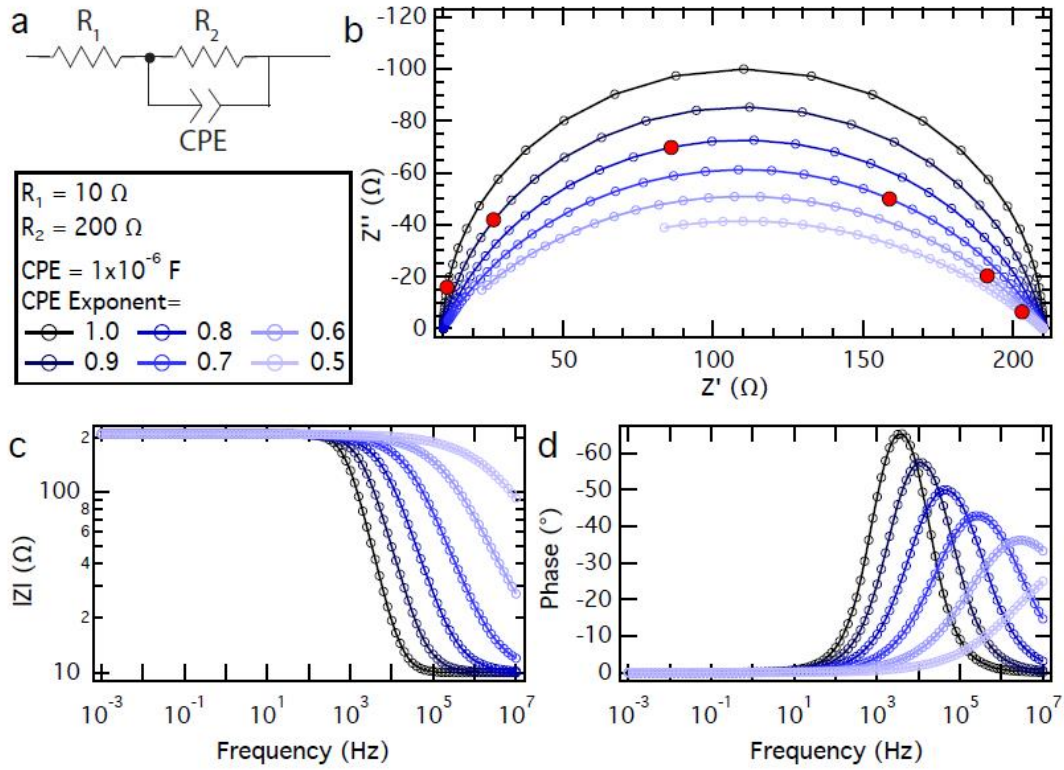


Figure 1.25. (a) Equivalent circuit. (b) Nyquist plot. Bode (c) Magnitude and (d) Phase plot versus the frequency from simulation using the presented values for R_1 , R_2 and CPE. The exponent of CPE was changed from the ideal case between 1 and 0.5. The red points in the Nyquist plot correspond to the 10000 Hz frequency. The simulation was conducted from 10 MHz to 1 mHz.

In order to use IS as a tool to examine real system it is necessary to correlate its physical properties with electrical circuit elements. This allows the system to be represented by an equivalent electrical circuit model that can be used to interpret and analyze the IS response of the system.

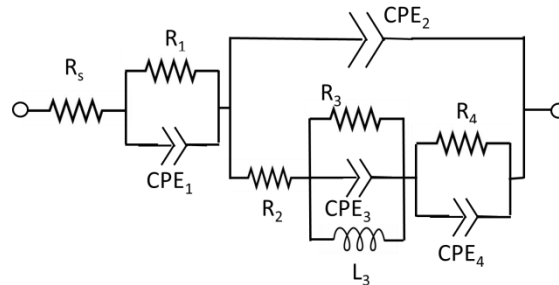


Figure 1.26. Equivalent circuit employed for fitting the impedance spectra of perovskite solar cells.

The general equivalent electrical circuit employed in the group to fit the PSC spectra is presented in Figure 1.26. This model has been built from my PhD work and other Dr. Pauporté's group works on PSCs. It will be discussed throughout this doctoral thesis. The indexes 1 to 4 go from high to low frequencies. R_s is the series resistance due to the cell contacts and external wires. It is determined by extrapolating the spectrum on the Re-axis at very high frequency.

The good practices and the protocols to follow to get reliable IS measurements of PSC have been detailed by Pauporté et al. in Ref. [128]. They have been followed throughout my work.

References

- [1] « Solar Cells - Chemistry Encyclopedia - structure, metal, equation, The pn Junction ». [En ligne]. Disponible sur: <http://www.chemistryexplained.com/Ru-Sp/Solar-Cells.html>. [Consulté le: 03-oct-2018].
- [2] J.-P. Correa-Baena *et al.*, « Promises and challenges of perovskite solar cells », *Science*, vol. 358, n° 6364, p. 739, nov. 2017.
- [3] « Progress in Inorganic Chemistry, Volume 48 », *Wiley.com*. [En ligne]. Disponible sur: <https://www.wiley.com/en-us/Progress+in+Inorganic+Chemistry%2C+Volume+48-p-9780470167069>. [Consulté le: 24-oct-2018].
- [4] M. A. Green, A. Ho-Baillie, et H. J. Snaith, « The emergence of perovskite solar cells », *Nat. Photonics*, vol. 8, p. 506, juin 2014.
- [5] T. J. Savenije *et al.*, « Thermally Activated Exciton Dissociation and Recombination Control the Carrier Dynamics in Organometal Halide Perovskite », *J. Phys. Chem. Lett.*, vol. 5, n° 13, p. 2189-2194, juill. 2014.
- [6] M. Grätzel, « The light and shade of perovskite solar cells », *Nat. Mater.*, vol. 13, p. 838, août 2014.
- [7] G. Li, R. Zhu, et Y. Yang, « Polymer solar cells », *Nat. Photonics*, vol. 6, p. 153, févr. 2012.
- [8] Q. Dong *et al.*, « Electron-hole diffusion lengths > 175 μm in solution-grown $\text{CH}_3\text{NH}_3\text{PbI}_3$ single crystals », *Science*, vol. 347, n° 6225, p. 967, févr. 2015.
- [9] D. B. Mitzi, « Synthesis, Structure, and Properties of Organic-Inorganic Perovskites and Related Materials », in *Progress in Inorganic Chemistry*, Wiley-Blackwell, 2007, p. 1-121.
- [10] N. Pellet *et al.*, « Mixed-Organic-Cation Perovskite Photovoltaics for Enhanced Solar-Light Harvesting », *Angew. Chem. Int. Ed.*, vol. 53, n° 12, p. 3151-3157, févr. 2014.
- [11] A. Kojima, K. Teshima, Y. Shirai, et T. Miyasaka, « Organometal Halide Perovskites as Visible-Light Sensitizers for Photovoltaic Cells », *J. Am. Chem. Soc.*, vol. 131, n° 17, p. 6050-6051, mai 2009.
- [12] J.-H. Im, C.-R. Lee, J.-W. Lee, S.-W. Park, et N.-G. Park, « 6.5% efficient perovskite quantum-dot-sensitized solar cell », *Nanoscale*, vol. 3, n° 10, p. 4088-4093, 2011.
- [13] M. M. Lee, J. Teuscher, T. Miyasaka, T. N. Murakami, et H. J. Snaith, « Efficient Hybrid Solar Cells Based on Meso-Superstructured Organometal Halide Perovskites », *Science*, vol. 338, n° 6107, p. 643, nov. 2012.

- [14] H.-S. Kim *et al.*, « Lead Iodide Perovskite Sensitized All-Solid-State Submicron Thin Film Mesoscopic Solar Cell with Efficiency Exceeding 9% », *Sci. Rep.*, vol. 2, p. 591, août 2012.
- [15] J. Nakazaki et H. Segawa, « Evolution of organometal halide solar cells », *J. Photochem. Photobiol. C Photochem. Rev.*, vol. 35, p. 74-107, juin 2018.
- [16] J. Burschka *et al.*, « Sequential deposition as a route to high-performance perovskite-sensitized solar cells », *Nature*, vol. 499, p. 316, juill. 2013.
- [17] K. Liang, D. B. Mitzi, et M. T. Prikas, « Synthesis and Characterization of Organic-Inorganic Perovskite Thin Films Prepared Using a Versatile Two-Step Dipping Technique », *Chem. Mater.*, vol. 10, n° 1, p. 403-411, janv. 1998.
- [18] G. E. Eperon, V. M. Burlakov, P. Docampo, A. Goriely, et H. J. Snaith, « Morphological Control for High Performance, Solution-Processed Planar Heterojunction Perovskite Solar Cells », *Adv. Funct. Mater.*, vol. 24, n° 1, p. 151-157, sept. 2013.
- [19] M. Liu, M. B. Johnston, et H. J. Snaith, « Efficient planar heterojunction perovskite solar cells by vapour deposition », *Nature*, vol. 501, p. 395, sept. 2013.
- [20] L. K. Ono, M. R. Leyden, S. Wang, et Y. Qi, « Organometal halide perovskite thin films and solar cells by vapor deposition », *J Mater Chem A*, vol. 4, n° 18, p. 6693-6713, 2016.
- [21] P. Zhang *et al.*, « Perovskite Solar Cells with ZnO Electron-Transporting Materials », *Adv. Mater.*, vol. 30, n° 3, p. 1703737, nov. 2017.
- [22] J.-Y. Jeng *et al.*, « CH₃NH₃PbI₃ Perovskite/Fullerene Planar-Heterojunction Hybrid Solar Cells », *Adv. Mater.*, vol. 25, n° 27, p. 3727-3732, juin 2013.
- [23] C.-H. Chiang, Z.-L. Tseng, et C.-G. Wu, « Planar heterojunction perovskite/PC71BM solar cells with enhanced open-circuit voltage via a (2/1)-step spin-coating process », *J Mater Chem A*, vol. 2, n° 38, p. 15897-15903, 2014.
- [24] Q. Lin, A. Armin, R. C. R. Nagiri, P. L. Burn, et P. Meredith, « Electro-optics of perovskite solar cells », *Nat. Photonics*, vol. 9, p. 106, déc. 2014.
- [25] J. You *et al.*, « Moisture assisted perovskite film growth for high performance solar cells », *Appl. Phys. Lett.*, vol. 105, n° 18, p. 183902, nov. 2014.
- [26] W. Nie *et al.*, « High-efficiency solution-processed perovskite solar cells with millimeter-scale grains », *Science*, vol. 347, n° 6221, p. 522, janv. 2015.
- [27] H. Zhou *et al.*, « Interface engineering of highly efficient perovskite solar cells », *Science*, vol. 345, n° 6196, p. 542, août 2014.
- [28] M. Xiao *et al.*, « A Fast Deposition-Crystallization Procedure for Highly Efficient Lead Iodide Perovskite Thin-Film Solar Cells », *Angew. Chem.*, vol. 126, n° 37, p. 10056-10061, juill. 2014.
- [29] Y. Wu *et al.*, « Retarding the crystallization of PbI₂ for highly reproducible planar-structured perovskite solar cells via sequential deposition », *Energy Environ. Sci.*, vol. 7, n° 9, p. 2934-2938, 2014.
- [30] N. J. Jeon *et al.*, « Compositional engineering of perovskite materials for high-performance solar cells », *Nature*, vol. 517, p. 476, janv. 2015.
- [31] M. Saliba *et al.*, « Cesium-containing triple cation perovskite solar cells: improved stability, reproducibility and high efficiency », *Energy Environ. Sci.*, vol. 9, n° 6, p. 1989-1997, 2016.
- [32] M. Saliba *et al.*, « Incorporation of rubidium cations into perovskite solar cells improves photovoltaic performance », *Science*, vol. 354, n° 6309, p. 206, oct. 2016.

- [33] W. S. Yang *et al.*, « High-performance photovoltaic perovskite layers fabricated through intramolecular exchange », *Science*, vol. 348, n° 6240, p. 1234, juin 2015.
- [34] N. Ahn, D.-Y. Son, I.-H. Jang, S. M. Kang, M. Choi, et N.-G. Park, « Highly Reproducible Perovskite Solar Cells with Average Efficiency of 18.3% and Best Efficiency of 19.7% Fabricated via Lewis Base Adduct of Lead(II) Iodide », *J. Am. Chem. Soc.*, vol. 137, n° 27, p. 8696-8699, juill. 2015.
- [35] C. Roldán-Carmona *et al.*, « High efficiency methylammonium lead triiodide perovskite solar cells: the relevance of non-stoichiometric precursors », *Energy Environ. Sci.*, vol. 8, n° 12, p. 3550-3556, 2015.
- [36] D.-Y. Son *et al.*, « Self-formed grain boundary healing layer for highly efficient CH₃ NH₃ PbI₃ perovskite solar cells », *Nat. Energy*, vol. 1, p. 16081, juin 2016.
- [37] D. Bi *et al.*, « Efficient luminescent solar cells based on tailored mixed-cation perovskites », *Sci. Adv.*, vol. 2, n° 1, janv. 2016.
- [38] Y. C. Kim *et al.*, « Beneficial Effects of PbI₂ Incorporated in Organo-Lead Halide Perovskite Solar Cells », *Adv. Energy Mater.*, vol. 6, n° 4, p. 1502104, déc. 2015.
- [39] K. T. Cho *et al.*, « Highly efficient perovskite solar cells with a compositionally engineered perovskite/hole transporting material interface », *Energy Environ. Sci.*, vol. 10, n° 2, p. 621-627, 2017.
- [40] W. S. Yang *et al.*, « Iodide management in formamidinium-lead-halide-based perovskite layers for efficient solar cells », *Science*, vol. 356, n° 6345, p. 1376, juin 2017.
- [41] N. Arora *et al.*, « Perovskite solar cells with CuSCN hole extraction layers yield stabilized efficiencies greater than 20% », *Science*, vol. 358, n° 6364, p. 768, nov. 2017.
- [42] Z. Tang *et al.*, « Hysteresis-free perovskite solar cells made of potassium-doped organometal halide perovskite », *Sci. Rep.*, vol. 7, n° 1, p. 12183, sept. 2017.
- [43] L. Calió, S. Kazim, M. Grätzel, et S. Ahmad, « Hole-Transport Materials for Perovskite Solar Cells », *Angew. Chem. Int. Ed.*, vol. 55, n° 47, p. 14522-14545, oct. 2016.
- [44] P. Wang, Z. Shao, M. Ulfa, et T. Pauporté, « Insights into the Hole Blocking Layer Effect on the Perovskite Solar Cell Performance and Impedance Response », *J. Phys. Chem. C*, vol. 121, n° 17, p. 9131-9141, mai 2017.
- [45] J. Song *et al.*, « Low-temperature SnO₂-based electron selective contact for efficient and stable perovskite solar cells », *J Mater Chem A*, vol. 3, n° 20, p. 10837-10844, 2015.
- [46] J. P. Correa Baena *et al.*, « Highly efficient planar perovskite solar cells through band alignment engineering », *Energy Env. Sci*, vol. 8, n° 10, p. 2928-2934, 2015.
- [47] Q. Jiang *et al.*, « Enhanced electron extraction using SnO₂ for high-efficiency planar-structure HC(NH₂)₂PbI₃-based perovskite solar cells », *Nat. Energy*, vol. 2, p. 16177, nov. 2016.
- [48] L. Xiong *et al.*, « Performance enhancement of high temperature SnO₂-based planar perovskite solar cells: electrical characterization and understanding of the mechanism », *J Mater Chem A*, vol. 4, n° 21, p. 8374-8383, 2016.
- [49] M. Park, J.-Y. Kim, H. J. Son, C.-H. Lee, S. S. Jang, et M. J. Ko, « Low-temperature solution-processed Li-doped SnO₂ as an effective electron transporting layer for high-performance flexible and wearable perovskite solar cells », *Nano Energy*, vol. 26, p. 208-215, août 2016.

- [50] H. Chen *et al.*, « Enhanced Performance of Planar Perovskite Solar Cells Using Low-Temperature Solution-Processed Al-Doped SnO₂ as Electron Transport Layers », *Nanoscale Res. Lett.*, vol. 12, n° 1, p. 238, mars 2017.
- [51] G. Yang *et al.*, « Interface engineering in planar perovskite solar cells: energy level alignment, perovskite morphology control and high performance achievement », *J Mater Chem A*, vol. 5, n° 4, p. 1658-1666, 2017.
- [52] W. Ke *et al.*, « Cooperative tin oxide fullerene electron selective layers for high-performance planar perovskite solar cells », *J. Mater. Chem. A*, vol. 4, n° 37, p. 14276-14283, 2016.
- [53] E. H. Anaraki *et al.*, « Highly efficient and stable planar perovskite solar cells by solution-processed tin oxide », *Energy Env. Sci.*, vol. 9, n° 10, p. 3128-3134, 2016.
- [54] J.-Y. Chen, C.-C. Chueh, Z. Zhu, W.-C. Chen, et A. K.-Y. Jen, « Low-temperature electrodeposited crystalline SnO₂ as an efficient electron-transporting layer for conventional perovskite solar cells », *Sol. Energy Mater. Sol. Cells*, vol. 164, p. 47-55, mai 2017.
- [55] S. Lin *et al.*, « Efficient and stable planar hole-transport-material-free perovskite solar cells using low temperature processed SnO₂ as electron transport material », *Org. Electron.*, vol. 53, p. 235-241, févr. 2018.
- [56] Q. Jiang *et al.*, « Planar-Structure Perovskite Solar Cells with Efficiency beyond 21% », *Adv. Mater.*, vol. 29, n° 46, p. 1703852, oct. 2017.
- [57] Q. Zhang, C. S. Dandeneau, X. Zhou, et G. Cao, « ZnO Nanostructures for Dye-Sensitized Solar Cells », *Adv. Mater.*, vol. 21, n° 41, p. 4087-4108, juill. 2009.
- [58] Zhong Lin Wang, « Zinc oxide nanostructures: growth, properties and applications », *J. Phys. Condens. Matter*, vol. 16, n° 25, p. R829, 2004.
- [59] H. Liu, Z. Huang, S. Wei, L. Zheng, L. Xiao, et Q. Gong, « Nano-structured electron transporting materials for perovskite solar cells », *Nanoscale*, vol. 8, n° 12, p. 6209-6221, 2016.
- [60] J. You *et al.*, « Low-Temperature Solution-Processed Perovskite Solar Cells with High Efficiency and Flexibility », *ACS Nano*, vol. 8, n° 2, p. 1674-1680, févr. 2014.
- [61] Z. Lin *et al.*, « Interface studies of the planar heterojunction perovskite solar cells », *Sol. Energy Mater. Sol. Cells*, vol. 157, p. 783-790, déc. 2016.
- [62] J. Huang, K.-X. Wang, J.-J. Chang, Y.-Y. Jiang, Q.-S. Xiao, et Y. Li, « Improving the efficiency and stability of inverted perovskite solar cells with dopamine-copolymerized PEDOT:PSS as a hole extraction layer », *J Mater Chem A*, vol. 5, n° 26, p. 13817-13822, 2017.
- [63] J. Mo *et al.*, « Enhanced efficiency of planar perovskite solar cells via a two-step deposition using DMF as an additive to optimize the crystal growth behavior », *J Mater Chem A*, vol. 5, n° 25, p. 13032-13038, 2017.
- [64] R. Sandoval-Torrientes *et al.*, « Modified Fullerenes for Efficient Electron Transport Layer-Free Perovskite/Fullerene Blend-Based Solar Cells », *ChemSusChem*, vol. 10, n° 9, p. 2023-2029, mars 2017.
- [65] G. E. Eperon, S. D. Stranks, C. Menelaou, M. B. Johnston, L. M. Herz, et H. J. Snaith, « Formamidinium lead trihalide: a broadly tunable perovskite for efficient planar heterojunction solar cells », *Energy Environ. Sci.*, vol. 7, n° 3, p. 982-988, 2014.
- [66] D. B. Mitzi, « Templating and structural engineering in organic-inorganic perovskites », *J Chem Soc Dalton Trans*, n° 1, p. 1-12, 2001.

- [67] C. C. Stoumpos, C. D. Malliakas, et M. G. Kanatzidis, « Semiconducting Tin and Lead Iodide Perovskites with Organic Cations: Phase Transitions, High Mobilities, and Near-Infrared Photoluminescent Properties », *Inorg. Chem.*, vol. 52, n° 15, p. 9019-9038, août 2013.
- [68] Z. Yang *et al.*, « Unraveling the Exciton Binding Energy and the Dielectric Constant in Single-Crystal Methylammonium Lead Triiodide Perovskite », *J. Phys. Chem. Lett.*, vol. 8, n° 8, p. 1851-1855, avr. 2017.
- [69] C. S. Ponseca *et al.*, « Organometal Halide Perovskite Solar Cell Materials Rationalized: Ultrafast Charge Generation, High and Microsecond-Long Balanced Mobilities, and Slow Recombination », *J. Am. Chem. Soc.*, vol. 136, n° 14, p. 5189-5192, avr. 2014.
- [70] L. Etgar *et al.*, « Mesoscopic CH₃NH₃PbI₃/TiO₂ Heterojunction Solar Cells », *J. Am. Chem. Soc.*, vol. 134, n° 42, p. 17396-17399, oct. 2012.
- [71] A. Amat *et al.*, « Cation-Induced Band-Gap Tuning in Organohalide Perovskites: Interplay of Spin-Orbit Coupling and Octahedra Tilting », *Nano Lett.*, vol. 14, n° 6, p. 3608-3616, juin 2014.
- [72] C. Yi *et al.*, « Entropic stabilization of mixed A-cation ABX₃ metal halide perovskites for high performance perovskite solar cells », *Energy Environ. Sci.*, vol. 9, n° 2, p. 656-662, 2016.
- [73] K. Wojciechowski, M. Saliba, T. Leijtens, A. Abate, et H. J. Snaith, « Sub-150 °C processed meso-superstructured perovskite solar cells with enhanced efficiency », *Energy Environ. Sci.*, vol. 7, n° 3, p. 1142-1147, 2014.
- [74] B. Conings, L. Baeten, C. De Dobbelaere, J. D'Haen, J. Manca, et H.-G. Boyen, « Perovskite-Based Hybrid Solar Cells Exceeding 10% Efficiency with High Reproducibility Using a Thin Film Sandwich Approach », *Adv. Mater.*, vol. 26, n° 13, p. 2041-2046, déc. 2013.
- [75] B. Cai, Y. Xing, Z. Yang, W.-H. Zhang, et J. Qiu, « High performance hybrid solar cells sensitized by organolead halide perovskites », *Energy Environ. Sci.*, vol. 6, n° 5, p. 1480-1485, 2013.
- [76] E. Edri, S. Kirmayer, D. Cahen, et G. Hodes, « High Open-Circuit Voltage Solar Cells Based on Organic-Inorganic Lead Bromide Perovskite », *J. Phys. Chem. Lett.*, vol. 4, n° 6, p. 897-902, mars 2013.
- [77] J. T.-W. Wang *et al.*, « Low-Temperature Processed Electron Collection Layers of Graphene/TiO₂ Nanocomposites in Thin Film Perovskite Solar Cells », *Nano Lett.*, vol. 14, n° 2, p. 724-730, févr. 2014.
- [78] D. B. Mitzi, « Thin-Film Deposition of Organic-Inorganic Hybrid Materials », *Chem. Mater.*, vol. 13, n° 10, p. 3283-3298, oct. 2001.
- [79] O. Malinkiewicz *et al.*, « Perovskite solar cells employing organic charge-transport layers », *Nat. Photonics*, vol. 8, p. 128, déc. 2013.
- [80] O. Malinkiewicz *et al.*, « Metal-Oxide-Free Methylammonium Lead Iodide Perovskite-Based Solar Cells: the Influence of Organic Charge Transport Layers », *Adv. Energy Mater.*, vol. 4, n° 15, p. 1400345, juin 2014.
- [81] A. S. Subbiah, A. Halder, S. Ghosh, N. Mahuli, G. Hodes, et S. K. Sarkar, « Inorganic Hole Conducting Layers for Perovskite-Based Solar Cells », *J. Phys. Chem. Lett.*, vol. 5, n° 10, p. 1748-1753, mai 2014.
- [82] Q. Chen *et al.*, « Planar Heterojunction Perovskite Solar Cells via Vapor-Assisted Solution Process », *J. Am. Chem. Soc.*, vol. 136, n° 2, p. 622-625, janv. 2014.

- [83] Q. Chen *et al.*, « Controllable Self-Induced Passivation of Hybrid Lead Iodide Perovskites toward High Performance Solar Cells », *Nano Lett.*, vol. 14, n° 7, p. 4158-4163, juill. 2014.
- [84] Y. Li *et al.*, « Fabrication of Planar Heterojunction Perovskite Solar Cells by Controlled Low-Pressure Vapor Annealing », *J. Phys. Chem. Lett.*, vol. 6, n° 3, p. 493-499, févr. 2015.
- [85] T. Du, N. Wang, H. Chen, H. Lin, et H. He, « Comparative Study of Vapor- and Solution-Crystallized Perovskite for Planar Heterojunction Solar Cells », *ACS Appl. Mater. Interfaces*, vol. 7, n° 5, p. 3382-3388, févr. 2015.
- [86] J. A. Christians, R. C. M. Fung, et P. V. Kamat, « An Inorganic Hole Conductor for Organo-Lead Halide Perovskite Solar Cells. Improved Hole Conductivity with Copper Iodide », *J. Am. Chem. Soc.*, vol. 136, n° 2, p. 758-764, janv. 2014.
- [87] G. A. Sepalage *et al.*, « Copper(I) Iodide as Hole-Conductor in Planar Perovskite Solar Cells: Probing the Origin of J-V Hysteresis », *Adv. Funct. Mater.*, vol. 25, n° 35, p. 5650-5661, août 2015.
- [88] W.-Y. Chen *et al.*, « Low-cost solution-processed copper iodide as an alternative to PEDOT:PSS hole transport layer for efficient and stable inverted planar heterojunction perovskite solar cells », *J. Mater. Chem. A*, vol. 3, n° 38, p. 19353-19359, 2015.
- [89] W. Sun *et al.*, « Room-temperature and solution-processed copper iodide as the hole transport layer for inverted planar perovskite solar cells », *Nanoscale*, vol. 8, n° 35, p. 15954-15960, 2016.
- [90] H. Wang *et al.*, « Efficient and Stable Inverted Planar Perovskite Solar Cells Employing CuI as Hole-Transporting Layer Prepared by Solid-Gas Transformation », *Energy Technol.*, vol. 5, n° 10, p. 1836-1843, juill. 2017.
- [91] M. D. Irwin, D. B. Buchholz, A. W. Hains, R. P. H. Chang, et T. J. Marks, « p -Type semiconducting nickel oxide as an efficiency-enhancing anode interfacial layer in polymer bulk-heterojunction solar cells », *Proc. Natl. Acad. Sci.*, vol. 105, n° 8, p. 2783, févr. 2008.
- [92] J.-Y. Jeng *et al.*, « Nickel Oxide Electrode Interlayer in $\text{CH}_3\text{NH}_3\text{PbI}_3$ Perovskite/PCBM Planar-Heterojunction Hybrid Solar Cells », *Adv. Mater.*, vol. 26, n° 24, p. 4107-4113, mars 2014.
- [93] J. Cui *et al.*, « $\text{CH}_3\text{NH}_3\text{PbI}_3$ -Based Planar Solar Cells with Magnetron-Sputtered Nickel Oxide », *ACS Appl. Mater. Interfaces*, vol. 6, n° 24, p. 22862-22870, déc. 2014.
- [94] J. E. Jaffe, T. C. Kaspar, T. C. Droubay, T. Varga, M. E. Bowden, et G. J. Exarhos, « Electronic and Defect Structures of CuSCN », *J. Phys. Chem. C*, vol. 114, n° 19, p. 9111-9117, mai 2010.
- [95] S. Ye *et al.*, « CuSCN -Based Inverted Planar Perovskite Solar Cell with an Average PCE of 15.6% », *Nano Lett.*, vol. 15, n° 6, p. 3723-3728, juin 2015.
- [96] P. Qin *et al.*, « Inorganic hole conductor-based lead halide perovskite solar cells with 12.4% conversion efficiency », *Nat. Commun.*, vol. 5, p. 3834, mai 2014.
- [97] S. Seo *et al.*, « An ultra-thin, un-doped NiO hole transporting layer of highly efficient (16.4%) organic-inorganic hybrid perovskite solar cells », *Nanoscale*, vol. 8, n° 22, p. 11403-11412, 2016.
- [98] W. Chen *et al.*, « Hybrid interfacial layer leads to solid performance improvement of inverted perovskite solar cells », *Energy Environ. Sci.*, vol. 8, n° 2, p. 629-640, 2015.
- [99] X. Yin *et al.*, « High Efficiency Inverted Planar Perovskite Solar Cells with Solution-Processed NiOx Hole Contact », *ACS Appl. Mater. Interfaces*, vol. 9, n° 3, p. 2439-2448, janv. 2017.
- [100] J. You *et al.*, « Improved air stability of perovskite solar cells via solution-processed metal oxide transport layers », *Nat. Nanotechnol.*, vol. 11, p. 75, oct. 2015.

- [101] X. Yin *et al.*, « Highly Efficient Flexible Perovskite Solar Cells Using Solution-Derived NiOx Hole Contacts », *ACS Nano*, vol. 10, n° 3, p. 3630-3636, mars 2016.
- [102] N. Y. Nia, F. Matteocci, L. Cina, et A. Di Carlo, « High-Efficiency Perovskite Solar Cell Based on Poly(3-Hexylthiophene): Influence of Molecular Weight and Mesoscopic Scaffold Layer », *ChemSusChem*, vol. 10, n° 19, p. 3854-3860, mai 2017.
- [103] Y. Zhang, M. Elawad, Z. Yu, X. Jiang, J. Lai, et L. Sun, « Enhanced performance of perovskite solar cells with P3HT hole-transporting materials via molecular p-type doping », *RSC Adv*, vol. 6, n° 110, p. 108888-108895, 2016.
- [104] J. W. Jung *et al.*, « Flexible and highly efficient perovskite solar cells with a large active area incorporating cobalt-doped poly(3-hexylthiophene) for enhanced open-circuit voltage », *J Mater Chem A*, vol. 5, n° 24, p. 12158-12167, 2017.
- [105] X. Jiang *et al.*, « High-Performance Regular Perovskite Solar Cells Employing Low-Cost Poly(ethylenedioxythiophene) as a Hole-Transporting Material », *Sci. Rep.*, vol. 7, p. 42564, févr. 2017.
- [106] A. E. Labban *et al.*, « Improved Efficiency in Inverted Perovskite Solar Cells Employing a Novel Diarylamino-Substituted Molecule as PEDOT:PSS Replacement », *Adv. Energy Mater.*, vol. 6, n° 11, p. 1502101, mars 2016.
- [107] W. Lee *et al.*, « Acidity-Controlled Conducting Polymer Films for Organic Thermoelectric Devices with Horizontal and Vertical Architectures », *Sci. Rep.*, vol. 6, p. 33795, sept. 2016.
- [108] S. Wang *et al.*, « Role of 4-tert-Butylpyridine as a Hole Transport Layer Morphological Controller in Perovskite Solar Cells », *Nano Lett.*, vol. 16, n° 9, p. 5594-5600, sept. 2016.
- [109] E. J. Juarez-Perez, M. R. Leyden, S. Wang, L. K. Ono, Z. Hawash, et Y. Qi, « Role of the Dopants on the Morphological and Transport Properties of Spiro-MeOTAD Hole Transport Layer », *Chem. Mater.*, vol. 28, n° 16, p. 5702-5709, août 2016.
- [110] J. Burschka *et al.*, « Tris(2-(1H-pyrazol-1-yl)pyridine)cobalt(III) as p-Type Dopant for Organic Semiconductors and Its Application in Highly Efficient Solid-State Dye-Sensitized Solar Cells », *J. Am. Chem. Soc.*, vol. 133, n° 45, p. 18042-18045, nov. 2011.
- [111] L. Huang *et al.*, « Efficient and stable planar perovskite solar cells with a non-hygroscopic small molecule oxidant doped hole transport layer », *Electrochimica Acta*, vol. 196, p. 328-336, avr. 2016.
- [112] T. Leijtens, J. Lim, J. Teuscher, T. Park, et H. J. Snaith, « Charge Density Dependent Mobility of Organic Hole-Transporters and Mesoporous TiO₂ Determined by Transient Mobility Spectroscopy: Implications to Dye-Sensitized and Organic Solar Cells », *Adv. Mater.*, vol. 25, n° 23, p. 3227-3233, mai 2013.
- [113] O. Rana, R. Srivastava, R. Grover, M. Zulfequar, M. Husain, et M. N. Kamalasanan, « Charge transport studies in thermally evaporated 2,2',7,7'-tetrakis-(N,N-di-4-methoxyphenylamino)-9,9'-spirobifluorene (spiro-MeOTAD) thin film », *Synth. Met.*, vol. 161, n° 9, p. 828-832, mai 2011.
- [114] H. J. Snaith et M. Grätzel, « Enhanced charge mobility in a molecular hole transporter via addition of redox inactive ionic dopant: Implication to dye-sensitized solar cells », *Appl. Phys. Lett.*, vol. 89, n° 26, p. 262114, déc. 2006.
- [115] D. Poplavskyy et J. Nelson, « Nondispersive hole transport in amorphous films of methoxy-spirofluorene-arylamine organic compound », *J. Appl. Phys.*, vol. 93, n° 1, p. 341-346, déc. 2002.
- [116] L. Yang *et al.*, « Conjugated Small Molecule for Efficient Hole Transport in High-Performance p-i-n Type Perovskite Solar Cells », *Adv. Funct. Mater.*, vol. 27, n° 31, p. 1702613, juill. 2017.

- [117] U.-H. Lee *et al.*, « Diphenyl-2-pyridylamine-Substituted Porphyrins as Hole-Transporting Materials for Perovskite Solar Cells », *ChemSusChem*, vol. 10, n° 19, p. 3780-3787, sept. 2017.
- [118] T. Malinauskas *et al.*, « Branched methoxydiphenylamine-substituted fluorene derivatives as hole transporting materials for high-performance perovskite solar cells », *Energy Environ. Sci.*, vol. 9, n° 5, p. 1681-1686, 2016.
- [119] P. Gratia *et al.*, « A Methoxydiphenylamine-Substituted Carbazole Twin Derivative: An Efficient Hole-Transporting Material for Perovskite Solar Cells », *Angew. Chem. Int. Ed.*, vol. 54, n° 39, p. 11409-11413, juill. 2015.
- [120] M. Saliba *et al.*, « A molecularly engineered hole-transporting material for efficient perovskite solar cells », *Nat. Energy*, vol. 1, p. 15017, janv. 2016.
- [121] T. Liu *et al.*, « Critical parameters in TiO₂/ZrO₂/Carbon-based mesoscopic perovskite solar cell », *J. Power Sources*, vol. 293, p. 533-538, oct. 2015.
- [122] F. Zhang, X. Yang, H. Wang, M. Cheng, J. Zhao, et L. Sun, « Structure Engineering of Hole-Conductor Free Perovskite-Based Solar Cells with Low-Temperature-Processed Commercial Carbon Paste As Cathode », *ACS Appl. Mater. Interfaces*, vol. 6, n° 18, p. 16140-16146, sept. 2014.
- [123] Z. Li *et al.*, « Laminated Carbon Nanotube Networks for Metal Electrode-Free Efficient Perovskite Solar Cells », *ACS Nano*, vol. 8, n° 7, p. 6797-6804, juill. 2014.
- [124] C.-Y. Chan, Y. Wang, G.-W. Wu, et E. Wei-Guang Diao, « Solvent-extraction crystal growth for highly efficient carbon-based mesoscopic perovskite solar cells free of hole conductors », *J. Mater. Chem. A*, vol. 4, n° 10, p. 3872-3878, 2016.
- [125] L. Liang, Y. Cai, X. Li, M. K. Nazeeruddin, et P. Gao, « All that glitters is not gold: Recent progress of alternative counter electrodes for perovskite solar cells », *Nano Energy*, vol. 52, p. 211-238, oct. 2018.
- [126] G. Grancini *et al.*, « One-Year stable perovskite solar cells by 2D/3D interface engineering », *Nat. Commun.*, vol. 8, p. 15684, juin 2017.
- [127] S. J. Fonash, *Solar cell device physics*, 2nd ed. Burlington, MA: Academic Press/Elsevier, 2010.
- [128] D. Pitarch-Tena, T. T. Ngo, M. Vallés-Pelarda, T. Pauporté, et I. Mora-Seró, « Impedance Spectroscopy Measurements in Perovskite Solar Cells: Device Stability and Noise Reduction », *ACS Energy Lett.*, vol. 3, n° 4, p. 1044-1048, avr. 2018.

Chapter II

Preparation of $\text{CH}_3\text{NH}_3\text{PbI}_3$ Layers and Cell Performances

This chapter is dedicated to the preparation methods of $\text{CH}_3\text{NH}_3\text{PbI}_3$ that I developed and to the study of the related solar cells. We also show the characterizations of these layers and cells. The $\text{CH}_3\text{NH}_3\text{PbI}_3$ layer was sandwiched between a contact made of a hole blocking layer (*bl*- TiO_2) and a scaffold layer (*meso*- TiO_2) (ETL) on one side and the hole transporting material layer (HTM) on the other side. The *bl*- TiO_2 was deposited by the spray pyrolysis technique. The *meso*- TiO_2 , the $\text{CH}_3\text{NH}_3\text{PbI}_3$ active layer and the HTM layer were prepared by spin coating. In the present chapter, we focus on the preparation methods of $\text{CH}_3\text{NH}_3\text{PbI}_3$ active layer (hereafter called MAPI), and on their characterizations. Two types of MAPI are studied in Chapter II, namely MAPI(1)-SO, and MAPI(2). Another HP, MAPI(1)-SOF, will be introduced and used in Chapter IV and V. (1) and (2) are associated to the number of step for the preparation, while SO (for DMSO) and SOF (for DMSO and DMF) stand for the solvent employed in their precursor solution. For the sake of comparison MAPI(1)-SO and MAPI(2) layers will be investigated in detail first. Then, we will show the cell characteristics and the impedance spectroscopy investigation of MAPI(1)-SO PSCs.

II.1. Introduction

Organic-inorganic halide perovskites are materials of high interest due to their promising properties in photovoltaic technology. This tremendous attention is shown by the rapid increase in the number of publications per year dedicated to these photovoltaic materials and related devices (see Chapter I, Figure 1.7). Kojima et al incorporated $\text{CH}_3\text{NH}_3\text{PbI}_3$ and $\text{CH}_3\text{NH}_3\text{PbBr}_3$ perovskites as light harvester materials in a liquid dye-sensitized solar cells for the first time in 2009[1]. Three years later, Kim et al succeed in realizing a stable solid-state $\text{CH}_3\text{NH}_3\text{PbI}_3$ perovskite solar cells. Since then, the PCE of perovskite solar cells (PSC) has raised continuously[2]. Today, the highest performance of perovskite solar cells has reached 23.3%.

Besides their excellent opto-electronic properties, the organo-metal halide perovskites can be prepared by various techniques. To the best of our knowledge, there are four main preparation

methods of perovskite layers reported in the literature. The conventional preparation methods from solutions are categorized into one-step deposition[2]–[7] and two-step sequential deposition[8], [9],[10]. Perovskite layers are also prepared by dual source vapor deposition[11]–[15] and vapor assisted solution process[16]–[19]. The conventional method was found to be easy and low-cost, therefore many groups use this method. In general, the precursor solution of perovskite is prepared by mixing the powder of RAX (R: methyl, formamidine; X: I, Br) and PbX_2 (X: I, Br, Cl) at the stoichiometry or non-stoichiometry molar ratio in high boiling point aprotic solvents such as Dimethylformamide (DMF), Dimethyl sulfoxide (DMSO), N-Méthyl-2-pyrrolidone (NMP), γ -Butyro-lactone (GBL), *etc.*..., at low temperature ($\sim 70^\circ\text{C}$) for several minutes. This solution is used to form organometal halide perovskite through spin-coating or dip-coating[20]. One-step deposition method proposes a fast-crystallization by dripping an anti-solvent such as chlorobenzene, toluene, diethyl-ether, *etc.* during spin-coating to trigger the formation of the perovskite layer. Because of its simplicity, the one-step deposition method has become the most popular thin film deposition technique of perovskite solar cells[1]. A two-step sequential deposition method has been introduced for the first time by Burschka et al. in the fabrication of perovskite solar cells, although this method was originally developed by Mitzi et al in 1998[9], [10]. Typically, the two-step sequential deposition method is started by spin-coating a PbI_2 in DMF solution onto the oxide film. This PbI_2 film is subsequently converted into a perovskite film through dipping or spin-coating of MAI in iso-propanol solution[8]. An annealing process is then necessary to form a complete crystallized perovskite layer either for the one-step or the two-step deposition methods. The two-step method is more advantageous for the morphology control of the perovskite layer compared to the one-step deposition method due to a better confinement of PbI_2 into the mesoporous network of TiO_2 .

Deposition of perovskite layer has also been developed by using unconventional methods based on high vacuum such as dual-source vapor deposition and vapor assisted solution processes [15]. The fabrication process based on high vacuum aims at getting extremely uniform and pinholes-free perovskite layers. Several advantages can be observed for this preparation method such as: (1) it is much easier to get high purity film when formed by sublimating the powder precursors after outgassing under a vacuum environment; (2) the vapor method is also suitable for depositing multilayered thin film; (3) the wettability issues in the solution process can be

eliminated in vapor deposition and, consequently, this method can be used to deposit thin film on various substrates [15].

The preparation of perovskite films under vacuum was first reported in 1980 by Salau who synthesizes KPbI_3 from PbI_2 and KI as precursors[21]. Then, in 1999, Mitzi et al also reported the thin-film deposition of organic-inorganic hybrid materials using a single source thermal ablation technique [22]. Dual-source vapor deposition is a modified method from the previous ones, which was proposed by Liu et al in 2013. They used PbCl_2 and $\text{CH}_3\text{NH}_3\text{I}$ as precursors in order to form $\text{CH}_3\text{NH}_3\text{Pb}_{3-x}\text{Cl}_x$ perovskite structure[11]. In 2014, Malinkiewicz et al also realized a pure $\text{CH}_3\text{NH}_3\text{PbI}_3$ perovskite layer using a high vacuum chamber and from PbI_2 and $\text{CH}_3\text{NH}_3\text{I}$ sources [12]. The films obtained were uniform as confirmed by AFM with a root mean square (RMS) roughness of 5 nm and uniform grain sizes with an average value at 150 nm[13]. In general, the conditions for dual-source vapor deposition are as follow: The precursor materials (PbX ($\text{X} = \text{I}, \text{Cl}$) and $\text{CH}_3\text{NH}_3\text{I}$ are contained in the crucibles that are heated to their sublimation temperatures. The distance between the crucibles and the target substrates is fixed at ~ 20 cm[12] and the typical pressure used is 10^{-5} to 10^{-6} Torr [11], [12]. Dual-source vapor deposition is typically performed at high temperature. Yang at al. developed a new approach of low temperature vapor deposition by combining the two-step sequential deposition method and the dual-source deposition method[16]. Typically, they starts by depositing a PbI_2 layer on a compact TiO_2 layer, Then, the layer was annealed for 2 h in $\text{CH}_3\text{NH}_3\text{I}$ vapor at 150°C in a N_2 flow atmosphere in order to form the MAPI perovskite. This method provided a uniform grain structure with grain size up to the micrometer, full surface coverage and a complete conversion of the precursors into a perovskite film.

II.2. Preparation methods of MAPI-based solar cells

As stated earlier, the perovskite layer is sandwiched between an ETL and a HTM layer. Here we explain the preparation of each of these layers.

II.2.1. Preparation of the blocking layer (*bl*- TiO_2)

The blocking TiO_2 layer is prepared by using the spray pyrolysis technique from a solution containing 0.6 mL of titanium isopropoxide (TTIP) purchased from Alfa Aesar and 0.4 mL of acetylacetone from Alfa Aesar and then dissolved in 7 mL of isopropanol. Before spraying, the

substrates were placed for 15 min at 455°C . We used compressed air to carry out the solution. The sprayed samples were kept at 455°C for 40 min before to let it cool down to room temperature. A schematic of this process shown in Figure 2.1.

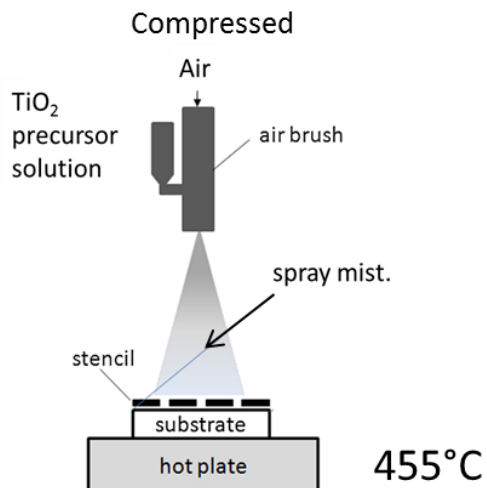


Figure 2.1. Schematic illustration of spray pyrolysis deposition technique.

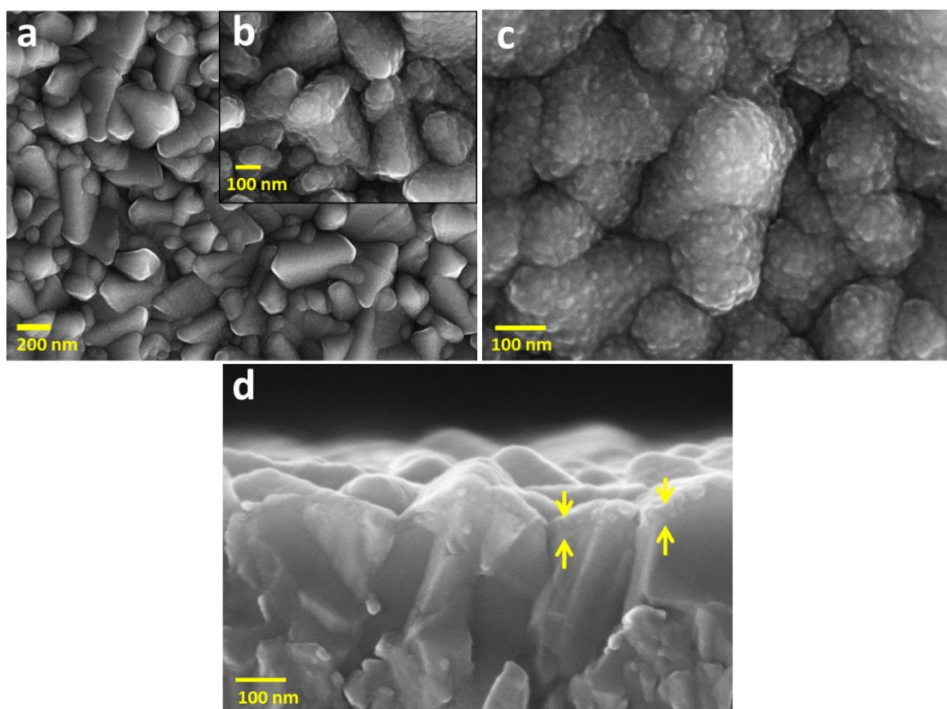


Figure 2.2. (a-c) SEM top views of the blocking TiO_2 layer: (c) SEM zoom view of (a). (d) Cross-sectional view of the sprayed TiO_2 blocking layer.

The blocking layer made by this method was highly conformal and perfectly covered the FTO grains. No porosity was found and the layer was perfectly compact. From Figure 2.2c the grains size of the TiO_2 layer was about 20-25 nm while the thickness of the layer was estimated at 30-35 nm from SEM cross-sectional observation (Figure 2.2d).

II.2.2. Preparation of the mesoporous layer (*meso-TiO₂*)

The mesoporous layer was prepared by spin-coating. The 30NRD TiO_2 paste purchased from Dyesol was diluted at various ratios in ethanol. We tested the 1:6, 1:8, 1:10 ratios. Increasing the dilution ratio increased the thickness of the mesoporous layer. The effect of this variation on the perovskite solar cells is also presented in Chapter V. The solution was spin-coated at 5000 rpm (acceleration 2500 rpm/s) for 20 s and formed layer was dried at 125°C for 10 min. Finally, the samples were annealed at 500°C for 30 min.

II.2.3. Preparation of MAPI layers

In our work, a two-step sequential and one-step deposition technique have been used. These two deposition methods were realized by spin coating. The detailed procedure of each technique is now explained.

Two-step sequential deposition method (Figure 2.3)

- Step 1: PbI_2 was dissolved in N,N-dimethylformamide at a concentration of 461 mg.mL^{-1} and stirred at 70°C for 20 min until full dissolution. Then, we added 30 μL of concentrated HCl (37%). 50 μL of this solution was deposited on top of the oxide electron transport layer (ETL) and spun at 4000 rpm, 4000 rpm/s, for 30 s.
- Step 2: 40 mg of methylammonium iodide (MAI) was dissolved in 1 mL 2-propanol. 100 μL of MAI solution was dropped on top of PbI_2 layer (wait 20 s) and spun at 4000 rpm, 4000 rpm/s, for 30 s. The sample was subsequently annealed at 115°C for 1h to form a perovskite layer (dark-brown color). This layer then called as MAPI(2) in the following.

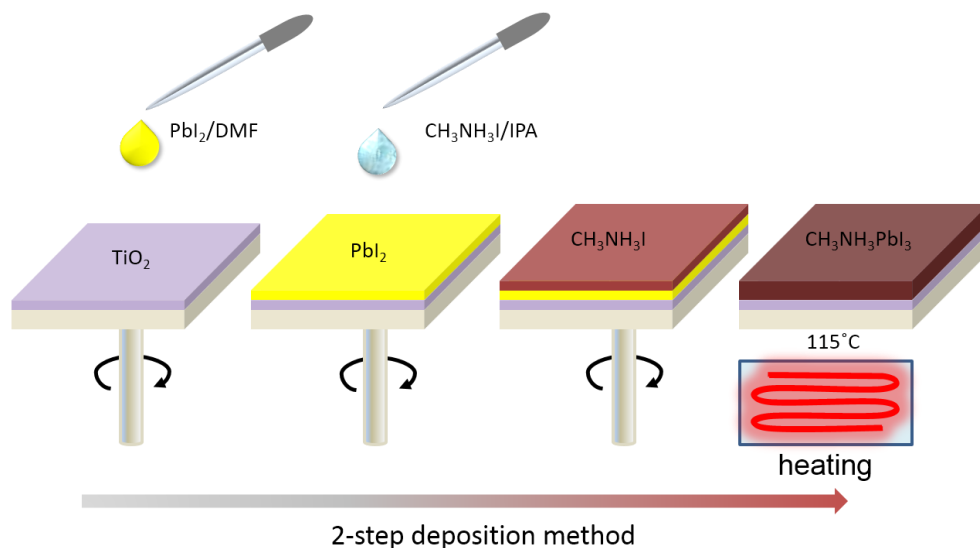


Figure 2.3. Schematic of the two-step sequential deposition method of MAPI layer.

One-step deposition method (Figure 2.4)

- MAPI prepared by one step then called MAPI(1)-SO: 50 μL of a 1.2 M perovskite precursor in dimethyl sulfoxide solution (553 mg of PbI_2 and 190 mg of MAI in 1 mL of DMSO) was spin-coated on top of the electron transport layer by a two step spinning program: (1) Rotation at 1000 rpm, 200 rpm/s for 10 s and (2) Rotation at 6000 rpm, 6500 rpm/s for 35 s. 110 μL of chlorobenzene anti-solvent was dropped on top the perovskite layer during the second step program 10 s prior to the end of the program to trigger the fast-crystallization of the perovskite. The samples were then annealed at 105°C for 1h.

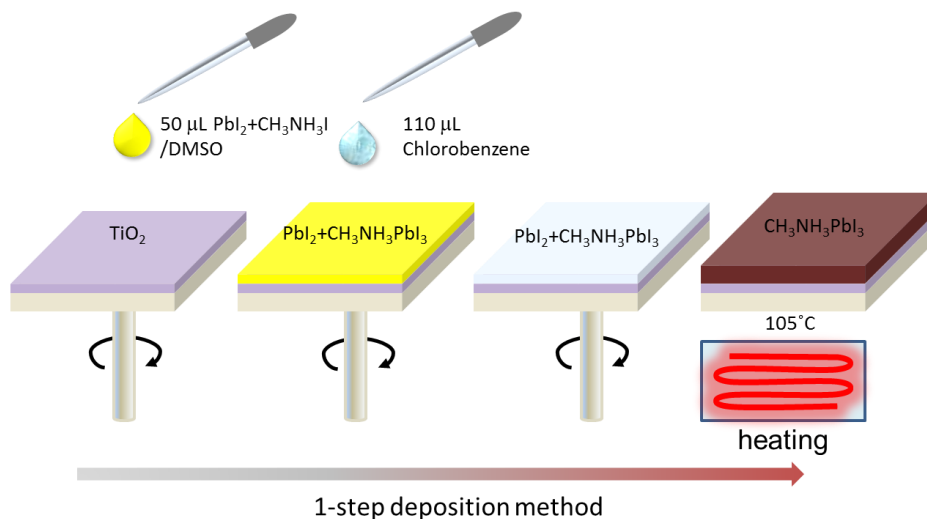


Figure 2.4. Schematic of the one-step deposition method of MAPI layer.

These two deposition methods produce uniform and smooth layers which lead to high performances solar cells.

II.2.4. Preparation of the hole transporting material layer (HTM)

Spiro-OMeTAD was used as the HTM. A solution was prepared by dissolving 72 mg of Spiro-OMeTAD in 1 ml chlorobenzene. Then, 17.5 μL of bis(trifluoromethylsulfonyl)imide lithium salt solution (LiTFSI) solution (520 mg in 1 mL ACN), 28 μL of TBP (tert-butylpyridine) and 6 μL of tris (2-1H-pyrazol-1-yl) - 4-tert-butylpyridine) – cobalt (III) -tris (bis (trifluoromethylsulfonyl) imide) (300 mg in 1 mL ACN) were added to this solution. 35 μL of the HTM solution was spin-coated at 4000 rpm for 20 s.

II.2.5. Preparation of the back contact

A gold (Au) metal layer was used as back contact for all prepared cells. This layer was deposited on top of the HTM layer by using thermal evaporation with a deposition pressure as low as 5×10^{-5} mbar . The gold layer thickness was about 70-80 nm.

II.3. Characterization of the MAPI layers prepared by the one-step and the two-step methods

II.3.1. Morphology properties

The MAPI layer was deposited onto the oxide TiO_2 bi-layer (*bl*- TiO_2 and *meso*- TiO_2). For the two-step deposition method, we could observe separately the step 1 (PbI_2 layer) (Figure 2.5a) and step 2 where the perovskite MAPI(2) was formed after the annealing process (Figure 2.5b). A non-uniform grain size was observed in the perovskite prepared by the two-step method. On the other hand, for the one-step deposition method, we could observe directly the MAPI(1)-SO layer after the heating process and found the grain sizes to be more uniform.

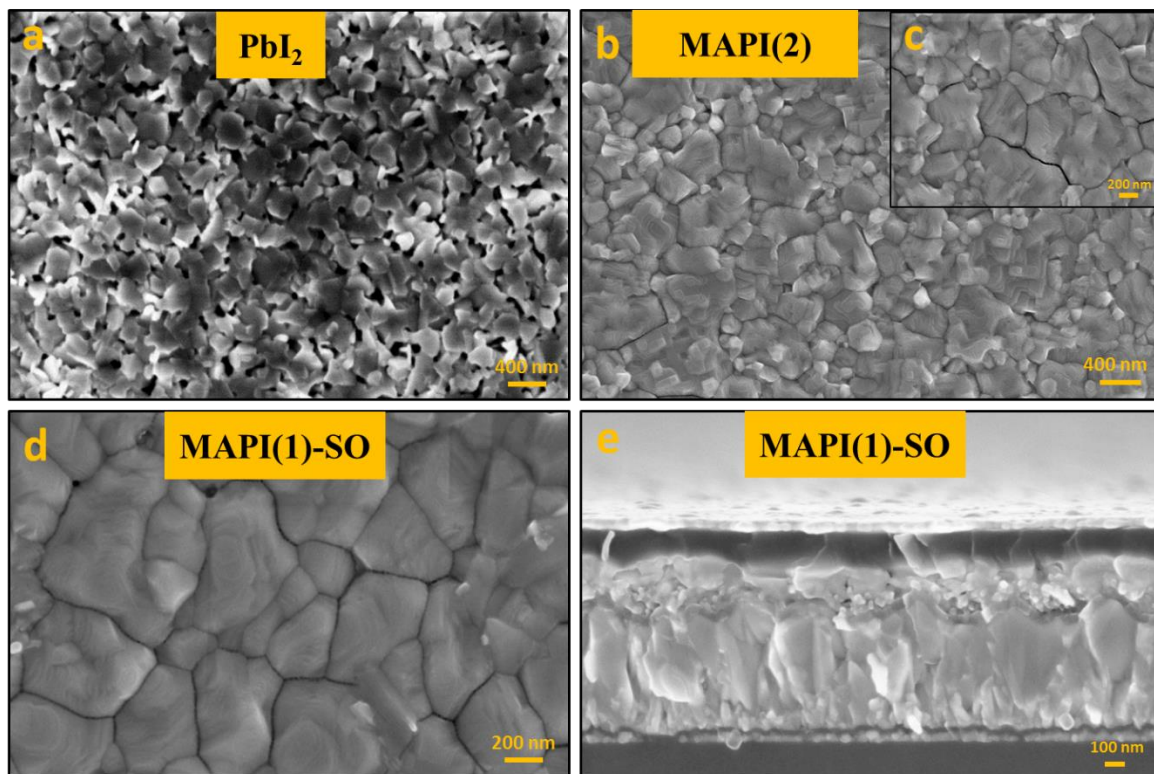


Figure 2.5. Top-view of (a) PbI_2 layer and (b,c) MAPI(2) layer. (d) MAPI(1)-SO layer deposited on TiO_2 oxide layer. (e) Cross-sectional view of a complete perovskite solar cell by integrating a MAPI(1)-SO layer.

II.3.2. XRD

Figure 2.6 compares the XRD patterns of MAPI(1)-SO and MAPI(2) layers. They were deposited onto the FTO coated by the oxide TiO_2 layers. It shows a well-crystalline MAPI perovskite either for one-step or two-step deposition methods. The XRD patterns exhibit different peak intensities depending on the deposition method: MAPI(1)-SO shows a better growth of perovskite compared to the two-step MAPI (MAPI(2)). The presence of the (001) PbI_2 diffraction peak at 12.8° appeared in both cases but with different intensities. In MAPI(2), it is higher than in MAPI(1)-SO. This appearance is a sign that the initial precursor PbI_2 is not fully converted into MAPI [23], [24]. However, we can note that in the literature, several papers claim that the PbI_2 peak is necessary in order to get high performance devices [25]–[28].

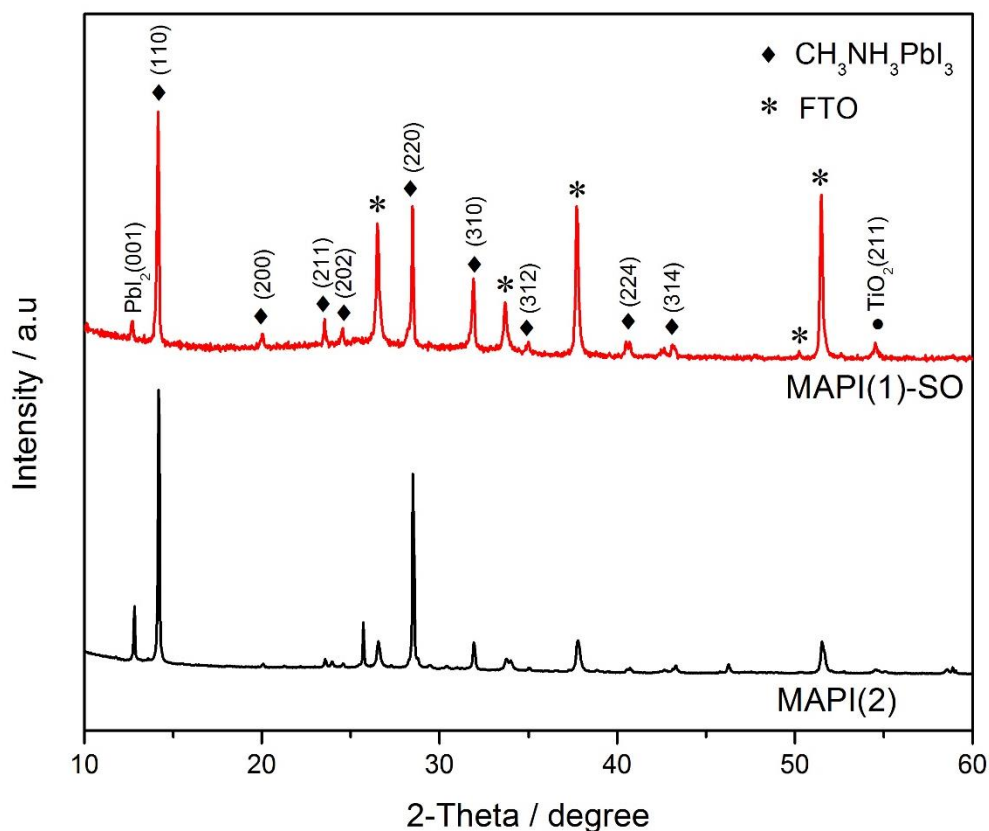


Figure 2.6. XRD patterns of $\text{CH}_3\text{NH}_3\text{PbI}_3$ perovskite deposited on the TiO_2 oxide layer through one-step and two-step deposition methods.

II.3.3. Optical characterizations

Figure 2.7a and 2.7c show the absorbance and photoluminescence (PL) spectra of $\text{MAPI}(2)/\text{TiO}_2$ and $\text{MAPI}(1)\text{-SO}/\text{TiO}_2$ heterostructures, respectively. The $\text{MAPI}(2)$ spectrum is characterized by a high absorbance from near-UV to the near infra-red wavelength region while the absorbance of the $\text{MAPI}(1)\text{-SO}$ continuously increases below the absorption edge. The PL spectra show an emission at the same wavelength (770 nm) for the two MAPI . The band gap of both MAPI has been calculated using Tauc's plots as shown in Figure 2.7b and 2.7d. The band gap value is found at ~ 1.59 eV in both cases which corresponds to an absorption onset at 770 nm. No difference is found between MAPI prepared by 1-step and 2-step deposition techniques for the direct bandgap and PL emission.

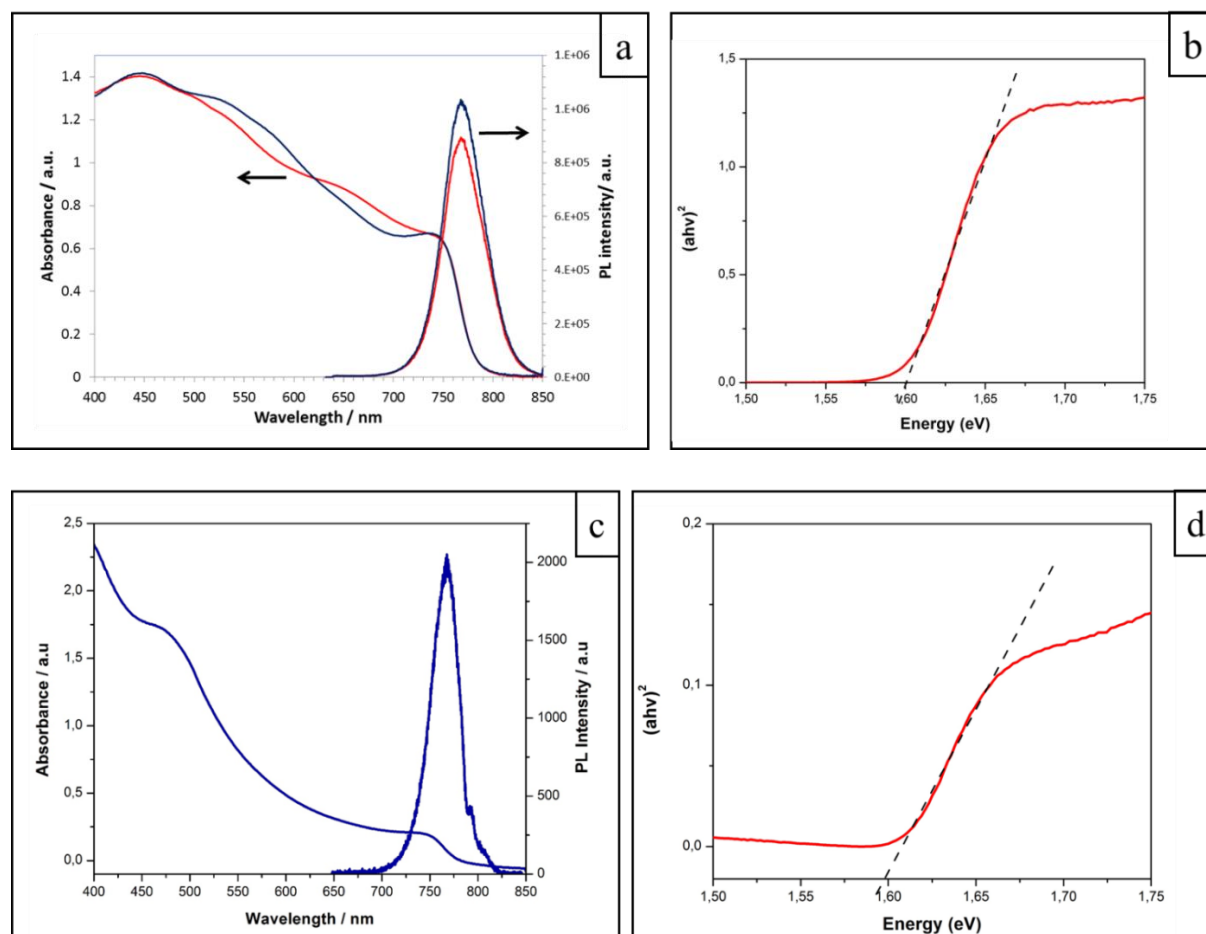


Figure 2.7. (a) Absorbance and PL spectra of MAPI(1)-SO on glass (red curves) and on FTO/TiO₂ (dark blue curves). (c) Absorbance and PL spectra of one-step MAPI. Tauc plots of (b) MAPI(2) and (d) MAPI(1)-SO deposited on FTO/TiO₂ layers.

II.4. Devices performances

PCEs and J - V curve parameters of cells employing the two different MAPI are gathered in Table 2.1. The V_{oc} is higher for MAPI(1)-SO compared to MAPI(2) but the best PCE is found with MAPI(2) (Figure 2.8b), The PCE is then 18.18% with slightly higher J_{sc} and FF. The cells with MAPI(2) show rather high hysteresis with an hysteresis index (HI) at 23% for the best cell and 17.4% for average (Table 2.1) (Figure 2.8a and 2.8b). The HI parameter is defined as:

$$HI(\%) = \frac{(PCE)_{REV} - (PCE)_{FOR}}{(PCE)_{AVG}} \quad (2.1)$$

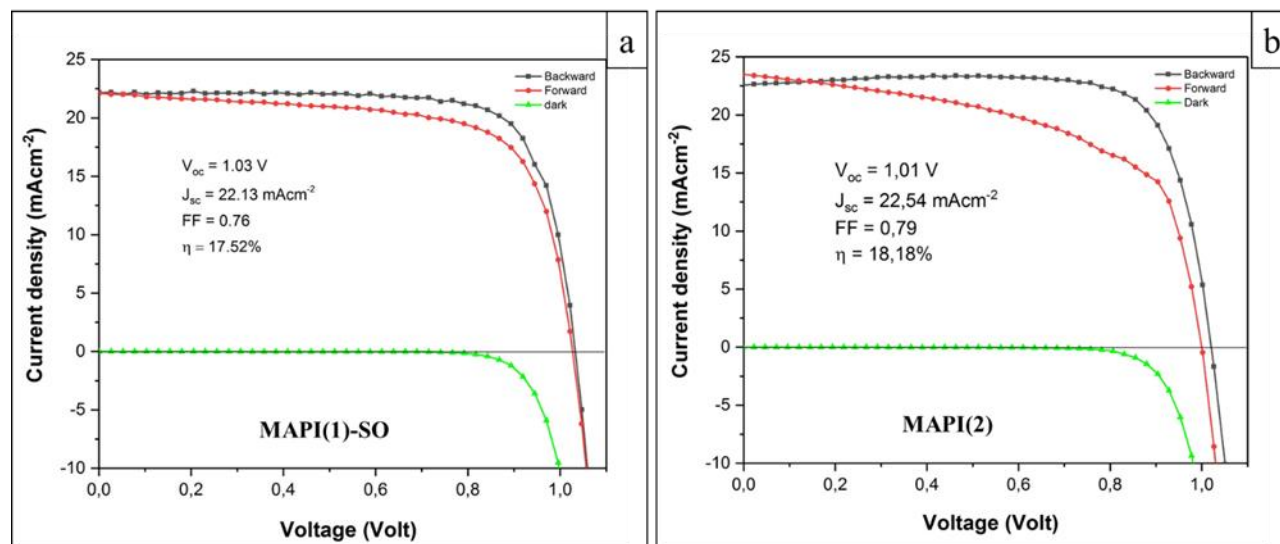
with $(PCE)_{REV}$, $(PCE)_{FOR}$ and $(PCE)_{AVG}$ the power conversion efficiencies determined on the reverse scan, forward scan and by averaging both, respectively.

The average cells for MAPI(1)-SO had a quite large HI (19.5%). We have also found a better stability for MAPI(1)-SO combined with Spiro-OMeTAD as hole transporting material than MAPI(2). This stability could be seen by measuring the cells several times. For MAPI(2) cells, the cells could only be measured 2 or 3 times with almost the same PCE. Then after, their PCE tends to decrease very fast or the cells could not work anymore. On the other hand, for the MAPI(1)-SO, the cells could be measured much more times with a small decrease in PCE. Therefore, for these cells, we have been able follow the change in the device performances with the scan rate in both scanning direction, backward and forward (Figure 2.8c).

Table 2.1. *J-V* curve parameters of cells with MAPI(1)-SO and MAPI(2) perovskites.

| Sample | Scan direction | Voc (V) | Jsc ($\text{mA}\cdot\text{cm}^{-2}$) | FF (%) | PCE (%) | HI (%) |
|------------|----------------|-------------|--|--------------|--------------|--------|
| MAPI(1)-SO | Reverse* | 1.03 | 22.13 | 76.79 | 17.52 | 10.1 |
| | Forward* | 1.02 | 22.07 | 69.89 | 15.84 | |
| | Avg Rev | 1.01 (0.01) | 20.98 (0.71) | 75.97 (1.9) | 16.16 (0.77) | 19.5 |
| | Avg For | 0.99 (0.01) | 20.97 (0.7) | 63.35 (4.32) | 13.29 (1.45) | |
| MAPI(2) | Reverse* | 1.01 | 22.54 | 79.11 | 18.18 | 23.0 |
| | Forward* | 1.00 | 23.43 | 61.54 | 14.43 | |
| | Avg Rev | 1.00 (0.01) | 21.86 (0.62) | 76.30 (2.85) | 16.81 (0.88) | 17.4 |
| | Avg For | 1.00 (0.01) | 22.81 (0.66) | 61.70 (3.41) | 14.12 (0.52) | |

*the best cell. In the brackets are standard deviation. Number of cells averaged is 10 cells.



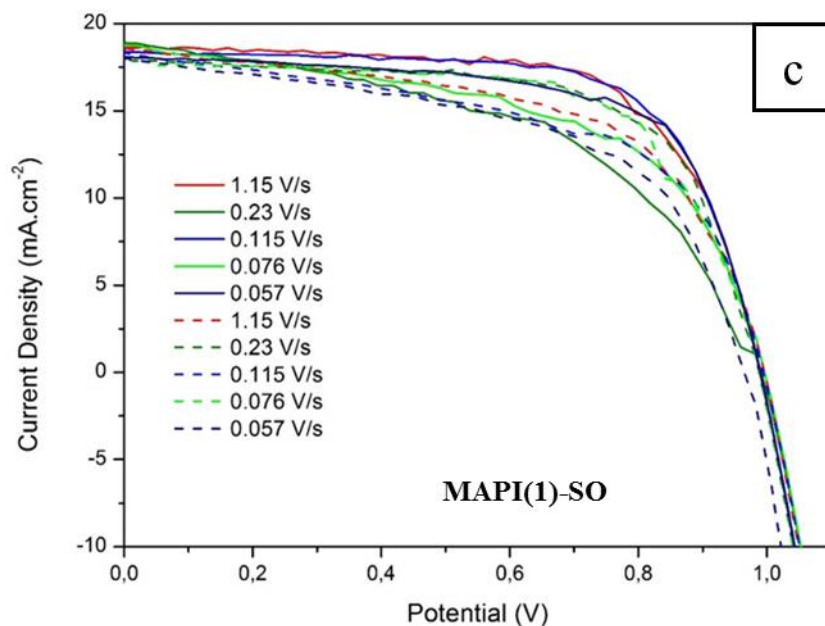
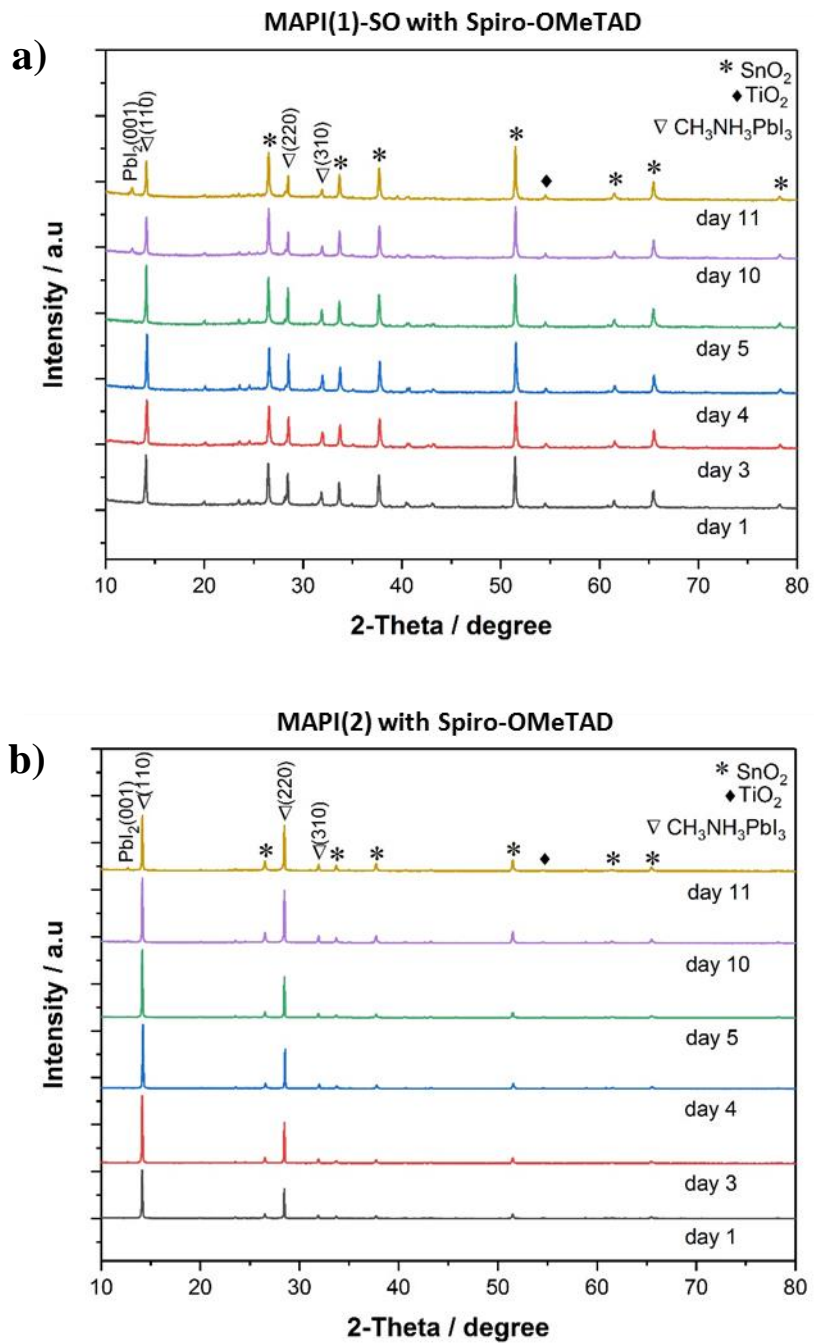


Figure 2.8. *J-V* curves of the best cells in reverse and forward scan direction (under light) and in dark of: (a) MAPI(1)-SO; (b) MAPI(2). (c) Effect of reverse (full line) and forward (dashed line) scan rate variation on *J-V* curves measurement of a $\text{TiO}_2/\text{MAPI(1)-SO}/\text{Spiro-OMeTAD}$ solar cell.

II.5. Aging study of MAPI layers

The aging of MAPI(1)-SO and MAPI(2) layers covered and not by Spiro-OMeTAD has been followed by XRD measurements (Figure 2.9). From the figures, we can observe that the PbI_2 peak (001) tend to appear from day 10 for both techniques when Spiro-OMeTAD has been deposited on top of the perovskite with very small intensity for MAPI(2) and slightly higher for MAPI(1)-SO. The intensity of this peak increases with time, while, concomitantly, the intensity of the MAPI peaks decreases. Surprisingly, in the samples prepared without Spiro-OMeTAD, the PbI_2 peak appear very early (day 2) for MAPI(1)-SO but it appears in day 10 for MAPI(2) that is the same time with the sample using Spiro-OMeTAD. Although, the PbI_2 peak appeared earlier for MAPI(1)-SO, from the *J-V* measurement in several batch of cells, we clearly observed that the cells prepared by 2-step technique MAPI(2) is less stable compared to 1-step MAPI(1)-SO. We have noticed that the MAPI(1)-SO cells still kept high performance even when the yellow PbI_2 phase started to appear.



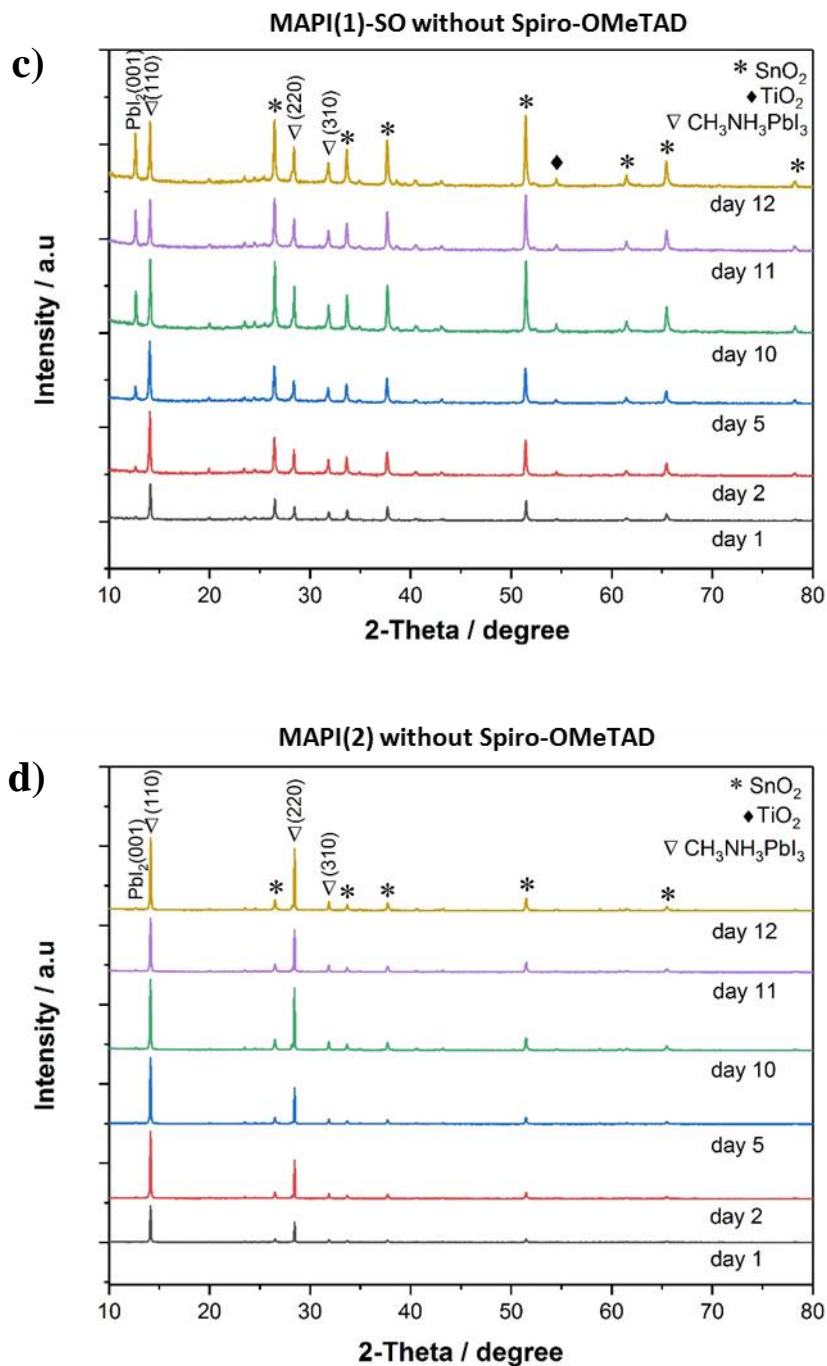


Figure 2.9. XRD pattern of; (a,c) MAPI(1)-SO and (b,d) MAPI(2) with and without Spiro-OMeTAD layer deposited on TiO_2 layer.

II.6. PL spectrum and PL decay study

The time integrated PL spectra of MAPI on glass and on TiO_2 are provided in Figure 2.10a and 2.10b for the MAPI(1)-SO and MAPI(2), respectively. They are characterized by an emission centered at 764 nm for both conditions. It is clearly seen that the emission is maximum when MAPI is deposited on glass substrate. The intensity of PL becomes lower with the presence of an electron transport layer (TiO_2) due to the charge transfer to TiO_2 which quenches the sample PL. These samples have also been investigated by time-correlated single-photon counting measurement (TCSPC). The measured curves are shown in Figure 2.10c.

The decay curves have been first normalized and fitted by the biexponential function:

$$PL(t) = y_0 + Ae^{-t/\tau_{fast}} + Be^{-t/\tau_{slow}} \quad (2.2)$$

The relative contribution of each of these two terms to the static PL has been evaluated by integrating the relative exponential traces.

The integral is equal to the product of the amplitude and the decay time. We can define the fast and the slow component relative contributions as:

$$\text{RC}_{fast}(\%) = A\tau_{fast} / (A\tau_{fast} + B\tau_{slow}) \quad (2.3a)$$

$$\text{RC}_{slow}(\%) = B\tau_{slow} / (A\tau_{fast} + B\tau_{slow}) \quad (2.3b)$$

The fast component, τ_{fast} , is assigned to free-carrier recombination at the surface, while the slow one, τ_{slow} is related to the bulk for carriers propagating deeper in the perovskite material [29], [30]. The measured values for four different samples are provided in Table 2.2. For MAPI(1)-SO on glass, we found 55 ns and 137 ns for τ_{fast} and τ_{slow} , respectively. Their RCs were calculated at 61.3% and 38.6%, respectively. On the other hand, for MAPI(2) deposited on glass, the lifetimes were shorter, measured at 26.7 ns for τ_{fast} and 94.8 ns for τ_{slow} , with also a high RC of 55.2% for the former. The higher lifetime of MAPI(1)-SO shows less bulk defects in this material. It might also explain the better stability found for MAPI(1)-SO.

In the presence of the TiO_2 layers, τ_{fast} is higher for MAPI(1)-SO, 13.2 ns, compared to MAPI(2) with a measured value at 1.3 ns. On the other hand, the slow part for both deposition techniques is almost the same, measured at 26.6 ns and 26.5 ns for MAPI(1)-SO and MAPI(2), respectively.

The better electron charge injection for MAPI(2) is in good agreement with the higher J_{sc} measured for these cells compared to the MAPI(1)-SO cells (see Table 2.1).

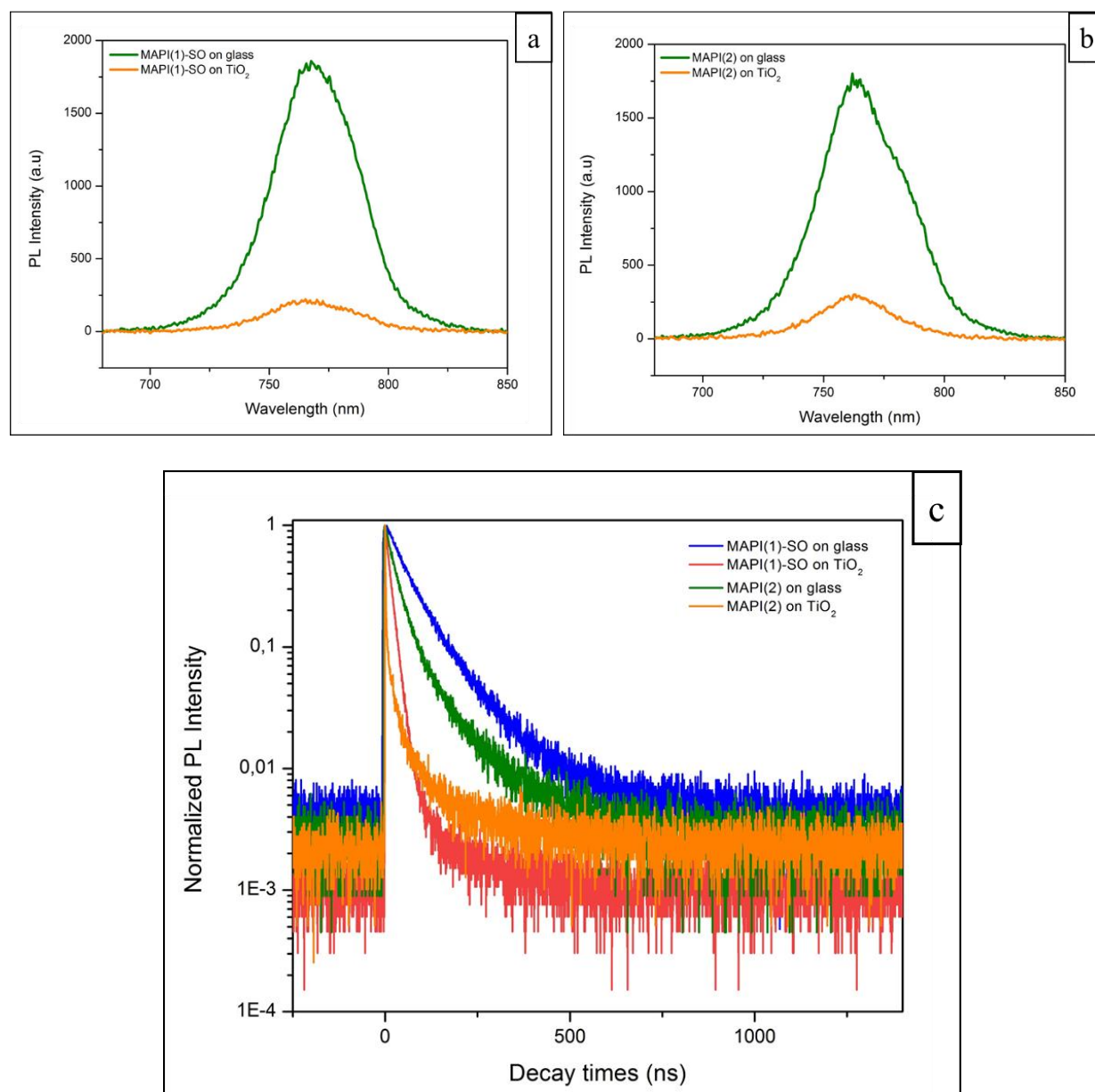


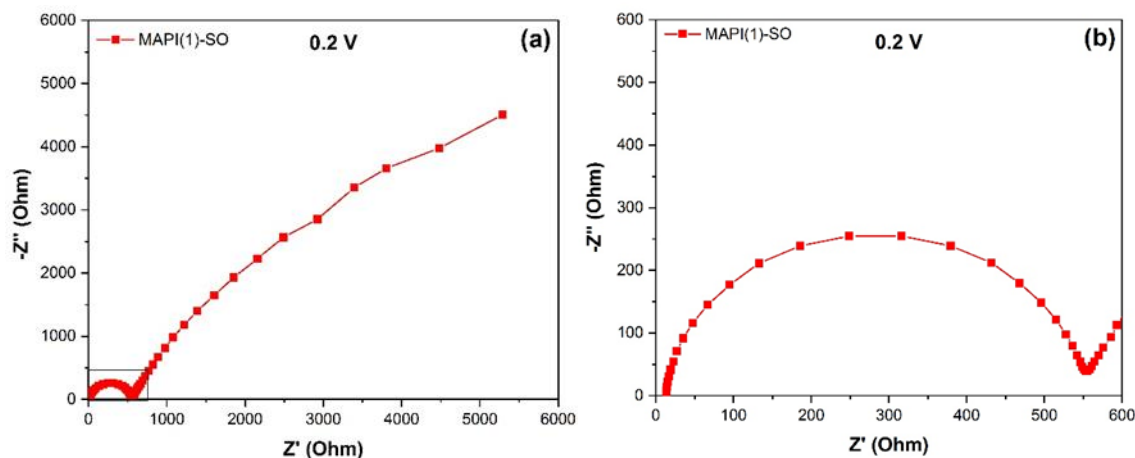
Figure 2.10. (a,b) Photoluminescence spectra of MAPI(1)-SO (a) and MAPI(2) (b) deposited on glass and on TiO_2 layers (excitation at 470 nm by a diode laser). (c) Time-correlated single-photon counting curves of the photoluminescence of the (a) and (b) MAPI samples.

Table 2.2. Parameters of TCSPC of 1-step and 2-step MAPI deposited on glass and on TiO_2 . The curves have been fitted by a bi-exponential decay equation.

| Samples | τ_{fast} (ns) | $\text{RC}_{\text{fast}}(\%)$ | τ_{slow} (ns) | $\text{RC}_{\text{slow}}(\%)$ |
|------------------------------|---------------------------|-------------------------------|---------------------------|-------------------------------|
| MAPI(1)-SO on glass | 55 | 61.3 | 137 | 38.6 |
| MAPI(1)-SO on TiO_2 | 13.2 | 75.6 | 26.6 | 24.3 |
| MAPI(2) on glass | 26.7 | 55.2 | 94.8 | 44.7 |
| MAPI(2) on TiO_2 | 1.3 | 29.6 | 26.5 | 70.3 |

II.7. Impedance study of the MAPI solar cells

To get deeper information about the MAPI cell functioning, they have been investigated by Impedance Spectroscopy (IS). We focus on the IS study of the MAPI(1)-SO cells due to the observed lower stability of the MAPI(2) cells upon the impedance measurements. The impedance spectra recorded at two different voltages, 0.2 V and 0.6 V, are presented in Figure 2.11a-d as Nyquist plots. The spectra were characterized by two main arcs of circle. The frequency transition between them lies at 260-500 Hz. An intermediate arc of circle could appear as a shoulder of the low frequency loop (see Figure 2.11e and 2.11f). It shows the occurrence of a middle frequency relaxation. We did not observe the inductive loop at the intermediate frequencies for MAPI(1)-SO whereas we have reported the appearance of this loop for MAPI(2) cells in Ref.[31].



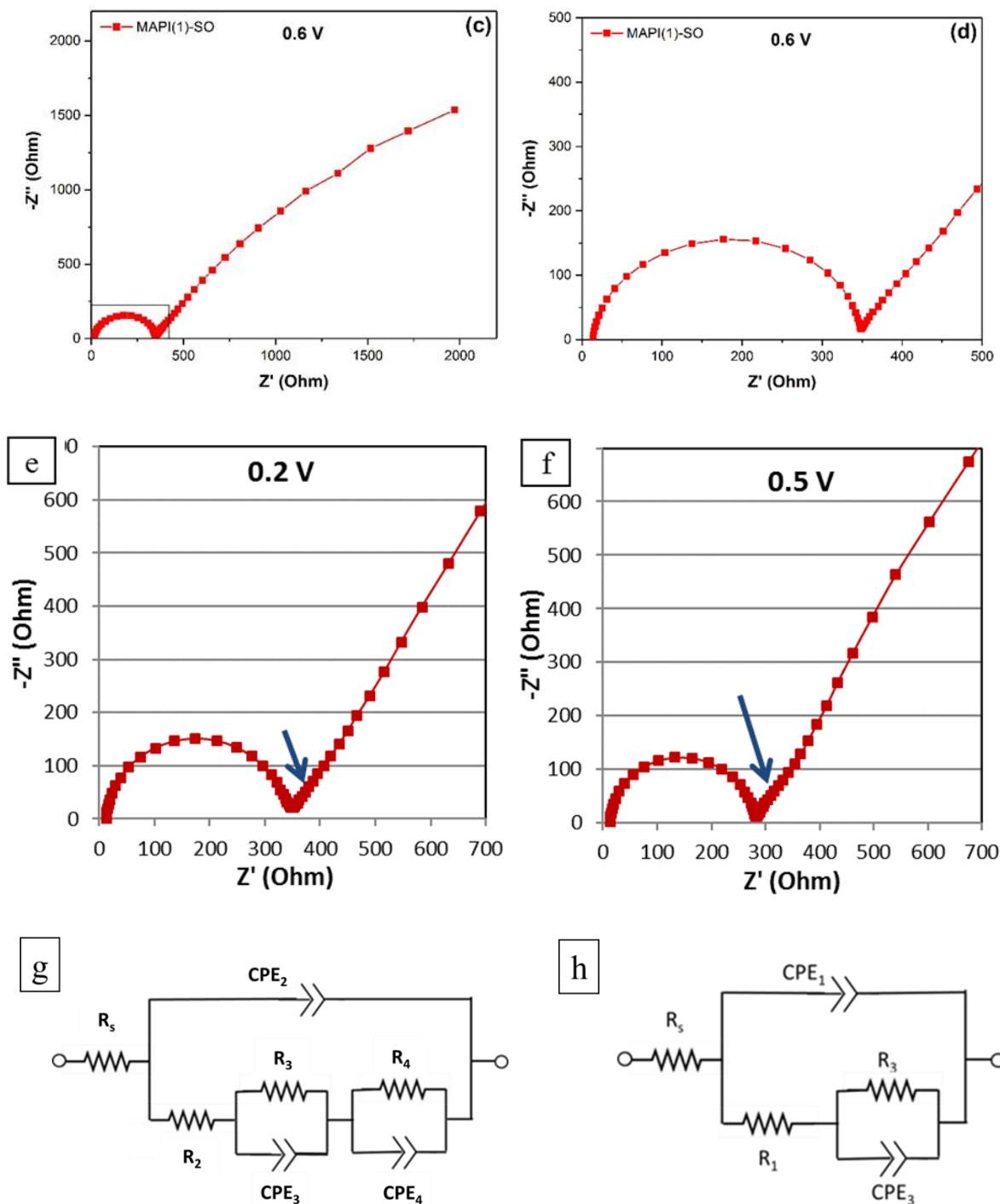


Figure 2.11. Nyquist plots of impedance spectra of PSCs prepared with MAPI(1)-SO perovskite measured under light (a-f) at 0.2V (a,b) and 0.6V (c,d) applied voltages. Zoom view at (e) 0.2V and (f) 0.5V. (g) Three relaxations and (h) two relaxations equivalent electrical circuits.

The general equivalent electrical circuit (EEC) used to fit the spectra is shown in Figure 2.11g. This circuit is simplified compared to the one presented Chapter I, Figure 1.26. R_s is a series resistance measured by extrapolating the high frequency loop to the x-axis. It is mainly due to gold and FTO contact electrodes and external wires. The high frequency and low frequency arcs of circle were fitted by the $R_2//\text{CPE}_2$ and $R_4//\text{CPE}_4$ electrical circuits, respectively. Due to the complexity and non-general occurrence of the middle frequency relaxation, the $R_3//\text{CPE}_3$ circuit has been neglected in most cases and will not be discussed in detail. The arcs of circle in the spectra were not strictly semicircles and showed some dispersion. The fit required the use of constant phase elements (CPE) to model the capacitive behavior as detailed in our previous work [31]. The equivalent capacitances have been then calculated from these CPEs using the Brug's protocol described in Ref. [32].

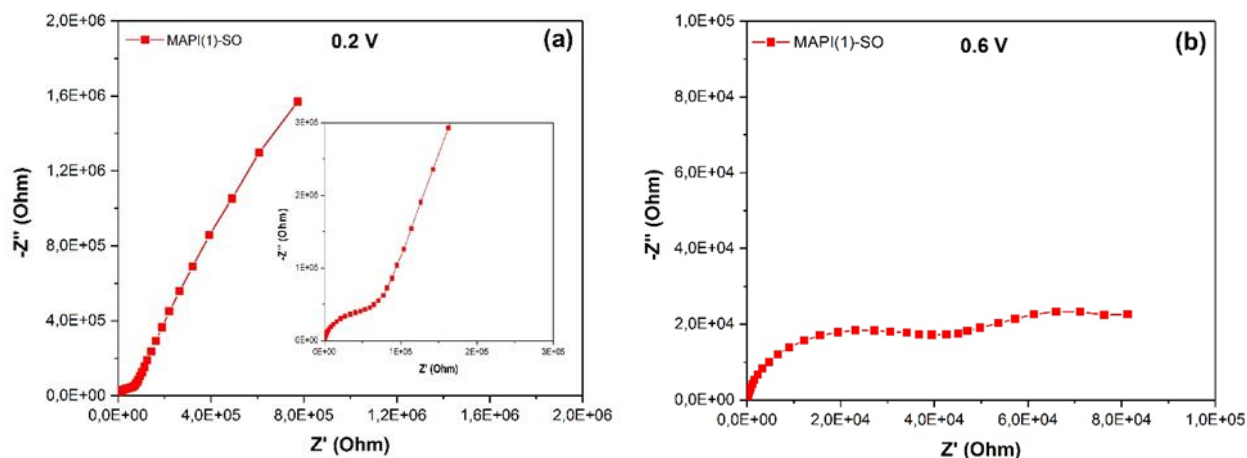


Figure 2.12. Nyquist plots of impedance spectra of MAPI(1)-SO PSCs measured in the dark at 0.2V (a) and 0.6V (b) applied voltages.

The cells have also been characterized in the dark. Typical spectra for MAPI(1)-SO perovskite are shown in Figure 2.12a and 2.12b. Two relaxations are found and compared to the spectra measured under light, the high and low frequency resistances were larger. The frequency transition between the two loops was in the 5-20 Hz range.

Using the EEC of Figure 2.11g,h, the various electrical parameters have been determined over a large frequency range. The high frequency capacitance C_2 was extracted from the CPE_2 parameters (See Chapter 1 section I.6.5). C_2 values as a function of V_{appl} are displayed in Figure 2.13. Figure 2.13a shows that for various solar cell batches the C_2 values were the same and that light had no influence on this parameter. Figures 2.13 also shows that for MAPI(1)-SO

perovskite, C_2 remains practically constant between 0 and 0.6V and slightly increases at higher V_{appl} . All these observations show that C_2 is mainly related to the intrinsic dielectric relaxation of the bulk perovskites [31], [33]. It corresponds to the geometrical capacitance of the perovskite layer. In Figure 2.13, below 0.6V, C_2 ranges between $5\text{--}6 \times 10^{-8} \text{ F}$ ($1.2\text{--}1.5 \times 10^{-8} \text{ F.cm}^2$) for MAPI(1)-SO. This capacitance is expressed by $C = \epsilon_r \epsilon_0 S / d$, with ϵ_0 the vacuum permittivity ($8.85 \times 10^{-12} \text{ F.m}^{-1}$), ϵ_r the relative permittivity, S the cell surface area and d the perovskite layer thickness. Because the organolead perovskite layer is not perfectly smooth (Figure 2.5), one must take into account the roughness factor, ρ , $S = \rho S_{\text{geo}}$, with S_{geo} the geometric surface area. ϵ_r is reported for MAPI in the literature, however, various values can be found: 6.5 [34], 22 [35], 23 [35], 24.1 [36], [37], 31.9 [34], 37 [35], and 70 [34]. C_2 can be estimated taking the following values: $S = 0.24 \text{ cm}^2$, $\rho = 1.2$ to 2, $\epsilon_r = 30$ and $d = 300$ to 500 nm. One finds then $1.5 \times 10^{-8} \text{ F} < C_1 < 4.2 \times 10^{-8} \text{ F}$, which is in good agreement with the obtained experimental data. The constancy of this parameter with V_{appl} up to 0.6V shows that no significant charge accumulation occurs at the contact in these PSCs and that, unlike DSSCs, no chemical capacitance is found [38]–[40]. The slight C_2 increase above 0.6V could be due to the charge carrier accumulation in TiO_2 above this V_{appl} [33].

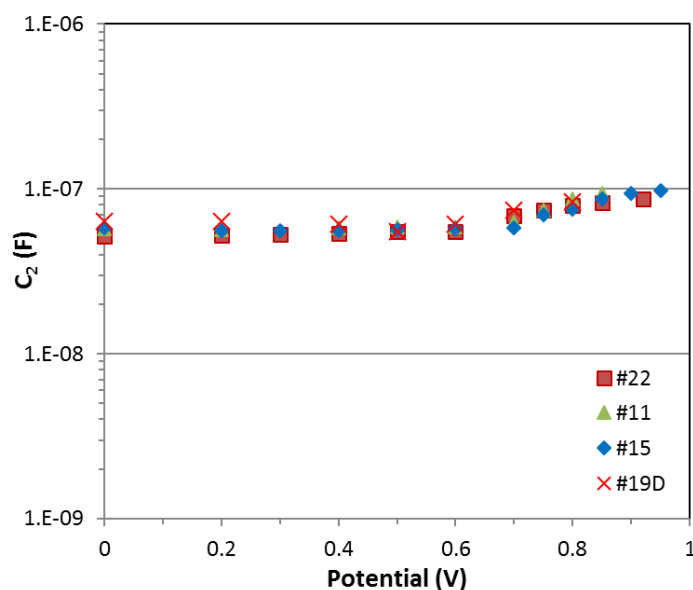


Figure 2.13. Effects of batch and of light shining on the C_2 parameter of MAPI(1)-SO cells under various applied potentials (Under light: full symbols; in the dark: cross symbol, #; cell number).

Figure 2.14a compares for MAPI(1)-SO and MAPI(2) the high frequency resistance R_2 determined from the fitting of the impedance spectra measured over a large V_{appl} . In Ref.[31], the Pauporté's group has shown that this resistance scale with the TiO_2 blocking layer thickness and crystallinity. We will also demonstrate in Chapter 3 and 4 that this resistance has a contribution from the HTM.

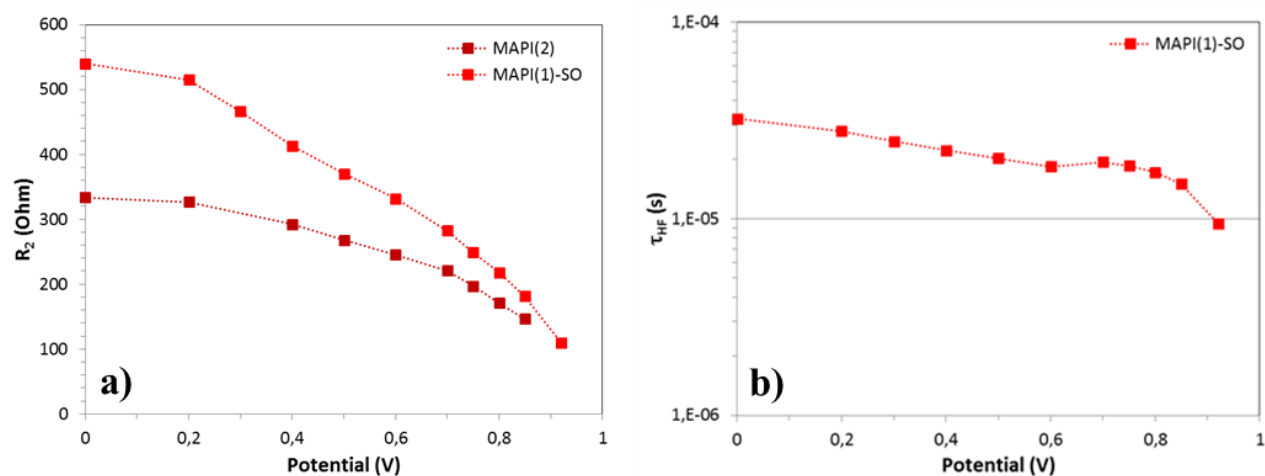


Figure 2.14. (a) Variation of R_2 with V_{appl} for various perovskite (MAPI(2) is a cell prepared with a two-step perovskite); (b) The high frequency relaxation time for MAPI(1)-SO cell as a function of the applied voltage.

Figure 2.14b displays the high frequency relaxation time defined as $\tau_{\text{HF}} = R_2 C_2$ of the MAPI(1)-SO cells. The low frequency capacitance, C_4 , of cells with various perovskites has been extracted from the fit of the impedance spectra. Figure 2.15a shows that this parameter increases with V_{appl} . C_4 increases dramatically by 2-3 orders of magnitude under the light shining. This surprising effect has been well-described in the literature [41]. It has been assigned to the displacement of the ions, their accumulation at the interface and charge compensation under light shining.

PSCs are known to present J - V curves with a hysteresis between the forward and the reverse scan direction. This hysteresis effect corresponds to a capacitive behavior and can be further studied by IS measurements. In the case of MAPI(1)-SO PSC, we have selected several solar cells, which preparation covered a long period of time, with various hysteresis. The amplitude of the hysteresis has been quantified using the hysteresis index (HI) (Eq. 2.1).

Clearly, in Figure 2.15b, the C_4 parameter scale with HI(%).

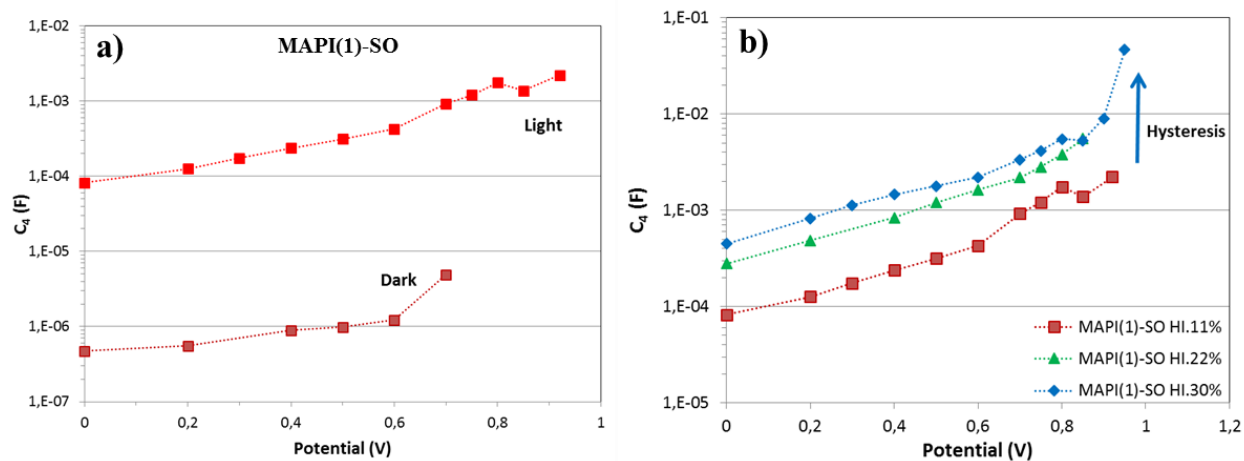


Figure 2.15. (a) Effect of perovskite and light shining on the low frequency C_4 parameter. (b) Low frequency C_4 parameter of MAPI(1)-SO cells for hysteresis indexes (HI) of 11%, 22% and 30%.

The low frequency resistance, R_4 is presented in Figure 2.16a for the MAPI(1)-SO cell under light and in the dark. Figure 2.16b shows that this resistance decreases in a large extent with light shining and that dark R_4 tends to light R_4 at high V_{appl} . This decrease was also found for instance by Pockett et al. for measurements at the V_{oc} for various light intensities [42]. This resistance can be considered as an estimation of the recombination resistance. The resistance decreases with the applied voltage and then more recombinations occur by increasing this parameter. $\tau_{\text{LF}} = R_4 C_4$ is the relaxation time calculated at low frequency. Figure 2.16b shows that it lies in the several seconds range. It shows the occurrence of a slow process which is the ionic relaxation in the perovskite near the interfaces. The slow ionic movements and redistribution govern the recombination phenomena occurring in the cells.

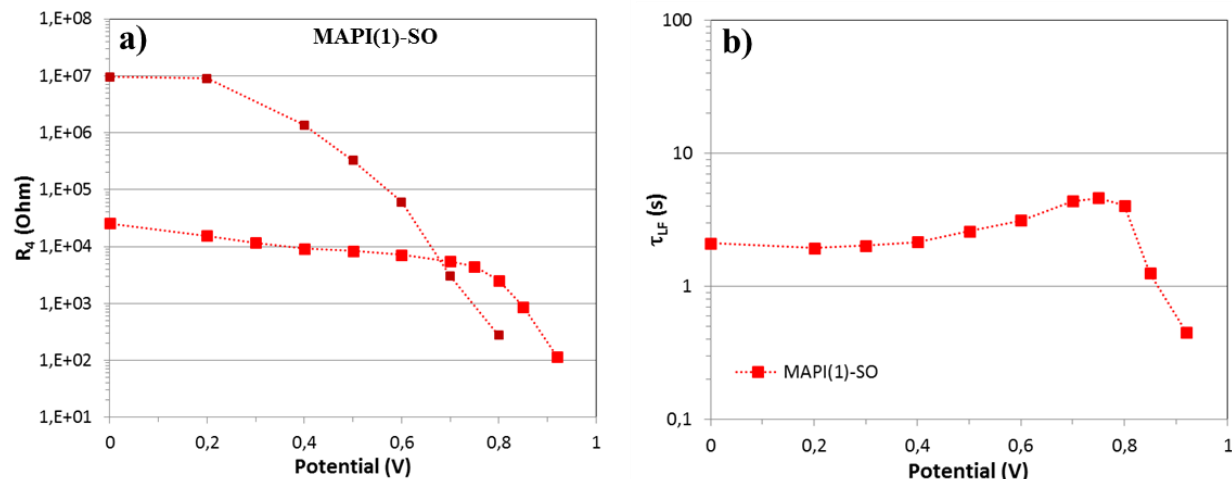


Figure 2.16. MAPI(1)-SO cell at various voltage (a) low frequency resistance R_4 in the dark (red square) and under light (dark red square). (b) low frequency relaxation time, τ_{LF} , of the PSCs measured under light.

II.8. Conclusion

We have optimized two different deposition techniques of MAPI for perovskite solar cell application. The corresponding layers have been named MAPI(1)-SO and MAPI(2). The 1-step deposition technique is based on a fast-crystallization by dripping an anti-solvent (chlorobenzene in our case) on a precursor solution film upon spinning. The 2-step deposition technique has a great advantage in term of morphology control of the perovskite layer compared to the 1-step one due to a better confinement of PbI_2 into the nano-porous network of TiO_2 . SEM images showed that the perovskite grain size for 1-step is more uniform than 2-step technique. The bandgap for both deposition techniques were found to be the same, it was measured at around 1.59 eV. The structural characteristics also showed the same properties with a slightly higher PbI_2 intensity peak for the MAPI(2). Through the optimization of both deposition techniques, the best PCE for MAPI(1)-SO and MAPI(2) cells was 17.52% and 18.18%, respectively. The photoluminescence and lifetime measurements have been applied in order to understand the structural quality of the perovskite film. The higher lifetime measured on MAPI(1)-SO is assigned to a better film crystallinity. The impedance analysis has been developed for the MAPI(1)-SO cells that will be further employed in the next chapters. A first equivalent electrical circuit has been proposed to fit the data and first assignments of the various electrical elements

have been done. They will be refined in the next chapters where further IS investigations have been carried out.

References

- [1] A. Kojima, K. Teshima, Y. Shirai, and T. Miyasaka, “Organometal halide perovskites as visible-light sensitizers for photovoltaic cells,” *J Am Chem Soc*, vol. 131, 2009.
- [2] H.-. S. Kim *et al.*, “Lead iodide perovskite sensitized all-solid-state submicron thin film mesoscopic solar cell with efficiency exceeding 9 %,” *Sci Rep*, vol. 2, 2012.
- [3] K. Wojciechowski, M. Saliba, T. Leijtens, A. Abate, and H. J. Snaith, “Sub-150 [degree]C processed meso-superstructured perovskite solar cells with enhanced efficiency,” *Energy Environ. Sci.*, vol. 7, no. 3, pp. 1142–1147, 2014.
- [4] Conings Bert, Baeten Linny, De Dobbelaere Christopher, D’Haen Jan, Manca Jean, and Boyen Hans-Gerd, “Perovskite-Based Hybrid Solar Cells Exceeding 10% Efficiency with High Reproducibility Using a Thin Film Sandwich Approach,” *Adv. Mater.*, vol. 26, no. 13, pp. 2041–2046, Dec. 2013.
- [5] B. Cai, Y. Xing, Z. Yang, W.-H. Zhang, and J. Qiu, “High performance hybrid solar cells sensitized by organolead halide perovskites,” *Energy Environ. Sci.*, vol. 6, no. 5, pp. 1480–1485, 2013.
- [6] E. Edri, S. Kirmayer, D. Cahen, and G. Hodes, “High Open-Circuit Voltage Solar Cells Based on Organic–Inorganic Lead Bromide Perovskite,” *J. Phys. Chem. Lett.*, vol. 4, no. 6, pp. 897–902, Mar. 2013.
- [7] J. T.-W. Wang *et al.*, “Low-Temperature Processed Electron Collection Layers of Graphene/TiO₂ Nanocomposites in Thin Film Perovskite Solar Cells,” *Nano Lett.*, vol. 14, no. 2, pp. 724–730, Feb. 2014.
- [8] J. Burschka *et al.*, “Sequential deposition as a route to high-performance perovskite-sensitized solar cells,” *Nature*, vol. 499, 2013.
- [9] D. B. Mitzi, “Thin-Film Deposition of Organic–Inorganic Hybrid Materials,” *Chem. Mater.*, vol. 13, no. 10, pp. 3283–3298, Oct. 2001.
- [10] K. Liang, D. B. Mitzi, and M. T. Prikas, “Synthesis and Characterization of Organic–Inorganic Perovskite Thin Films Prepared Using a Versatile Two-Step Dipping Technique,” *Chem. Mater.*, vol. 10, no. 1, pp. 403–411, Jan. 1998.
- [11] M. Liu, M. B. Johnston, and H. J. Snaith, “Efficient planar heterojunction perovskite solar cells by vapour deposition,” *Nature*, vol. 501, 2013.
- [12] O. Malinkiewicz *et al.*, “Perovskite solar cells employing organic charge-transport layers,” *Nat. Photonics*, vol. 8, p. 128, Dec. 2013.
- [13] Malinkiewicz Olga *et al.*, “Metal-Oxide-Free Methylammonium Lead Iodide Perovskite-Based Solar Cells: the Influence of Organic Charge Transport Layers,” *Adv. Energy Mater.*, vol. 4, no. 15, p. 1400345, Jun. 2014.
- [14] A. S. Subbiah, A. Halder, S. Ghosh, N. Mahuli, G. Hodes, and S. K. Sarkar, “Inorganic Hole Conducting Layers for Perovskite-Based Solar Cells,” *J. Phys. Chem. Lett.*, vol. 5, no. 10, pp. 1748–1753, May 2014.
- [15] L. K. Ono, M. R. Leyden, S. Wang, and Y. Qi, “Organometal halide perovskite thin films and solar cells by vapor deposition,” *J. Mater. Chem. A*, vol. 4, no. 18, pp. 6693–6713, 2016.

- [16] Q. Chen *et al.*, “Planar heterojunction perovskite solar cells via vapor-assisted solution process,” *J Am Chem Soc*, vol. 136, 2014.
- [17] Q. Chen *et al.*, “Controllable Self-Induced Passivation of Hybrid Lead Iodide Perovskites toward High Performance Solar Cells,” *Nano Lett.*, vol. 14, no. 7, pp. 4158–4163, Jul. 2014.
- [18] Y. Li *et al.*, “Fabrication of planar heterojunction perovskite solar cells by controlled low-pressure vapor annealing,” *J Phys Chem Lett*, vol. 6, 2015.
- [19] T. Du, N. Wang, H. Chen, H. Lin, and H. He, “Comparative Study of Vapor- and Solution-Crystallized Perovskite for Planar Heterojunction Solar Cells,” *ACS Appl. Mater. Interfaces*, vol. 7, no. 5, pp. 3382–3388, Feb. 2015.
- [20] Y. Takeoka, K. Asai, M. Rikukawa, and K. Sanui, “Systematic Studies on Chain Lengths, Halide Species, and Well Thicknesses for Lead Halide Layered Perovskite Thin Films,” *Bull. Chem. Soc. Jpn.*, vol. 79, no. 10, pp. 1607–1613, Oct. 2006.
- [21] A. M. Salau, “Fundamental absorption edge in $\text{PbI}_2\text{:KI}$ alloys,” *Sol. Energy Mater.*, vol. 2, no. 3, pp. 327–332, Apr. 1980.
- [22] D. B. Mitzi, M. T. Prikas, and K. Chondroudis, “Thin Film Deposition of Organic–Inorganic Hybrid Materials Using a Single Source Thermal Ablation Technique,” *Chem. Mater.*, vol. 11, no. 3, pp. 542–544, Mar. 1999.
- [23] L. Zheng *et al.*, “Improved light absorption and charge transport for perovskite solar cells with rough interfaces by sequential deposition,” *Nanoscale*, vol. 6, no. 14, pp. 8171–8176, 2014.
- [24] Y. Wu *et al.*, “Retarding the crystallization of PbI_2 for highly reproducible planar-structured perovskite solar cells via sequential deposition,” *Energy Environ. Sci.*, vol. 7, no. 9, pp. 2934–2938, 2014.
- [25] T. Du, C. H. Burgess, J. Kim, J. Zhang, J. R. Durrant, and M. A. McLachlan, “Formation, location and beneficial role of PbI_2 in lead halide perovskite solar cells,” *Sustain. Energy Fuels*, vol. 1, no. 1, pp. 119–126, 2017.
- [26] T. J. Jacobsson *et al.*, “Unreacted PbI_2 as a Double-Edged Sword for Enhancing the Performance of Perovskite Solar Cells,” *J. Am. Chem. Soc.*, vol. 138, no. 32, pp. 10331–10343, Aug. 2016.
- [27] Kim Young Chan *et al.*, “Beneficial Effects of PbI_2 Incorporated in Organo-Lead Halide Perovskite Solar Cells,” *Adv. Energy Mater.*, vol. 6, no. 4, p. 1502104, Dec. 2015.
- [28] D. H. Cao *et al.*, “Remnant PbI_2 , an unforeseen necessity in high-efficiency hybrid perovskite-based solar cells?,” *APL Mater.*, vol. 2, no. 9, p. 091101, Sep. 2014.
- [29] D. Shi *et al.*, “Low trap-state density and long carrier diffusion in organolead trihalide perovskite single crystals,” *Science*, vol. 347, no. 6221, p. 519, Jan. 2015.
- [30] F. Staub *et al.*, “Beyond Bulk Lifetimes: Insights into Lead Halide Perovskite Films from Time-Resolved Photoluminescence,” *Phys Rev Appl.*, vol. 6, no. 4, p. 044017, Oct. 2016.
- [31] P. Wang, Z. Shao, M. Ulfa, and T. Pauporté, “Insights into the Hole Blocking Layer Effect on the Perovskite Solar Cell Performance and Impedance Response,” *J. Phys. Chem. C*, vol. 121, no. 17, pp. 9131–9141, May 2017.
- [32] G. J. Brug, A. L. G. van den Eeden, M. Sluyters-Rehbach, and J. H. Sluyters, “The analysis of electrode impedances complicated by the presence of a constant phase element,” *J. Electroanal. Chem. Interfacial Electrochem.*, vol. 176, no. 1, pp. 275–295, Sep. 1984.
- [33] H.-S. Kim *et al.*, “Mechanism of carrier accumulation in perovskite thin-absorber solar cells,” *Nat. Commun.*, vol. 4, p. 2242, Jul. 2013.

- [34]L. Pedesseau *et al.*, “Dielectric properties of hybrid perovskites and drift-diffusion modeling of perovskite cells,” 2016, vol. 9743, pp. 97430N-9743-9.
- [35]A. Guerrero *et al.*, “Properties of Contact and Bulk Impedances in Hybrid Lead Halide Perovskite Solar Cells Including Inductive Loop Elements,” *J. Phys. Chem. C*, vol. 120, no. 15, pp. 8023–8032, Apr. 2016.
- [36]J. M. Frost, K. T. Butler, and A. Walsh, “Molecular ferroelectric contributions to anomalous hysteresis in hybrid perovskite solar cells,” *APL Mater.*, vol. 2, no. 8, p. 081506, Jul. 2014.
- [37]A. Pockett *et al.*, “Characterization of Planar Lead Halide Perovskite Solar Cells by Impedance Spectroscopy, Open-Circuit Photovoltage Decay, and Intensity-Modulated Photovoltage/Photocurrent Spectroscopy,” *J. Phys. Chem. C*, vol. 119, no. 7, pp. 3456–3465, Feb. 2015.
- [38]C. Magne, T. Moehl, M. Urien, M. Grätzel, and T. Pauporté, “Effects of ZnO film growth route and nanostructure on electron transport and recombination in dye-sensitized solar cells,” *J. Mater. Chem. A*, vol. 1, no. 6, pp. 2079–2088, 2013.
- [39]Y. Kusumawati, M. Hosni, M. A. Martoprawiro, S. Cassaignon, and T. Pauporté, “Charge Transport and Recombination in TiO₂ Brookite-Based Photoelectrodes,” *J. Phys. Chem. C*, vol. 118, no. 41, pp. 23459–23467, Oct. 2014.
- [40]Y. Kusumawati, M. A. Martoprawiro, and T. Pauporté, “Effects of Graphene in Graphene/TiO₂ Composite Films Applied to Solar Cell Photoelectrode,” *J. Phys. Chem. C*, vol. 118, no. 19, pp. 9974–9981, May 2014.
- [41]E. J. Juarez-Perez *et al.*, “Photoinduced Giant Dielectric Constant in Lead Halide Perovskite Solar Cells,” *J. Phys. Chem. Lett.*, vol. 5, no. 13, pp. 2390–2394, Jul. 2014.
- [42]A. Pockett, G. E. Eperon, N. Sakai, H. J. Snaith, L. M. Peter, and P. J. Cameron, “Microseconds, milliseconds and seconds: deconvoluting the dynamic behaviour of planar perovskite solar cells,” *Phys. Chem. Chem. Phys.*, vol. 19, no. 8, pp. 5959–5970, 2017.

Chapter III

Molecular and Polymeric Hole Transporting Material for High Performance Perovskite Solar Cells

In this chapter, perovskite solar cells incorporating a molecular and a polymeric hole transporting material (HTM) are compared. The 1-step MAPI perovskite (MAPI(1)-SO) will be used as the active layer in this study, and the device structure will be the conventional architecture where the perovskite is sandwiched between the *bl*-TiO₂ combined with *meso*-TiO₂ ETL and a HTM layer. The molecular HTM is the classical Spiro-OMeTAD which will be compared to P3HT chosen as a rather cheap and efficient polymeric HTM.

III.1. Introduction

The hole transporting material (HTM) is a key component of the device to achieve high efficiency (See Chapter I, Section I.5.3). It must accept the holes photogenerated in the perovskite and present a good hole mobility. The other properties sought for are an excellent thermal, morphological and photochemical stability, and good hydrophobic properties to protect the perovskite materials from moisture.

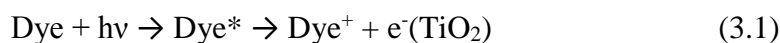
Organic HTMs can be essentially divided into two subclasses depending on their molecular weight: molecular and polymeric HTMs. The latter have important advantages in terms of processability, thermal and mechanical stability, and higher intrinsic hole mobility. On the other hand, molecular HTMs are beneficial in terms of synthetic reproducibility, well-defined molecular weight and structure. The most popular and efficient molecular HTM employed in the literature is 2,2',7,7'-tetrakis(N,N-di-p-ethoxyphenylamine)-9,9'-spirobifluorene (Spiro-OMeTAD) (Figure 3.1a). Spiro-OMeTAD is employed routinely with two additives bis(trifluoromethane)sulfoimide (LiTFSI) (Figure 3.1d) and 4-*tert*-butylpyridine (tBP) (Figure 3.1c). LiTFSI favor the oxidation and then the p-doping of Spiro-OMeTAD [1]. tBP molecules have been shown to prevent LiTFSI aggregation, to improve its distribution and to provide a better interface between the HTM layer and the perovskite layer [2].

The oxidation of Spiro-OMeTAD is required to get a HTM suitable for PSC application. Compared to its pristine form, the oxidized one has a conductivity higher by several orders of

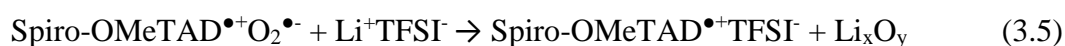
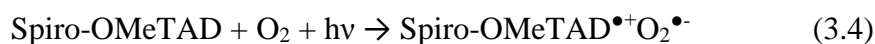
magnitude. Oxidized Spiro-OMeTAD is characterized by an absorption band in the 450-550 nm spectral range and can then be followed by spectrophotometry.

The oxidation mechanism of Spiro-OMeTAD was first studied in relation to the solid-state dye-sensitized solar cell (ssDSSC) application (See Chapter I, Section I.3). Different oxidation mechanisms have been proposed in the literature. They can be direct, by a strong oxidant, or by molecular oxygen. In the latter case, the assistance of annealing, additives, light and/or acids is required.

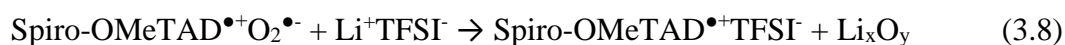
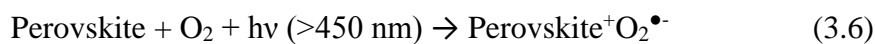
The effect of light was first proposed by Bach and coll. for ssDSSCs [3]. In their mechanism, electrons coming from excited dyes are captured by oxygen and the oxidized Spiro-OMeTAD is created by regeneration of the oxidized dye. In the reactions, LiTFSI functions either as a catalyst or a stabilizer of the oxidized Spiro-OMeTAD. The mechanism is written as:



A similar mechanism has been suggested later for PSCs by Wang et al [4]. They have shown a wavelength dependent mechanism. Spiro-OMeTAD can be directly oxidized as a radical cation by O_2 using short wavelength irradiations:



Whereas, for long wavelength radiations (>450 nm), a three step mechanism would occur:



On the other hand, Snaith et al. have described the oxidation of Spiro-OMeTAD without light and dye/perovskite assistance [1]. They have proposed a two-step mechanism: first, the formation of an oxidized Spiro-OMeTAD from equilibrium between Spiro-OMeTAD with O₂ (3.9). Second, by adding LiTFSI, the balance is disturbed because the superoxide radical O₂^{•-} reacts with Li⁺ to form Li₂O and Li₂O₂, and finally Spiro-OMeTAD^{•+}TFSI⁻ is generated (3.10).

The mechanism could be written as:



Li et al. have stated that the latter reaction is slow [5]. Adding an acid, such as H₃PO₄, accelerates the reaction and favors the oxidation in the presence of LiTFSI. Moreover, NaTFSI, which is inactive without acid, becomes active and promotes the oxidation reaction in the presence of acid.

Fang et al. [6] have reported the activation of Spiro-OMeTAD oxidation in the presence of LiTFSI by annealing at 80°C and, better, at 140 °C.

In the case of Co(III) complex dopants, the oxidation of Spiro-OMeTAD has been described as direct with the direct and rapid formation of the radical cation [7]. Using a Co(III) complex with a higher redox potential (by playing on the ligands) favors the oxidation reaction. They have also shown that Co(II) complexes are inactive [7].



The two main polymer HTMs for PSC are poly(triarylamine) (PTAA) and Poly(3-hexylthiophene-2,5-diyl) (P3HT) (Figure 3.1b) [8]–[16]. Both have conjugated chains and exhibit a rather high stability [16]. P3HT is a thiophene based polymer with attached (CH₂)₅CH₃ side chains (Figure 3.1b). PTAA presents the same triphenylamine groups as Spiro-OMeTAD and is also the only polymeric semiconductor giving high efficiency PSCs (above 22% [8]). However, the very high cost of this compound renders its use not competitive for a large-scale application [17]. On the other hand, P3HT is much cheaper to produce than PTAA and Spiro-OMeTAD (Table 1 Ref.[9]). As regards to its facile processing method and desirable hole conductivity, P3HT is regarded as a good HTM candidate for PSC.

This compound is promising for robust, temperature resistant devices. For instance, recently, Zheng et al. [10] showed the better stability at high temperature (up to 85°C) of additive-free P3HT- cells compared to the Spiro-OMeTAD ones. The efficiency of P3HT-based PSCs remains lower than that of PTAA but promising. Jung et al. [11] have reported a PCE above 16% by cobalt doping of P3HT, while Nia et al. [12] found that using a rather thick mesoporous TiO₂ layer combined with large P3HT polymers of 124 kDa can give rise to a maximum PCE of 16.2%. Molecular *p*-type doping by using F4TCNQ, which acts as an electron acceptor, has been reported to increase the P3HT conductivity from $1.1 \times 10^{-5} \text{ S.cm}^{-1}$ to $5.6 \times 10^{-4} \text{ S.cm}^{-1}$ and then the cell performances [13]. Cobalt has also been reported for the *p*-doping of P3HT.[24] However, the most popular P3HT dopants/additives are LiTFSI and tBP (Figure 3.1d and 3.1c). LiTFSI increases the carrier density [14], [15] and slightly decreases the P3HT HOMO level [15]. tBP increases the mobility of the charge carriers and has no effect on the polymer HOMO level [15]. The P3HT conductivity was measured by Heo et al. [14] to change from $5.0 \times 10^{-5} \text{ S.cm}^{-1}$ without additive to $1.6 \times 10^{-3} \text{ S.cm}^{-1}$ with LiTFSI and tBP additives. Another strategy adopted by Park et al. [16] to enhance the layer compactness and conductivity was to prepare P3HT nanofibrils obtained via the π -conjugation of the thiophene rings. Jimenez-Lopez et al. [18] have found that, in spite of the comparable HOMO level of Spiro-OMeTAD and P3HT HTMs, the V_{oc} difference is about 200 mV. Photo-physical measurements comparing doped Spiro-OMeTAD and undoped P3HT have suggested that the V_{oc} limitation for the latter is due to trap mediated recombinations and less efficient hole transfer [18].

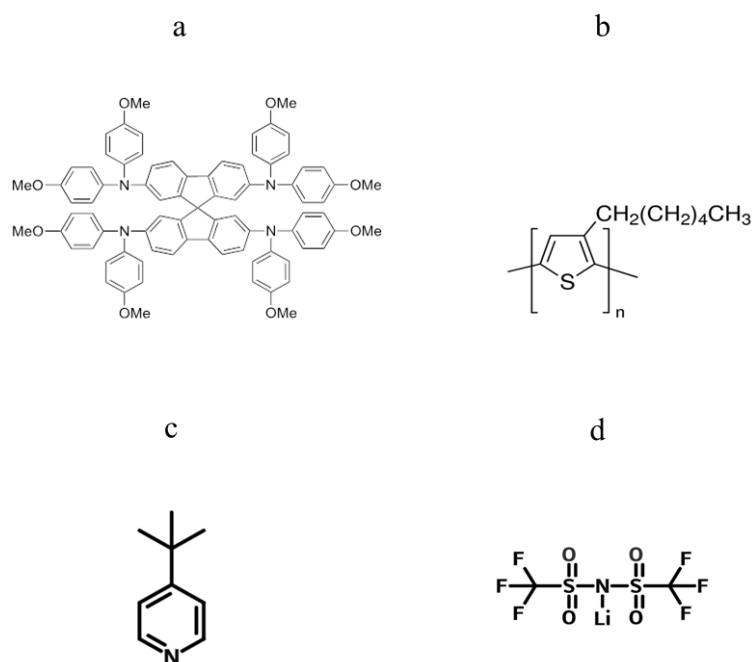


Figure 3.1. (a) Molecular structure of Spiro-OMeTAD, (b) P3HT, (c) 4-tert-butylpyridine (tBP) and (d) bis(trifluoromethane)sulfoimide (LiTFSI).

III.2. Experimental

The *bl*-TiO₂, *meso*-TiO₂, and MAPI layers were prepared according to the procedures described in Chapter II Section II.2. In the following, we detail the preparation of Spiro-OMeTAD and P3HT layers.

III.2.1. Spiro-OMeTAD layer preparation

For the doped Spiro-OMeTAD cells, a solution was prepared by dissolving 72 mg of Spiro-OMeTAD in 1 mL chlorobenzene. Then, 17.5 μ L of LiTFSI solution (520 mg in 1 mL ACN), 28.8 μ L of tBP (4-*tert*-butylpyridine, 96% Sigma-Aldrich) and 6 μ L of tris(2-(1H-pyrazol-1-yl)-4-*tert*-butylpyridine)cobalt(III) tri[bis(trifluoromethane)sulfonimide] (FK209 from Dyesol) (300 mg in 1 mL ACN) were added to this solution. The solution of undoped Spiro-OMeTAD (cells noted *Spiro-Un*) was the same without the chemical additives. 35 μ L of these HTM solutions was spin-coated at 4000 rpm for 20 s. Finally, the device was completed by thermally evaporating a 70-80 nm thick gold back contact on the Spiro-OMeTAD layer. The solar cell surface area delimited by the back contact was about 0.24 cm².

III.2.2. P3HT layer preparation

The P3HT solution was prepared by dissolving 15 mg of high molecular weight (MW) P3HT (Merck SP001 lisicon®) in 1 mL chlorobenzene. The cells prepared with P3HT without additive are denoted *P3HT-Un*. For the *P3HT-Li* cells, 7.5 μL of a LiTFSI solution (170 mg in 1 mL acetonitrile (ACN)) and 7.5 μL of tBP solution (1 mL in 1 mL ACN) were added to the P3HT solution. In the case of *P3HT-Co* cells, 18 μL of ACN, 6 μL of FK209 Co solution (10.5 mg in 5 mL ACN) and 6 μL tBP were added. The P3HT precursor solutions were stirred on a hotplate at 55 °C for 1 h in the glovebox to ensure a full solubilization before use. The solutions were spin-coated at room temperature on top of the perovskite layer at 4000 rpm for 20 s (4000 rpm/s acceleration). 35 μL of the HTM solution was dropped once the 4000 rpm speed was reached. (see Section III.2.3 for more details). Finally, the device was completed by thermally evaporating a 70-80 nm thick gold back contact on the P3HT layer. The solar cell surface area delimited by the back contact was about 0.24 cm².

III.2.3. P3HT spin-coating technique

Preliminary tests were carried-out to optimize the spin-coating technique of P3HT. The first technique, noted Drop-Spin, consisted in dropping the HTM solution on top of the perovskite layer and then to start the spin-coating program. The second technique, noted Spin-Drop, consisted in starting the program and then dropping the solution once the acceleration phase was finished. The averaged results are gathered in Table 3.1. The Drop-Spin technique gave better results in the case of P3HT-Un. On the other hand, a higher efficiency and, importantly, a lower hysteresis were found with the Spin-Drop technique applied to the P3HT-Li solution. This technique was retained in the following.

Table 3.1. Averaged photovoltaic *J-V* curve parameters and power conversion efficiencies of PSCs prepared by Drop-Spin and Spin-Drop the P3HT precursor solutions. (AM1.5G filtered 100 mW cm⁻² illumination).

| Samples | Spin coating process | Scan direction | V _{oc} (V) | J _{sc} (mA.cm ⁻²) | FF (%) | PCE (%) |
|---------|----------------------|----------------|---------------------|--|--------|---------|
| P3HT-Un | Drop-Spin | Rev | 0.88 | 16.6 | 60.6 | 8.9 |
| | | For | 0.87 | 17.2 | 56.7 | 8.5 |
| | Spin-Drop | Rev | 0.91 | 15.4 | 59.6 | 8.3 |
| | | For | 0.895 | 15.635 | 55.53 | 7.8 |
| P3HT-Li | Drop-Spin | Rev | 0.935 | 16.9 | 70.1 | 11.2 |
| | | For | 0.91 | 16.3 | 36 | 5.2 |
| | Spin-Drop | Rev | 0.94 | 16.8 | 71.7 | 11.3 |
| | | For | 0.92 | 16.4 | 47.2 | 7.1 |

III.3. Optical characterizations

P3HT has been chosen as a model conjugated polymer HTM for PSC application and is compared to the benchmark Spiro-OMeTAD HTM. Absorbance spectra before and after normalization of doped and undoped P3HT layers on glass are shown in Figure 3.2a and Figure 3.2b, respectively. High-MW P3HT is a purple-colored semiconductor compound (Figure 3.2a) and has a bandgap of 1.9-2.0 eV. The layers are characterized by a broad absorption peak between 400 and 650 nm which is related to π - π^* absorption transitions at 525 nm, 560 nm and 605 nm. The absorbance peak at 525 nm provides information on the degree of conjugation in the P3HT chains [19]. The maximum absorbance value remains about the same after doping (Figure 3.2a). On the other hand, the band at 605 nm is related to the interchain order [19]. The spectra show that the presence of LiTFSI and, more importantly, the cobalt salt increases this parameter (Figure 3.2b). The Spiro-OMeTAD spectra are presented in Figure 3.2c. They are characterized by an absorption band at 340-430 nm. No significant change could be observed with doping in this case. Spiro-OMeTAD is a wide bandgap (about 3.0 eV) molecular semi-conductor, transparent over most of the visible wavelength region.

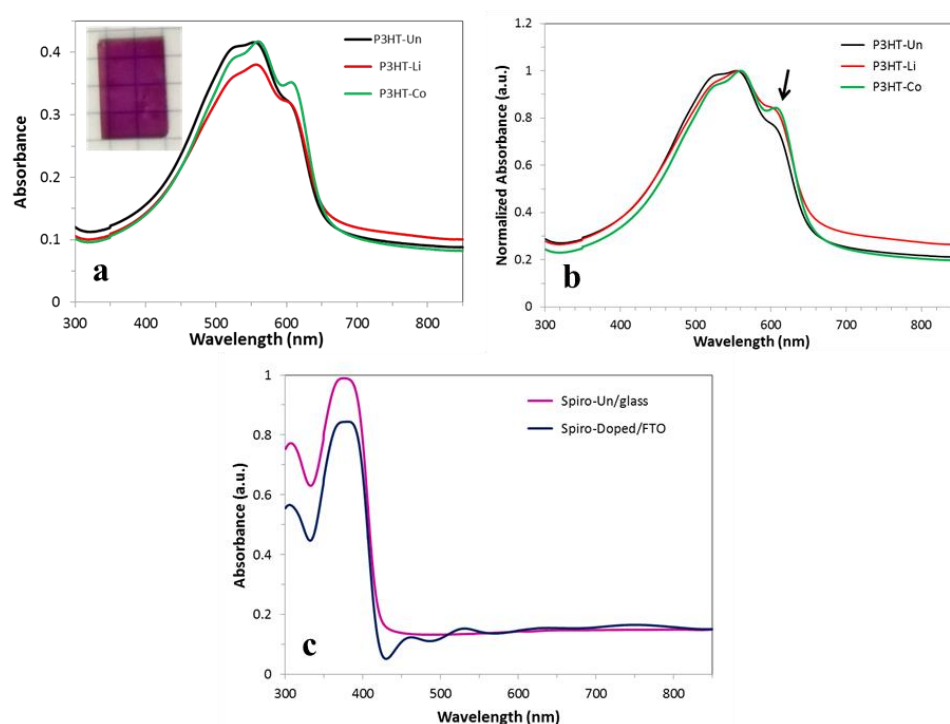


Figure 3.2. Absorbance curves. (a) Doped and undoped P3HT on glass. Inset: layer picture. (b) Normalized absorbance spectra of doped and undoped P3HT layers on glass. (c) Spiro-OMeTAD undoped on glass and Spiro-OMeTAD doped on FTO/Glass (No layer could be deposited directly on glass in this case and the substrate change explain the observed waves above 420 nm).

III.4. Perovskite solar cells results

The PSC device structure is shown in Figure 3.3a. The effects of HTM material and doping on the J - V curves are shown in Figure 3.3b. The average and best photovoltaic parameters of P3HT and Spiro-OMeTAD-based solar cells with various dopings are gathered in Table 3.2. Doping has an important effect on the Spiro-OMeTAD cells. The best power conversion efficiency (PCE) for Spiro-Doped cells is 17.7%. These cells present high J_{sc} and FF. Without doping, the performances drop dramatically with a maximum PCE measured at 5.1%. Spiro-Un devices suffer from a low FF that can be attributed to the low HTM conductivity and therefore high charge transport resistances. The J_{sc} and V_{oc} parameters are also reduced. On the other hand, the effect of doping is not so dramatic in the case of the polymer-based cells. The best additives for the performances are LiTFSI and tBP. P3HT-Li cells could achieve a PCE of 13.4 % which is one of the highest PCE reported for P3HT-HTM based PSCs. P3HT-Li cells exhibit an improved fill factor parameter (FF) and, in a less extend, better J_{sc} and V_{oc} compared to P3HT-Un. However, LiTFSI and tBP additives are detrimental for the J - V curve hysteresis. Table 3.2 shows that doping with Co-salt and tBP (P3HT-Co cells) results in an intermediate behavior (slight increase in efficiency and hysteresis compared to P3HT-Un). All the P3HT cells showed a lower V_{oc} than the Spiro-Doped ones in agreement with Jiménez-López et al.'s findings [18].

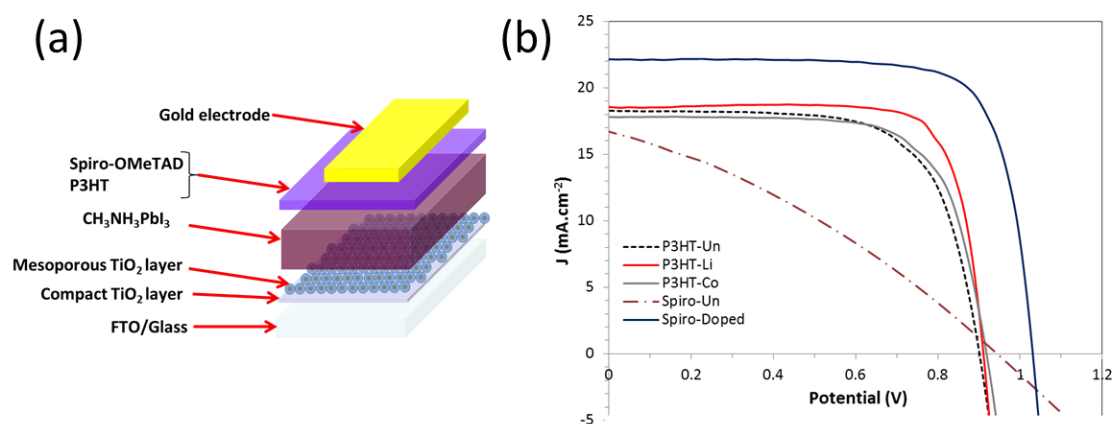


Figure 3.3. (a) Exploded schematic view of the perovskite solar cells. (b) Typical J - V curve of solar cells prepared with various doped and undoped P3HT and Spiro-OMeTAD HTM layers (reverse scan).

Table 3.2. Effect of HTM and additives on the J-V curve parameters (AM1.5 filtered 100 mW.cm⁻²). Avg: averaged values; Rev: reverse scan direction; For: forward scan direction.

| Samples | Scan direction | V _{oc} (V) | J _{sc} (mA.cm ⁻²) | FF (%) | PCE(%) |
|--------------------|----------------|---------------------|--|-------------|-------------|
| P3HT-Li | Max (Rev) | 0.91 | 18.36 | 79.7 | 13.4 |
| | Max (For) | 0.90 | 16.96 | 44.6 | 6.8 |
| | Avg (Rev) | 0.90 | 16.70 | 78.8 | 11.8 |
| | Avg (For) | 0.89 | 14.60 | 43.9 | 5.7 |
| P3HT-Co C-doped | Max (Rev) | 0.92 | 17.68 | 70.7 | 11.5 |
| | Max (For) | 0.90 | 17.43 | 55.9 | 8.8 |
| | Avg (Rev) | 0.91 | 17.27 | 69.9 | 11.0 |
| | Avg (For) | 0.90 | 16.94 | 52.2 | 8.0 |
| P3HT-Un | Max (Rev) | 0.90 | 18.11 | 68.6 | 11.2 |
| | Max (For) | 0.89 | 19.81 | 54.4 | 9.6 |
| | Avg (Rev) | 0.87 | 17.87 | 65.9 | 10.2 |
| | Avg (For) | 0.85 | 19.36 | 48.3 | 8.0 |
| Spiro- doped | Max (Rev) | 1.01 | 22.15 | 78.2 | 17.7 |
| | Max (For) | 1.00 | 22.72 | 63.0 | 14.5 |
| | Avg (Rev) | 1.01 | 20.83 | 76.5 | 16.1 |
| | Avg (For) | 0.99 | 21.02 | 59.3 | 12.4 |
| Spiro-Un | Max (Rev) | 0.94 | 16.67 | 32.6 | 5.13 |
| | Max (For) | 0.94 | 16.44 | 26.6 | 4.10 |
| | Avg (Rev) | 0.91 | 12.61 | 27.2 | 3.46 |
| | Avg (For) | 0.91 | 12.07 | 21.7 | 2.59 |

Number of cells averaged is 10 cells.

III.5. Impedance spectroscopy study of perovskite solar cells

To gain deeper insights into the effects of the HTM material type and doping on the cell functioning, the various devices have been fully investigated by IS. The solar cell electrical response to a small ac perturbation applied to the devices polarized at various potentials has been investigated. The cells were analyzed under light illumination and over a wide frequency range. Figure 3.4 shows Nyquist plots of spectra recorded in the 600 kHz-20 mHz range for doped and undoped Spiro-OMeTAD cells (a-d) and P3HT-based cells (e-h). Four different features can be distinguished noted **1** to **4**. **1**, **2** and **4** are arcs of circle observed at very high, high and low frequencies, respectively. **1** is only observed in the case of the undoped Spiro-OMeTAD cells. **3** is an inductive loop found at intermediate frequency for P3HT-Un and P3HT-Co. The general equivalent electrical circuit used to fit the spectra is shown in Figure 3.5a. The simplified EECs that have been used to analyze each kind of cell are presented in Figure 3.5b-d. Because the arcs of circle are not semi-circles, they have been fitted using R//CPE circuits (see Chapter I, Section I.6.5).

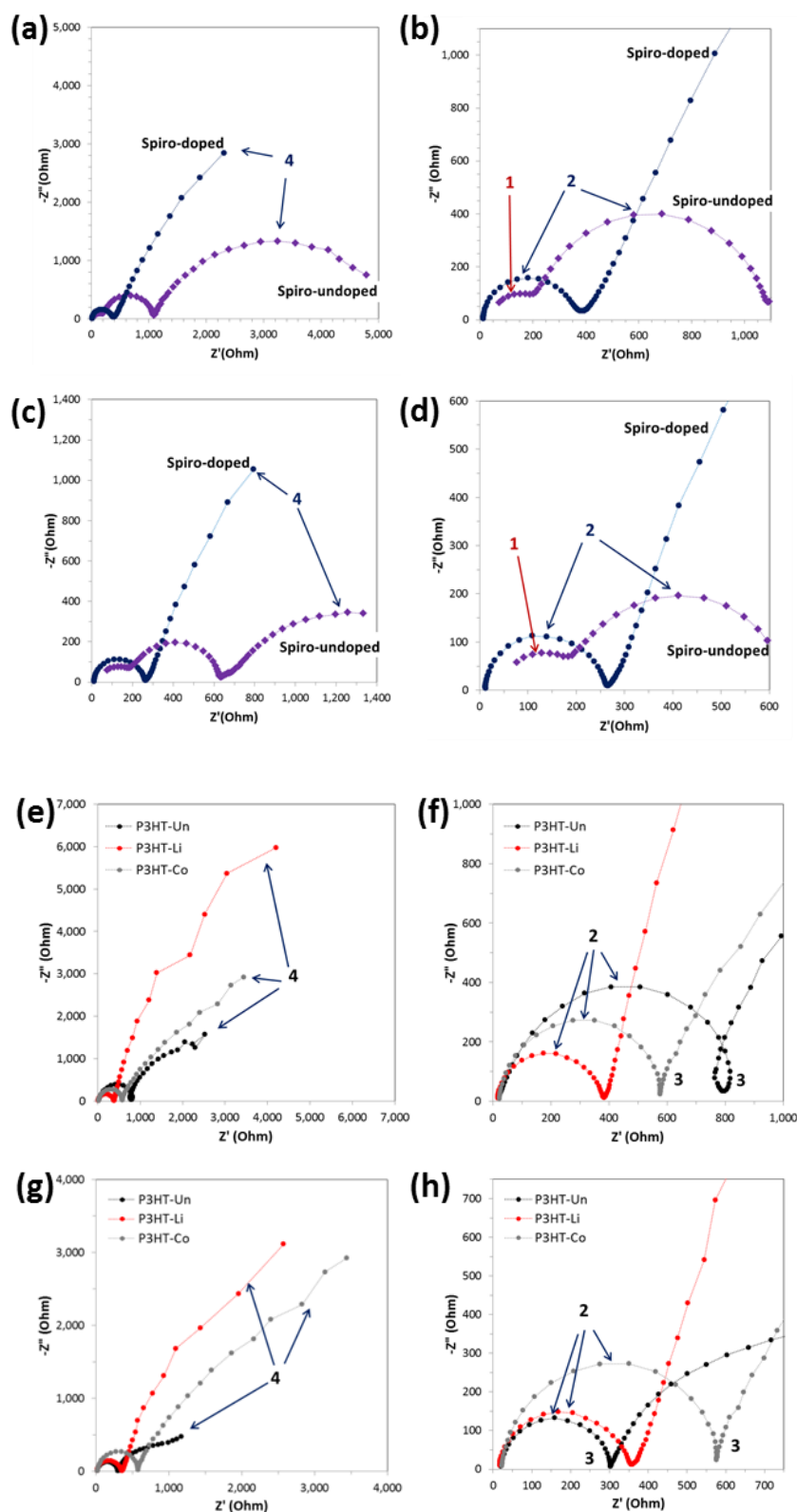


Figure 3.4. Impedance spectra Nyquist plots of (a,b) Spiro-based PCS at 0.0V, (c,d) Spiro-based PCS at 0.6V, (e,f) P3HT-based PSC at 0.0V and (g,h) P3HT-based PSC at 0.6V. (b), (d), (f) and (h) are zoom views at high frequencies of (a), (c), (e) and (g) respectively.

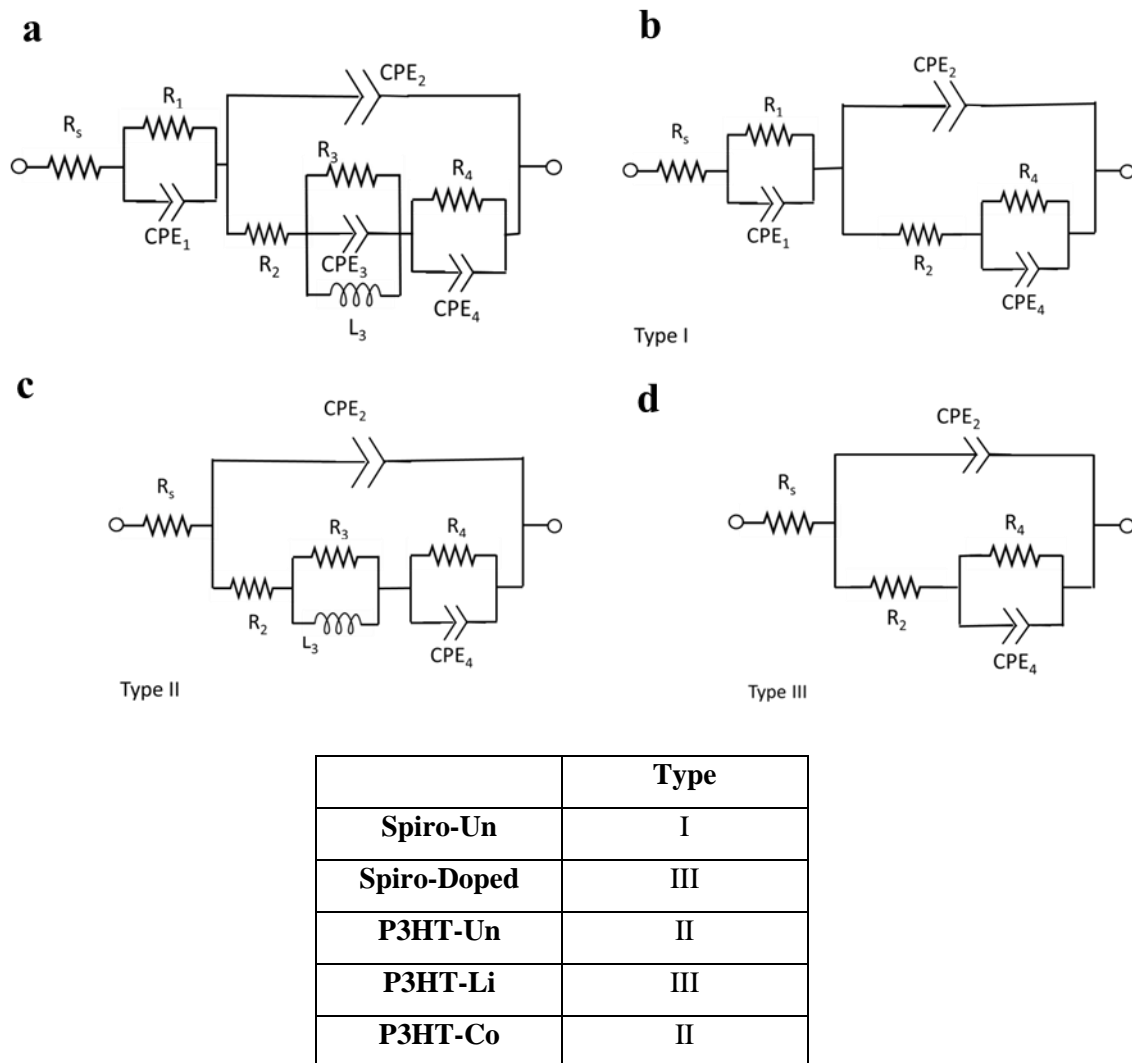


Figure 3.5. (a) General equivalent electrical circuits used to fit the impedance spectra. (b-d) Electrical equivalent circuits used to fit the Spiro-OMeTAD and P3HT impedance spectra. The type of EEC employed for fitting the various kind of cells is summarized in the table.

The very high frequency relaxation loop noted **1** is only observed for Spiro-Un cells. It is assigned to the relaxation of the Spiro-OMeTAD layer. The values of C_1 and R_1 are reported in Figure 3.6a as a function of V_{appl} . These parameters are unchanged with V_{appl} up to 0.7 V and their average values are $1.4 \cdot 10^{-8} \text{ F.cm}^{-2}$ and $48 \text{ } \Omega.\text{cm}^2$, respectively. From R_1 and d , the Spiro-OMeTAD layer thickness (measured at about 150 nm (Figure 3.6c)), the conductivity, σ_{HTM} , is calculated according to $\sigma_{\text{Spiro}} = d/R_1$. It is determined at $3 \times 10^{-7} \text{ S.cm}^{-1}$. From C_1 and d , ϵ_r the relative permittivity is given by $C_1 = \epsilon_r \epsilon_0 / d$, with ϵ_0 the vacuum permittivity ($8.85 \times 10^{-12} \text{ F.m}^{-1}$), and calculated at 2.4 for undoped Spiro-OMeTAD. The low conductivity of undoped Spiro-OMeTAD explain that the HTM relaxation arc of circle can be observed in the IS spectra. The conductivity of the other HTMs is higher by several orders of magnitude (for

instance the conductivity of doped Spiro-OMeTAD can reach values higher than $10^{-3} \text{ S.cm}^{-1}$ [20]) and the relaxation frequency of this layer is shifted toward higher frequencies. The very high frequency loop **1** is not observed then and the resistive contribution of the HTM layer is then small and included in R_s , R_s is the high frequency resistance measured by extrapolating the **1** or **2** high frequency loops to the x-axis. It is mainly due to the electrical contribution of the gold and FTO contact electrodes and to external wires. Undoped P3HT has a rather high conductivity due to charge transport through the long chain of the conjugated polymer. R_s results shown in Figure 3.6b suggest a better conductivity through LiTFSI doping whereas the series resistance is not significantly affected by the Co complex-doping.

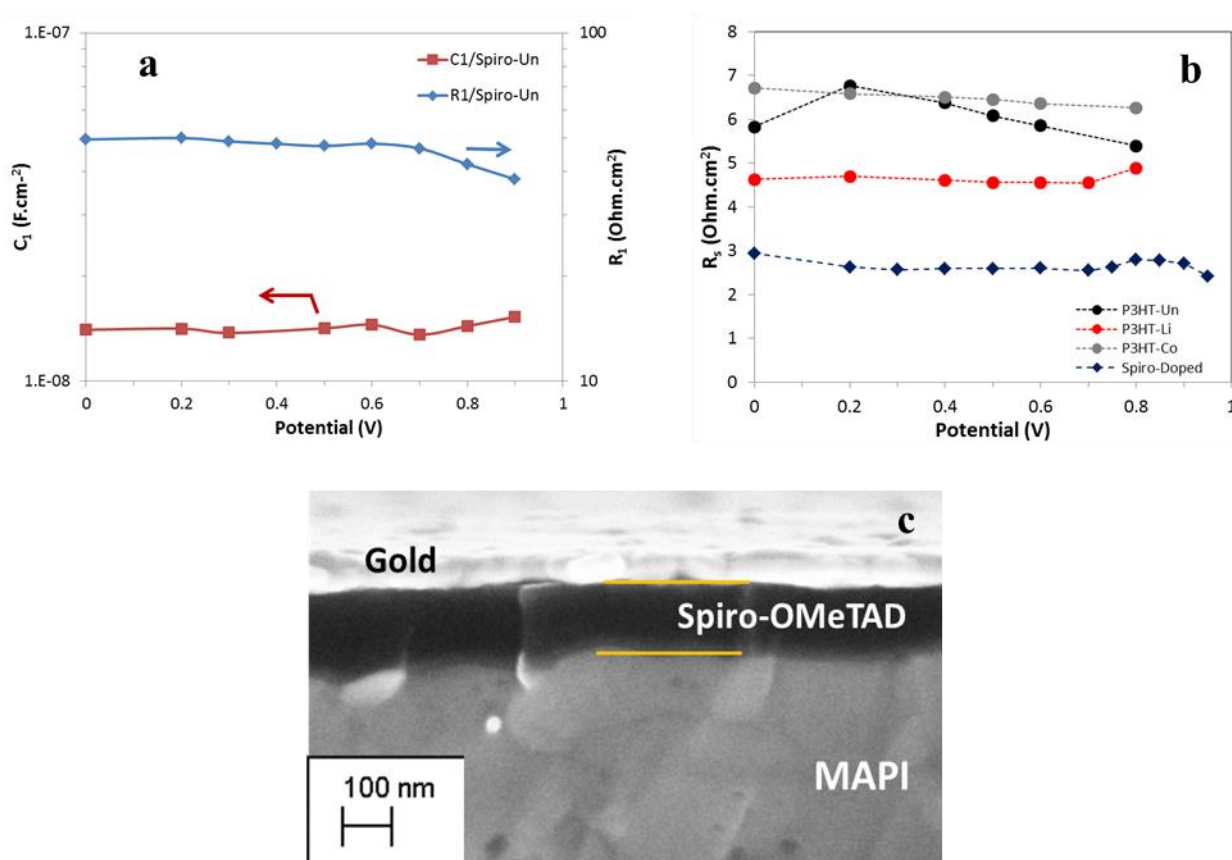


Figure 3.6. (a) High frequency C_1 and R_1 at various V_{appl} measured on Spiro-Un cells. (b) R_s measured at various V_{appl} for PSCs prepared with Doped Spiro-OMeTAD and P3HT HTMs. (c) SEM Cross-sectional view of the Spiro-OMeTAD layer.

The high frequency relaxation **2** has been analyzed by extracting C_2 and R_2 . C_2 is insensitive to light and is related to the dielectric relaxation of MAPI [21]. In Figure 3.7a, C_2 are similar for the various cells since the same MAPI(1)-SO is used in the investigated PSCs. The fact that the C_2 curves of P3HT-Un and P3HT-Co cells depart from the general trend can be assigned to the difficulty of accurately determining C_2 when the inductive loop is present. R_2 is influenced by doping. It decreases with the applied voltage for the undoped HTM (or

P3HT-Co) while it decreases slowly or remains unchanged over a large V_{appl} range for Spiro-Doped and P3HT-Li cells, respectively (Figure 3.7b). Juarez-Perez et al. have assigned R_2 to a charge transfer resistance. Pockett et al [22], found a scaling of this parameter with light intensity at the V_{oc} and have assigned it to a recombination resistance. However, R_2 is a complex element that gathers several contributions. Nevertheless, in the present case, the fact that R_2 is not affected by the HTM layer resistance and that it changes with the HTM (all other parameters being kept identical), shows that this parameter is strongly affected by the interface between the HTM and the perovskite.

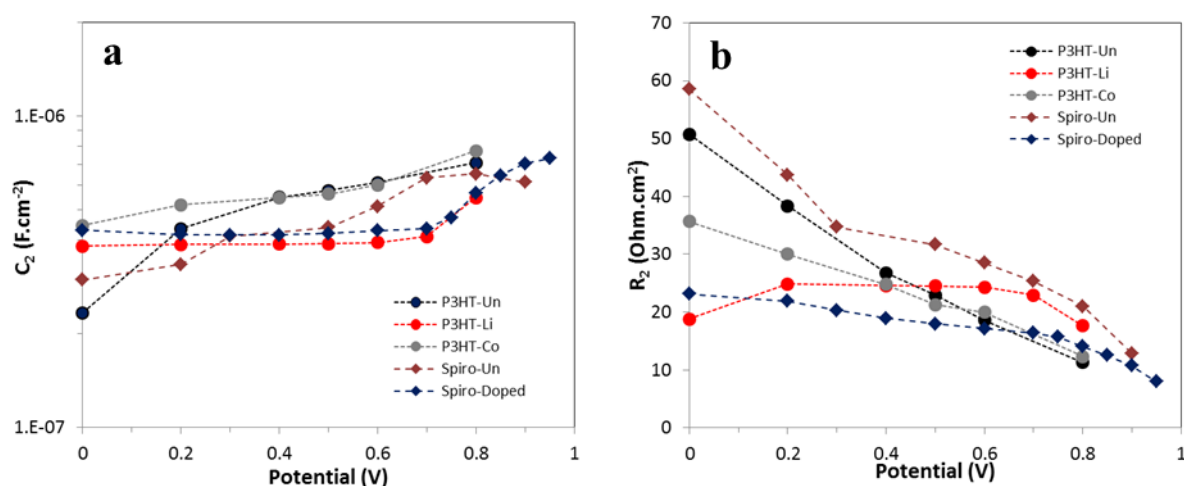


Figure 3.7. Effects of HTM and doping on the variation of C_2 (a) and R_2 (b) parameters with V_{appl} .

The low frequency loop was analyzed as a R_4 //CPE₄ circuit. R_4 is related to the recombination phenomena at the interfaces and the higher R_4 , the lower the recombination. Figure 3.8a shows the effects of HTM and doping on this resistance. Higher R_4 values are measured for LiTFSI and *t*BP doped Spiro-OMeTAD and P3HT cells compared to the undoped ones. For undoped Spiro-OMeTAD, R_4 is low and, importantly, continuously decreases with V_{appl} . This is in agreement with the low FF of these cells (Table 3.2). On the other hand, to get a high FF, a flat curve up to high voltage before a steep decrease near the V_{oc} is required and is the signature of a high FF as found for Spiro-Doped cells. R_4 is also in good agreement with the lower V_{oc} of the undoped Spiro cells. LiTFSI in the Spiro cells improves the conductivity by promoting the molecular HTM oxidation by O₂ while *t*BP favors the uniformity of the HTM layer and avoids accumulation of Li salt at the interface [2], [23], [24]. Interface improvement is important to lower the recombination and enlarge the cell V_{oc} and FF. The P3HT-Li curve crosses the Spiro-Doped curve and decreases more rapidly at high V_{appl} in agreement with the lower V_{oc} of the former cells. P3HT-Un and P3HT-Co have an intermediate behavior. Lower R_4 is in agreement with the lower V_{oc} of these cells and the lower slope of P3HT-Li compared

to the other P3HT cells is in agreement with the higher FF of P3HT-Li devices. It is interesting to compare the R_2 and R_4 curves. While their shapes are close, the values of these components have an opposite behavior: the higher R_2 , the lower R_4 . These observations show that R_2 cannot be considered as a pure recombination resistance.

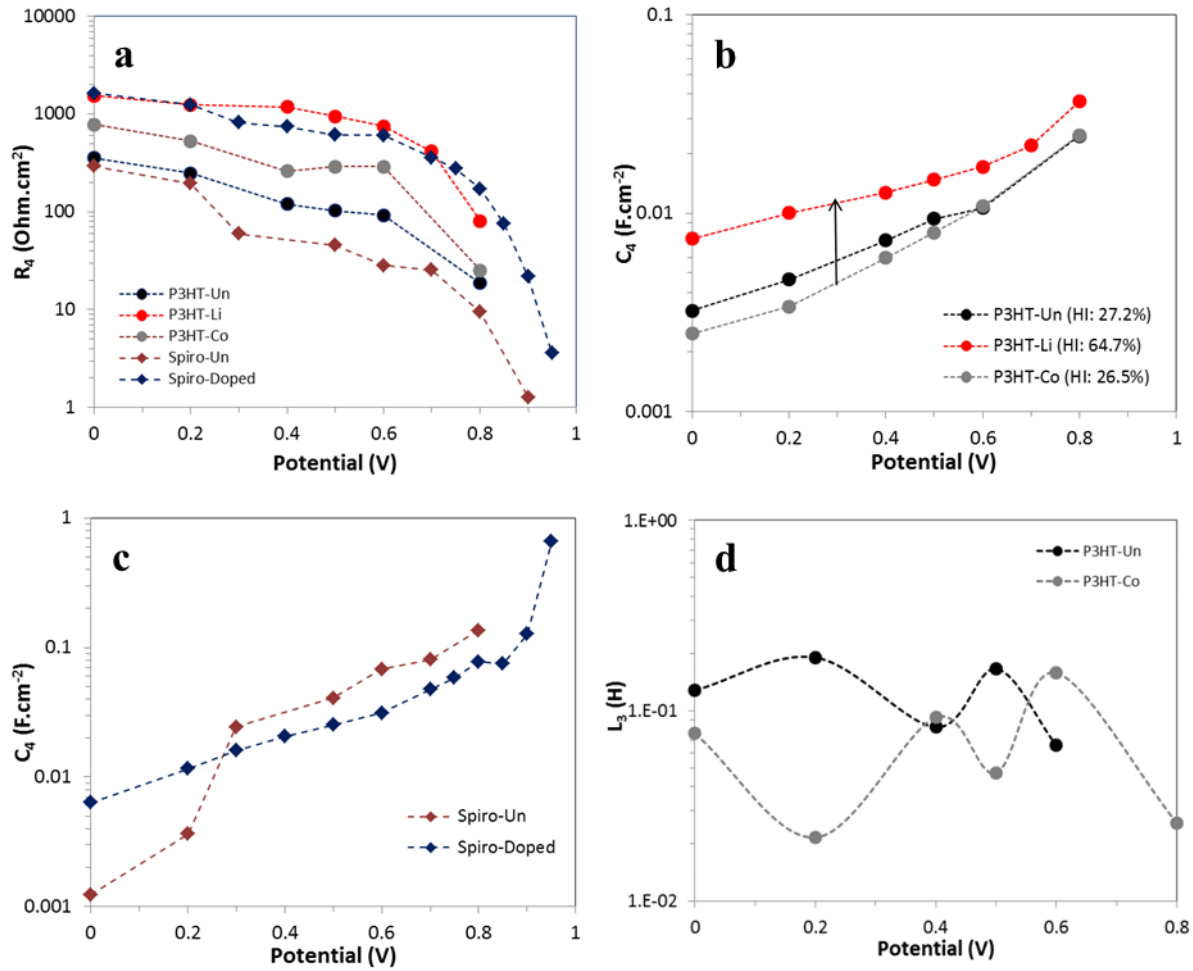


Figure 3.8. Effects of HTM and doping on the variation with V_{appl} of R_4 (a) and C_4 (b) parameters. Effect of V_{appl} on C_4 of (c) pristine and doped Spiro-OMeTAD solar cells and on L_3 of (d) P3HT-Un and P3HT-Co solar cells.

C_4 , the low frequency capacitance is strongly affected by the light shining and we have shown in Ref.[21] that it is related to the hysteresis of the J - V curves. It is generally admitted that this effect is related to the accumulation of mobile ions (and ion vacancies) at the interface near the contacts due to ion migration under an electric field. It alters the band structure at the interface and modulate the barrier heights for electron/hole collection. This effect is detected at low frequencies due to the slow moving of ions and charge compensation. It is strongly affected by the interfaces between the selective contacts and the perovskite layer [25]. C_4 is plotted as a function of V_{appl} for various HTMs in Figure 3.8b and Figure 3.8c. They show a

contribution of the HTM/perovskite interface on this parameter since, for instance, the curves are different for the pristine P3HT cell and the doped ones (Figure 3.8b). This capacitance induces the hysteresis found between the forward and the reverse J - V scans (Table 3.2) and is correlated to the hysteresis index, HI, which has been defined in Chapter II section II.4.

In Figure 3.8b, the P3HT-Un curve (HI=26.5%) is below the P3HT-Co curve (HI=27.2%). C_4 is 4-5 times higher for P3HT-Li, this cell having a very large HI of 64.7%. The present observations confirm our previous analysis of C_4 for PSCs prepared with various perovskite absorbers [21]. The C_4 curves of the Spiro-OMeTAD cells are shown in Figure 3.8c. The Spiro-Un curve has a S-shape and increases more rapidly than the Spiro-Doped curve. It can be deduced that additives improve the interface between the molecular HTM and MAPI. The improvement could be notably a consequence of the tBP. It has been shown for instance that this compound when present at the perovskite surface, increases the hydrophobicity of the perovskite layer by its attachment to the perovskite Pb^{2+} by its nitrogen atom, the tertiary butyl group surrounding at the outside [25]. We can suppose then that this additive is attached at the perovskite surface, reduces the interfacial defects and favors the hole transfer from the perovskite to the HTM layer [2], [24], [25].

The intermediate frequency range is characterized by the presence of an inductive loop for the P3HT-Un and P3HT-Co cells. This loop is found for the polymer HTM cells with a lower performance and is not observed for the doped and undoped Spiro-OMeTAD cells. L_2 Inductance versus applied voltage curves attained from the fitting of the impedance spectra of the different samples under illumination are plotted in Figure 3.8d. Higher L_2 values are found for P3HT-Un compared to P3HT-Co. Anaya et al. [26] found an increase of L with the increase of TiO_2 /perovskite interface and deduced a correlation between the inductance and the electron injection processes. Our results show that the inductance can be induced by phenomena occurring at the perovskite/HTM interface. However, in PSC, the charge injection toward both selective contacts is very fast (in the nanoseconds scale) whereas the relaxation frequency (and then characteristic time) of the inductive loop is only 100-200 Hz. If an inductive element in impedance spectra can be related to complex multistep processes [27], [28], further studies are still needed to clarify the origin of this feature in IS spectra of PSCs [28], [29].

III.6. Photoluminescence (PL) spectrum and decay studies

The PL spectra of Spiro-OMeTAD and P3HT, with and without additives, deposited on top of MAPI(1)-SO perovskite are shown in Figure 3.9a and 3.9b. They are characterized by a single emission peak centered at 768 nm for Spiro-OMeTAD and at 766 nm for P3HT with negligible differences with and without additives. The time-correlated single-photon counting (TCSPC) curves have been measured to characterize the effect of additives in the case of MAPI(1)-SO/Spiro-OMeTAD and MAPI(1)-SO/P3HT samples. The measured curves are shown in Figure 3.9c and 3.9d. The curves have been fitted by a bi-exponential decay function as described in chapter II section II.6, where RC_{fast} and RC_{slow} are the relative contribution of the components and τ_{fast} and τ_{slow} the fast and the slow lifetime components, respectively. Both lifetimes and their relative contribution for various samples are provided in Table 3.3.

The TCSPC decay curves for perovskite/HTM samples are displayed in Figure 3.9c and 3.9d for Spiro-OMeTAD and P3HT, respectively. The fit results are gathered in Table 3.3. We can see that the lifetimes are very short when MAPI(1)-SO is in contact with the undoped and doped HTMs. Both, τ_{fast} and τ_{slow} are faster in the case of P3HT undoped compared to the doped ones. The Li-doped P3HT sample has the slowest hole transfer. This finding is in agreement with the average J_{sc} provided in Table 3.2.

The Spiro-OMeTAD samples have a more complex behavior. For undoped, the RC_{fast} contribution dominates. The second lifetime is rather slow (91.5 ns) but its contribution is low. For the doped sample, τ_{fast} is the same as for the undoped sample while τ_{slow} is much faster but with a larger RC. For both HTMs, the lifetimes are shorter than those measured for the MAPI(1)-SO on TiO_2 (see Table 2.2, Chapter II). Therefore, we can conclude that the charge transfer is limited at the ETM contact and not the the HTM one. Consequently, the TCSPC data cannot be directly correlated with the cell performances.

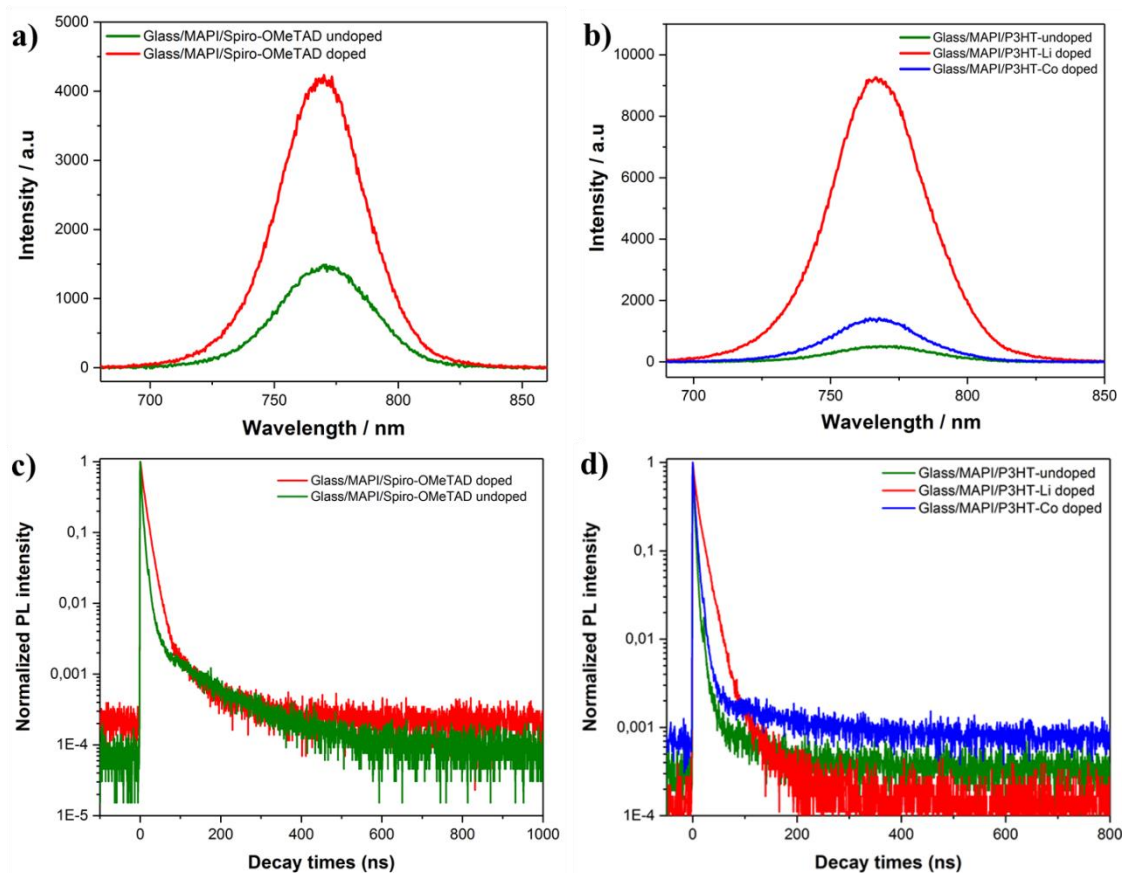


Figure 3.9. PL spectra of (a) Glass/MAPI(1)-SO/Spiro-OMeTAD and (b) Glass/MAPI(1)-SO/P3HT samples. Time-correlated single-photon counting curves of (c) Glass/MAPI(1)-SO/Spiro-OMeTAD and (d) Glass/MAPI(1)-SO/P3HT samples with and without additives.

Table 3.3. Parameters of TCSPC of Spiro-OMeTAD and P3HT deposited on MAPI(1)-SO/glass. Curves fitted by a bi-exponential decay equation.

| Perovskite | Samples | τ_{fast} (ns) | $\text{RC}_{\text{fast}}(\%)^a$ | τ_{slow} (ns) | $\text{RC}_{\text{slow}}(\%)^a$ |
|------------------------|----------------------|---------------------------|---------------------------------|---------------------------|---------------------------------|
| P3HT/MAPI(1)-SO/glass | P3HT-undoped | 2.88 | 84.6 | 13.41 | 15.4 |
| | P3HT-Co doped | 3.96 | 70.6 | 11.44 | 29.3 |
| | P3HT-Li doped | 12.95 | 91.8 | 35.23 | 8.2 |
| Spiro/MAPI(1)-SO/glass | Spiro-OMeTAD undoped | 8.28 | 85.1 | 91.54 | 14.9 |
| | Spiro-OMeTAD doped | 7.87 | 37.7 | 16.56 | 62.3 |

III.7. Conclusion

In summary, we have fully characterized and compared the electrical J - V and impedance responses of PSCs prepared with the benchmark molecular Spiro-OMeTAD HTM and the P3HT conducting polymer selected as a low-cost efficient HTM. Impedance spectroscopy has been measured over a large frequency and applied potential ranges. For both compounds, cells have been prepared without and with doping. Doping the molecular HTM by LiTFSI and tBP increases dramatically the power conversion efficiency from 5.1% to 17.7%. We have shown that the performances of undoped Spiro-OMeTAD cells are limited by the HTM layer resistance and we have determined the conductivity of the layer at $3 \times 10^{-7} \text{ S.cm}^{-1}$ and its relative permittivity at 2.4. The analysis of the R_4 parameter has also evidenced that the performance of Spiro-Un cells is limited by strong recombinations occurring at the HTM/perovskite interface. On the other hand, the performances of the P3HT-based cell were increased in less extent by doping. Using LiTFSI and tBP additives lead to the best performance. We have shown that they eliminate the intermediate frequency inductive loop which is beneficial since inductor acts as a short at low frequency which reduces the impedance for charge transfer. The additives limit the charge recombination at the interface, reduce the interfacial defects and favors the hole transfer from the perovskite to the HTM layer. Importantly, we have shown that P3HT conductivity is not the main limiting parameter for the cell performances because the thiophene chain presents correct conducting properties even without doping. We have also found that increasing the interchain order does not produce a significant enhancement of the PSC efficiency. In many papers, the authors analyze the beneficial effect of doping conjugated polymer HTM especially P3HT, as due to an increase of the conductivity [11], [13]. The present work, shows that the limitation due to the conductivity of the undoped polymer is negligible (a slight increase of the series resistance), but that additives affect the perovskite/HTM interface, reduce the recombination, render the recombination resistance poorly dependent on the applied voltage and then improves the fill factor parameter. The TR-PL measurements have shown a fast charge transfer between the perovskite and HTMs. Finally, the present work has confirmed the correlation between the capacitance determined at low impedance frequency and the hysteresis feature typical of PSCs. In the next chapter, we investigate new molecular carbazole compounds for an application as HTMs in PSCs.

References

- [1] A. Abate *et al.*, « Lithium salts as “redox active” p-type dopants for organic semiconductors and their impact in solid-state dye-sensitized solar cells », *Phys. Chem. Chem. Phys.*, vol. 15, n° 7, p. 2572-2579, 2013.
- [2] E. J. Juarez-Perez, M. R. Leyden, S. Wang, L. K. Ono, Z. Hawash, et Y. Qi, « Role of the Dopants on the Morphological and Transport Properties of Spiro-MeOTAD Hole Transport Layer », *Chem. Mater.*, vol. 28, n° 16, p. 5702-5709, août 2016.
- [3] U. B. Cappel, T. Daeneke, et U. Bach, « Oxygen-Induced Doping of Spiro-MeOTAD in Solid-State Dye-Sensitized Solar Cells and Its Impact on Device Performance », *Nano Lett.*, vol. 12, n° 9, p. 4925-4931, sept. 2012.
- [4] S. Wang, W. Yuan, et Y. S. Meng, « Spectrum-Dependent Spiro-OMeTAD Oxidation Mechanism in Perovskite Solar Cells », *ACS Appl. Mater. Interfaces*, vol. 7, n° 44, p. 24791-24798, nov. 2015.
- [5] Z. Li *et al.*, « Acid Additives Enhancing the Conductivity of Spiro-OMeTAD Toward High-Efficiency and Hysteresis-Less Planar Perovskite Solar Cells », *Adv. Energy Mater.*, vol. 7, n° 4, p. 1601451, oct. 2016.
- [6] Y. Fang, X. Wang, Q. Wang, J. Huang, et T. Wu, « Impact of annealing on spiro-OMeTAD and corresponding solid-state dye sensitized solar cells », *Phys. Status Solidi A*, vol. 211, n° 12, p. 2809-2816, août 2014.
- [7] J. Burschka, F. Kessler, M. K. Nazeeruddin, et M. Grätzel, « Co(III) Complexes as p-Dopants in Solid-State Dye-Sensitized Solar Cells », *Chem. Mater.*, vol. 25, n° 15, p. 2986-2990, août 2013.
- [8] W. S. Yang *et al.*, « Iodide management in formamidinium-lead-halide-based perovskite layers for efficient solar cells », *Science*, vol. 356, n° 6345, p. 1376, juin 2017.
- [9] M. Zhang, M. Lyu, H. Yu, J.-H. Yun, Q. Wang, et L. Wang, « Stable and Low-Cost Mesoscopic CH₃NH₃PbI₂Br Perovskite Solar Cells by using a Thin Poly(3-hexylthiophene) Layer as a Hole Transporter », *Chem. – Eur. J.*, vol. 21, n° 1, p. 434-439, oct. 2014.
- [10] H. Zheng *et al.*, « The influence of perovskite layer and hole transport material on the temperature stability about perovskite solar cells », *Sol. Energy*, vol. 159, p. 914-919, janv. 2018.
- [11] J. W. Jung *et al.*, « Flexible and highly efficient perovskite solar cells with a large active area incorporating cobalt-doped poly(3-hexylthiophene) for enhanced open-circuit voltage », *J Mater Chem A*, vol. 5, n° 24, p. 12158-12167, 2017.
- [12] N. Y. Nia, F. Matteocci, L. Cina, et A. Di Carlo, « High-Efficiency Perovskite Solar Cell Based on Poly(3-Hexylthiophene): Influence of Molecular Weight and Mesoscopic Scaffold Layer », *ChemSusChem*, vol. 10, n° 19, p. 3854-3860, mai 2017.
- [13] Y. Zhang, M. Elawad, Z. Yu, X. Jiang, J. Lai, et L. Sun, « Enhanced performance of perovskite solar cells with P3HT hole-transporting materials via molecular p-type doping », *RSC Adv*, vol. 6, n° 110, p. 108888-108895, 2016.
- [14] J. H. Heo et S. H. Im, « CH₃NH₃PbI₃/poly-3-hexylthiophen perovskite mesoscopic solar cells: Performance enhancement by Li-assisted hole conduction », *Phys. Status Solidi RRL – Rapid Res. Lett.*, vol. 8, n° 10, p. 816-821, août 2014.
- [15] Y. Guo, C. Liu, K. Inoue, K. Harano, H. Tanaka, et E. Nakamura, « Enhancement in the efficiency of an organic–inorganic hybrid solar cell with a doped P3HT hole-transporting layer on a void-free perovskite active layer », *J. Mater. Chem. A*, vol. 2, n° 34, p. 13827-13830, 2014.

- [16] M. Park, J.-S. Park, I. K. Han, et J. Y. Oh, « High-performance flexible and air-stable perovskite solar cells with a large active area based on poly(3-hexylthiophene) nanofibrils », *J Mater Chem A*, vol. 4, n° 29, p. 11307-11316, 2016.
- [17] Y. Rong, L. Liu, A. Mei, X. Li, et H. Han, « Beyond Efficiency: the Challenge of Stability in Mesoscopic Perovskite Solar Cells », *Adv. Energy Mater.*, vol. 5, n° 20, p. 1501066, sept. 2015.
- [18] J. Jiménez-López, W. Cambarau, L. Cabau, et E. Palomares, « Charge Injection, Carriers Recombination and HOMO Energy Level Relationship in Perovskite Solar Cells », *Sci. Rep.*, vol. 7, n° 1, p. 6101, juill. 2017.
- [19] P. J. Brown *et al.*, « Effect of interchain interactions on the absorption and emission of poly(3-hexylthiophene) », *Phys Rev B*, vol. 67, n° 6, p. 064203, févr. 2003.
- [20] W. H. Nguyen, C. D. Bailie, E. L. Unger, et M. D. McGehee, « Enhancing the Hole-Conductivity of Spiro-OMeTAD without Oxygen or Lithium Salts by Using Spiro(TFSI)₂ in Perovskite and Dye-Sensitized Solar Cells », *J. Am. Chem. Soc.*, vol. 136, n° 31, p. 10996-11001, août 2014.
- [21] P. Wang, M. Ulfa, et T. Pauporté, « Effects of Perovskite Monovalent Cation Composition on the High and Low Frequency Impedance Response of Efficient Solar Cells », *J. Phys. Chem. C*, vol. 122, n° 4, p. 1973-1981, févr. 2018.
- [22] A. Pockett, G. E. Eperon, N. Sakai, H. J. Snaith, L. M. Peter, et P. J. Cameron, « Microseconds, milliseconds and seconds: deconvoluting the dynamic behaviour of planar perovskite solar cells », *Phys. Chem. Chem. Phys.*, vol. 19, n° 8, p. 5959-5970, 2017.
- [23] S. Wang *et al.*, « Role of 4-tert-Butylpyridine as a Hole Transport Layer Morphological Controller in Perovskite Solar Cells », *Nano Lett.*, vol. 16, n° 9, p. 5594-5600, sept. 2016.
- [24] Y.-H. Wu *et al.*, « Incorporating 4-tert-Butylpyridine in an Antisolvent: A Facile Approach to Obtain Highly Efficient and Stable Perovskite Solar Cells », *ACS Appl. Mater. Interfaces*, vol. 10, n° 4, p. 3602-3608, janv. 2018.
- [25] B. Chen, M. Yang, S. Priya, et K. Zhu, « Origin of J-V Hysteresis in Perovskite Solar Cells », *J. Phys. Chem. Lett.*, vol. 7, n° 5, p. 905-917, mars 2016.
- [26] M. Anaya *et al.*, « Electron injection and scaffold effects in perovskite solar cells », *J. Mater. Chem. C*, vol. 5, n° 3, p. 634-644, 2017.
- [27] A. Guerrero *et al.*, « Properties of Contact and Bulk Impedances in Hybrid Lead Halide Perovskite Solar Cells Including Inductive Loop Elements », *J. Phys. Chem. C*, vol. 120, n° 15, p. 8023-8032, avr. 2016.
- [28] I. Zarazua, J. Bisquert, et G. Garcia-Belmonte, « Light-Induced Space-Charge Accumulation Zone as Photovoltaic Mechanism in Perovskite Solar Cells », *J. Phys. Chem. Lett.*, vol. 7, n° 3, p. 525-528, févr. 2016.
- [29] P. Wang, Z. Shao, M. Ulfa, et T. Pauporté, « Insights into the Hole Blocking Layer Effect on the Perovskite Solar Cell Performance and Impedance Response », *J. Phys. Chem. C*, vol. 121, n° 17, p. 9131-9141, mai 2017.

Chapter IV

New Hole Transporting Materials for Perovskite Solar Cells

In this chapter, we detail several new HTMs provided by the Laboratoire de Physicochimie des Polymères et des Interfaces (LPPI-EA 2528) at the Université de Cergy-Pontoise. The new HTMs are coded as **B74**, **B186**, **DM1**, **DM2**, **DM1P**, **iDM1**, **iDM2**, and **iDM4**. The properties of these HTMs will be discussed and then their application to perovskite solar cells (PSCs) will be tested. $\text{CH}_3\text{NH}_3\text{PbI}_3$ (MAPI) was used as the perovskite absorber material for testing these new HTMs. MAPI(1)-SO was employed to realize solar cells based on the **B74** and **B186** HTMs, while the DMs and i-DM HTMs were tested with MAPI(2), MAPI(1)-SO, and FAMA perovskites. In the end of the chapter, iDMs HTMs are also tested with MAPI(1)-SOF. An optimized device was composed of a thin compact TiO_2 layer, a mesoporous TiO_2 layer filled and capped with the hybrid perovskite, a HTM layer and finally a thermally evaporated Au back contact.

IV.1. Introduction

The hole transporting material (HTM) is an important element in perovskite solar cells. We can note that several groups have successfully fabricated HTM-free PSCs [1]–[5]. Unfortunately, the efficiency in this case remains rather low compared to cells with an HTM layer. The most popular HTM used in PSCs is Spiro-OMeTAD, which was primarily employed in DSSCs.[6] Because of its low conductivity, it must be employed with additives. LiTFSI salt and t-BP are the most common additives of Spiro-OMeTAD, while Cobalt (III) complexes are also used in combination of the two former additives as we have explained in Chapter III, Section III.1.

Due to a long synthesis process and relatively high cost of the classic Spiro-OMeTAD, designing new HTMs that can be easily prepared at low cost by a short process has become an important challenge for the researchers. Importantly, for the molecular design, the HOMO energy level must be compatible with the perovskite top valence band energy in order to provide the suitable driving force for charge transfer. Furthermore, its LUMO level must be significantly higher than that of the perovskite absorber bottom of the conduction band to block the photogenerated electrons (large bandgap). Moreover, the HTM must have a

sufficient hole mobility as well as excellent thermal, morphological and photochemical stabilities. A good hydrophobic property is also sought for to protect the perovskite materials from moisture.

Some small organic molecules have the ability to act as a HTM in PSCs. Wang et al. [7] have discussed the incorporation of small molecules in terms of photovoltaic properties, device performances and stability. The interest of using small molecules as HTMs in PSCs lies on its distinct molecular structure with a precise molecular weight and in their easy synthesizing process with high purity and yield that can therefore be reproduced for industrial production.[8] The first observation in using organic small molecules as HTM for solar cells was by Tang and Albrecht in 1975.[9] They used a small molecule namely chlorophyll-a which sandwiched in two metals, unfortunately the efficiency was very low (in order of 10^{-3} %).[9] There are several families of organic small molecules available for HTM application such as pyrene, thiophene, porphyrins, carbazoles, etc.[10]

Carbazole derivatives HTMs have been employed in PSCs for several years and their interest has been pointed out due to their low-cost starting material, good chemical and environmental stability, their reactive sites can react with a variety of functional groups to fine-tune their electronic and optical properties.[11] A low-cost carbazole based small molecule material, 1,3,6,8-tetra(N,N-p-dimethoxyphenylamino)-9-ethylcarbazole has led to a performance (17.8%) comparable to the benchmark Spiro-OMeTAD HTM (18.6%).[12] Daskeviciene et al. [13] have also synthesized and incorporated a simple carbazole-based conjugated enamine V950 into PSCs that showed an efficiency close to 18%. They have stated that this HTM is promising to be commercially viable in PSC modules. A methoxydiphenylamine-substituted carbazole HTM was also synthesized and applied to PSC by Gratia et al. [14] and Malinauskas et al. [15], which resulted in a 16.91% and 19.96% PCEs, respectively, which were comparable to that of the Spiro-OMeTAD based PCS of the study. Lu et al. [16] reported three low-cost and star-shaped carbazoles based HTM (coded as SGT-405(3,6), SGT-410(3,6) and SGT-411(3,6)) through a simple synthesis and molecular engineering. The cells based on SGT-405(3,6) exhibited a remarkable efficiency of 18.87% which was better than the PSC-based on Spiro-OMeTAD HTM(17.71%).

IV.2. Experimental

Preparation of the perovskite layers

As mentioned earlier, the cells based on new HTMs were prepared with different perovskite absorbers, namely MAPI(1)-SO, MAPI(2), MAPI(1)-SOF, and FAMA. The preparation technique of the first two perovskites have detailed in Chapter II section II.2.3, and MAPI(1)-SOF preparation can be found in Chapter V section V.2.2. FAMA is a perovskite with the $\text{FA}_{0.87}\text{MA}_{0.13}\text{Pb}(\text{I}_{0.87}\text{Br}_{0.17})_3$ composition (FA^+ being the formamidium cation). For its preparation, the precursor solution contained 1M FAI, 0.2M MABr, 1.1M PbI_2 and 0.22 M PbBr_2 dissolved in a 4:1 volume ratio mixture of DMF and DMSO. 45 μL of the perovskite precursor solution was spin-coated on FTO/ TiO_2 (BL) /meso- TiO_2 at 1000 rpm for 20 s (acceleration 200 rpm/s) and then at 6000 rpm for 30 s (acceleration 3000 rpm/s). During the second step, after 20s, 100 μL Chlorobenzene was dripped on the sample. The perovskite layer was finally annealed at 100 °C for 1 h.

Preparation of hole transport layer

The HTM solution incorporating the new HTMs were prepared by following the Spiro-OMeTAD procedure. Firstly, 72 mg of the HTM was dissolved in 1 mL chlorobenzene. Then, 17.5 μL of LiTFSI stock solution (520 mg in 1 mL ACN), 28 μL of tBP (4-*tert*-butylpyridine, 96% Sigma-Aldrich) and 6 μL of tris(2-(1H-pyrazol-1-yl)-4-*tert*-butylpyridine)cobalt(III)tri[bis(trifluoromethane)sulfonamide] (FK209 from Dyesol) was added to the solution. 35 μL of this HTM solution was spin-coated at 4000 rpm for 20 s.

IV.3. Dendritic carbazole B186 and B74 based HTM

As discussed in Chapter III, organic HTMs can be essentially divided into two subclasses depending on their molecular weight: molecular and polymeric HTMs. The polymeric materials have important advantages as HTM in terms of processability, thermal and mechanical stability, and higher intrinsic mobility.[17]–[20] On the other hand, molecular HTMs are beneficial in terms of synthetic reproducibility, well-defined molecular weight and structure. In a collaborative work, the LPPI has designed and synthesized a new type of molecule which is supposed to encompass the best of both molecular and polymeric HTMs. This HTM is a new core carbazole based material named B186. The photovoltaic properties of B186 have been compared with its simple molecular B74 counterpart and with the benchmark

Spiro-OMeTAD. One must note that these molecules have been theoretically investigated by the "Complex System Modeling" team of our laboratory and that these results are provided in our Ref [21]. They will not be discussed here.

IV.3.1. Molecular structure and physico-chemical properties of B186 and B74

The molecular structures of the two investigated molecules are presented in Figure 4.1. In both HTMs, the *N*-alkylated core group (three carbazoles in the case of B186) are end-capped by di(4-methoxyphenyl)aminyl function in 3,6 positions. These groups are electron rich and modulate the optoelectrochemical and electrical properties of the compounds. The methoxy groups have a good interaction with perovskite surface notably with Pb(II) ion.[22] Additionally, their presence in *para* positions of phenyl rings of the diphenylamino moiety favors the charge transport properties and reduces the charge recombination. It should results in a better device performances.[23]–[25] Additionally, the methoxy groups render the molecules more soluble in organic solvents. It has been also reported that the alkyl chain at *N*-position of carbazole favors the infiltration into a perovskite networks.[26]

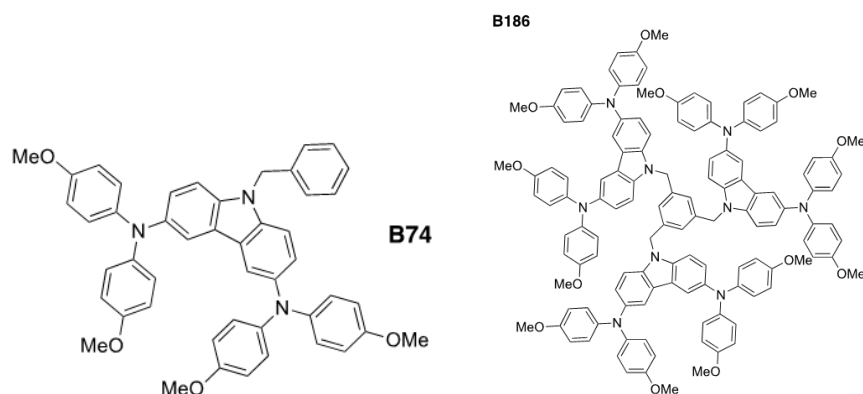


Figure 4.1. Molecular structure of B74 (left) and B186 (right) HTMs.

Table 4.1. Comparative thermal, optical and optoelectrochemical properties of carbazole HTMs (B74, B186) and Spiro-OMeTAD.

| Compound | MW (g/mol) | T _d (°C) | T _g (°C) | E _g ^{opt} (eV) | E _{HOMO} ^c (eV) | E _{LUMO} ^f (eV) |
|---------------------|---------------|------------------------|------------------------|---------------------------------------|--|--|
| B74 | 711.85 | 336 ^c | 66 ^c | 2.77 ^c | - 4.67 | - 1.90 |
| B186 | 1979.36 | 384 | 146 | 2.50 | - 4.53 | - 2.03 |
| Spiro-OMeTAD | 1225.43 | <i>n. a.</i> | 125 ^g | 3.00 ^c | - 4.45 | - 1.45 |

Table 4.1 shows that B186 presents a good thermal stability with a decomposition temperatures (T_d) value higher than 380°C, a value high enough for an application in electronic devices. The differential scanning calorimetry (DSC) study of B186 revealed no melting point until 280°C and exhibited a glass transition temperature (T_g) at 146°C which is higher than that of B74 (66°C) and Spiro-OMeTAD (125°C). This can be attributed to the higher molecular weight of B186 compared to B74 and Spiro-OMeTAD (Table 4.1). The HOMO level of these new HTMs was found slightly deeper than that of Spiro-OMeTAD. However, the driving force must remain sufficient for hole transfer in PSC application (Figure 4.2b).

IV.3.2. Solar cells performances

The prepared carbazole compounds were studied as HTMs in PSC structures, using the one-step deposited MAPI(1)-SO perovskite as the absorber material. A typical PSC device structure as well as the energy alignment of the different device components are shown in Figure 4.2. An optimized device was composed of a thin compact TiO₂ layer, a mesoporous TiO₂ layer filled and capped with the MAPI(1)-SO perovskite, a HTM layer and finally a thermally evaporated Au back contact (the preparation of each layer is detailed in Chapter II). According to our theoretical [21] and experimental energy band diagrams, B74 and B186 are suitable for the application and should work as the benchmark Spiro-OMeTAD compound. The best current-density-voltage ($J-V$) curves for the various HTMs are displayed in Figure 4.3a. Best and average $J-V$ curve parameters under one sun, as well as their standard deviations, are gathered in Table 4.2.

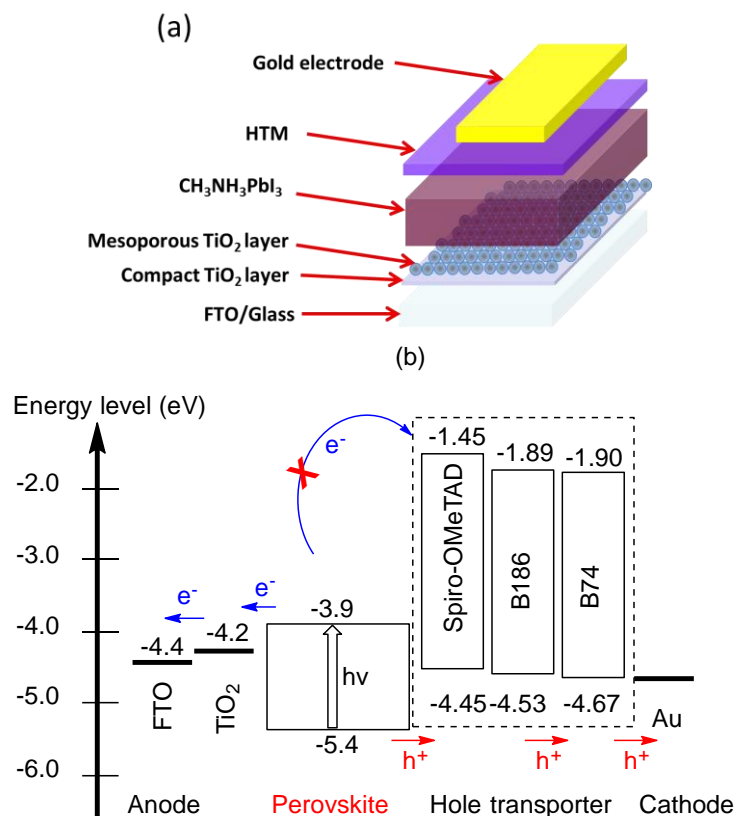


Figure 4.2. (a) Device structure and (b) energy level alignment of the various device components.

Table 4.2 shows that, compared to B74, employing the dendritic core B186 molecule enhances the solar cell performances. Indeed, the best PSC efficiency increased from 11.5% to 14.6% by increasing the HTM molecular size. This improvement was mainly due to a larger J_{sc} that can be linked to a better charge extraction and transport. Moreover, the use of B186 was found more flexible and gave more reproducible results. For B186, we also tested the layers with and without dopant and we found that the presence of dopant is very important to increase the conductivity of the HTM. The average parameter values reported in Table 4.2 show that it dramatically rises all the cells parameters. The best B186 PCE was below the efficiency of the benchmark Spiro-OMeTAD cells that could reach ~17.7%. B74 and B186 cells presented also a large hysteresis. Since such hysteresis differences between carbazole and Spiro-OMeTAD cells were observed for cells from the same batch (exactly the same perovskite deposition conditions), we can relate them to surface defects that would be present at the interface between the carbazole HTMs and the perovskite. Undoped B186 HTM resulted in very low cell performances (PCE at 0.2%) due to very low J_{sc} and FF (Table 4.2). The J - V curve was typical of a highly resistive device and problems of charge injection and transport occurred (Figure 4.3a).

B186 was also tested in combination with another perovskite absorber, $\text{FA}_{0.87}\text{MA}_{0.13}\text{Pb}(\text{I}_{0.87}\text{Br}_{0.17})_3$ (the preparation of this perovskite is described in the Section IV.2). The B186 cell efficiency reached a maximum of 14.45% then and, interestingly, the hysteresis was reduced in a large extent. EQE curves have been recorded and are reported in Figure 4.3b for MAPI(1)-SO cells. They all presented an edge below 800 nm due to the absorbance properties of MAPI. The Spiro-OMeTAD cell showed high EQE values and then excellent charge collection and transport. EQE was lower for the B186 cell and was the worst for the B74 one, showing a lack of hole collection and transport effectiveness in this case. As expected, integrated J_{sc} values obtained from the EQE curves (14.56, 19.40, 20.33 $\text{mA}\cdot\text{cm}^{-2}$ for B74, B186 and Spiro-OMeTAD, respectively) are close to the J_{sc} value obtained from the $J-V$ measurement of these cells (14.75, 19.79 and 20.98 $\text{mA}\cdot\text{cm}^{-2}$, respectively).

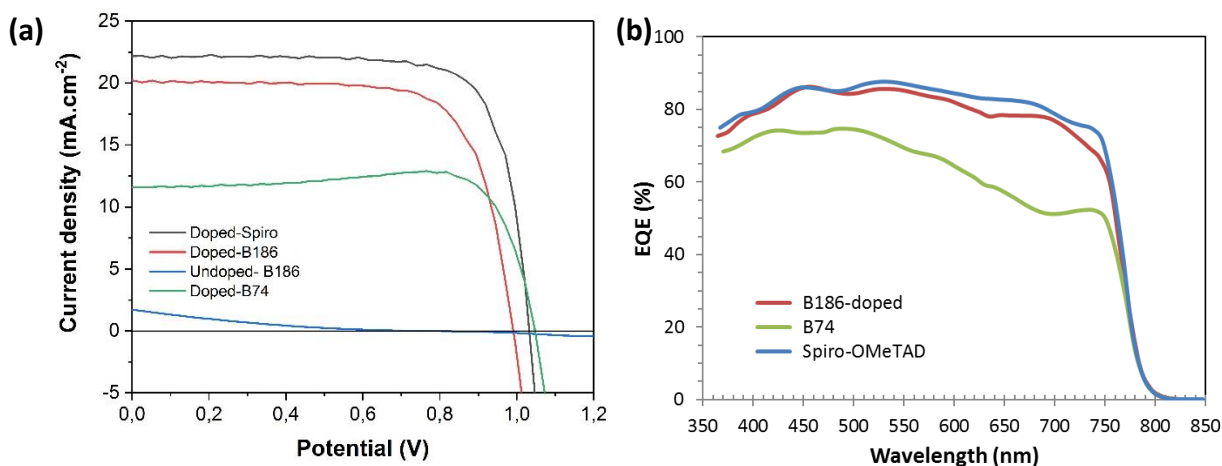


Figure 4.3. (a) $J-V$ curves of the best photovoltaic PSCs measured under AM1.5G filtered 100 $\text{mW}\cdot\text{cm}^{-2}$ illuminations. (b) EQE curves of PSCs prepared with various HTM. (a) and (b) are MAPI(1)-SO cells.

Table 4.2. Best and average $J-V$ curve parameters of the solar cells prepared with **Spiro-OMeTAD**, **B74** and **B186** HTM. The standard deviations are given in brackets.

| Sample | Scan direction | | V_{oc} / V | $J_{\text{sc}} / \text{mA}\cdot\text{cm}^{-2}$ | FF/ % | PCE/ % |
|-------------------|------------------|-------------------|----------------------------|--|-------------|--------------|
| MAPI(1)-SO | | | | | | |
| B186-doped | Rev ^a | Best ^c | 0.98 | 20.11 | 73.27 | 14.59 |
| | | Avg ^d | 0.96 (0.03) | 19.6 (1.33) | 70.4 (3.00) | 13.44 (0.91) |
| | For ^b | Avg | 0.92 (0.02) | 19.8 (1.39) | 33.8 (8.01) | 6.33 (1.79) |

| | | | | | | |
|--|-----|------|--------------|--------------|--------------|---------------|
| B186-undoped | Rev | Best | 0.74 | 1.52 | 16.89 | 0.19 |
| | | Avg | 0.73 (0.016) | 1.31 (0.27) | 16.31 (0.37) | 0.16 (0.03) |
| | For | Best | 0.74 | 1.44 | 16.64 | 0.17 |
| | | Avg | 0.73 (0.013) | 1.41 (0.27) | 16.26 (0.32) | 0.164 (0.029) |
| B74 | Rev | Best | 0.94 | 14.75 | 93.71 | 11.51 |
| | | Avg | 0.92 (0.021) | 13.03 (1.50) | 80.1 (13.1) | 10.7 (1.04) |
| | For | Avg | 0.91(0.070) | 15.05 (1.15) | 38.0 (2.87) | 5.2 (0.37) |
| Spiro-OMeTAD | Rev | Best | 1.01 | 22.15 | 78.22 | 17.68 |
| | | Avg | 1.01 (0.02) | 20.83 (0.63) | 76.5 (2.70) | 16.10 (1.00) |
| | For | Avg | 0.987 (0.02) | 21.02 (1.06) | 59.3 (2.91) | 12.42 (1.22) |
| FA_{0.87}MA_{0.13}Pb(I_{0.87}Br_{0.17})₃ | | | | | | |
| B186-doped | Rev | Best | 1.03 | 20.21 | 69.23 | 14.45 |
| | | Avg | 0.98 (0.04) | 19.45 (0.90) | 67.78 (4.89) | 12.99 (1.31) |
| | For | Best | 0.98 | 20.19 | 62.69 | 12.42 |
| | | Avg | 0.94 (0.04) | 19.49 (0.97) | 52.59 (9.21) | 9.72 (2.19) |

^a Reverse scan direction; ^b Forward scan direction; ^c Best solar cell values; ^d Average values; In the brackets are standard deviation. Number of cells averaged is 10 cells.

IV.3.3. Stability tracking of B186- and B74-caped MAPI(1)-SO layers and solar cells

The effect of the new HTMs on the stabilization of perovskite was studied over several weeks. A first experiment consisted in following the XRD patterns of glass/FTO/TiO₂/MAPI(1)-SO/HTM (B74, B186 and Spiro-OMeTAD) assemblies, which were stored in a desiccator placed under the ambient conditions of the laboratory. The results are shown in Figure 4.4. It is observed that PbI₂ (diffraction peak at 12.7°), the degradation product of MAPI(1)-SO, is formed more slowly in the case of the B74 overlayer compared to Spiro-OMeTAD. The B186 layer presents an intermediate behaviour. Using this HTM clearly slows down the degradation

of MAPI(1)-SO compared to Spiro-OMeTAD. This behaviour is in good agreement with our contact angle measurements results reported in Ref.[21]. Indeed, perovskite is known to be sensitive to moisture due to the hygroscopic nature of methylammonium. Then, the more hydrophobic is the HTM, the slower is the perovskite degradation since the HTM better protects it to moisture.

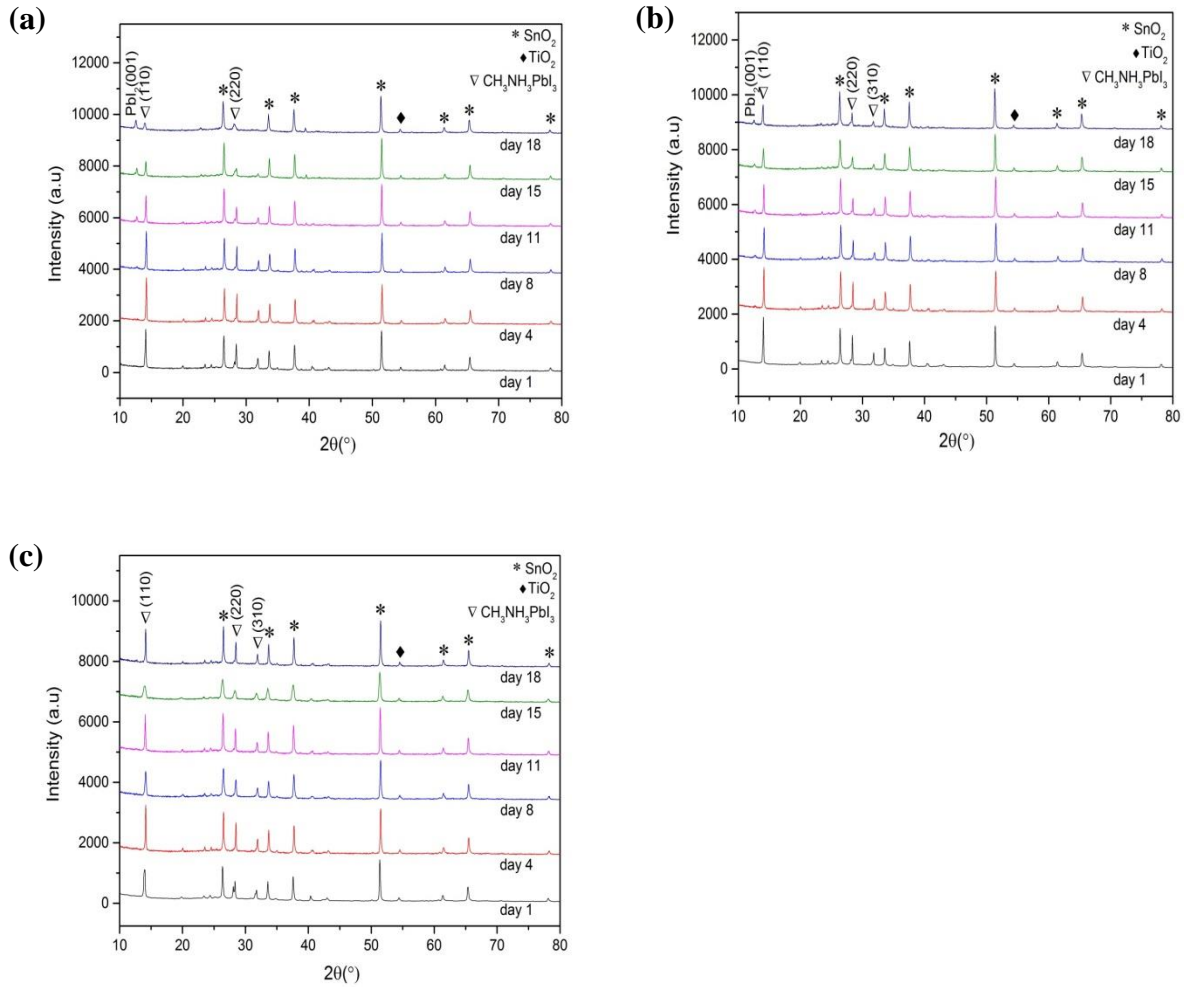


Figure 4.4. Evolution of XRD patterns of Glass/FTO/TiO₂/MAPI(1)-SO/HTM assemblies stored under ambient conditions (a) Spiro-OMeTAD, (b) B186, and (c) B74.

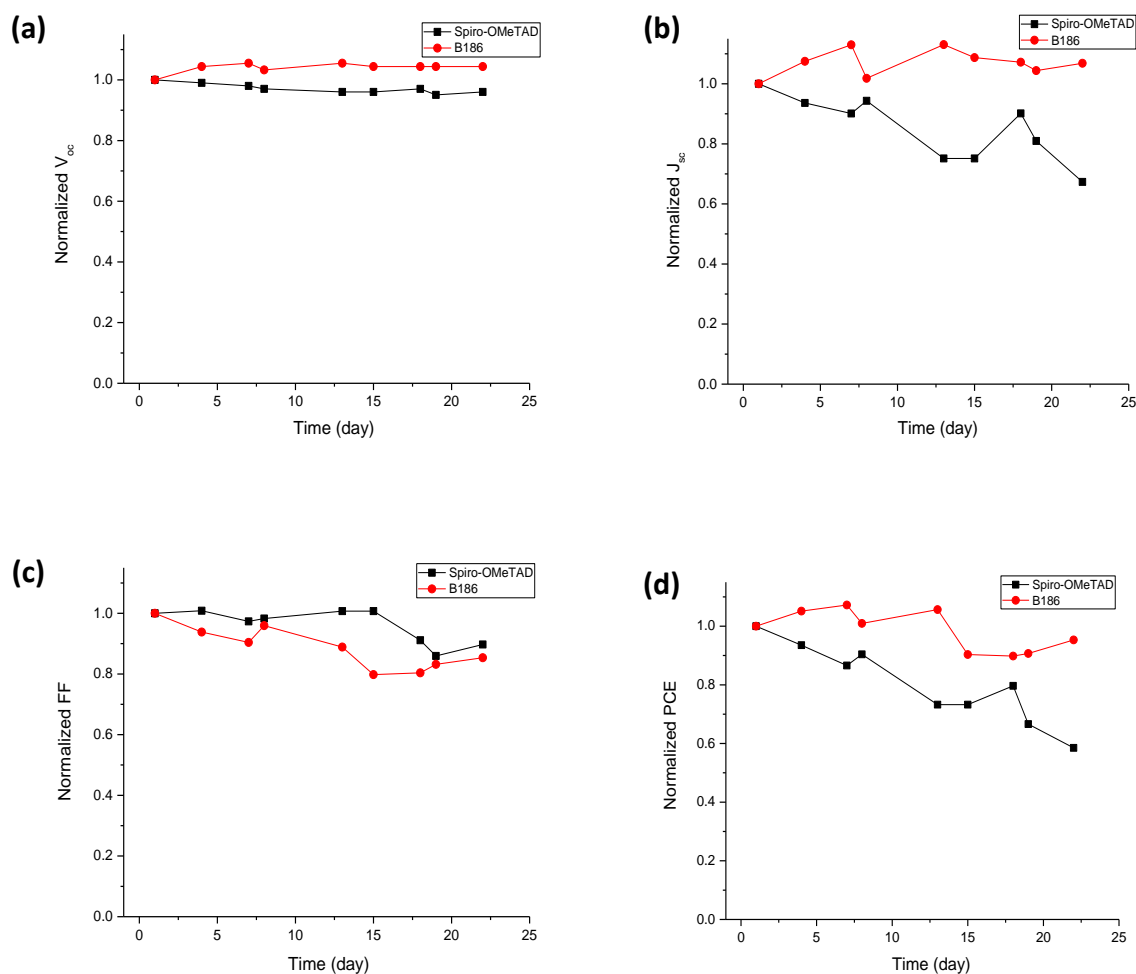


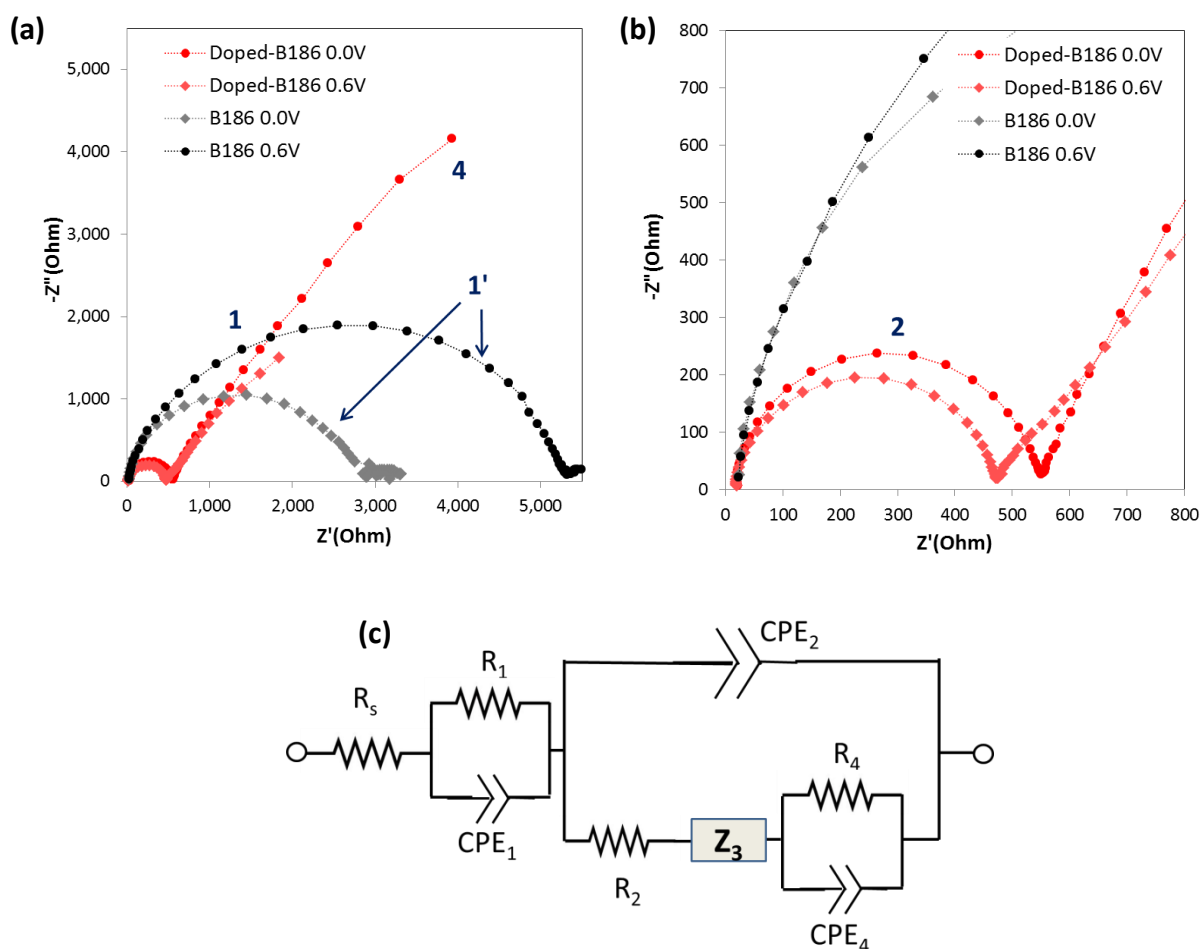
Figure 4.5. Evolution of device performances and J - V curve parameters with storage time for **B186** and Spiro-OMeTAD unencapsulated device cells. (a) Normalized V_{oc} ; (b) Normalized J_{sc} ; (c) Normalized FF and (d) Normalized PCE.

For B186, the carbazole derivative that exhibits the best solar cell performances, the evolutions of the PCE and of the J - V curve parameters were followed for more than three weeks. In-between the measurements, the cells were stored in a glove-box. In Figure 4.5, they are compared to those of a Spiro-OMeTAD cell. B186 exhibits a high stability for the V_{oc} and the J_{sc} parameters. After more than three weeks, the PCE was decreased by only 5% for B186 while it was more than 40% with Spiro-OMeTAD. The former compound then act as a good barrier and protects satisfactorily the MAPI(1)-SO absorber layer.

IV.3.4. Impedance study of B186 and the doping effect

An impedance study (IS) was carried out in order to deeply understand the behavior of the new HTM, B186 and its doping effect. Figure 4.6 shows the Nyquist plot impedance spectra of doped (doped-B186) and undoped B186 (B186) measured at 0.0 V and at 0.6 V applied

potentials. Two main arcs of circle characterized the spectra. The low-frequency relaxation is labeled 4 and the high-frequency is labeled 2 in Figure 4.6. At the foot of the second loop, there is another impedance feature (arc of circle) which gives the Z_3 element in the general equivalent electrical circuit (EEC) of Figure 4.6c. Dramatic changes are observed between the doped and undoped B186 cells. In the absence of dopant, the spectra are dominated by a large loop with a large impedance, which size increases with the applied potential. This loop is flattened and was deconvoluted into two relaxations, labeled 1 and 1' in Figure 4.6a. The spectra have been analyzed using the simplification of general EEC shown in Figure 4.6d and Figure 4.6e for doped and undoped B186 cells, respectively.



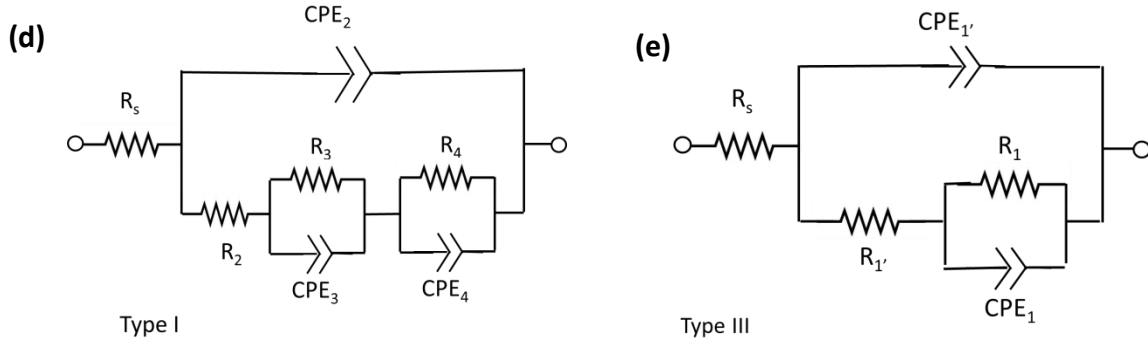


Figure 4.6. Nyquist plots of impedance spectra of (a,b) of doped and undoped B186 based PSCs. (b) is a zoom view at high frequencies of (a). (c) General equivalent electrical circuit used to fit the impedance spectra. (d,e) Simplified EECs used to fit the impedance spectra of (d) doped B186 and (e) undoped B186 based PSCs.

C_1 values of undoped cells have been determined and plotted in Figure 4.7a. C_1 does not change with the applied voltage and shows no charge accumulation effect. This parameter is measured at about $1.5 \times 10^{-8} \text{ F.cm}^{-2}$ for pristine B186 cells and is assigned to the bulk dielectric capacitance of the B186 layer. This capacitance is expressed by $C/S = \epsilon_r \epsilon_0 / d = C_1$, with ϵ_0 the vacuum permittivity ($8.85 \times 10^{-12} \text{ F.m}^{-1}$), ϵ_r the HTM relative permittivity, S the cell surface area and d the HTM layer thickness. The thickness of B186 layer is about 200 nm from a cross-section measurement shown in Figure 4.7d. Therefore ϵ_{B186} is found at 3.3. The relaxation 1 is then assigned to the B186 layer and R_1 is the resistance of the B186 layer. Its values at various applied voltage are displayed in Figure 4.7b. R_1 do not change significantly with the applied voltage. From R_1 , the conductivity of the B186 layer, σ_{B186} , is calculated according to $\sigma_{\text{B186}} = d/R_1$ and then found at $1.0 \times 10^{-7} \text{ S.cm}^{-1}$.

With LiTFSI and Co(III) complex, the conductivity of the HTM increases by several orders of magnitude due to the strong oxidation.[27][28] Consequently, the relaxation time of the B186 layer decreases dramatically and this feature is not observed in the impedance spectra measured below 600 kHz of doped-B186 cells in Figure 4.6.

From relaxation 2, C_2 was calculated and is reported in Figure 4.7c. C_2 did not vary significantly up to 0.6V. For MAPI(1)-SO cells, the average values ranged between 1.1 and $1.4 \times 10^{-8} \text{ F.cm}^{-2}$. This capacitance is analyzed as the dielectric capacitance of the $\text{CH}_3\text{NH}_3\text{PbI}_3$ layer. The slight increase in C_2 above 0.6V is assigned to some charge accumulations. The assignment was confirmed by preparing cells with another hybrid perovskite absorber, mixing both monovalent cations and anions and with composition $\text{FA}_{0.87}\text{MA}_{0.13}\text{Pb}(\text{I}_{0.87}\text{Br}_{0.17})_3$

(FAMA).[29] Actually, C_2 changed with the HP. C_2 of FAMA reported in Figure 4.7c did not vary with the HTM but was significantly lower than that of MAPI(1)-SO.

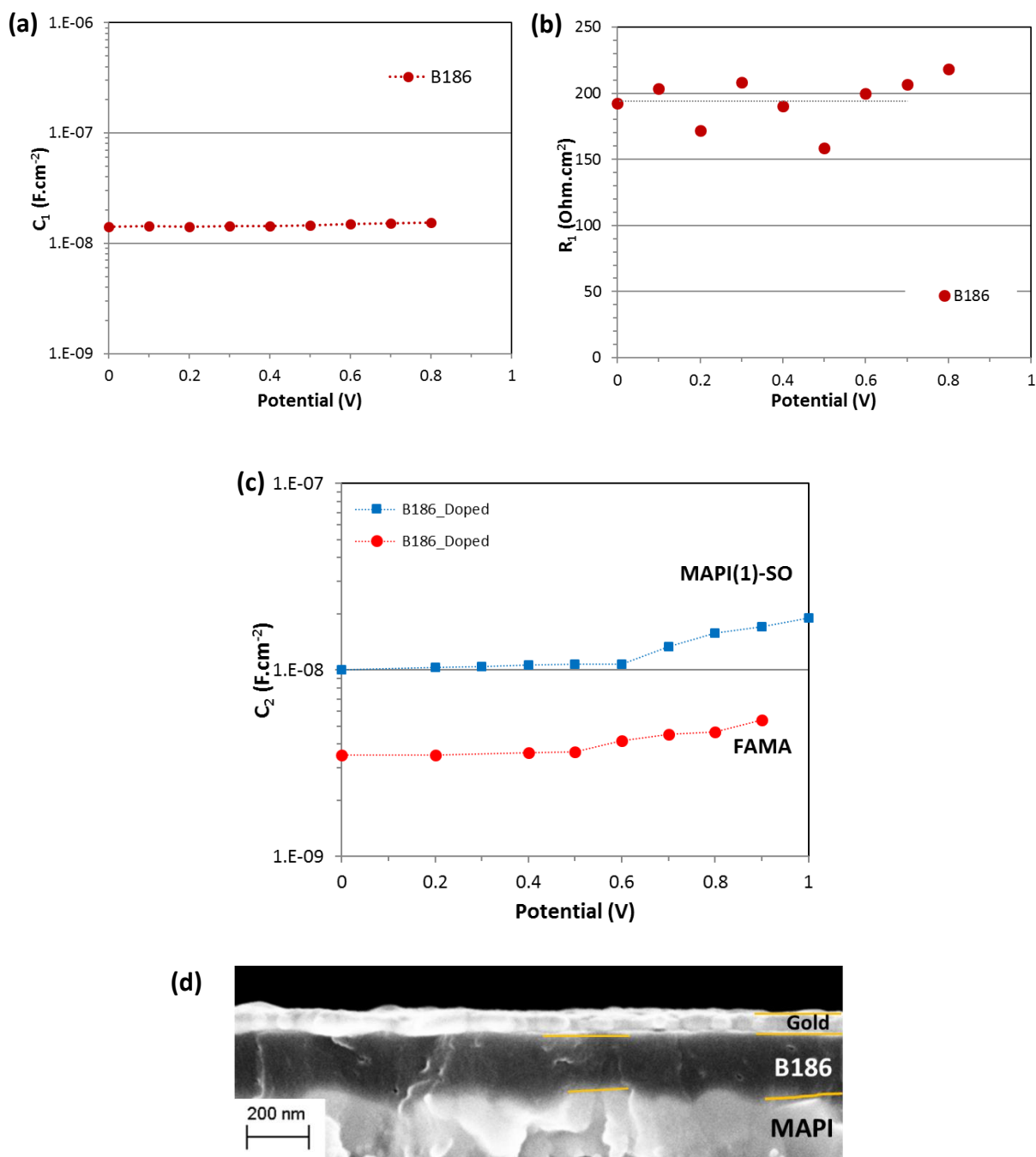


Figure 4.7. C_1 (a) and R_1 (b) versus the applied voltage of undoped MAPI(1)-SO/B186 PSCs. (c) C_2 versus the applied voltage of PSCs prepared with B186 in combination of two different hybrid perovskite absorbers, MAPI(1)-SO and FAMA. (d) SEM cross-sectional view of a B186 based PSC.

The low frequency loop was analyzed as a $R_4//CPE_4$ circuit. C_4 is assigned to charge accumulation at the interfaces. The formation of a defective interface is likely at the origin of the small amplitude and not well-defined low frequency loop in the case of the undoped B186

solar cells (Figure 4.6a). In Figure 4.8a the variation of C_4 with V_{appl} for the two different HPs are compared. The curves are rather similar and in the reproducibility uncertainty.

R_4 is related to the recombination phenomena at the interfaces and the higher R_4 , the lower the recombination. To get a high FF, a flat curve up to high voltage before a steep decrease near the V_{oc} is expected and is the signature of a high FF. Figure 4.8b shows the R_4 versus V_{appl} curves for B186 and Spiro-OMeTAD. A rapid decrease of R_4 curve of the B186 cells is in agreement with a rather low FF and V_{oc} compared to the doped Spiro-OMeTAD cells (Table 4.2).

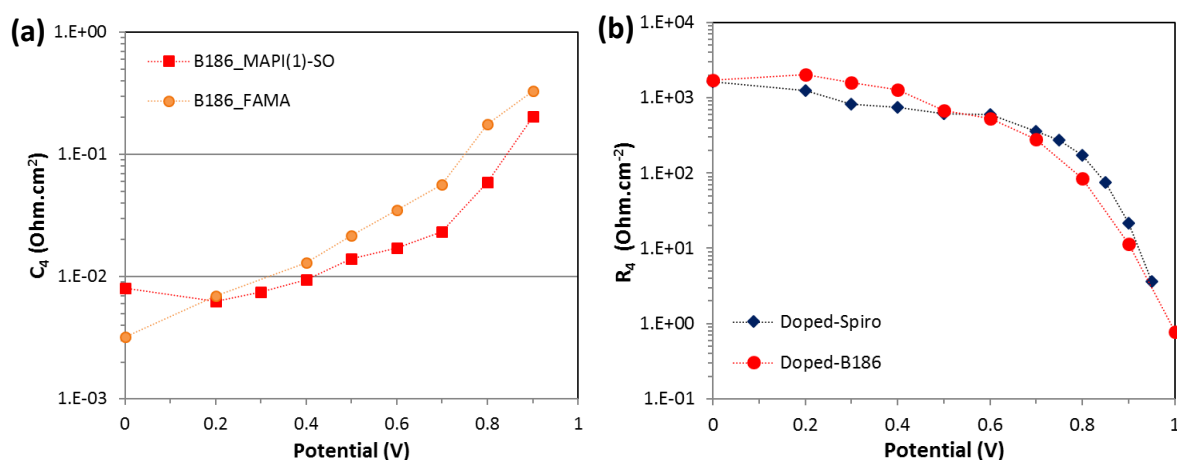


Figure 4.8. (a) C_4 of doped B186 cells versus applied potential of two different hybrid perovskite, MAPI(1)-SO and FAMA. (b) R_4 of doped B186 cell measured at various potential.

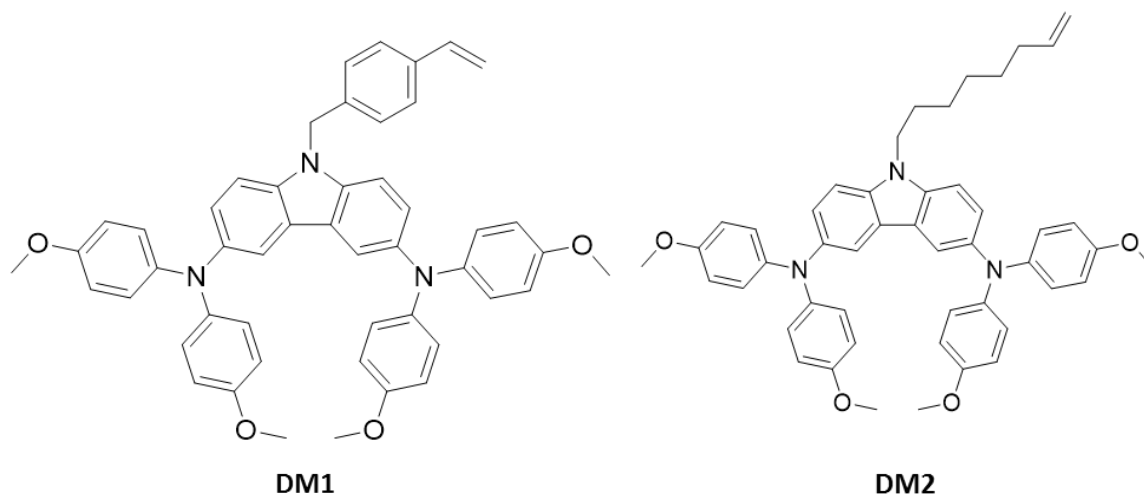
IV.3.5. Conclusion

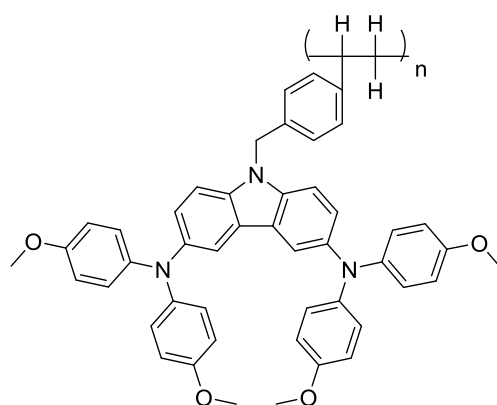
Two carbazole based molecular HTMs (B74 and B186) designed for PSC application have been studied. These compounds showed high thermal stability and suitable frontier energy levels compared to that of perovskite absorber. From the results, it is shown that these HTMs operated less efficiently than the benchmark Spiro-OMeTAD. Because of their suitable energy level with the perovskite, the PSC based on B186 and B74 HTMs yielded a maximum overall efficiency of 14.6% and 11.5%, respectively. We have also shown that low hysteresis could be obtained by using a FAMA HP. The use of additive was necessary to dramatically increase the conductivity of the B186 layers. Interestingly, we have found that these new HTMs clearly slow down the degradation of the MAPI perovskite layer and of the devices compared to Spiro-OMeTAD. The cells have been studied by the impedance spectroscopy (IS) technique. For undoped B186, the presence of large arc of circle at very high-frequency has been shown the signature of an unoptimized HTM layer with a low conductivity. The

analysis of this loop has allowed us to determine the ϵ_r and σ of undoped B186. The low-frequency part is the impedance response of the interfaces. It was reduced and noisy for undoped B186 cells due to a defective interface. The doping improved dramatically the quality of perovskite/HTM interface and then the charge transfer, and it allowed the achievement of high PCE.

IV.4. DM-based HTM for perovskite solar cells

This section is dedicated to the study of carbazole-based HTMs with a low molecular weight denoted DM1 and DM2. Their molecular structures are shown in Figure 4.9. We have also investigated a similar HTM bearing a long polymeric aliphatic and non-conducting chain noted DM1P (Figure 4.9). The average molecular weight of DM1P is ca. 43 000 g.mol⁻¹. DM1 and DM2 bear a polymerizable function on the side chain at the N-position, thus they can potentially be transformed into their corresponding polymeric materials. Structurally, the 3,6-bis(di(4-methoxyphenyl)aminy)carbazole is a popular building block commonly found in efficient molecular or polymeric HTM. The HTMs contained methoxy groups that should ensure a good interaction with perovskite material surface, notably with Pb(II) ion.[22] These materials have been synthesized at the LPPI and we have investigated them in perovskite photovoltaic devices.



**DM1P****Figure 4.9.** Molecular structure of **DM1**, **DM2**, and **DM1P** HTMs.

IV.4.1. The physico-chemical properties of the DM molecules

Their main properties are gathered in Table 4.3. DM1 and DM2 have low T_g values, due to their low MW, while T_g of the polymer DM1P is much higher (186°C). These molecules are semiconductors with a bandgap of about 2.8 eV. They are transparent over most of the visible light with a light absorption onset at ca 450 nm. The E_{HOMO} of DM1 and DM2 is similar to that of the B74 and B186 carbazole compounds and should allow a correct hole transfer between the perovskite and the HTM. On the other hand, the E_{HOMO} of DM1P (-4.47 eV) is similar to that of Spiro-OMeTAD (-4.45 eV).

Table 4.3. Thermal, optical and optoelectrochemical properties of DM1, DM2, and DM1P HTMs.

| Compound | MW (g/mol) | T_d ($^\circ\text{C}$) | T_g ($^\circ\text{C}$) | E_g^{opt} (eV) | E_{HOMO}^e (eV) | E_{LUMO}^f (eV) |
|-------------|---------------|----------------------------|----------------------------|----------------------------|-----------------------------|-----------------------------|
| DM1 | 737.88 | 415 | 73 | 2.80 | -4.60 | -1.80 |
| DM2 | 731.92 | 414 | 50 | 2.80 | -4.65 | -1.85 |
| DM1P | 43000 | 405 | 186 | 2.73 | -4.47 | -1.74 |

IV.4.2. Performance of solar cells

The new carbazole compounds have been tested for an application as HTM in perovskite solar cells using MAPI(1)-SO, MAPI(2) and FAMA as the HP. The preparation of these perovskites absorber can be found in Chapter II for both MAPI and in Annex I for FAMA. An optimized device was composed of a thin compact TiO₂ layer, a mesoporous TiO₂ layer filled and capped with the perovskite absorber, a HTM layer and finally a thermally evaporated Au back contact (the preparation of each layer detailed in Chapter II). The PSC device structure is shown in Figure 4.2a. The band energy alignment of the different device components are presented in Figure 4.10.

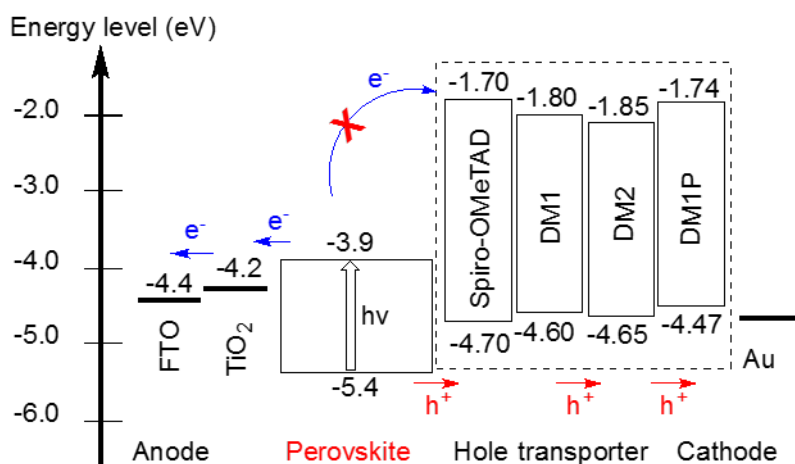


Figure 4.10. Energy level alignment of different device components.

The best results were achieved with MAPI(2) and these cells are discussed below. The best and average *J-V* curve parameters and power conversion efficiencies (PCEs) are gathered in Table 4.4. They are compared to benchmark Spiro-OMeTAD cells produced during the same batches. The best efficiency was measured for the DM1P HTM with maximum values as high as 13.24%. DM1 gave rise to cells with a PCE higher than 12% and the DM2 cells had a slightly lower PCEs with a maximum at 11.7%. The best result with DM1 is due to the higher FF parameter. It is also noteworthy that the DM2 cells exhibited the highest J_{sc} , with values close to that of the Spiro-OMeTAD cells (Table 4.4 and Figure 4.11). The cells with the polymer HTM had deceiving performances. We have noted that without dopant, the efficiency of DM1P cells was very low (below 0.7%) because the polymeric chain used was quite long and was not conjugated. Therefore, this chain was not profitable for the layer conductivity. Their *J-V* curves are typical of highly resistive devices and problems of charge injection and transport occurred. For undoped DM1P HTM, the device suffered from a very low FF that can

be attributed to the low HTM conductivity and therefore high charge transport resistances. For all the carbazole HTMs, the V_{oc} of the cells were lower than the Spiro-OMeTAD ones. It suggests the occurrence of more recombinations at the perovskite/HTM interface.

Table 4.4. Best and averaged J - V curve parameters and PCE for cells prepared with MAPI(2).

| HTM | Scan direction | V_{oc} (V) | J_{sc} (mA.cm ⁻²) | FF (%) | η (%) |
|----------------------|-------------------|--------------|---------------------------------|--------------|--------------|
| DM1 | Rev (Best) | 0.99 | 17.99 | 68.4 | 12.26 |
| | For (Best) | 0.99 | 18.6 | 59.65 | 11.08 |
| | Rev (Avg) | 0.97 | 20.69 | 58.18 | 11.63 |
| | For (Avg) | 0.97 | 20.92 | 49.89 | 10.07 |
| DM2 | Rev (Best) | 0.97 | 21.31 | 56.18 | 11.73 |
| | For (Best) | 0.97 | 21.02 | 48.00 | 9.84 |
| | Rev (Avg) | 0.97 | 21.42 | 54.12 | 11.32 |
| | For (Avg) | 0.96 | 21.16 | 43.98 | 8.97 |
| DM1P with dopants | Rev (Best) | 0.92 | 18.98 | 75.53 | 13.24 |
| | For (Best) | 0.95 | 16.94 | 48.01 | 7.70 |
| | Rev (Avg) | 0.91 | 15.95 | 76.04 | 11.09 |
| | For (Avg) | 0.93 | 17.98 | 42.62 | 7.18 |
| DM1P without dopants | Rev (Best) | 0.84 | 3.77 | 21.24 | 0.67 |
| | For (Best) | 0.83 | 3.96 | 21.6 | 0.71 |
| | Rev (Avg) | 0.74 | 2.374 | 20.708 | 0.39 |
| | For (Avg) | 0.82 | 3.21 | 20.08 | 0.55 |
| Spiro-OMeTAD | Rev (Best) | 1.01 | 22.15 | 78.75 | 17.68 |
| | For (Best) | 1.00 | 22.72 | 63.02 | 14.45 |
| | Rev (Avg) | 1.01 | 21.32 | 75.63 | 16.33 |
| | For (Avg) | 1.01 | 22.14 | 62.81 | 14.05 |

Number of cells averaged is 10 cells.

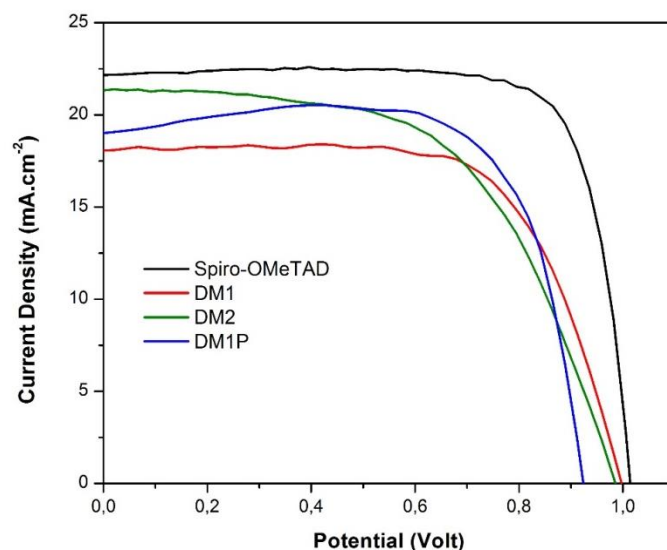


Figure 4.11. *J-V* curves of the best PSCs measured under AM1.5G filtered 100 mW.cm⁻² illuminations at reverse scan direction.

IV.4.3. Light soaking effect on perovskite solar cells performances

Interestingly, we have noted that, the obtaining of the maximum PCE with the DM1 and DM2 HTMs required a rather long light soaking under the solar simulator. The first measurements gave low PCEs. However, with time, this parameter continuously increased before to stabilize. The parameters provided in Table 4.4 are the stabilized ones. Figure 4.12 shows the *J-V* curve evolution upon light soaking for 25 min in the case of DM1/MAPI(2) (Figure 4.12a) and for 1h20 min in the case of DM2/MAPI(2) (Figure 4.12b). Two parameters increased with the light soaking, the FF and the J_{sc} . They are presented in Table 4.5a and 4.5b for DM1/MAPI(2) and DM2/MAPI(2) cells, respectively. It suggests that the light irradiation decreases the resistance of the cell. Under light shining electron-hole are photogenerated in the perovskite. The holes transferred to the HTM act as a strong oxidant, which oxidize the carbazole compound. It is known for instance that Spiro-OMeTAD requires oxidation to be efficient as HTM.[30] It is the role of the cobalt complex to oxidized directly Spiro-OMeTAD while LiTFSI acts as a chemical mediator which promotes the reaction between Spiro-OMeTAD and O₂ (See Chapter III, Section 3.1). These additives have been employed with the carbazole HTMs, however, the rapid change in the *J-V* curves under light shining shows that they are not sufficient. A further photo-oxidation is required to get efficient cells.

PbI₂ has a deeper valence band than MAPI, the presence of unreacted PbI₂ in the MAPI(2) could produce more oxidizing holes and then favor the oxidation of the HTM.

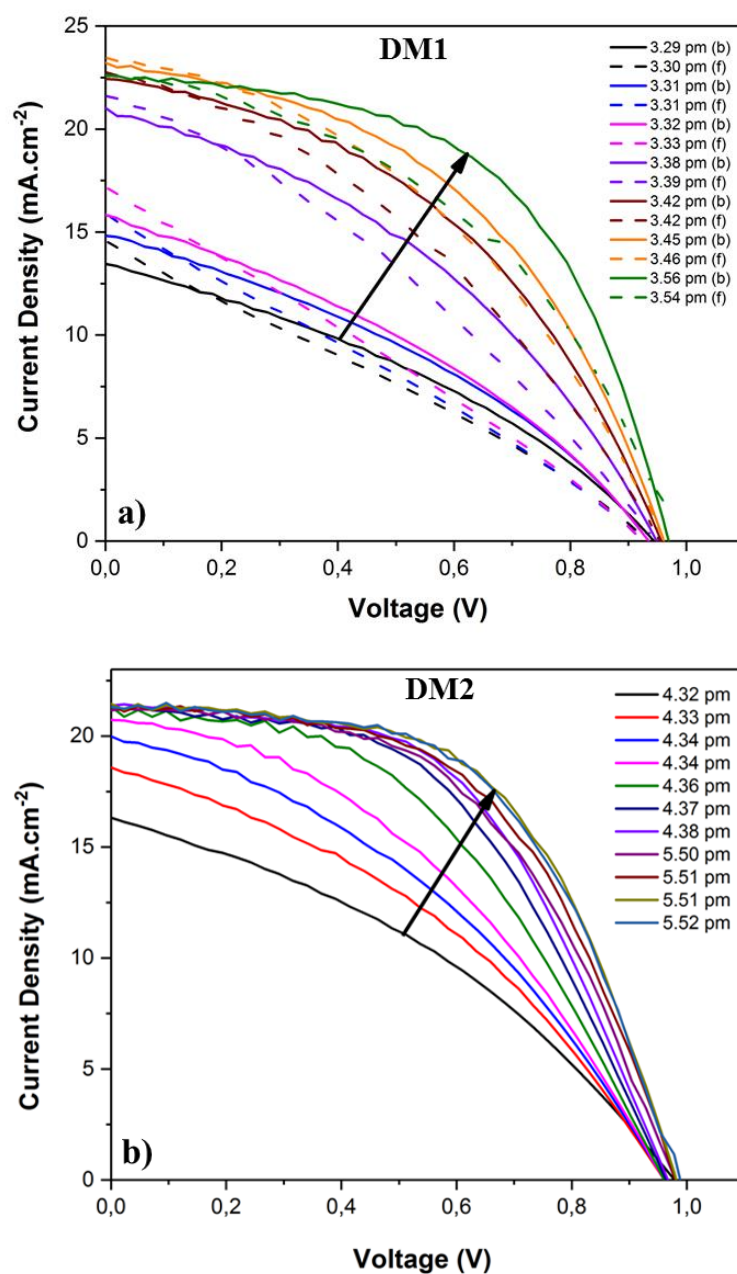


Figure 4.12. Light soaking effect on $J-V$ curve of perovskite solar cells prepared with (a) DM1 and (b) DM2 as hole transport material.

Table 4.5a. Light soaking effect on the $J-V$ curve parameters and PCE for cells prepared with DM1/MAPI(2).

| HTM | Scan direction | Time | V_{oc} (V) | J_{sc} (mA.cm^{-2}) | FF (%) | η (%) |
|-----|----------------|------|--------------|----------------------------------|--------|------------|
| DM1 | Rev | 3h29 | 0.94 | 13.46 | 34.63 | 4.39 |
| | For | 3h30 | 0.93 | 14.58 | 28.35 | 3.83 |
| | Rev | 3h31 | 0.93 | 14.88 | 35.20 | 4.88 |

| | | | | | | |
|--|------------|-------------|-------------|--------------|--------------|--------------|
| | For | 3h31 | 0.92 | 15.92 | 27.65 | 4.05 |
| | Rev | 3h32 | 0.93 | 15.84 | 34.37 | 5.06 |
| | For | 3h33 | 0.92 | 17.21 | 27.43 | 4.34 |
| | Rev | 3h38 | 0.95 | 20.89 | 38.80 | 7.66 |
| | For | 3h39 | 0.94 | 21.61 | 33.03 | 6.71 |
| | Rev | 3h42 | 0.95 | 22.49 | 43.15 | 9.26 |
| | For | 3h42 | 0.95 | 22.70 | 37.23 | 8.03 |
| | Rev | 3h45 | 0.96 | 23.18 | 46.19 | 10.28 |
| | For | 3h46 | 0.96 | 23.44 | 40.99 | 9.19 |
| | Rev | 3h50 | 0.96 | 23.92 | 51.68 | 11.88 |
| | For | 3h50 | 0.96 | 23.94 | 45.06 | 10.36 |
| | Rev | 3h53 | 0.96 | 24.17 | 54.07 | 12.61 |
| | For | 3h53 | 0.96 | 24.17 | 47.24 | 10.99 |
| | Rev | 3h56 | 0.97 | 22.58 | 54.50 | 11.91 |
| | For | 3h57 | 0.98 | 22.62 | 44.03 | 9.75 |

Table 4.5b. Light soaking effect on the J - V curve parameters and PCE for cells prepared with DM2/MAPi(2).

| HTM | Scan direction | Time | V_{oc} (V) | J_{sc} (mA.cm ⁻²) | FF (%) | η (%) |
|-----|----------------|-------------|--------------|---------------------------------|--------------|--------------|
| DM2 | Rev | 4h32 | 0.98 | 16.29 | 36.32 | 5.78 |
| | | 4h33 | 0.96 | 18.52 | 37.54 | 6.66 |
| | | 4h34 | 0.96 | 20.70 | 40.11 | 7.96 |
| | | 4h36 | 0.96 | 21.13 | 45.71 | 9.26 |
| | | 4h37 | 0.96 | 21.30 | 50.14 | 10.28 |
| | | 4h38 | 0.97 | 21.40 | 52.71 | 10.90 |
| | | 4h50 | 0.98 | 21.12 | 51.72 | 10.69 |
| | | 4h51 | 0.98 | 21.20 | 53.99 | 11.22 |
| | | 4h51 | 0.98 | 21.32 | 56.18 | 11.74 |
| | | 4h52 | 0.98 | 21.31 | 55.61 | 11.66 |
| | For | 4h32 | 0.94 | 17.84 | 26.94 | 4.50 |

| | | | | | | |
|--|--|-------------|-------------|--------------|--------------|-------------|
| | | 4h34 | 0.96 | 19.89 | 38.19 | 7.29 |
| | | 4h38 | 0.95 | 21.32 | 42.48 | 8.57 |
| | | 4h39 | 0.95 | 21.32 | 43.08 | 8.75 |
| | | 4h52 | 0.96 | 21.24 | 41.46 | 8.49 |
| | | 4h53 | 0.98 | 21.23 | 41.23 | 8.58 |
| | | 4h53 | 0.96 | 21.24 | 41.64 | 8.49 |
| | | 4h56 | 0.98 | 21.24 | 45.99 | 9.55 |
| | | 4h57 | 0.98 | 21.08 | 46.43 | 9.55 |
| | | 4h58 | 0.98 | 21.03 | 48.00 | 9.85 |

After stabilization, the effect of the scan rate on the J - V curves of the carbazole cells was investigated. Figure 4.13 shows the results for DM1 and DM1P cells. The hysteresis decreased significantly when the scan rate was reduced down to 0.1 V.s^{-1} . Then the reverse and the forward scan poorly change with the scan rate.

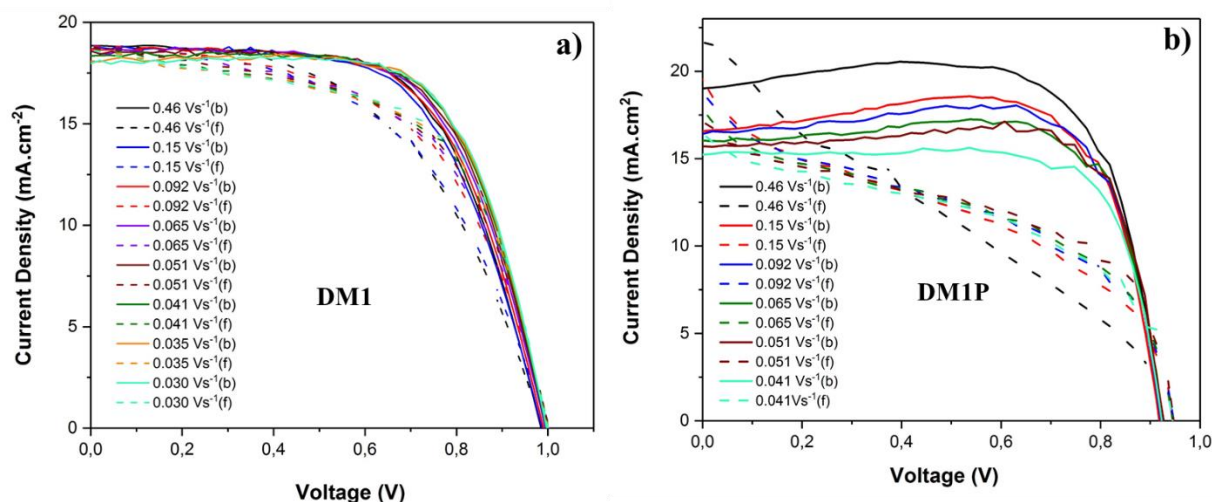


Figure 4.13. Effect of scan rate of (a) DM1-based and (b) DM1P-based perovskite solar cells.

The cells prepared with MAPI(2) and DM1P (which is not polymerizable) did not show such an increase of the PCE with light soaking.

The DM HTMs were also tested with the one-step MAPI(1)-SO absorber. The best PCE and averaged values are gathered in Table 4.4b. For all the DM, the efficiency was lower and the hysteresis was higher than with MAPI(2). We have noted that for all the DM HTM, there was

no improvement by light soaking. It could be due to a different perovskite surface morphology that lead directly to a good interface with the HTMs.

Table 4.6. Best and averaged J-V curve parameters and PCE for cells prepared with MAPI(1)-SO.

| HTM | Scan direction | V _{oc} (V) | J _{sc} (mA.cm ⁻²) | FF (%) | η(%) |
|----------------------|----------------|---------------------|--|--------|-------|
| DM1 | Rev (Best) | 0.98 | 17.38 | 70.81 | 12.09 |
| | For (Best) | 0.98 | 16.95 | 52.77 | 8.77 |
| | Rev (Avg) | 0.94 | 13.35 | 59.06 | 5.95 |
| | For (Avg) | 0.95 | 13.74 | 43.12 | 5.59 |
| DM2 (60 mM) | Rev (Best) | 0.79 | 18.86 | 62.94 | 9.39 |
| | For (Best) | 0.73 | 17.59 | 20.58 | 2.66 |
| | Rev (Avg) | 0.80 | 18.2 | 60.44 | 8.92 |
| | For (Avg) | 0.73 | 16.77 | 19.82 | 2.43 |
| DM1P with dopants | Rev (Best) | 0.90 | 15.85 | 74.31 | 10.71 |
| | For (Best) | 0.92 | 15.03 | 41.1 | 5.73 |
| | Rev (Avg) | 0.91 | 14.54 | 73.29 | 9.71 |
| | For (Avg) | 0.92 | 13.58 | 49.08 | 6.14 |

Number of cells averaged is 5 cells.

In the end, we also tested the DM HTMs with FAMA perovskite but unfortunately the performances were very low at <1% PCE. This very low efficiency might be due to the not proper band alignment between the DM HTMs and the FAMA perovskite.

IV.4.4. Conclusion

A DM series of HTMshas been studied for perovskite solar cells application. Because of their suitable energy level to the perovskite absorber, the best PSCs based on DM1, DM2, and DM1P could achieved 12.2%, 11.7%, and 13,2%, respectively when they were combined with MAPI(2) perovskite absorber. We found that DM1 and DM2 showed a significantly PCE increase due to the light soaking when they were tested with MAPI(2) perovskite. But this phenomena was not found for the DM1P with MAPI(2) and for all DMx series HTMs with MAPI(1)-SO HP. We have also noted that the hysteresis of DM1 can be reduced by slowing down the scan rate of J-V curve measurement. In the end, we tried to combine the DMx HTMs with FAMA perovskite, unfortunately the PCEs were very low at less than 1%.

IV.5. iDM HTM-based perovskite solar cells

In this section, we propose the study another series of carbazole-based HTMs with low molecular weight denoted iDM1, iDM2, and iDM4. Figure 4.14 shows the molecular structure of each molecule. Structurally, the iDM-based HTMs bear 2,7 substituted carbazole. These iDM-based molecule HTMs are similar to that DM-based HTMs. The difference between these two groups is the internal conjugation of the structure. DM-based HTMs bear a polymerizable function on the side chain at the N-position while iDM-based HTMs go through the C-C bonding in the carbazole molecule. It results that iDM HTMs resemble more in their internal conjugation to Spiro-OMeTAD than DM-based HTMs.

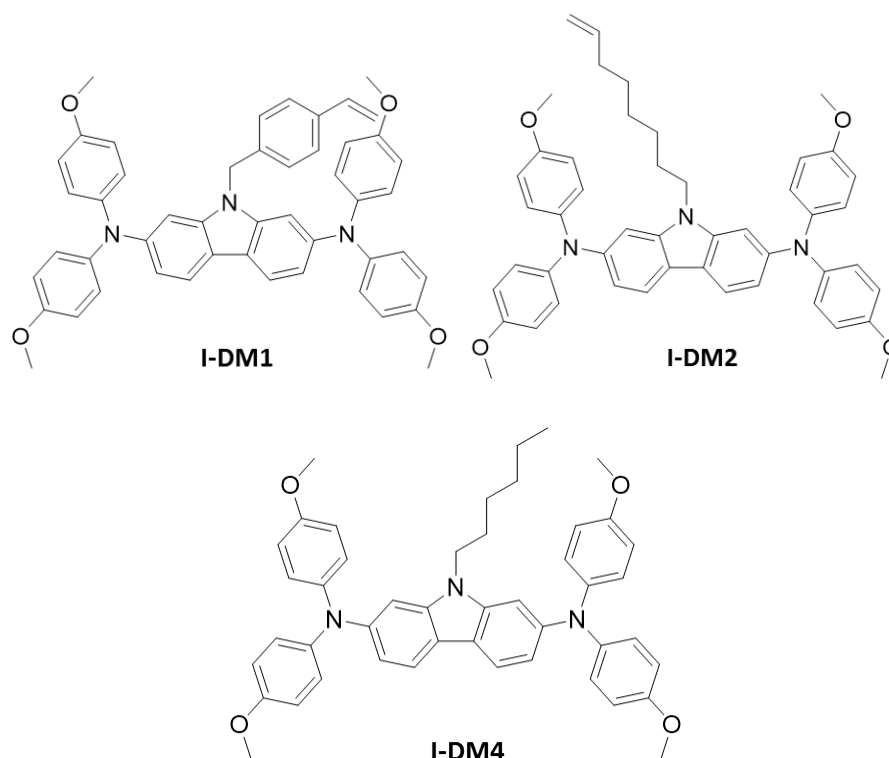


Figure 4.14. Molecular structure of iDM1, iDM2, and iDM4 hole transport materials.

IV.5.1. The physico-chemical properties of the iDM molecules

Table 4.7 gathers the main properties of the iDM series HTM. iDM2 and iDM4 have low T_g values while iDM1 is much higher (151°C). These molecules are semiconductors with a bandgap of 2.9 eV for iDM2 and iDM4, and 2.77 eV for iDM1. The E_{HOMO} level of these series HTMs is much lower than that of Spiro-OMeTAD (-4.45 eV) and the other HTMs studied in this Chapter.

Table 4.7. Thermal, optical and optoelectrochemical properties of **iDM1**, **iDM2**, and **iDM4** HTMs.

| Compound | MW (g/mol) | T_d(°C) | T_g (°C) | E_g^{opt} (eV) | E_{HOMO}^e (eV) | E_{LUMO}^f (eV) |
|-----------------|-----------------------|--------------------------|---------------------------|---|--|--|
| iDM1 | 737.90 | 227 | 151 | 2.77 | -4.70 | -1.93 |
| iDM2 | 731.94 | 356 | 47 | 2.92 | -4.83 | -1.90 |
| iDM4 | 705.90 | 343 | 36 | 2.90 | -4.81 | -1.90 |

IV.5.2. Performances of solar cells

The iDM molecule series has been tested as HTM in a perovskite solar cell using MAPI(1)-SOF, MAPI(1)-SO, MAPI(2) and FAMA as the perovskite absorber. The preparation of MAPI(1)-SOF can be found in Chapter V section V.2.2, MAPI(1)-SO and MAPI(2) has detailed in Chapter II section II.2.3, and FAMA perovskite preparation is explained in the Section IV.2 of this chapter. As usual, an optimized device was composed of a thin compact TiO₂ layer, a mesoporous TiO₂ layer filled and capped with the perovskite absorber, a HTM layer and finally a thermally evaporated Au back contact

In the first testing, the iDMx series was incorporated with MAPI(1)-SO perovskite. It resulted in PCEs lower than 7% for all the HTMs. iDM1 gave rise to the highest PCE. The iDM2 reached 4.8% PCE while iDM4 only achieved 3.6%. Considering the not very bad efficiency of iDM1, further tests were realized using others perovskite absorber, namely MAPI(2), MAPI(1)-SOF, and FAMA. The results of the solar cell performances are gathered in Table 4.8. The *J-V* reverse scan curves for the best cells are plotted in Figure 4.15.

Table 4.8. Best and averaged *J-V* curve parameters and PCE for iDM1 cells prepared with MAPI(2), MAPI(1)-SOF, and FAMA.

| Perovskite | Scan direction | V_{oc} (V) | J_{sc} (mA.cm⁻²) | FF (%) | η(%) |
|-------------------|-----------------------|---------------------------|--|---------------|--------------|
| MAPI(2) | Rev (Best) | 0.92 | 18.92 | 80.78 | 14.10 |
| | For (Best) | 0.91 | 17.90 | 36.11 | 5.90 |
| | Rev (Avg) | 0.91 | 18.80 | 77.28 | 13.29 |
| | For (Avg) | 0.91 | 17.93 | 34.45 | 5.60 |
| MAPI(1)-SOF | Rev (Best) | 0.91 | 22.59 | 73.40 | 15.04 |
| | For (Best) | 0.89 | 22.60 | 25.57 | 5.12 |

| | | | | | |
|------|-------------------|-------------|--------------|--------------|--------------|
| FAMA | Rev (Avg) | 0.92 | 22.05 | 70.63 | 14.28 |
| | For (Avg) | 0.88 | 22.08 | 23.85 | 4.62 |
| | Rev (Best) | 1.01 | 22.33 | 62.06 | 14.04 |
| | For (Best) | 1.00 | 22.32 | 62.49 | 14.01 |
| | Rev (Avg) | 1.02 | 21.94 | 62.42 | 13.95 |
| | For (Avg) | 1.01 | 21.91 | 61.96 | 13.69 |

Number of cells averaged is 10 cells.

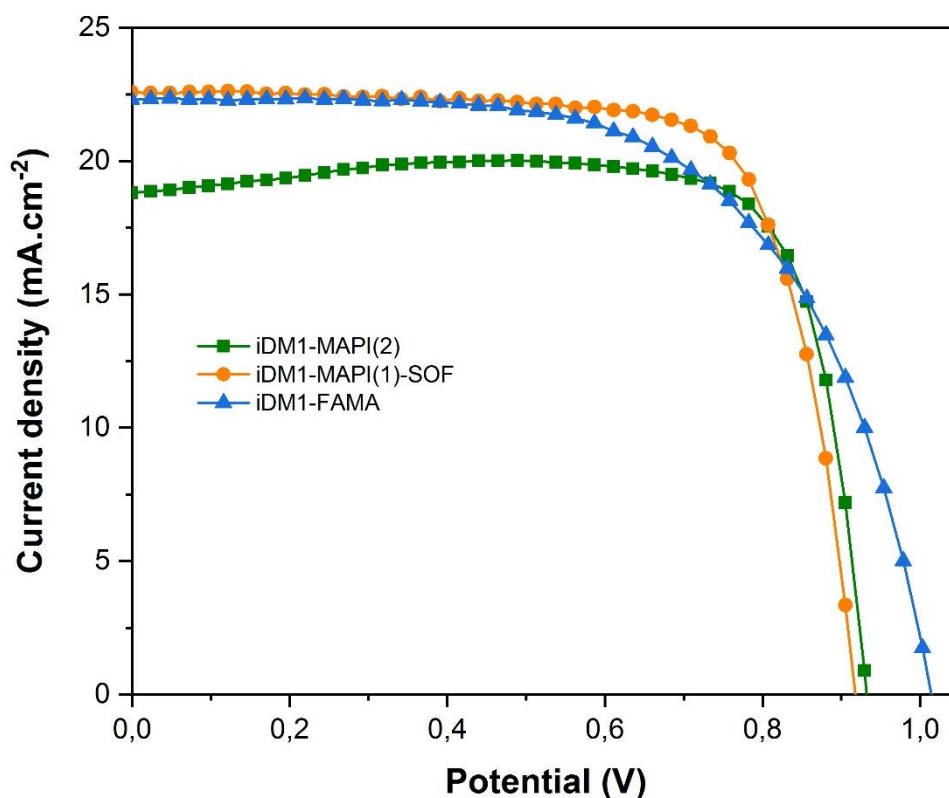


Figure 4.15. Best J - V reverse scan curves of the cells combining iDM1 HTM with perovskite absorber.

From the Table 4.8, we can see that the iDM1 achieved high efficiency: 14% with MAPI(2), 15% with MAPI(1)-SOF, and 14% with FAMA perovskite. While incorporated with MAPI perovskite, the cells showed a huge hysteresis. On the other hand, the cells showed no hysteresis when FAMA perovskite was used as solar light absorber (Figure 4.16). The V_{oc} and J_{sc} were rather high for FAMA-based cells while their FF was lower compared to the MAPI(2) and MAPI(1)-SOF cells. FAMA-based cells showed a J_{sc} as high as MAPI(1)-SOF cells which indicates a correct charge transfer from the perovskite to the hole transporting material.

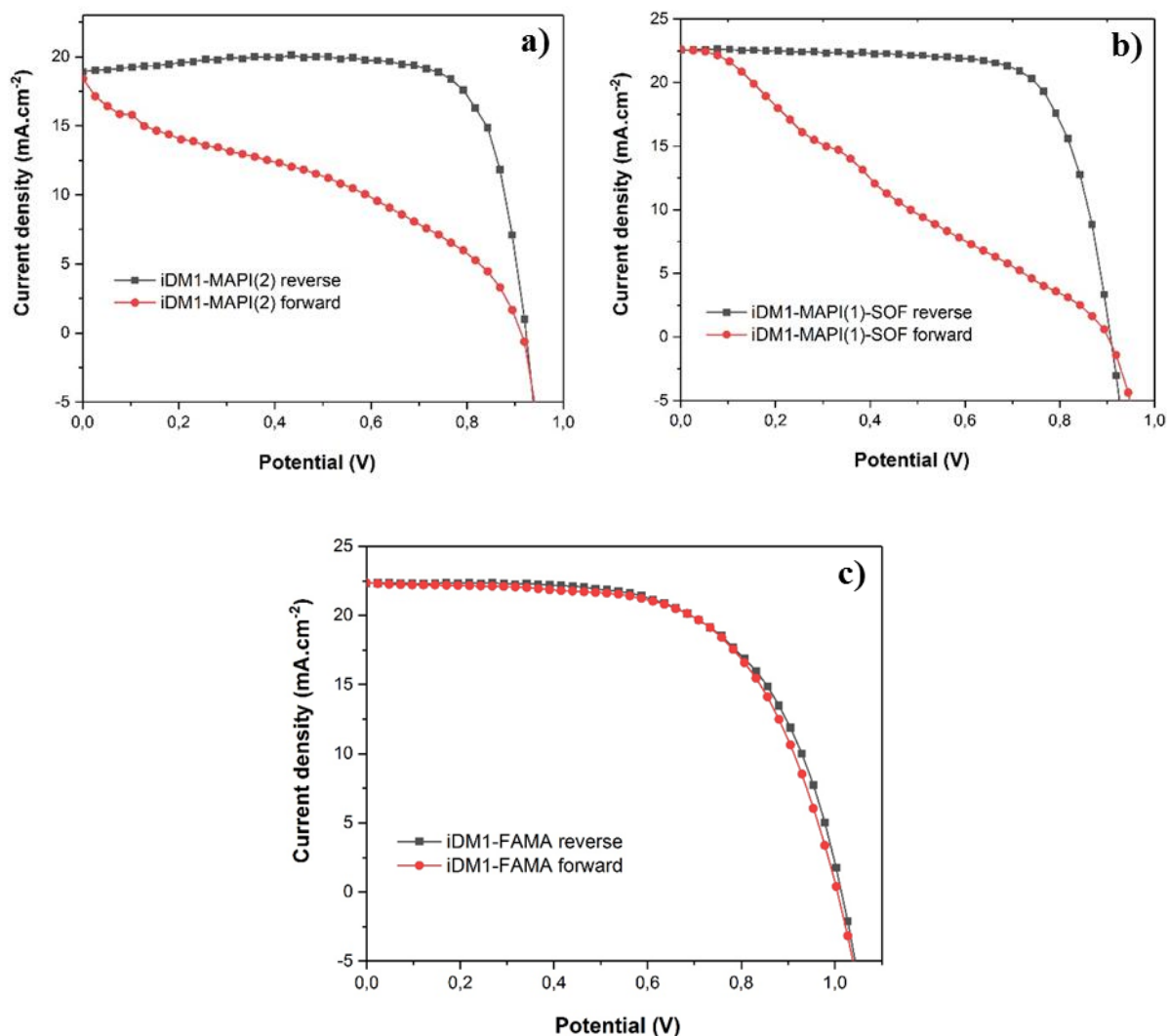


Figure 4.16. *J-V* curves of iDM1 measured on both directions (reverse and forward) on (a) MAPI(2), (b) MAPI(1)-SOF, and (c) FAMA.

IV.5.3. Conclusion

We have successfully tested the iDMx series HTMs for perovskite solar cells application. These HTMs have a proper band alignment to the perovskite absorber that can be a reason for a well charge transfer in the cell. The results showed that iDM1 is the best HTM among others with efficiency PCE as high as 15% when combined with MAPI(1)-SOF. Unfortunately, a huge hysteresis appears when iDM1 is combined with MAPI perovskite. We also showed that the *J*-*V* curves are almost hysteresis-free when iDM1 is combined with FAMA perovskite.

IV.6. General Conclusion

We have successfully investigated various new carbazole-based HTMs in perovskite solar cells. these molecules ranged from the big dendritic core B186 to the DMs and iDMs series with lower molecular weight. Various perovskite absorbers have been combined with them in order to study the behavior and to optimize the performances. For the cell performances, iDM1 showed the best result among others, at more than 15% of PCE with MAPI(1)-SOF as the perovskite absorber. Unfortunately, a huge hysteresis appeared in this cell. We noticed that in the case of B186 and iDM1, the same phenomena such a huge hysteresis has appeared for MAPI-based cells while it could be almost eliminated for iDM1/FAMA and it was reduced a lot in B186/FAMA cells.

References

- [1] Z. Ku, Y. Rong, M. Xu, T. Liu, and H. Han, "Full Printable Processed Mesoscopic CH₃NH₃PbI₃/TiO₂ Heterojunction Solar Cells with Carbon Counter Electrode," *Sci. Rep.*, vol. 3, p. 3132, Nov. 2013.
- [2] A. Mei *et al.*, "A hole-conductor-free, fully printable mesoscopic perovskite solar cell with high stability," *Science*, vol. 345, no. 6194, p. 295, Jul. 2014.
- [3] Z. Wei, H. Chen, K. Yan, and S. Yang, "Inkjet Printing and Instant Chemical Transformation of a CH₃NH₃PbI₃/Nanocarbon Electrode and Interface for Planar Perovskite Solar Cells," *Angew. Chem. Int. Ed.*, vol. 53, no. 48, pp. 13239–13243, Sep. 2014.
- [4] F. Zhang, X. Yang, H. Wang, M. Cheng, J. Zhao, and L. Sun, "Structure Engineering of Hole-Conductor Free Perovskite-Based Solar Cells with Low-Temperature-Processed Commercial Carbon Paste As Cathode," *ACS Appl. Mater. Interfaces*, vol. 6, no. 18, pp. 16140–16146, Sep. 2014.
- [5] Z. Wei, X. Zheng, H. Chen, X. Long, Z. Wang, and S. Yang, "A multifunctional C + epoxy/Ag-paint cathode enables efficient and stable operation of perovskite solar cells in watery environments," *J. Mater. Chem. A*, vol. 3, no. 32, pp. 16430–16434, 2015.
- [6] U. Bach *et al.*, "Solid-state dye-sensitized mesoporous TiO₂ solar cells with high photon-to-electron conversion efficiencies," *Nature*, vol. 395, p. 583, Oct. 1998.
- [7] J.-M. Wang *et al.*, "Small Molecule-Polymer Composite Hole-Transporting Layer for Highly Efficient and Stable Perovskite Solar Cells," *ACS Appl. Mater. Interfaces*, vol. 9, no. 15, pp. 13240–13246, Apr. 2017.
- [8] M. Saliba *et al.*, "A molecularly engineered hole-transporting material for efficient perovskite solar cells," *Nat. Energy*, vol. 1, p. 15017, Jan. 2016.
- [9] C. W. Tang and A. C. Albrecht, "Photovoltaic effects of metal-chlorophyll-a-metal sandwich cells," *J. Chem. Phys.*, vol. 62, no. 6, pp. 2139–2149, Mar. 1975.
- [10] Z. H. Bakr, Q. Wali, A. Fakharuddin, L. Schmidt-Mende, T. M. Brown, and R. Jose, "Advances in hole transport materials engineering for stable and efficient perovskite solar cells," *Nano Energy*, vol. 34, pp. 271–305, 2017.
- [11] N. Prachumrak *et al.*, "Novel Bis[5-(fluoren-2-yl)thiophen-2-yl]benzothiadiazole End-Capped with Carbazole Dendrons as Highly Efficient Solution-Processed Nondoped Red Emitters for

- Organic Light-Emitting Diodes,” *ACS Appl. Mater. Interfaces*, vol. 5, no. 17, pp. 8694–8703, Sep. 2013.
- [12] Z. Chen *et al.*, “Low-Cost Carbazole-Based Hole-Transport Material for Highly Efficient Perovskite Solar Cells,” *ChemSusChem*, vol. 10, no. 15, pp. 3111–3117, Jun. 2017.
- [13] M. Daskeviciene *et al.*, “Carbazole-based enamine: Low-cost and efficient hole transporting material for perovskite solar cells,” *Nano Energy*, vol. 32, pp. 551–557, Feb. 2017.
- [14] P. Gratia *et al.*, “A Methoxydiphenylamine-Substituted Carbazole Twin Derivative: An Efficient Hole-Transporting Material for Perovskite Solar Cells,” *Angew. Chem. Int. Ed.*, vol. 54, no. 39, pp. 11409–11413, Jul. 2015.
- [15] T. Malinauskas *et al.*, “Branched methoxydiphenylamine-substituted fluorene derivatives as hole transporting materials for high-performance perovskite solar cells,” *Energy Environ. Sci.*, vol. 9, no. 5, pp. 1681–1686, 2016.
- [16] C. Lu, I. T. Choi, J. Kim, and H. K. Kim, “Simple synthesis and molecular engineering of low-cost and star-shaped carbazole-based hole transporting materials for highly efficient perovskite solar cells,” *J. Mater. Chem. A*, vol. 5, no. 38, pp. 20263–20276, 2017.
- [17] C.-Y. Hsu, Y.-C. Chen, R. Y.-Y. Lin, K.-C. Ho, and J. T. Lin, “Solid-state dye-sensitized solar cells based on spirofluorene (spiro-OMeTAD) and arylamines as hole transporting materials,” *Phys Chem Chem Phys*, vol. 14, no. 41, pp. 14099–14109, 2012.
- [18] S. Holliday, J. E. Donaghey, and I. McCulloch, “Advances in Charge Carrier Mobilities of Semiconducting Polymers Used in Organic Transistors,” *Chem. Mater.*, vol. 26, no. 1, pp. 647–663, Jan. 2014.
- [19] A. C. Arias, J. D. MacKenzie, I. McCulloch, J. Rivnay, and A. Salleo, “Materials and Applications for Large Area Electronics: Solution-Based Approaches,” *Chem. Rev.*, vol. 110, no. 1, pp. 3–24, Jan. 2010.
- [20] J. Zaumseil and H. Sirringhaus, “Electron and Ambipolar Transport in Organic Field-Effect Transistors,” *Chem. Rev.*, vol. 107, no. 4, pp. 1296–1323, Apr. 2007.
- [21] T.-T. Bui *et al.*, “Design of dendritic core carbazole-based hole transporting materials for efficient and stable hybrid perovskite solar cells,” *Org. Electron.*, vol. 60, pp. 22–30, Sep. 2018.
- [22] A. Torres and L. G. C. Rego, “Surface effects and adsorption of methoxy anchors on hybrid lead iodide perovskites: Insights for spiro-MeOTAD attachment,” *J. Phys. Chem. C*, vol. 118, no. 46, pp. 26947–26954, 2014.
- [23] S. J. Park *et al.*, “Inverted planar perovskite solar cells with dopant free hole transporting material: Lewis base-assisted passivation and reduced charge recombination,” *J Mater Chem A*, vol. 5, no. 25, pp. 13220–13227, Jun. 2017.
- [24] V. Mimaite, J. Ostrauskaite, D. Gudeika, J. V. Grazulevicius, and V. Jankauskas, “Structure–properties relationship of hydrazones containing methoxy-substituted triphenylamino groups,” *Synth. Met.*, vol. 161, no. 15, pp. 1575–1581, 2011.
- [25] A. Sakalyte *et al.*, “Effect of Methoxy Substituents on the Properties of the Derivatives of Carbazole and Diphenylamine,” *J. Phys. Chem. C*, vol. 115, no. 11, pp. 4856–4862, Mar. 2011.
- [26] M. Ben Manaa *et al.*, “Study of the pore filling fraction of carbazole-based hole- transporting materials in solid-state dye-sensitized solar cells,” *Mediterr. J. Chem.*, vol. 5, no. 6, pp. 599–604, 2016.
- [27] W. H. Nguyen, C. D. Bailie, E. L. Unger, and M. D. McGehee, “Enhancing the Hole-Conductivity of Spiro-OMeTAD without Oxygen or Lithium Salts by Using Spiro(TFSI)₂ in Perovskite and Dye-Sensitized Solar Cells,” *J. Am. Chem. Soc.*, vol. 136, no. 31, pp. 10996–11001, Aug. 2014.

- [28] A. Abate *et al.*, “Lithium salts as ‘redox active’ p-type dopants for organic semiconductors and their impact in solid-state dye-sensitized solar cells,” *Phys. Chem. Chem. Phys.*, vol. 15, no. 7, pp. 2572–2579, 2013.
- [29] P. Wang, M. Ulfa, and T. Pauporté, “Effects of Perovskite Monovalent Cation Composition on the High and Low Frequency Impedance Response of Efficient Solar Cells,” *J. Phys. Chem. C*, vol. 122, no. 4, pp. 1973–1981, Feb. 2018.
- [30] M. Ulfa, T. Pauporté, T.-T. Bui, and F. Goubard, “Impact of Organic Hole Transporting Material and Doping on the Electrical Response of Perovskite Solar Cells,” *J. Phys. Chem. C*, vol. 122, no. 22, pp. 11651–11658, Jun. 2018.

Chapter V

Impact of the Oxide Layer on the Performances of Perovskite Solar Cells

The electron transport layer (ETL) is another key component of the perovskite solar cells. In this chapter, we study various oxides for ETL and their optimization. We describe the deposition method of each layer, characterize the layers and evaluate their performances in PSCs. We employed three different oxide layers in this study: planar tin dioxide (SnO_2) and a compact titanium dioxide ($bl\text{-TiO}_2$) layers for planar solar cells, and a combination of the compact titanium dioxide ($bl\text{-TiO}_2$) layer and of a mesoporous titanium dioxide ($meso\text{-TiO}_2$) prepared from nanoparticles. The latter is the conventional structure employed for perovskite solar cells (for instance in Chapters II, III and IV). SnO_2 and $meso\text{-TiO}_2$ layer have been deposited by spin-coating and the $bl\text{-TiO}_2$ was deposited by spray pyrolysis. In this study, we have compared two different structures of hybrid perovskite (HP) with different composition of cations: (1) $\text{CH}_3\text{NH}_3\text{PbI}_3$ (named MAPI perovskite) and (2) $\text{FA}_{1-x}\text{MA}_x\text{Pb}(\text{I}_{1-y}\text{Br}_y)_3$ (named FAMA) perovskite. To deeply understand the ability of the various perovskites to generate charges and inject them into the adjacent contacts, especially the oxide ETLs, we realized a detailed impedance spectroscopy (IS) study of the cells and time-resolved photoluminescence measurements.

V.1. Introduction

In the most popular architecture delivering high efficiency and stable power output, a TiO_2 mesoporous structure, deposited on top of a compact TiO_2 hole blocking layer is employed [1]. The HP absorber layer is placed in-between this layer and a p-type one usually made of a molecular semiconductor. The oxide layer blocks the hole transfer and ensures the electron transport [1]. On the other side, the p-type contact layer blocks the electrons and ensures the transport of holes between the absorber and the back contact [2], [3]. The drawback of TiO_2 is that it requires a high temperature sintering step ($>450^\circ\text{C}$) which is incompatible with the fabrication at low cost and with flexible devices. On the other hand, there has been a lot of research effort to develop simplified devices without mesoporous layer with the planar n-i-p cell structures. The n-type oxide hole blocking layer is pivotal for planar PSC. Such kind of

device employing compact TiO₂ electron transporting material (ETM) suffers from lower efficiency and large hysteresis of their *J-V* curves compared to the mesoscopic ones.

Recently, SnO₂ has emerged as the most promising n-type wide bandgap semiconductor to replace TiO₂ in planar PSCs [4]–[14]. The advantages of SnO₂ compared to TiO₂ are a deeper conduction band minimum, a wider bandgap (above 3.6 eV) and a high transparency over a large wavelength range as requested to maximize the solar light collected by the HP absorber. Moreover, SnO₂ has a high electron mobility (up to 240 cm²/(V.s) compared to $\approx 0.1\text{--}1$ cm²/(V.s) for TiO₂) [15]–[17] and it can be prepared at much lower temperature than TiO₂. In the literature, the main techniques employed for the preparation of SnO₂ layers are atomic layer deposition (ALD), spin-coating, chemical bath deposition (CBD) and electrodeposition [4]–[14]. In 2015, Baena et al. [5] fabricated planar PSCs based on SnO₂ layers formed by ALD at 120°C. They showed that planar PSC using TiO₂ are inherently limited due to conduction band misalignment when SnO₂ achieves a barrier-free energetic configuration. These cells were almost hysteresis-free. Jiang et al. [6] developed the spin-coating of a colloidal solution of SnO₂ for the preparation of the SnO₂ layer. The layers were annealed at 150°C. A PCE close to 20% was achieved almost free of hysteresis. They suggested that the SnO₂ deep conduction band, the high electron mobility and then the reduction of the energy barrier at the perovskite/electron transporting layer (ETL) interface enhances the electron extraction and eliminates the *J-V* curve hysteresis. Mg –doping into high temperature proceeded SnO₂ yield better PCEs than the undoped ones [7]. The PSC *J-V* curve parameters and PCE improvement was assigned to higher electron mobilities. Li-doping [8] and Al-doping [9] have also been reported to be beneficial for the PSC performances. Other works have focused on the SnO₂ surface engineering. Using a 3-aminopropyltriethoxysilane self-assembled monolayer (SAM) has demonstrated multifunction [10]: decrease of the work function of SnO₂ for an enlarged built-in potential; formation of high quality perovskite; passivation of trap states and hindering of electron back transfer and recombination reduction. On the other hand, surface fullerene layer has been described as promoting the electron transfer, passivating the SnO₂/perovskite interface and perovskite grain boundaries [11]. The use as the ETL of a SnO₂ layer two-step prepared (spin-coating and chemical bath deposition) and annealed at 180°C has resulted in PSCs with a *V*_{oc} as high as 1214 mV and a 20.7% PCE [12]. Electrodeposition has also been employed for SnO₂ ETL preparation. This solution-based (<100°C) processing method to synthesize crystalline SnO₂ has permitted to achieve a much lower PCE of 13.8% [13]. In the recent years, various works have shown that IS is a powerful technique for the

investigation of PSCs [1], [26]–[40]. For instance, we have employed this non-destructive technique to investigate various TiO_2 blocking layers [1], the use of various monovalent cations in the organo-lead perovskite [26], the effect of doping of the HTM on the PSC functioning (Chapter III and Refs[2][3]) and so on. The phenomena of charges (ions, electrons/holes) transfer and accumulation can be thoroughly investigated and followed by IS. The cells were analyzed under light illumination, over large applied voltage and frequency ranges. However, to our knowledge, in-depth investigations of the functioning and electrical response of efficient SnO_2 -based PSCs are very scarce in the literature. A noticeable exception is the work by Guerrero et al. [18]. These authors measured the impedance spectra of SnO_2 solar cells over a large applied potential range. The SnO_2 layer of the cell was prepared by ALD. However, they presented an inductive loop in the intermediate frequency range that we have reported as the signature of not optimized cells in our previous work (Chapter III, section 3.5 and Ref.[1]). This electrical feature could be due to aging since the cells were store several months before to be characterized.

V.2. Experimental section

V.2.1. Preparation of the oxide layers

- *TiO₂ blocking layer (bl-TiO₂) and TiO₂ mesoporous layer (meso-TiO₂)*

The preparation of these layers have been detailed in Chapter II, section II.2.

- *SnO₂ layer*

The optimized SnO_2 layer was prepared by spin-coating a colloidal dispersion of tin (IV) oxide (Alfa Aesar, 15% in H_2O) which was diluted with H_2O to 2.35%. This solution was stirred at least 30 min prior to use. 45 μL of the solution was spin-coated on top of clean FTO at 3000 rpm for 30 s and 1500 rpm/s of acceleration. The layer was then annealed at various temperatures. The optimum process was found to be coating 2 times with a 1h30 annealing at 123°C after each coating.

V.2.2. Preparation of the perovskite layers

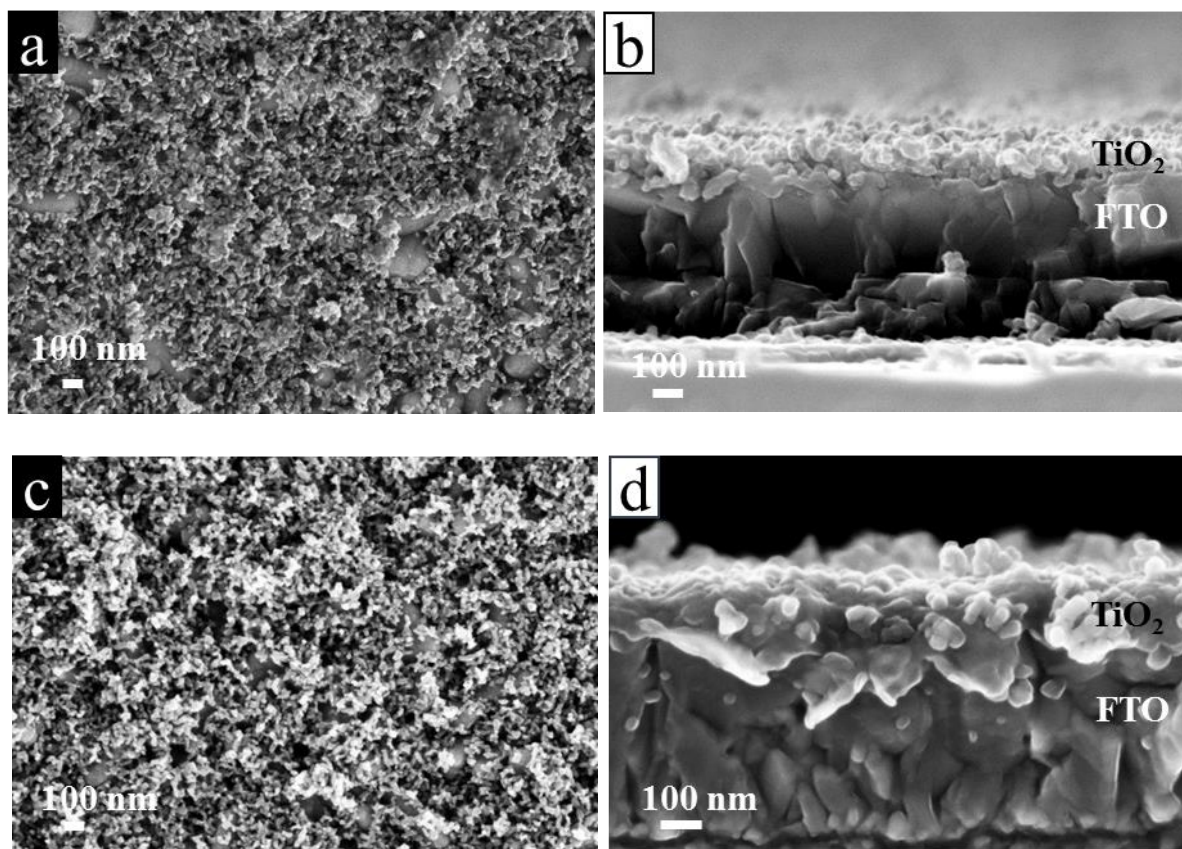
Three different perovskites have been investigated in this chapter: (1) $\text{CH}_3\text{NH}_3\text{PbI}_3$ prepared from precursors dissolved in DMSO. This layer is noted MAPI(1)-SO. (2) A $\text{CH}_3\text{NH}_3\text{PbI}_3$ layer prepared by a technique inspired by Park et al. for which the precursors were dissolved in a mixed DMF and DMSO solvent. This layer is noted MAPI(1)-SOF.. (3) The $\text{FA}_{0.87}\text{MA}_{0.13}\text{Pb}(\text{I}_{0.87}\text{Br}_{0.17})_3$ perovskite is labeled as FAMA. The preparation methods of

MAPI(1)-SO is detailed in Chapter II section II.2.3 and that of FAMA can be found in Chapter IV, section IV-2. The MAPI(1)-SOF used a one-step deposition technique and was synthesized by the following procedure:

- The perovskite solution was prepared by dissolving 461 mg of PbI_2 and 159 mg of MAI in 723 μL N, N-dimethylformamide and 81 μL dimethyl sulfoxide. The molar ratio between PbI_2 and MAI is 1:1. 45 μL of this solution was then spin-coated onto the SnO_2 layer by using a two-step program: spinning at 1000 rpm for 10 s and then at 4000 rpm for 20 s. At 7 s of the second step spinning program, 110 μL of chlorobenzene was slowly dripped onto the rotating substrate before the surface changed to turbid due to the rapid vaporization of DMF. The perovskite film was then heated at 105°C for 1h on a hotplate.

V.3. Effect of the mesoporous TiO_2 layer thickness

In this part, we present the effect of mesoporous TiO_2 thickness on the PSC performances. For this study, we operated various dilutions by ethanol of the NR-30D TiO_2 paste from Dyesol, namely 1:6; 1:8 and 1:10. Increasing the dilution decreased the layer thickness of the mesoporous layer as shown in Figure 5.1.



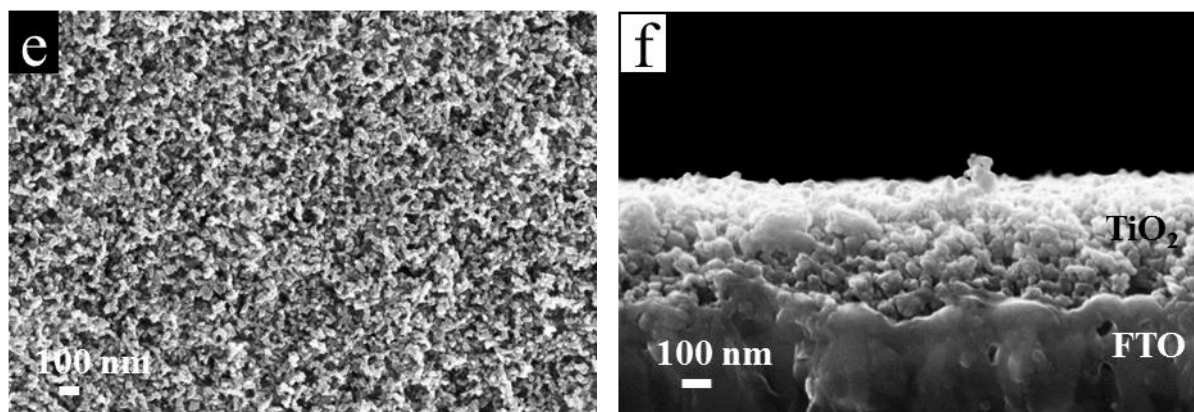


Figure 5.1. SEM views of TiO_2 mesoporous layer prepared using 1:10 (a-b), 1:8 (c-d) and 1:6 (e-f) paste dilutions.

Figure 5.1 shows the morphology of TiO_2 mesoporous layer for various dilutions. The layer for 1:10 dilution was very thin, 80-100 nm and the FTO crystallite tops were almost uncovered (Figure 5.1a and 5.1b). The 1:8 mass ratio led to a good coverage of the FTO surface with the average thickness at 120-140 nm (Figure 5.1c and 5.1d). Finally, the 1:6 mass ratio provided the thickest layer (Figure 5.1e and 5.1f). The average thickness was measured at 230-250 nm. For this thickness, we could not observe the FTO surface anymore.

The J - V curves of MAPI(1)-SO cells with various *meso*- TiO_2 layer thicknesses were measured at various scan rates in the reverse scan directions (from the open circuit to short circuit). They are shown in Figure 5.2. In every case, the curves more or less overlapped for scan rates lower than 0.1 V.s^{-1} . The average PSC performances and J - V parameters are gathered in Table 5.1. The best results were found for the 1:8 mass ratio. The performance change with the *meso*- TiO_2 layer thickness mainly arises from the J_{sc} parameter. We have measured the perovskite layer absorbance spectra of the various samples and Figure 5.2d shows no difference for the various TiO_2 layers. Consequently, the differences in J_{sc} are not due to different light collection, but to a best charge collection and transport for the intermediate *meso*- TiO_2 layer thickness. If the *meso*- TiO_2 layer is too thick, problems of impregnation with the perovskite material can occur and also the charge transport to the contact is more difficult. It explains the lower FF and J_{sc} observed in this case (Table 5.1). A too thin TiO_2 layer is detrimental for the charge collection.

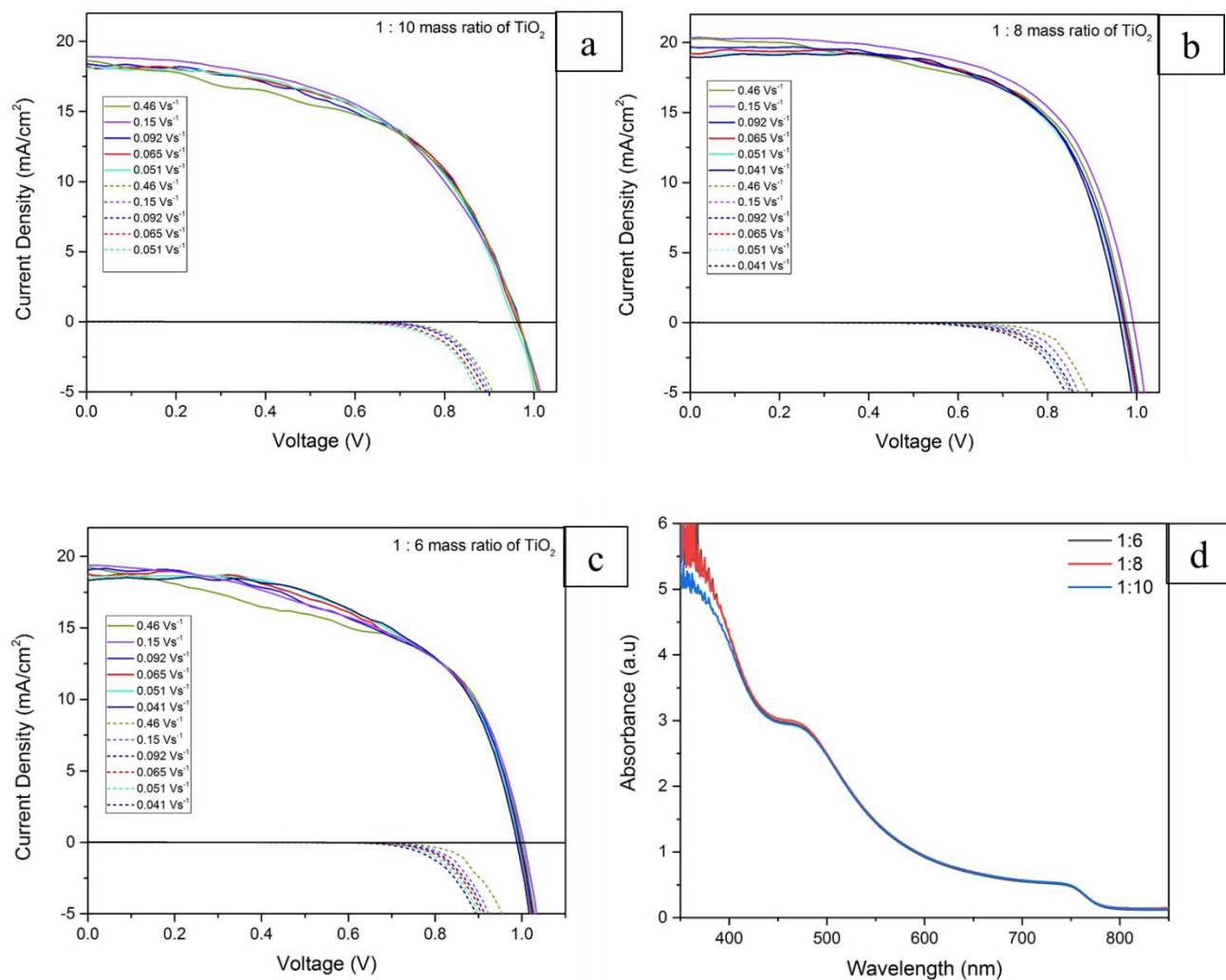


Figure 5.2. J - V curves of MAPI(2) solar cells prepared with various TiO_2 paste dilutions measured at various scan rates in the reverse direction. (a) 1:10 ; (b) 1:8 and (c) 1:6 paste dilutions. The dash lines are the dark currents. (d) Absorbance curve of various TiO_2 dilutions.

Table 5.1. Effect of mesoporous TiO_2 layer thickness on the average J - V curve parameters of MAPI(2) AM 1.5 100 mW/cm^2 illumination).

| Paste dilution | Scan direction | V_{oc} (V) | J_{sc} (mA/cm^2) | FF (%) | PCE (%) |
|----------------|----------------|--------------|--------------------------------------|--------|---------|
| 1:10 | Rev | 0.96 | 19.59 | 60.05 | 11.38 |
| | For | 0.95 | 19.43 | 57.87 | 10.68 |
| 1:8 | Rev | 0.96 | 20.73 | 60.04 | 11.90 |
| | For | 0.95 | 20.07 | 58.63 | 11.19 |
| 1:6 | Rev | 0.92 | 18.29 | 58.80 | 9.72 |
| | For | 0.88 | 18.51 | 52.79 | 8.73 |

TiO₂ is the most popular n-type semiconductor oxide for perovskite solar cells and is employed in a large extent in PSC research. Other oxides have also been investigated in the literature. Properties of several n-type wide bandgap oxides employed in perovskite solar cells are provided in Table 5.2.

Table 5.2. Opto-electronic properties of various n-type wide bandgap oxides used in PSCs.

| N-type Oxide | Main carrier mobility/ $\text{cm}^2 \text{V}^{-1} \text{s}^{-1}$ | Bandgap energy E_g /eV | E_c position/ vacuum |
|----------------------------------|---|-----------------------------|---------------------------|
| TiO ₂ | 0.1 – 4 | 3.2 | -4.0- -4.1 eV |
| ZnO | 20-150 | 3.3 | -4.2 eV |
| SnO ₂ | 3-35 | 3.5 | -4.5 eV |
| Zn ₂ SnO ₄ | 10–30 | 3.8 | -4.1 eV |
| SrTiO ₃ | 5-8 | 3.9 | -3.9 eV |

SnO₂ emerges as the most promising n-type wide bandgap semiconductor to replace TiO₂ in planar PSCs. It has been intensively studied by several groups and high performances have been reported [4]–[14]. These results are due to the properties of SnO₂ which has a wider bandgap, a lower conduction band energy, lower surface defects and a higher electron mobility compared to TiO₂ oxide. Because of its interesting properties, I have investigated a planar PSCs structure using SnO₂. These cells have been compared with planar devices using the TiO₂ blocking layer (*bl*-TiO₂) prepared by spray pyrolysis. In order to well-understand the working of this blocking layer, we have also investigated benchmark *bl*-TiO₂/*meso*-TiO₂ based solar cells (*meso*-TiO₂). The study of planar solar cells and the comparison with *meso*-TiO₂ will be presented in the last part of this chapter. Before, we detail our work for the optimization of the SnO₂ layer.

V.4. Optimization of the SnO₂ solar cells

In this section, we present the optimization of the SnO₂ solar cells. The optimized parameters are: the TCO (ITO/FTO), the perovskite, the preparation of SnO₂ (colloidal solution dilution, annealing temperature, annealing time and number of coating layer).

V.4.1. The TCO

In the literature, high-efficiency SnO₂ perovskite solar cells have been prepared either on ITO by Jiang et al. [6] or on FTO substrate by Anaraki et al. [12]. We have characterized both

substrates by SEM and AFM (Figure 5.3 and Figure 5.4) (the SEM and AFM imaging in section V.4 and V.5 have been performed by Sébastien Peralta, Laboratoire de Physico-chimie des Polymères et Interfaces (LPPI), Université de Cergy-Pontoise).

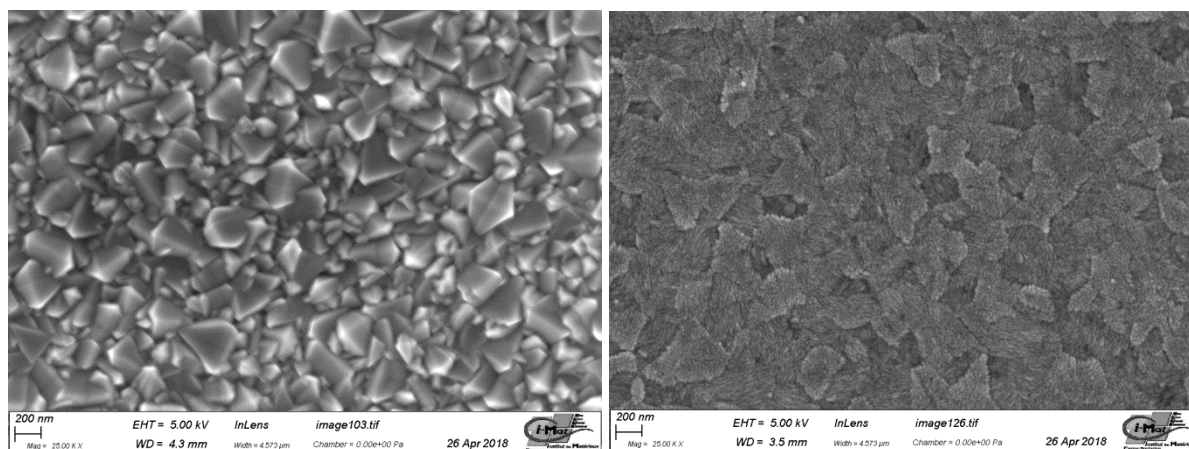


Figure 5.3. SEM views of FTO (left) and ITO (right).

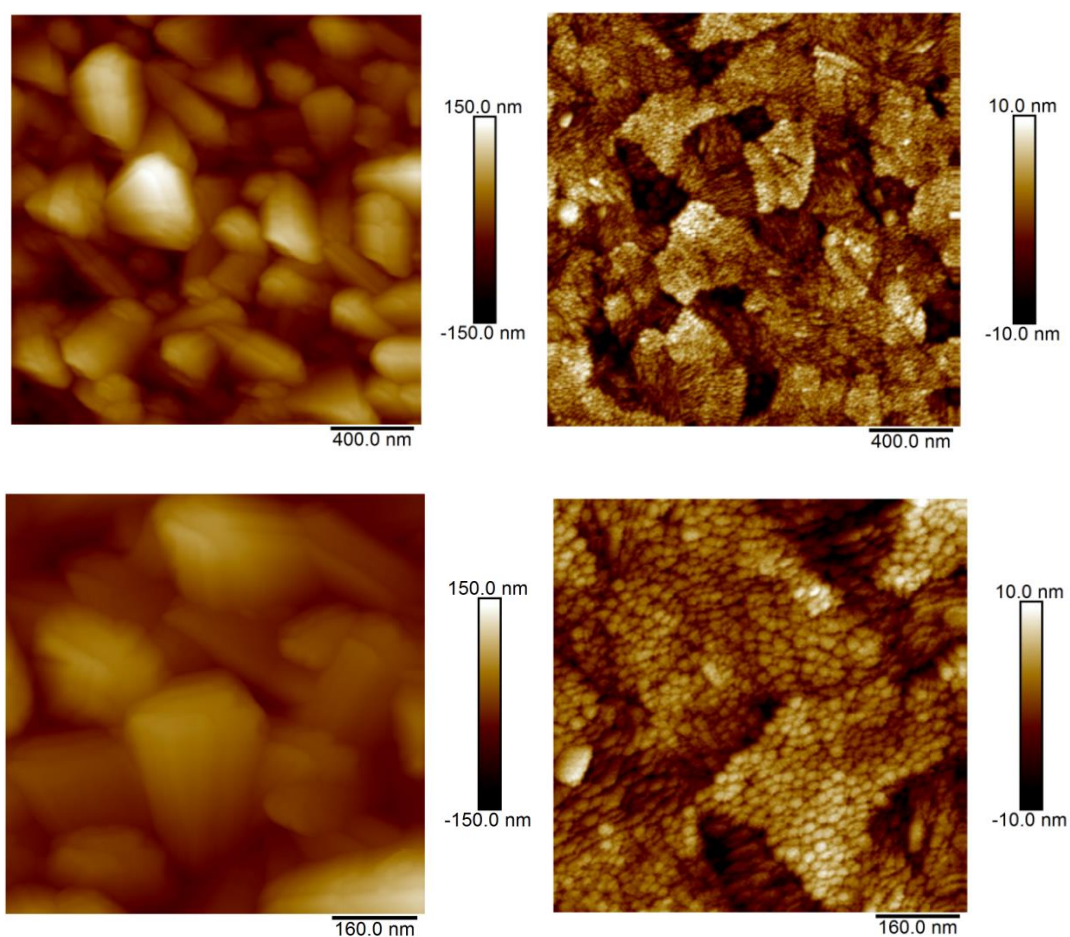


Figure 5.4. AFM views of FTO (left) and ITO (right).

Figures 5.3 and 5.4 show that the two substrates have a very different morphology. The FTO is made of large merged crystal grains. Their mean size is determined at 150-200 nm and both

SEM and AFM images are in agreement. The layer is rough with an RMS roughness estimated at 39 nm by AFM. On the other hand, the ITO layer is smooth with a measured RMS roughness at 3.5 nm, moreover, there is no crystal observed by SEM. Interestingly, the high magnification AFM images show that the layer is made of assembled and merged nanoparticles which mean size is estimated at about 20-25 nm.

The effect of the TCO substrate on J - V curve parameters is shown in Table 5.3. This optimization was done on SnO_2 , 1-time coating, annealed at 123°C for 30 min. The cells using ITO are characterized by a lower J_{sc} compared to FTO which suggests a problem of charge transfer and collection, consequently, higher PCE is found for FTO. Whereas the FTO (TEC7) used in our study is the same as the employed in high-efficiency TiO_2 PSCs, it is likely that our ITO is not optimum for the application even it has $10\Omega/\text{square}$ resistance. Also maybe an additional treatment such UV-Ozone is necessary to get high performance with this substrate.

Table 5.3. Summary of J - V parameters of two different TCO substrates.

| TCO | Perovskite | Direction | V_{oc} (V) | J_{sc} ($\text{mA}\cdot\text{cm}^{-2}$) | FF (%) | PCE (%) |
|-----|------------|-----------|---------------------|--|--------|---------|
| FTO | MAPI(1)-SO | Reverse | 0.65 | 18.00 | 44.82 | 5.30 |
| | | Forward | 0.69 | 17.90 | 46.43 | 5.75 |
| | FAMA | Reverse | 1.00 | 18.98 | 63.17 | 12.02 |
| | | Forward | 0.95 | 18.98 | 48.55 | 8.76 |
| ITO | MAPI(1)-SO | Reverse | 0.84 | 13.04 | 45.36 | 4.95 |
| | | Forward | 0.84 | 12.96 | 45.23 | 4.95 |
| | FAMA | Reverse | 0.99 | 14.82 | 64.67 | 9.50 |
| | | Forward | 0.97 | 14.28 | 49.23 | 6.96 |

We have measured the absorbance spectra of the substrates before and after deposition of the SnO_2 layer. In Figure 5.5, we can see that the glass/ITO substrate is more transparent than the glass/FTO one. The curves after the deposition of SnO_2 are very close to those of the substrates because SnO_2 is a wide bandgap semiconductor.

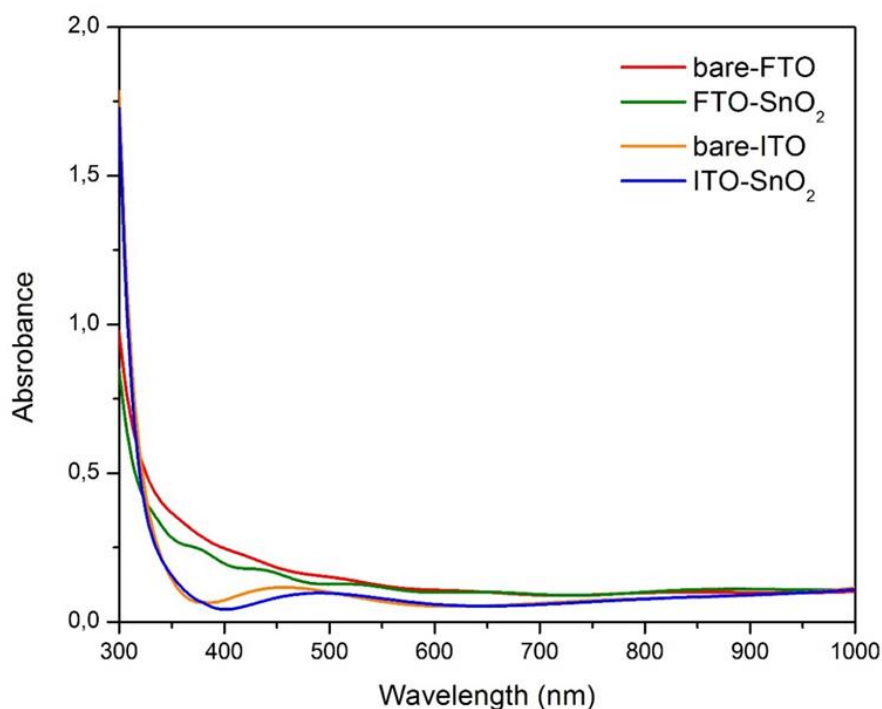


Figure 5.5. Absorbance curves of SnO₂ deposited on two different substrates.

V.4.2. The perovskite

V.4.2a. Comparison of MAPI and FAMA

Our group has developed and optimized the preparation techniques of MAPI by one and two-step deposition method (see Chapter II), as well as the one-step synthesis of multiple cation hybrid perovskites (HPs) (see Chapter IV). In this section, we compare MAPI(1)-SO, MAPI(1)-SOF, and FAMA combined with the SnO₂ electron transport layer (ETL). All HPs were synthesized by a one-step technique in which dripping with chlorobenzene anti-solvent was used to trigger the crystallization. Table 5.3 shows that MAPI(1)-SO does not give good performances. However, we tested another preparation technique of MAPI inspired by Park et al. which is hereafter noted MAPI(1)-SOF. The results of the devices based on MAPI(1)-SO and MAPI(1)-SOF combined with SnO₂ ETL are summarized in Table 5.4.

Table 5.4. *J-V* parameters of SnO₂ solar cells with MAPI(1)-SO and MAPI(1)-SOF.

| TCO | Perovskite | Direction | V _{oc} (V) | J _{sc} (mA.cm ⁻²) | FF (%) | PCE (%) |
|-----|-------------|-----------|---------------------|--|--------------|--------------|
| FTO | MAPI(1)-SO | Max (Rev) | 0.69 | 18.16 | 46.72 | 5.91 |
| | | Max (For) | 0.70 | 18.1 | 51.35 | 6.53 |
| | | Avg (Rev) | 0.65 | 18.00 | 44.82 | 5.30 |
| | | Avg (For) | 0.69 | 17.90 | 46.43 | 5.75 |
| | MAPI(1)-SOF | Max (Rev) | 1.01 | 21.92 | 68.84 | 15.28 |
| | | Max (For) | 0.97 | 21.98 | 56.40 | 12.08 |
| | | Avg (Rev) | 1.01 | 20.25 | 62.22 | 12.71 |
| | | Avg (For) | 0.97 | 20.91 | 52.02 | 10.50 |

Number of cells averaged is 5 cells.

This technique of MAPI preparation has given much better solar cell performances. We can suppose a better band alignment between MAPI(1)-SOF and SnO₂ which allows better charge electron transfer. The three *J-V* parameters are improved with MAPI(1)-SOF.

V.4.2b. Optimization of FAMA in SnO₂ cells

Various concentrations of FAMA precursor solution have been tested. The solution was stirred for 1h prior to the layer preparation. The 2.35% of the SnO₂ solution and 2-times coating was used in this investigation. The results of perovskite solar cell performances for various concentration of FAMA are gathered in Table 5.5.

Table 5.5. *J-V* parameters of SnO₂ PSC for various FAMA precursor solution concentrations.

| TCO | Perovskite concentration | Direction | V _{oc} (V) | J _{sc} (mA.cm ⁻²) | FF (%) | PCE (%) |
|-----|--------------------------|-----------|---------------------|--|--------------|--------------|
| FTO | 1.35 M 6000 rpm | Max (Rev) | 1.00 | 21.21 | 73.37 | 15.59 |
| | | Max (For) | 0.99 | 21.23 | 66.29 | 14.00 |
| | | Avg (Rev) | 1.00 | 20.91 | 70.00 | 14.58 |
| | | Avg (For) | 0.99 | 20.91 | 65.12 | 13.46 |
| | 1.35 M 4000 rpm | Max (Rev) | 1.02 | 18.12 | 72.73 | 13.45 |
| | | Max (For) | 1.01 | 18.14 | 62.32 | 11.45 |
| | | Avg (Rev) | 0.95 | 20.08 | 61.62 | 11.62 |

| | | | | | | |
|--|-------------------|------------------|-------------|--------------|--------------|--------------|
| | 1.5 M 6000 rpm | Avg (For) | 0.93 | 20.05 | 51.34 | 9.47 |
| | | Max (Rev) | 1.02 | 23.47 | 72.93 | 17.54 |
| | | Max (For) | 1.01 | 23.48 | 67.33 | 16.00 |
| | | Avg (Rev) | 1.01 | 22.00 | 72.69 | 16.22 |
| | | Avg (For) | 1.00 | 22.01 | 67.06 | 14.77 |
| | 1.7 M 6000 rpm | Max (Rev) | 0.93 | 2.99 | 38.02 | 1.05 |
| | | Max (For) | 0.90 | 2.93 | 36.92 | 0.97 |
| | | Avg (Rev) | 0.91 | 2.33 | 37.21 | 0.79 |
| | | Avg (For) | 0.87 | 2.30 | 38.42 | 0.76 |

Number of cells averaged is 5 cells.

The FAMA cells exhibit better performances than the MAPI ones. The best performances have been measured for the spin coating speed of 6000 rpm and spinning at a lower speed is detrimental for the device performances and the reproducibility. Increasing the precursor concentration is beneficial for the cells performances. At 1.5 M a highest PCE at 17.54% has been achieved with rather a low hysteresis. Meanwhile, very poor cell performances are found at 1.7 M of concentration where the solubility limit of the precursor is surpassed. We can suspect that undissolved powders are present which is signed by the red color of the perovskite film (see Figure 5.6).

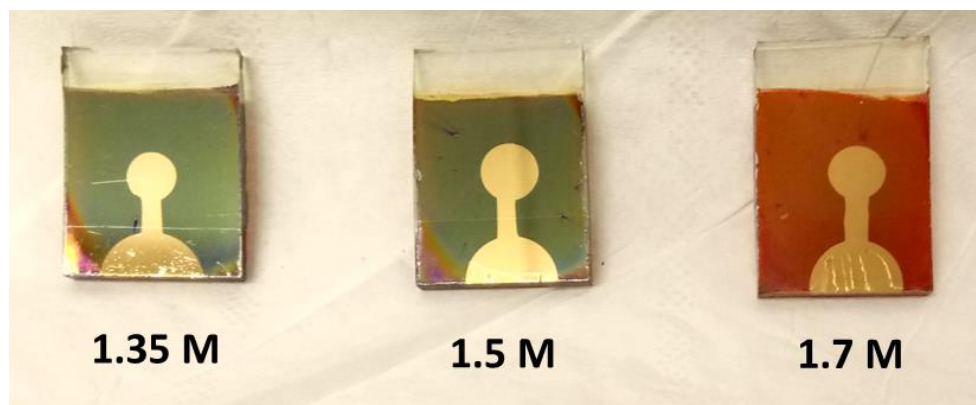


Figure 5.6. Perovskite solar cells devices with various perovskite molarities.

V.4.3. The SnO₂ preparation

The oxide blocking layer is a key component of the PSC to reach high efficiency. It must act as an efficient barrier between the transparent conducting oxide (TCO) and the perovskite to avoid the transfer of hole and then the recombination with the photogenerated electrons. Therefore this layer must well-cover the TCO layer, be pinhole- and crack-free, electrically

conductive and transparent to the visible and near-infrared light. On the other hand, this layer must be thin enough to limit the device series resistance. In the present work spin-coating was chosen as a low-temperature preparation technique. This technique is rather easy to implement, being performed under ambient conditions, using precursor dissolved in solution. At the first stage of the study, the process has been optimized for the application.

V.4.3a. The concentration of the SnO₂ colloidal solution

The layer has been prepared using a commercial solution of tin (IV) oxide (15% in H₂O) from Alfa Aesar. The concentration was adjusted by dilution in H₂O. Three different concentrations have been investigated: 2.35%, 4%, and 5.71%. The perovskite solar cells performances are summarized in Table 5.6.

Table 5.6. Summary of *J-V* parameters of various SnO₂ solution.

| Dilution | Scan direction | V _{oc} (V) | J _{sc} (mA.cm ⁻²) | FF (%) | PCE (%) |
|---------------------|----------------|---------------------|--|--------|---------|
| 2.35% | Avg (Rev) | 0.98 | 15.25 | 39.37 | 5.87 |
| | Avg (For) | 0.91 | 15.59 | 24.87 | 3.54 |
| 2.35% 2-coatings | Avg (Rev) | 1.05 | 23.03 | 75.44 | 18.22 |
| | Avg (For) | 1.04 | 23.02 | 71.21 | 17.03 |
| 4% | Avg (Rev) | 1.01 | 19.14 | 61.26 | 11.91 |
| | Avg (For) | 1.01 | 19.09 | 48.92 | 9.55 |
| 5.71% | Avg (Rev) | 1.02 | 20.67 | 72.55 | 15.24 |
| | Avg (For) | 1.03 | 20.71 | 61.10 | 12.98 |

Number of cells averaged is 5 cells.

Table 5.6 shows that increasing the dilution is detrimental to the efficiency and that the solar cell efficiency for a 2.35% dilution is very poor. The optimum thickness of SnO₂ was found at 2.35% dilution with 2-times coating that reached 18.22% with very low hysteresis compared to the other dilutions.

V.4.3b. Annealing temperature and time

The annealing temperature was studied for 30 min and 3h and three different temperatures were used in this study: 123°C, 195°C, and 350°C. The averaged cell *J-V* parameters and efficiencies are gathered in Table 5.7.

Table 5.7. Effect of annealing temperature and time of the SnO₂ layer on the *J-V* curve parameters.

| Annealing time | Annealing temperature | Scan direction | V _{oc} (V) | J _{sc} (mA.cm ⁻²) | FF (%) | PCE (%) |
|----------------|-----------------------|----------------|---------------------|--|--------|-------------|
| 30 min | 123°C | Max (Rev) | 1.00 | 20.41 | 71.18 | 14.55 |
| | | Max (For) | 1.01 | 20.44 | 61.03 | 12.62 |
| | | Avg (Rev) | 1.00 | 19.86 | 71.06 | 14.16(0.43) |
| | | Avg (For) | 1.01 | 19.86 | 61.79 | 12.41(0.17) |
| | 195°C | Max (Rev) | 1.04 | 21.45 | 72.08 | 16.14 |
| | | Max (For) | 1.05 | 21.5 | 63.72 | 14.44 |
| | | Avg (Rev) | 1.01 | 20.78 | 62.84 | 13.28(2.43) |
| | | Avg (For) | 1.02 | 20.69 | 57.77 | 12.25(2.30) |
| | 350°C | Max (Rev) | 1.01 | 22.65 | 51.39 | 11.80 |
| | | Max (For) | 0.94 | 22.49 | 46.56 | 9.81 |
| | | Avg (Rev) | 1.03 | 19.45 | 55.37 | 10.91 |
| | | Avg (For) | 0.94 | 22.48 | 46.56 | 9.81 |
| 3 h | 123°C | Max (Rev) | 1.05 | 23.03 | 75.44 | 18.22 |
| | | Max (For) | 1.04 | 23.02 | 71.21 | 17.03 |
| | | Avg (Rev) | 1.04 | 22.79 | 72.61 | 17.18 |
| | | Avg (For) | 1.03 | 22.76 | 68.19 | 16.06 |
| | 195°C | Max (Rev) | 1.02 | 23.28 | 66.10 | 15.73 |
| | | Max (For) | 0.99 | 23.34 | 56.12 | 12.98 |
| | | Avg (Rev) | 1.03 | 20.63 | 58.82 | 12.44(0.15) |
| | | Avg (For) | 1.03 | 20.26 | 58.28 | 12.14(0.44) |
| | 350°C | Max (Rev) | 1.04 | 24.06 | 63.57 | 15.98 |
| | | Max (For) | 1.00 | 24.08 | 56.37 | 13.56 |
| | | Avg (Rev) | 1.02 | 23.54 | 62.50 | 15.09 |
| | | Avg (For) | 0.96 | 23.51 | 55.92 | 12.70 |

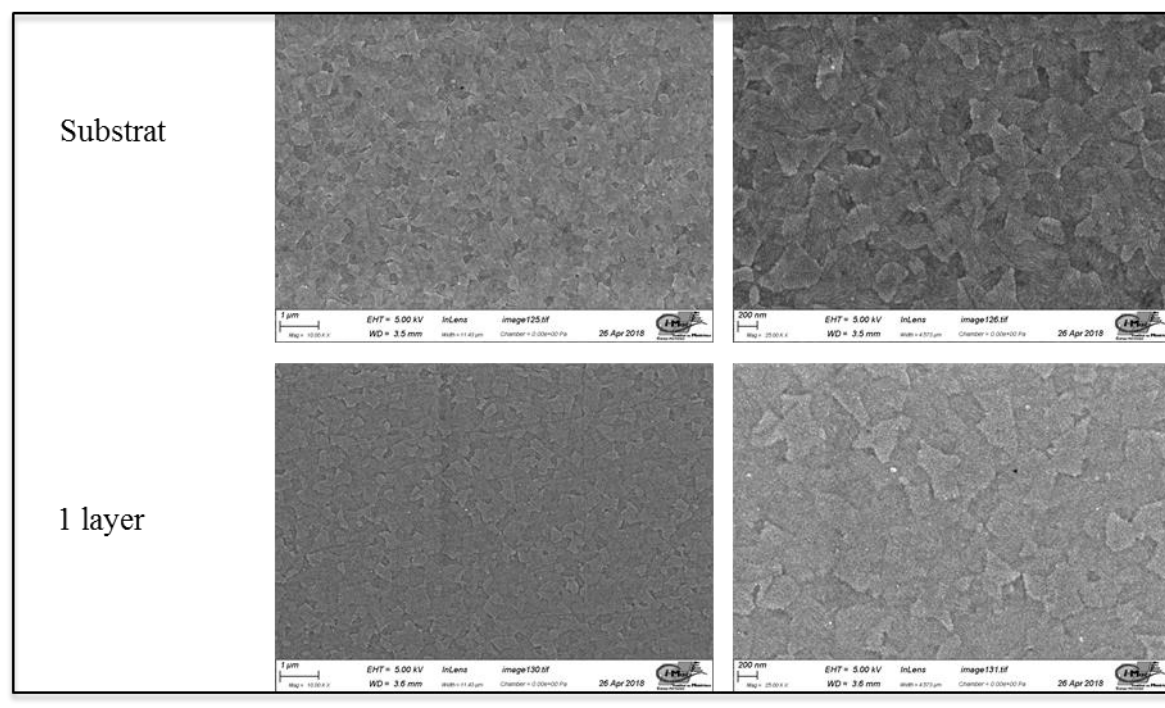
In the brackets are standard deviation. Number of cells averaged is 10 cells.

Better efficiencies are found after 3h of annealing time which might be due to a better sintering, water elimination and crystallization. The highest efficiency is achieved when the annealing temperature is 123°C and the best result is at 123°C for 3h annealing time.

V.4.3c. Number of coatings

The morphology of the SnO₂ layer for various numbers of coatings (spinnings) has been investigated by SEM and AFM. The number of coating was varied from 1 to 4 times and it has been tested for ITO and FTO substrates. The results are shown below for the glass /ITO and the glass/FTO substrates (Figure 5.7-5.10).

ITO



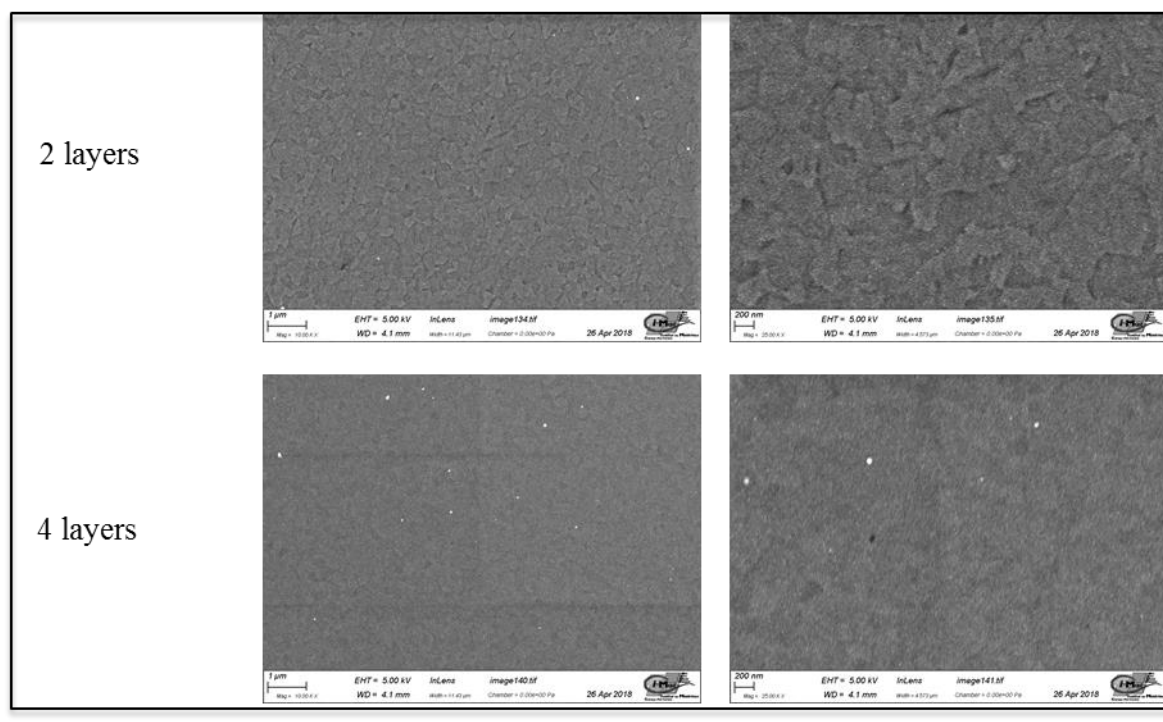
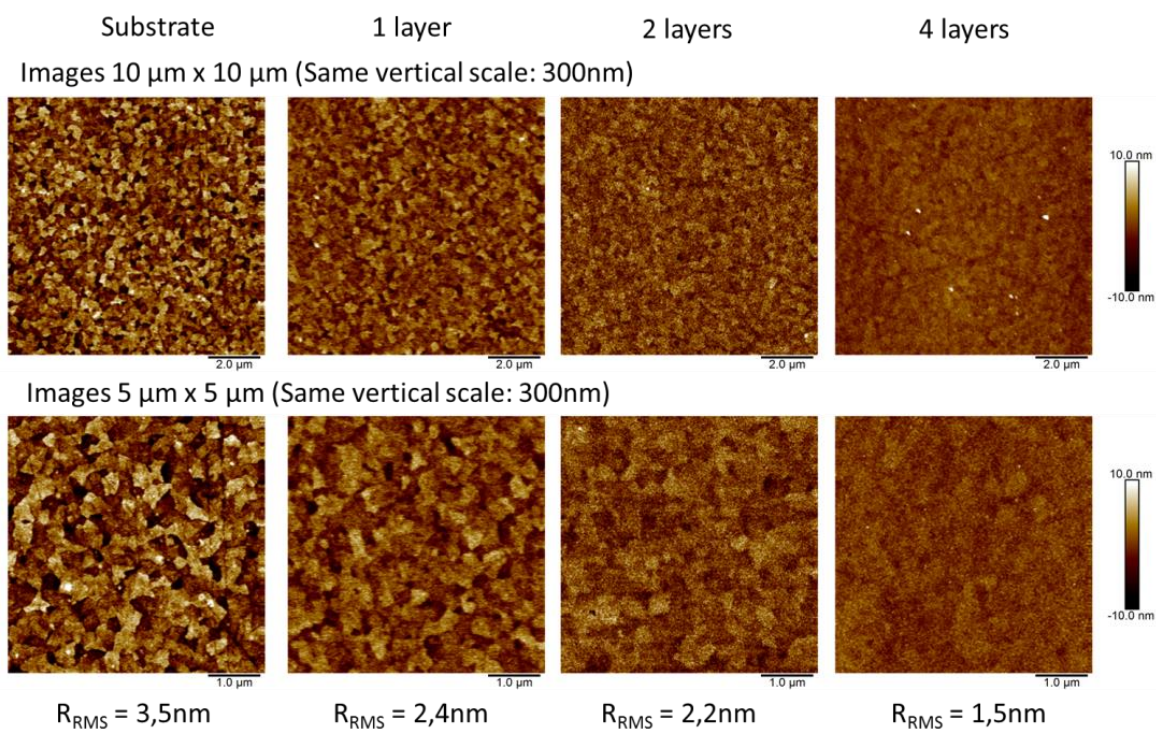


Figure 5.7. SEM-top view of various coating number of SnO₂ layer deposited on the glass/ITO substrate.



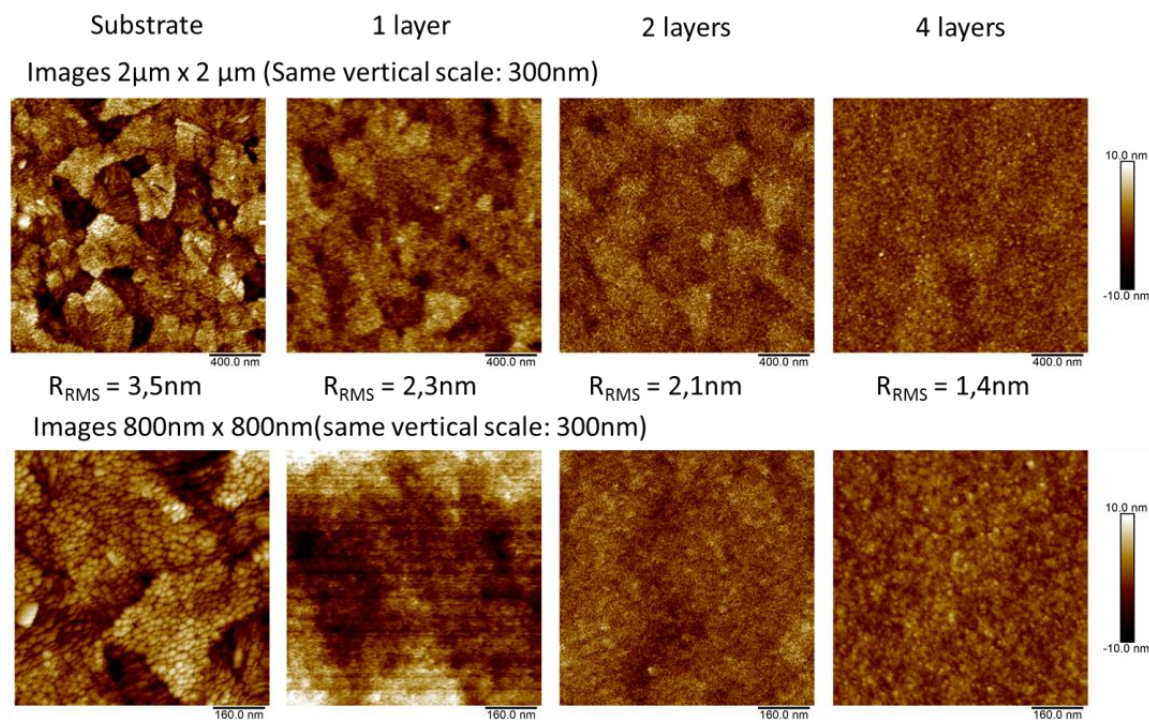


Figure 5.8. AFM images of various coating number of SnO_2 layer deposited on the glass/ITO substrate.

FTO

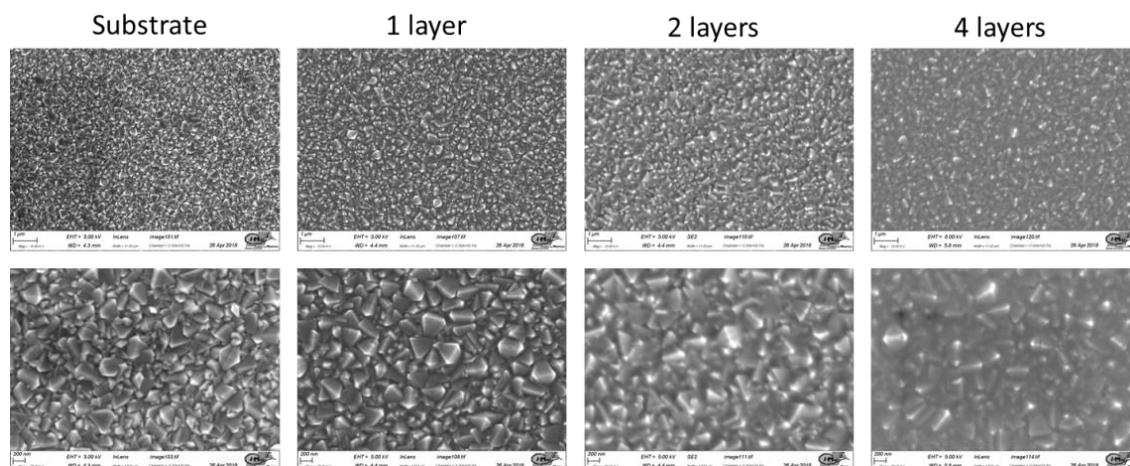


Figure 5.9. SEM-top view of various coating number of SnO_2 layer deposited on the glass/FTO substrate.

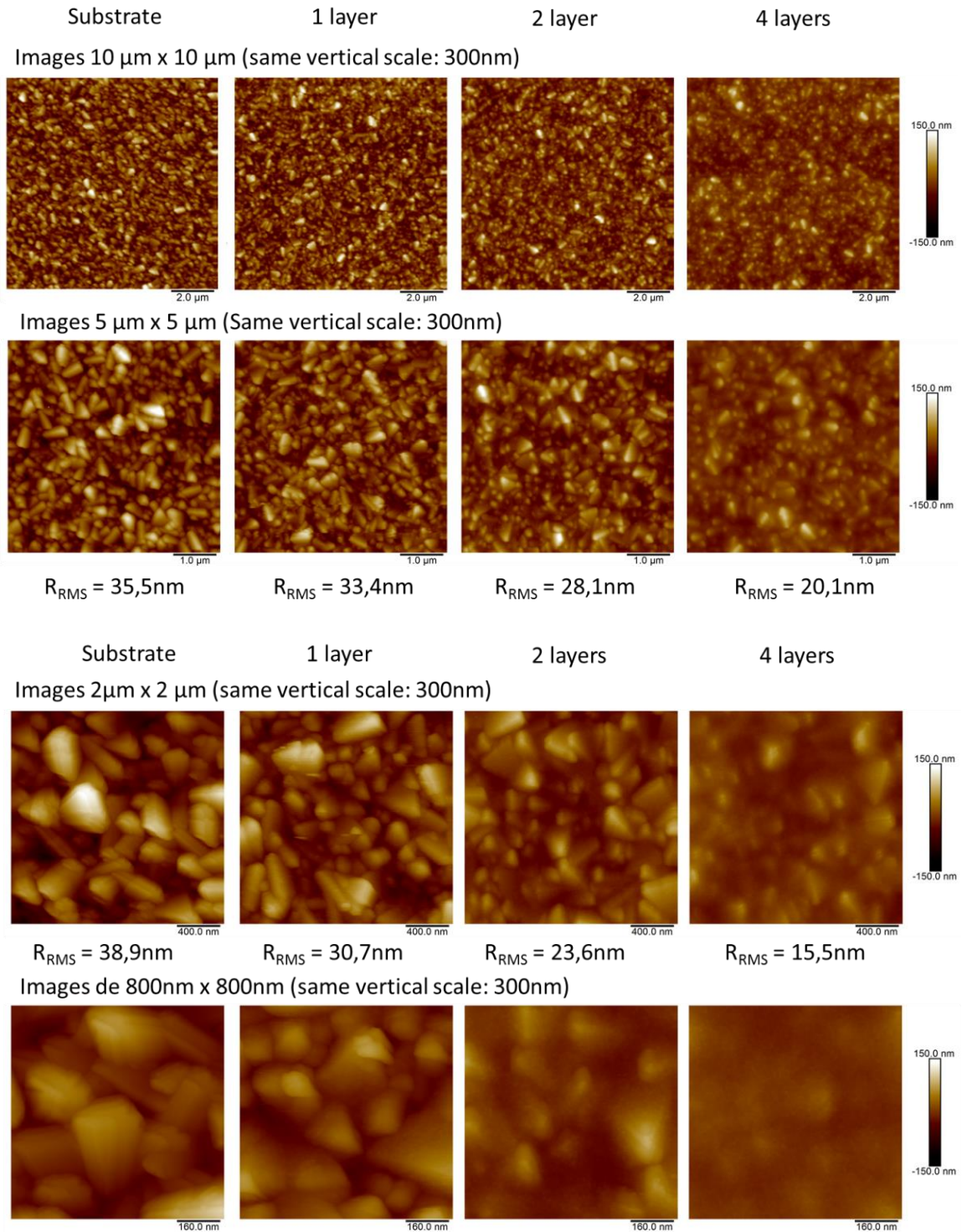


Figure 5.10. AFM images of various coating number of SnO_2 layer deposited on the glass/FTO substrate.

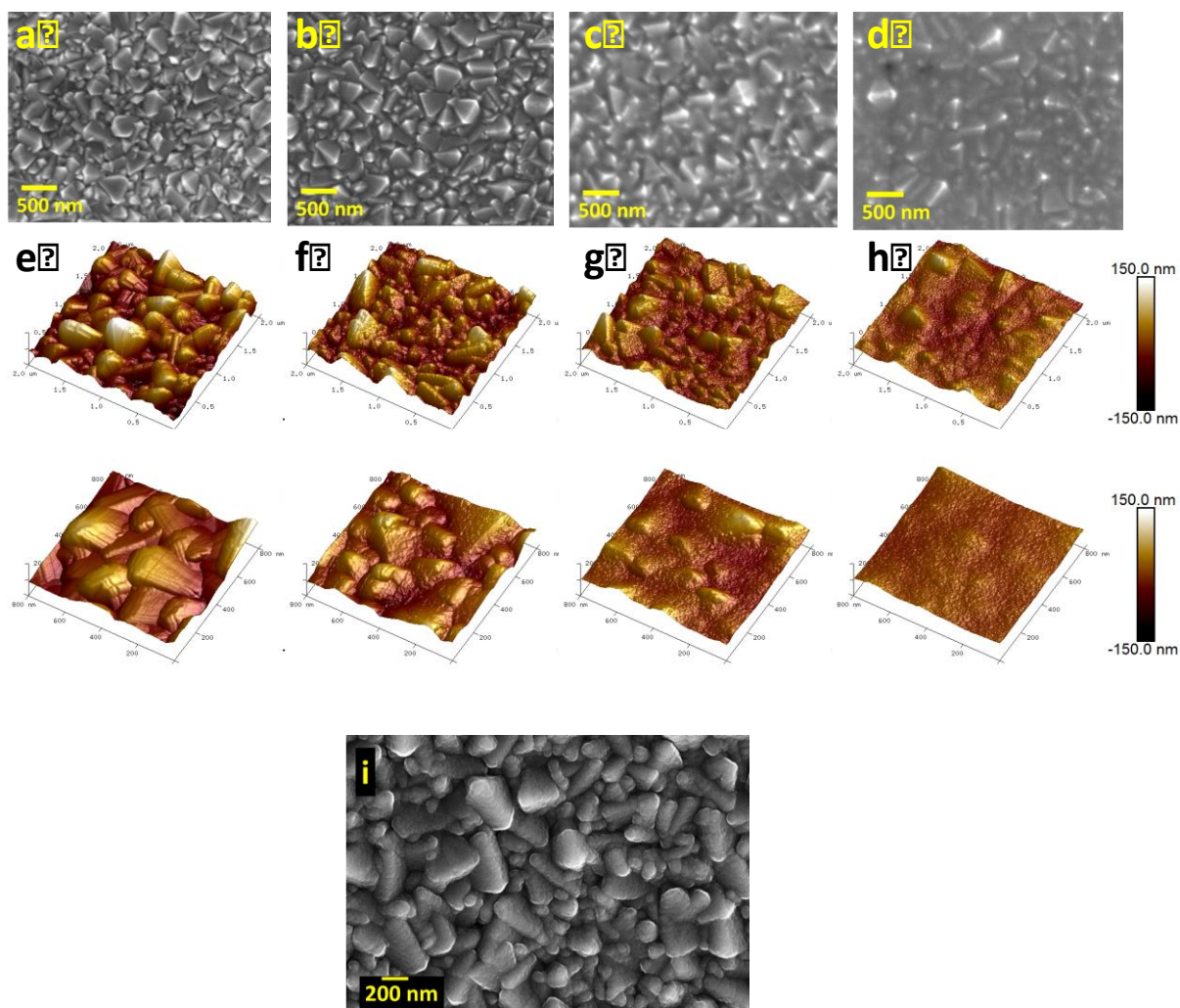


Figure 5.11. (a-d) SEM top view of the bare FTO substrate (a) and after 1 (b), 2 (c) and 4 (d) SnO₂ spin-coating step (4.5 μm x 3.5 μm). (e-h) AFM images of the bare FTO substrate (e) and after 1 (f), 2 (g) and 4 (h) SnO₂ spin-coating steps. (top) : 2 μm x 2 μm image; (bottom): 800 nm x 800 nm image (the vertical scale was 300 nm for all images). (i) SEM top view of the sprayed TiO₂ layer (*spr*-TiO₂).

As described in section (V.4.1), the ITO layer had a smooth morphology and was made of small crystallites. A smoothing effect was found with the increasing number of spin-coating. The roughness decreased from 3.5 nm to 1.4 nm between the bare ITO and the 4 coatings layer.

The FTO substrate was rather rough (see section V.4.1). Increasing the number of deposition steps increased the coating and the coverage of the substrate. After one coating, the aspect of the surface did not change significantly and the deposited layer was very thin. The FTO underlayer became less visible and was covered by a featureless layer of SnO₂ for 2-coatings. For 4-coatings, the surface has smoothed and only the top of the underlying FTO grains could still be seen. The roughness decreased from 38.9 nm to 15.5 nm by increasing the number of coating. It is noteworthy that all the layers were crack-free.

The morphology of the SnO₂ coatings was further characterized by AFM. The pictures are shown in Figure 5.11 (e-h). The deposition of the SnO₂ layer occurred preferentially at the troughs of the FTO grains. Consequently, the relief of the FTO underlayer disappeared gradually with the number of SnO₂ spin coating step. This effect has been quantified by the AFM measuring of the change in the roughness, ρ , defined as the ratio between the scanned surfaced over projected geometrical area. The data are gathered in Table 5.8. It decreases from 1.215 for the initial FTO to 1.056 for the 4-coatings sample. A similar trend is found with the root-mean square (RMS) roughness measured by AFM and reported in Table 5.8.

Table 5.8. Roughness parameters measured by AFM for the FTO/glass substrate before and after different numbers of SnO₂ coatings.

| Number of SnO ₂ coatings | ρ | R _{rms} (nm) |
|-------------------------------------|--------|-----------------------|
| 0 | 1.215 | 38.9 |
| 1 | 1.209 | 30.7 |
| 2 | 1.118 | 23.6 |
| 4 | 1.056 | 15.5 |

The effect of the number of coating on PSC performances has been measured and the results are reported in Table 5.9.

Table 5.9. Effect of the SnO₂ coating numbers on the PSC of *J-V* parameters.

| TCO | Number of coatings | Scan direction | | V _{oc} (V) | J _{sc} (mA.cm ⁻²) | FF (%) | PCE (%) |
|-----|--------------------|----------------|-----|---------------------|--|--------|---------|
| FTO | 1 time | Rev | Max | 1.00 | 20.34 | 72.01 | 14.67 |
| | | For | Max | 1.01 | 20.32 | 53.07 | 10.90 |
| | | Rev | Avg | 1.01 | 20.97 | 64.42 | 13.64 |
| | | For | Avg | 0.87 | 20.22 | 43.59 | 7.87 |
| | 2 times | Rev | Max | 1.03 | 20.80 | 71.88 | 15.53 |
| | | For | Max | 1.04 | 20.72 | 64.39 | 13.93 |
| | | Rev | Avg | 1.03 | 21.21 | 68.04 | 14.82 |
| | | For | Avg | 1.04 | 21.09 | 59.85 | 13.06 |
| | 3 times | Rev | Max | 1.04 | 19.59 | 68.06 | 13.98 |
| | | For | Max | 1.05 | 19.58 | 65.07 | 13.40 |

| | | | | | | | |
|-----|---------|------------|------------|-------------|--------------|--------------|--------------|
| | | Rev | Avg | 1.03 | 18.99 | 61.74 | 12.19 |
| | | For | Avg | 1.03 | 18.95 | 53.94 | 10.67 |
| | 4 times | Rev | Max | 1.03 | 18.44 | 66.99 | 12.77 |
| | | For | Max | 1.03 | 18.48 | 63.61 | 12.21 |
| | | Rev | Avg | 1.00 | 17.93 | 56.93 | 10.29 |
| | | For | Avg | 1.02 | 18.28 | 55.46 | 10.35 |
| | 1 time | Rev | Max | 1.03 | 15.79 | 76.47 | 12.52 |
| | | For | Max | 1.02 | 15.83 | 73.04 | 11.80 |
| | | Rev | Avg | 1.02 | 15.14 | 64.46 | 10.02 |
| | | For | Avg | 1.01 | 14.86 | 58.10 | 8.88 |
| ITO | 2 times | Rev | Max | 1.00 | 16.24 | 79.85 | 13.02 |
| | | For | Max | 1.00 | 16.24 | 72.87 | 11.89 |
| | | Rev | Avg | 1.02 | 15.73 | 74.03 | 11.84 |
| | | For | Avg | 1.01 | 15.75 | 68.46 | 10.89 |
| | 3 times | Rev | Max | 1.05 | 15.76 | 77.84 | 12.86 |
| | | For | Max | 1.02 | 15.95 | 75.13 | 12.23 |
| | | Rev | Avg | 1.04 | 15.78 | 75.37 | 12.36 |
| | | For | Avg | 1.06 | 15.50 | 70.44 | 11.52 |
| | 4 times | Rev | Max | 1.05 | 15.53 | 76.60 | 12.52 |
| | | For | Max | 1.05 | 15.52 | 72.87 | 11.89 |
| | | Rev | Avg | 1.04 | 15.65 | 71.31 | 11.66 |
| | | For | Avg | 0.96 | 14.29 | 70.90 | 9.87 |

Table 5.9 shows that the J_{sc} of ITO cells were lower than those of the FTO cells. With one coating the efficiency of FTO cells was relatively high, the hysteresis between the reverse and forward J - V curve scans was high and the performances showed dispersion. This behavior is explained by the presence of pinholes and of the not fully covering characteristic of the SnO_2 layer. For 3 and 4 coatings of SnO_2 , the cells showed a small hysteresis but the efficiency tend to decrease by increasing the number of coating time. The best result was found for 2-coatings with the highest efficiency and low hysteresis. This result is in line with the literature report of low performances for too thick or too thin SnO_2 layers [18].

For the ITO cells, the V_{oc} and J_{sc} did not markedly depend on the number of coatings. This parameter affected the FF with the best FF and PCE values for the 2-times coating while the lowest hysteresis was found for 3-times coatings. The best efficiency reached only 13.02 % with the glass/ITO substrate. We have also noted that when the glass/ITO substrate is used,

the second J-V measurement is better than the first one. As mentioned before, it is probable that the ITO used in the present work is not the best for the application.

V.5. Study of planar perovskite solar cells: A comparative study of SnO_2 and TiO_2

In this part, we compare planar FTO/ SnO_2 /FAMA solar cells with planar FTO/ TiO_2 /FAMA solar cells. The SnO_2 layer employed was the one optimized in section V.4.3 (2-times spinning , 2.35% dilution, annealing 3h at 123°C) For further discussion of the HP effect, FTO/ SnO_2 /MAPI(1)-SOF cells have also been studied. We also provide insights into the effect of the mesoporous oxide layer on the cell functioning and performances.

V.5.1. Optical characterization

The optical properties of the oxide layers were characterized by measuring their absorbance curves. Figure 5.12a compares the SnO_2 layer with the *spr*- TiO_2 layer and *spr*- TiO_2 /*meso*- TiO_2 bilayer. The absorbance of the SnO_2 layer was close to the substrate FTO/glass sample and its absorption edge was located below 350 nm. These samples were highly transparent over the visible/near infrared wavelength spectral range. On the other hand, the sprayed TiO_2 had an absorption edge red-shifted compared to the SnO_2 layer due to the lower bandgap of TiO_2 . The absorbance edge analysis resulted in an indirect bandgap of *spr*- TiO_2 measured at 3.45 eV (see Figure 5.12b). In Figure 5.12a, the *spr*- TiO_2 /*meso*- TiO_2 bilayer absorbance spectrum presents a lower absorbance in the visible region due to less diffuse light and more specular transmission. The absorption edge is slightly shifted and the Tauc analysis in Figure 5.12b gives an optical bandgap at 3.15 eV.

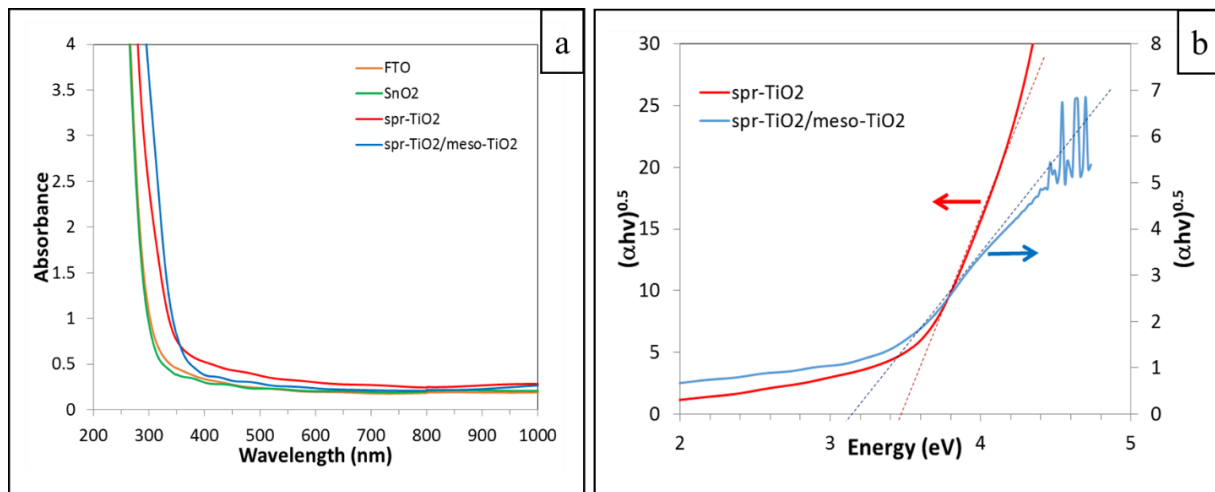


Figure 5.12. (a) Absorbance curves of different oxide layers deposited on FTO substrates and (b) Tauc's plot of *spr*- TiO_2 and *spr*- TiO_2 /*meso*- TiO_2 absorbance curves.

We have then characterized the absorbance of the FAMA perovskite layer deposited on these various oxides and of MAPI(1)-SOF perovskite deposited on SnO_2 . We observed that the presence of *meso*- TiO_2 does not increase the absorbance of the FAMA perovskite and then the absorbant loading.

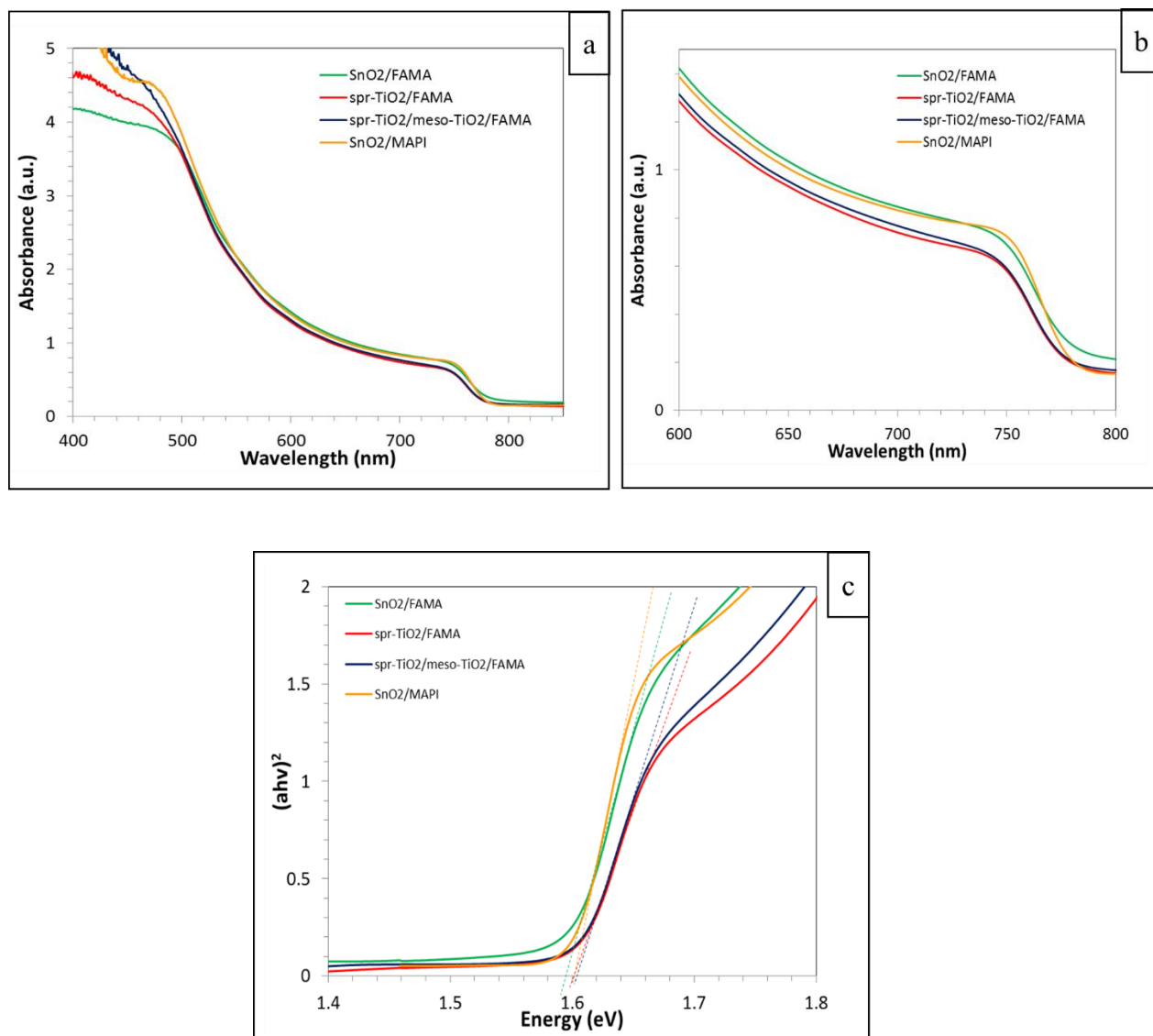


Figure 5.13. (a) Absorbance spectra, (b) absorption edge zoom-view and (c) Tauc's plot of FAMA and MAPI(1)-SOF prepared on various oxide layers.

The absorbance spectra of FAMA and MAPI(1)-SOF deposited on various oxide substrates are shown in Figure 5.13a. The organo-lead halide compounds absorb across the whole visible region with an edge at 780 nm. Figure 5.13a shows that FAMA is slightly more absorbing when prepared on the SnO_2 underlayer compared to the TiO_2 ones. The main difference between the spectra occurs below 500 nm. We also observe that the MAPI(1)-SOF absorbance curve is close to that of the FAMA curves. A zoom view of the absorption edge

shows a slightly steeper edge in the case of MAPI(1)-SOF compared to FAMA (Figure 5.13b). The Tauc plot gives a direct optical bandgap (E_g) at 1.59 eV-1.60 eV for both FAMA and MAPI(1)-SOF (Figure 5.13c).

V.5.2. Structural characterization

FAMA and MAPI(1)-SOF perovskites have also been characterized by XRD. The XRD patterns of these two perovskites deposited on SnO_2 (MAPI) and on various oxides (FAMA) are displayed in Figure 5.14.

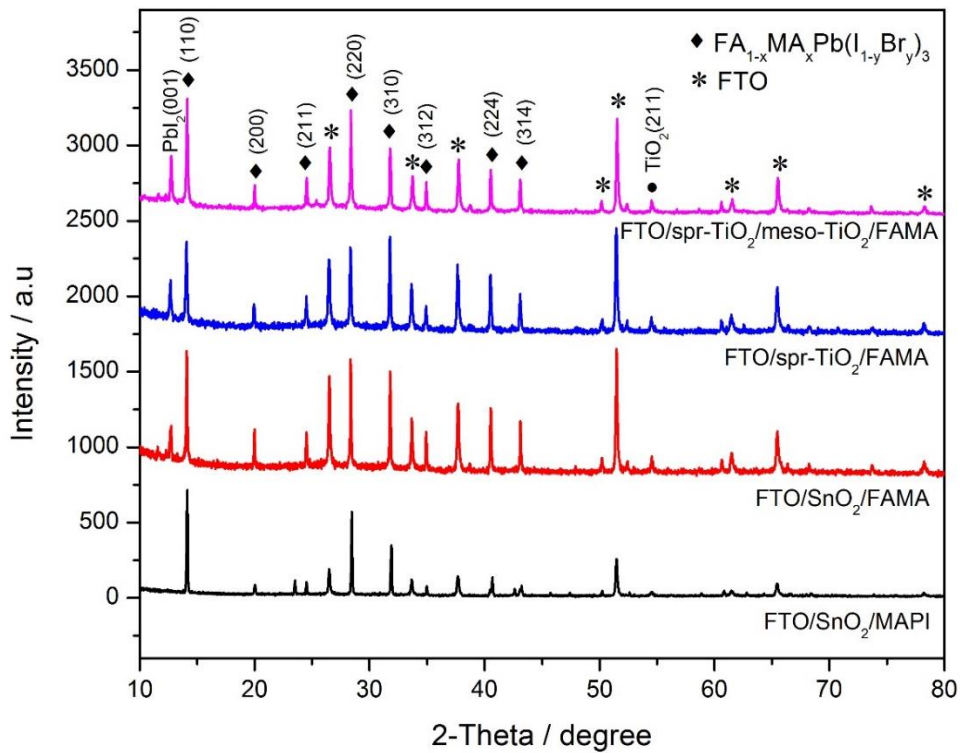


Figure 5.14. XRD patterns of FAMA deposited on various oxides layer and MAPI(1)-SOF on SnO_2 layer.

Both the FAMA perovskite deposited on various oxide layers and the MAPI(1)-SOF deposited on SnO_2 were well-crystallized. For FAMA, we note the presence of the (001) PbI_2 diffraction peak at 12.7° in all cases. This peak is less intense on SnO_2 and then less PbI_2 impurity is formed on this substrate. It is noteworthy that MAPI(1)-SOF on SnO_2 is pure phase with no PbI_2 impurity. However, in many papers, the presence of PbI_2 peaks in certain amount is reported even for high efficiency perovskite solar cells [20]–[23].

V.5.3. Morphological characterization

The perovskite surface morphology was probed by AFM (Figure 5.15). Large grains are observed for MAPI(1)-SOF. FAMA on SnO_2 and meso- TiO_2 have a similar aspect. The roughness quantification yields similar values for the various FAMA samples (Table 5.10). The MAPI(1)-SOF layer on SnO_2 is smoother and the layer is made of large grains with a 210 nm mean size. The FAMA grains have similar size, ranging between 126-155 nm, for the various oxide under-layers.

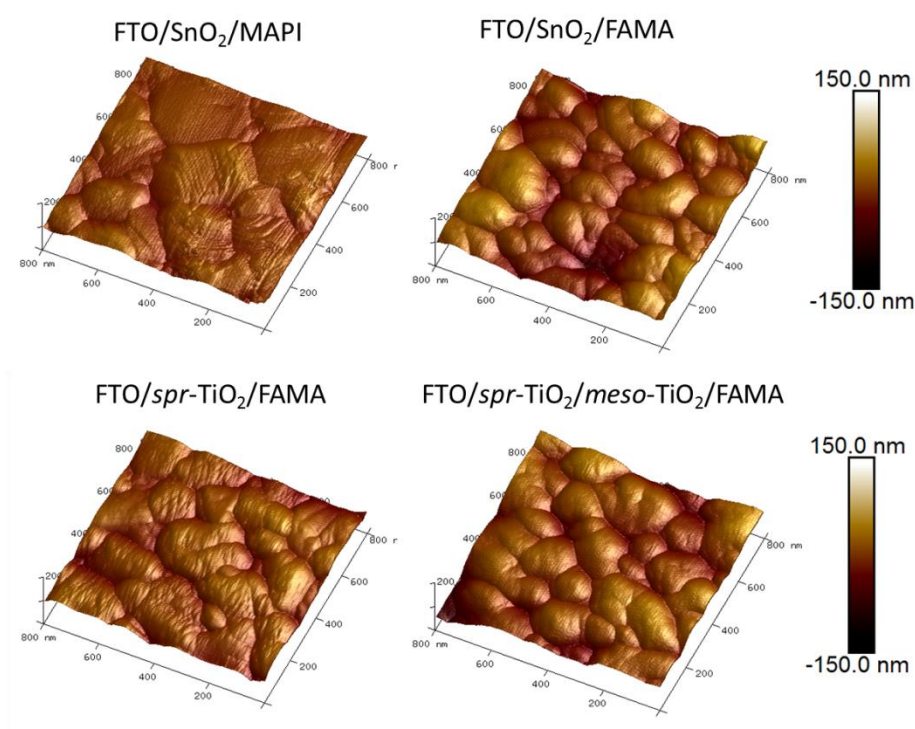


Figure 5.15. 800 nm x 800 nm AFM images of the perovskite layers deposited on the various oxide layers.

Table 5.10. Roughness, RMS roughness, grain size and standard deviation (in brackets) of perovskite layers deposited on the various oxides layer.

| Samples | ρ | RMS/ nm | Size/ nm |
|---|--------|---------|----------|
| FTO/ SnO_2 /MAPI-SOF | 1,05 | 11,9 | 210 (52) |
| FTO/ <i>spr</i> - TiO_2 /FAMA | 1,13 | 24,8 | 154 (93) |
| FTO/ <i>spr</i> - TiO_2 / <i>meso</i> - TiO_2 /FAMA | 1.14 | 29,0 | 126 (34) |
| FTO/ SnO_2 /FAMA | 1.15 | 26,8 | 145 (58) |

V.5.4. Solar cells

The planar architecture (Figure 5.16a) has been used for SnO₂ and *spr*-TiO₂, whereas, for the sake of comparison, we have also studied in parallel the mesoscopic TiO₂ cells (*meso*-TiO₂) which structure is presented in Figure 5.16b. Figure 5.16c is a cross-sectional view of the planar SnO₂/FAMA cell. It shows the large grains of FAMA and the absorber layer thickness is estimated at 380 nm. The cells have been electrically characterized under one sun illumination by measuring their *J-V* curves under reverse and forward voltage scan directions. The results are gathered in Table 5.11 and Figure 5.16d shows the *J-V* curves for the best cells.

In Table 5.11, the *J-V* curve parameters and the PCE of cells prepared using the SnO₂ ETL combined with either FAMA or MAPI(1)-SOF are reported. Actually, SnO₂/FAMA cells presented high performances, with a PCE reaching more than 18.2 %. Interestingly, these cells were almost hysteresis-free (hysteresis index, HI, at 6.7%) (Table 5.11 and Figure 5.16e). [3] These cells were also characterized by a high V_{oc} . It has been pointed out by some authors that the bottom of the conduction band of the HP must be closely aligned to the CB of SnO₂ to reach such high V_{oc} . [5]

With MAPI(1)-SOF, the efficiency was lower at 15.28 % and the hysteresis was rather high (HI at 23% for the best cell). Compared to the SnO₂/FAMA cells, the three *J-V* curve parameters were degraded and it suggests a worse energy matching and more recombination in this case.

SnO₂ cells have been compared to TiO₂ cells. We have found that the maximum PCE of the *meso*-TiO₂ cells (18.67 %) was higher than with SnO₂ but the hysteresis was much larger (HI equal to 36 %). Moreover, the key advantages of the planar SnO₂ cells are a simplified structure and a low temperature processing. Actually, the SnO₂ layer was annealed at a temperature as low as 123°C which is compatible with substrates that do not stand high temperature such as the plastic ones. In Table 5.11, we also report the performances of planar TiO₂ cells. If the performances were high (maximum PCE at 17.65 %), these cells suffered from a very large hysteresis. This behavior is completely different to the one of the planar SnO₂ devices which showed a low HI.

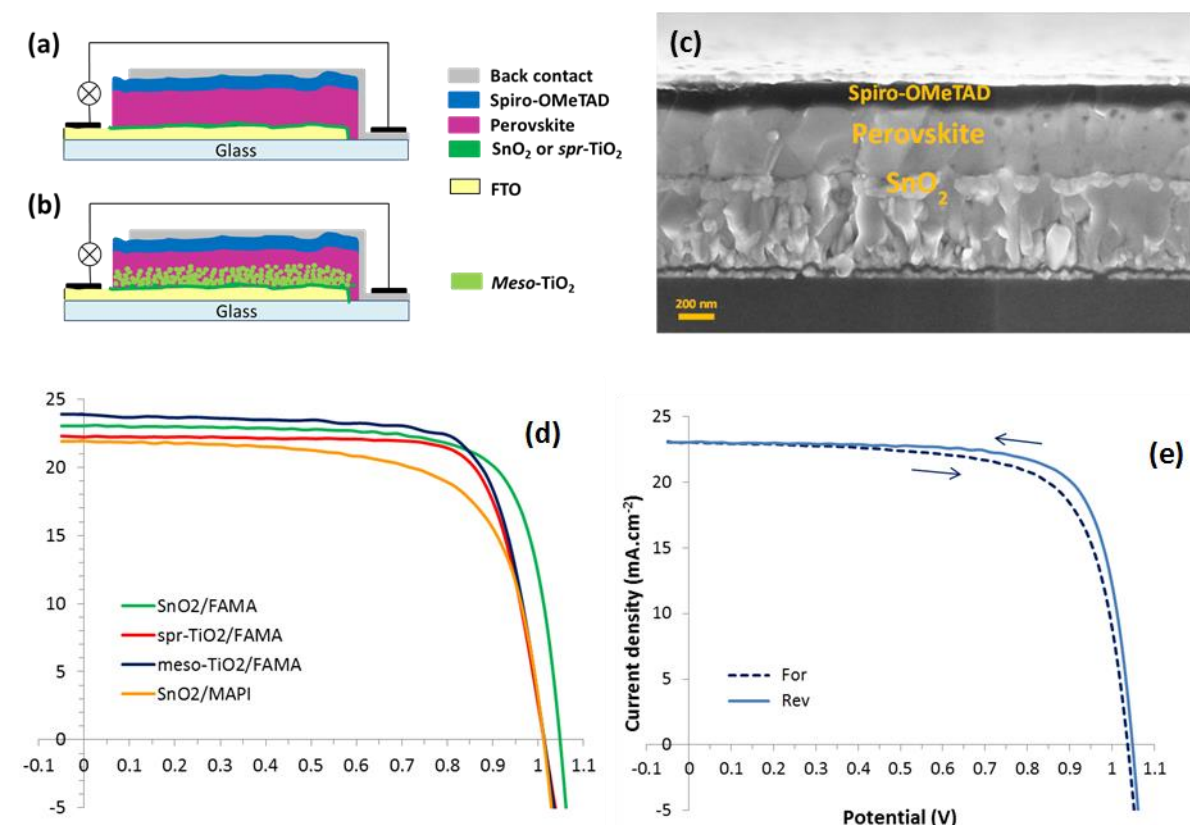


Figure 5.16. (a) Planar and (b) mesoscopic PSCs architectures. (c) Cross-sectional SEM view of a planar SnO₂/FAMA solar cell. (d) J - V curves under simulated AM 1.5 G illumination of the best cells with various assemblies. (e) J - V curve of a record SnO₂/FAMA solar cell measured in the reverse (full line) and forward (dashed line) voltage scan directions.

Table 5.11. Photovoltaic parameters of SnO₂-based, TiO₂-based planar solar cells and of meso-TiO₂ based solar cells under 100 mW.cm⁻² AM 1.5G illumination. The numbers in brackets are the standard deviations.

| Cells structure | Scan direction | V _{oc} (V) | J _{sc} (mA.cm ⁻²) | FF (%) | PCE (%) | HI (%) |
|------------------------------------|----------------|---------------------|--|--------------|--------------|--------|
| SnO ₂ planar (FAMA) | Max (Rev) | 1.05 | 23.03 | 75.44 | 18.22 | 6.7 |
| | Max (For) | 1.04 | 23.02 | 71.21 | 17.03 | |
| | Avg (Rev) | 1.04 (0.01) | 22.79 (0.44) | 72.61 (4.36) | 17.18 (1.44) | 6.7 |
| | Avg (For) | 1.03 (0.01) | 22.76 (0.48) | 68.19 (3.75) | 16.06 (1.22) | |
| SnO ₂ planar (MAPI-SOF) | Max (Rev) | 1.01 | 21.92 | 68.84 | 15.28 | 23.4 |
| | Max (For) | 0.97 | 21.98 | 56.40 | 12.08 | |
| | Avg (Rev) | 1.01 (0.03) | 20.25 (1.72) | 62.22 (4.76) | 12.71 (1.83) | 18.6 |
| | Avg (For) | 0.97 (0.02) | 20.91 (0.89) | 52.02 (3.10) | 10.55 (1.08) | |
| TiO ₂ planar | Max (Rev) | 1.01 | 22.49 | 77.50 | 17.65 | 52.8 |

| | | | | | | |
|---------------------------------|------------------|-------------|--------------|---------------|--------------|-------------|
| (FAMA) | Max (For) | 0.90 | 22.43 | 50.86 | 10.28 | |
| | Avg (Rev) | 1.01 (0.02) | 20.71 (1.12) | 66.91 (8.60) | 14.08 (2.14) | 61.2 |
| | Avg (For) | 0.94 (0.03) | 20.59 (1.19) | 38.64 (10.44) | 7.48 (1.89) | |
| Meso-TiO ₂ (FAMA) | Max (Rev) | 1.02 | 24.05 | 76.1 | 18.67 | 36.4 |
| | Max (For) | 1.01 | 23.24 | 55.02 | 12.92 | |
| | Avg (Rev) | 1.01 (0.01) | 23.34(0.67) | 75.93(1.33) | 17.93(0.49) | 43.2 |
| | Avg (For) | 0.989(0.01) | 23.27(2.60) | 50.72(2.60) | 11.55(0.82) | |

In the brackets are standard deviation. Number of cells averaged is 10 cells.

V.5.5. PL and decay lifetime study

Photoluminescence measurements can substantially improve our understanding of the complex nature of charge-carrier processes in metal-halide perovskites. These technologies have been implemented to study the charge injection at the selective contacts and to understand the effect of the oxide ETM and layer assemblies on the cell performances. Time integrated PL spectra of FAMA supported on various substrates are reported in Figure 5.17a. They are characterized by an emission centered at 774 nm. The maximum emission is measured for the FAMA layer deposited on blocking glass substrate. The PL intensity is lowered in the presence of an ETL due to charge transfer. Higher transfer is found for a contact made of planar SnO₂ compared to the planar *spr*-TiO₂ layer. This indicates a much efficient charge separation in the case of the SnO₂ contact. Figure 5.17a also shows that adding the mesoporous layer improves dramatically the quenching of the FAMA photoluminescence. Indeed, the mesoporous layer increases dramatically the contact area with FAMA. Also, this layer likely has a beneficial effect to optimize the energy barrier and contact between the two layers. The effect of the various selective contacts has also been investigated by time-correlated single-photon counting (TCSPC) measurements. The curves are displayed in Figure 5.17b. They have been fitted with a bi-exponential decay function as described in the Chapter II section II.6. The luminescence decay dynamics reflected by the fast-decay component, τ_{fast} , was assigned to free-carrier recombination at the surface and the slow-decay component, τ_{slow} , was assigned to the free-carrier recombination in the bulk for carriers propagating deeper in the material [24] [25]. The measured values for the various systems are gathered in Table 5.12. For pristine FAMA on glass, a fast lifetime constant was found at 82 ns and a slow one at 620 ns with a very high relative contribution (RC) of the latter (90.4%). The large values obtained show the good quality of the prepared perovskite material. For pristine MAPI(1)-SOF we found τ_{fast} =29 ns and τ_{slow} =301 ns (Table 5.12). The

fast component was close to the bulk single crystal one measured at 22 ns in Ref. [24] while the slow lifetime was much shorter at 301 ns (1032 ns was reported for MAPI single crystal [24]). Higher carrier lifetime for FAMA confirms that this material is better suited for high efficiency due to less defects. For the ETM contact, the SnO₂ planar layer was found to act efficiently since the time constants of FAMA decreased markedly when it was stacked with this material (11 ns and 129 ns) (Table 5.12). Planar SnO₂ is shown much more efficient than the planar *spr*-TiO₂ contact for which time constants were higher. Interestingly, our experiments show that a mesoporous TiO₂ layer is required to get highly efficient electron injection into TiO₂. Then, a slightly better charge injection than for SnO₂ was attained. It can explain the higher photocurrent achieved for the former cells (Figure 5.16d and Table 5.11). The highly efficient electron transfer from FAMA toward the SnO₂ layer developed here is remarkable since this oxide layer was prepared from a precursor solution at low temperature (123°C), whereas the *meso*-TiO₂ bilayer required high temperature annealing up to 455°C to operate more efficiently. Therefore, SnO₂ appears as the most interesting oxide ETM for the fabrication of efficient planar and flexible cells.

We have also employed the PL techniques to investigate the electron injection from MAPI(1)-SOF to SnO₂. The spectra and decay curves are presented in Figure 5.17c and 5.17d, respectively. The PL spectra are centered at about 770 nm and their intensity is reduced by the presence of the SnO₂ layer due to the ability of the SnO₂ to collect electronic charges. The MAPI(1)-SOF TCSPC curves have been fitted by a bi-exponential decay function which parameters are gathered in Table 5.12. The two time constants are markedly shortened when MAPI(1)-SOF is contacted by the SnO₂ layer and therefore SnO₂ allows the charge separation for the electrons photogenerated in MAPI(1)-SOF.

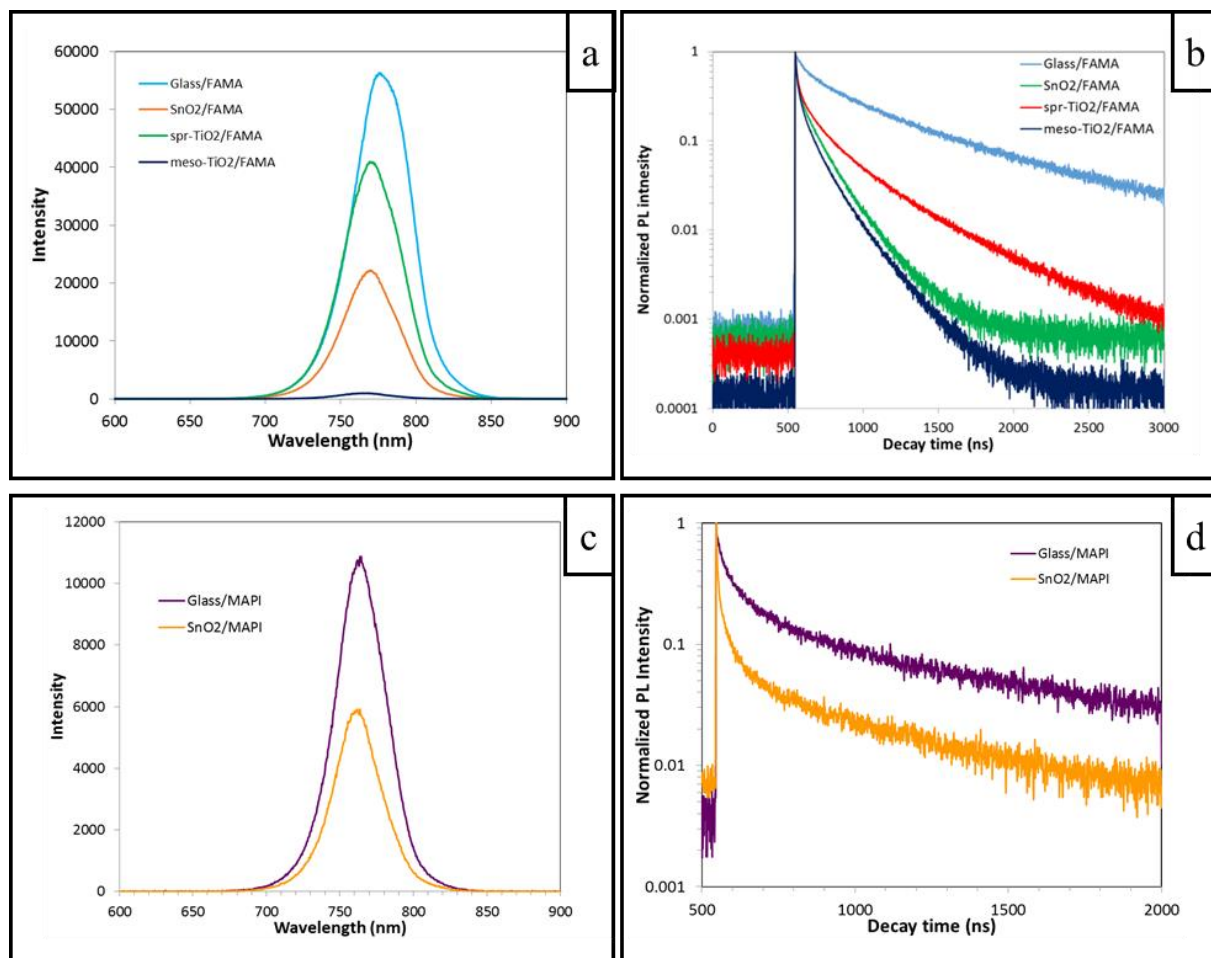


Figure 5.17. (a) Emission spectra of the FAMA layer on glass and supported on various oxide substrates. (b) Time-correlated single-photon counting curves of the photoluminescence of samples (a). (c) PL spectra of MAPI-SOF on glass and on SnO₂. (d) Time-correlated single-photon counting curves of the photoluminescence for MAPI-SOF on glass and on SnO₂ contact layer.

Table 5.12. Parameters of PL decays determined from the bi-exponential TCSP curve fitting. Fast and slow lifetimes and relative contributions of the fast and slow components.

| Perovskite | Sample | τ_{fast} (ns) | RC _{fast} (%) ^a | τ_{slow} (ns) | RC _{slow} (%) ^a |
|------------|-----------------------------|---------------------------|-------------------------------------|---------------------------|-------------------------------------|
| FAMA | Glass/FAMA | 82.0 | 9.6 | 619.8 | 90.4 |
| | SnO ₂ /FAMA | 11.1 | 12.6 | 128.7 | 87.4 |
| | spr-TiO ₂ /FAMA | 15.9 | 12.6 | 233.8 | 87.4 |
| | Meso-TiO ₂ /FAMA | 11.8 | 16.9 | 113.7 | 83.1 |
| MAPI-SOF | Glass/MAPI- | 28.7 | 17.2 | 300.9 | 82.8 |

| | | | | | |
|--|-------------------------|-----|-----|-------|------|
| | SOF | | | | |
| | SnO ₂ /MAPI- | 4.8 | 0.9 | 110.1 | 99.1 |
| | SOF | | | | |

^a Relative contribution (see Chapter II section II.6).

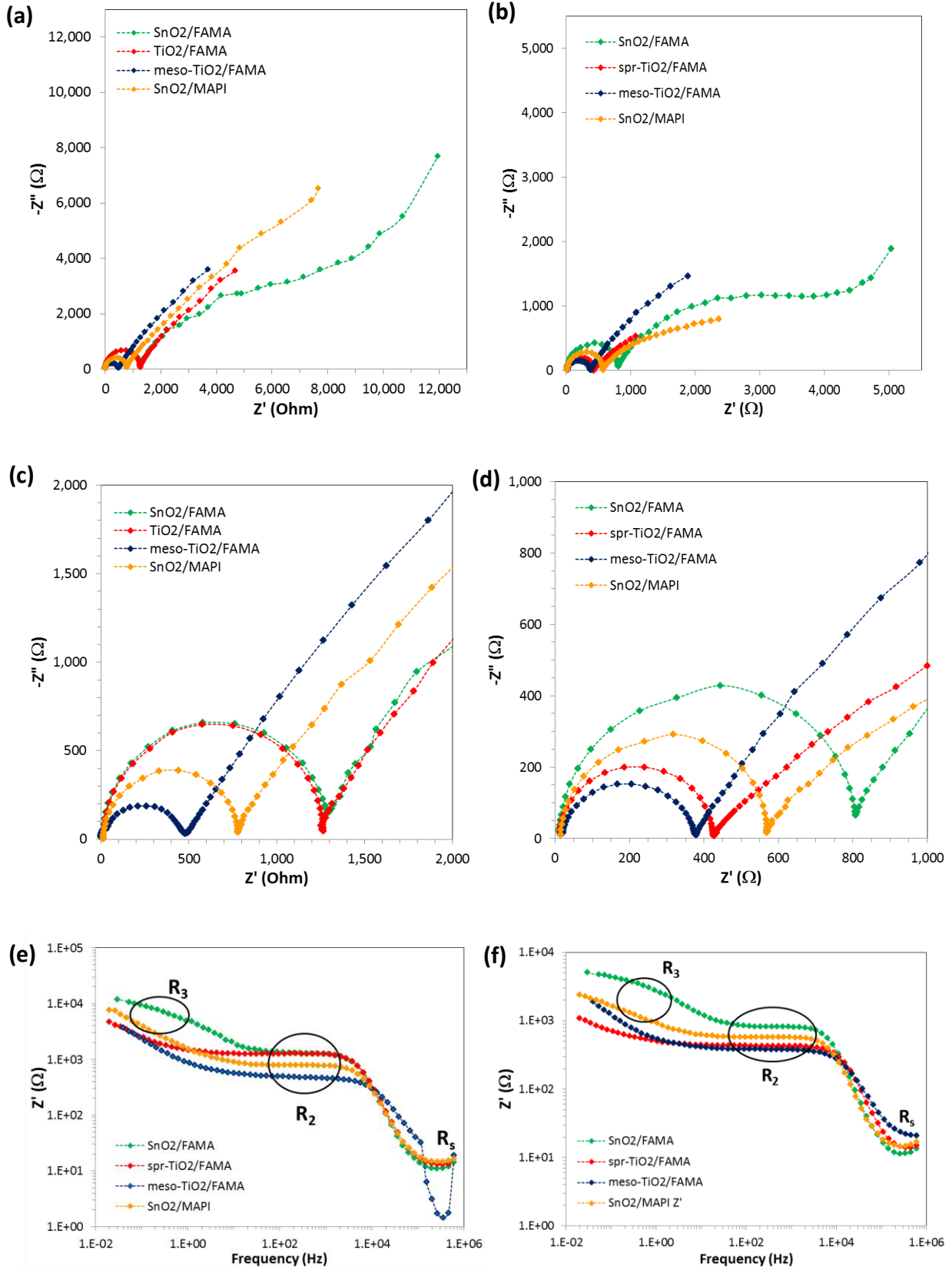
V.5.6. Impedance study of various oxide

Figure 5.18a-d show Nyquist plots of spectra recorded in the 600 kHz-20 mHz range at 0.0V and 0.6V applied voltages. The spectra of the whole cells were characterized by two main loops. One can point out that our SnO₂ cells did not show an inductive loop at the intermediate frequency. It confirms that large intermediate frequency inductive loop is a signature of poorly working cells. On the Nyquist plots, we can note that the low frequency loop had a different shape in the case of the SnO₂/FAMA cells with a rise below 1Hz which draw the beginning of a new loop. To better distinguish the various resistance and capacitance features in the spectra, other spectral representations have been employed. Figure 5.18e and 5.18f are the real part of the complex impedance as a function of the frequency for an applied potential of 0.0V and 0.6V, respectively. Three main resistive features are observed. At very high frequency, R_s is the series resistance due to wires and the resistances of the contacts. We also note the presence of a plateau at 100Hz-2kHz which corresponds to the high frequency resistance R_2 , defined by the first arc of circle. A low frequency resistance is defined by extrapolating the spectra at very low frequency. The very low frequency behavior of SnO₂/FAMA results in a large resistance at the steady state and then a high FF.

We have also calculated the complex capacitance of the spectra defined as:

$$C^* = C' + iC'' = \frac{1}{Zi\omega}$$

with i the square root of -1 and ω the angular frequency related to the ordinary frequency as $f = \omega/2\pi$. Figure 5.18g and 5.18h figure out the real part of the complex capacitance (C') for the various cells at 0.0V and 0.6V applied voltages. A first capacitive process is found at high frequency. It defines the capacitance C_2 . This parameter does not change significantly for the various cells and it is now well-assigned to the bulk capacitance of the perovskite [1]–[3], [18], [26]. Interestingly, we note on these figures a different shape for FAMA/SnO₂ and MAPI(1)-SOF/SnO₂ cells, with a capacitive feature in the 0.5Hz-10Hz region which is noted C_3 . At very low frequency, C_4 is defined for all the cells.



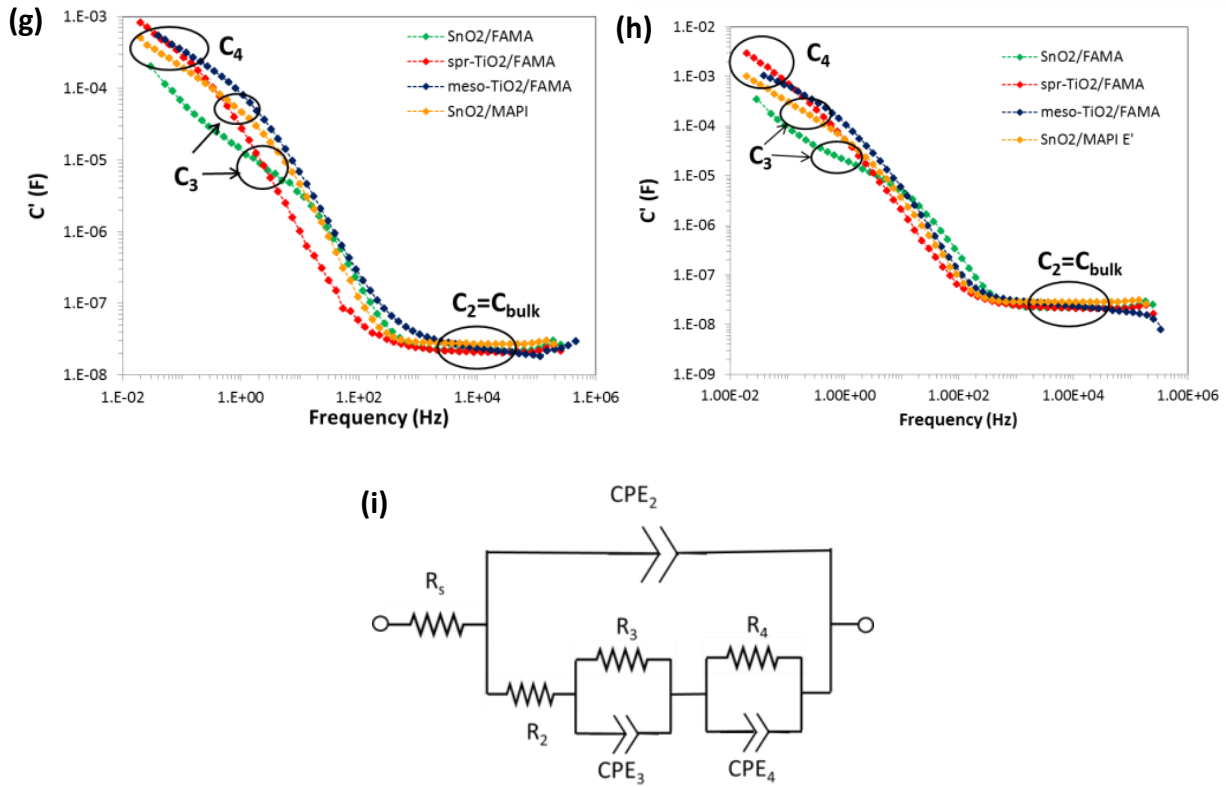
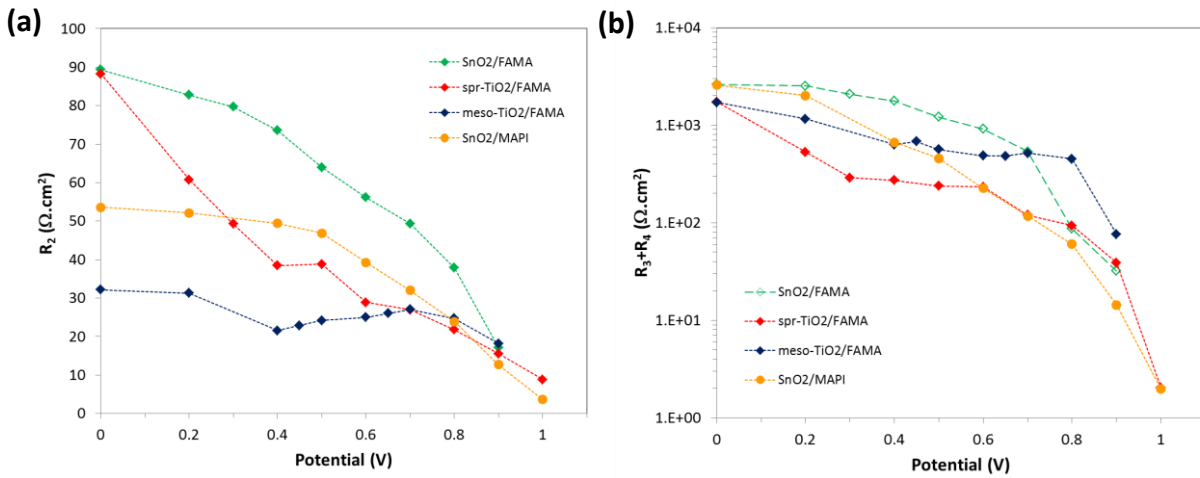


Figure 5.18. (a,b) Nyquist plots of the impedance spectra of cells with various ETL and HP assemblies. (c,d) High frequency zoom views of the spectra. (e,f) Real part of the complex impedance plotted versus the frequency. (g,h) Real part of the complex capacitance plotted versus the frequency. (a,c,e,g) Applied potential: 0.0V; (b,d,f,h) Applied potential: 0.6V. (i) Full equivalent electrical circuit used to fit the impedance spectra.

Based on these observations, the general electrical equivalent circuit (ECC) used to fit the spectra is presented in Figure 5.18i. It is obtained from the simplification of the EEC of Figure 1.26, Chapter 1. Because the arcs of circle are not semicircles, they have been fitted using R//CPE circuits with CPE being a constant phase element. The actual capacitances were extracted from the CPE parameters as described in our previous works [1]–[3], [26]. The various resistances and capacitances have been determined from the spectrum fits and plotted as a function of the applied voltages. R_2 is the high frequency resistance, plotted in Figure 5.19a. This parameter can vary in a large extent for cells with the same absorber (FAMA). It also varies in a large extent for cells with the same ETM layer and different HP. For instance, SnO₂/FAMA and SnO₂/MAPI-SOF curves have the same shape but R_2 is lower for MAPI-SOF compared to FAMA while they involve the same ETL. Therefore, this resistance is complex and gathers several contributions. From our results, it is clear that the main one is related to the interface between the oxide and the perovskite. Some authors have suggested that this resistance is a recombination resistance. In the present case, the curves for the SnO₂

cells, with higher resistances for the SnO₂/FAMA cells, which deliver a higher J_{sc} and FF, could be consistent with that interpretation. On the other hand, R_2 of the TiO₂ cells would be more complex.

R_3 and R_4 could be determined accurately in the case of the TiO₂ cells and of the SnO₂/MAPI-SOF cell. For the SnO₂/FAMA cell, the upward bending of the spectra observed at very low frequency rendered the determination of R_4 difficult and this parameter was underestimated in this case. The variation of R_3 with the applied potential is shown in Figure 5.19c. We suggest that R_3 and R_4 are recombination resistances. Their sum, plotted in Figure 5.19b, provides a good estimation of the recombination phenomena in the cells: the higher this parameter, the lower the recombination. The curve of the SnO₂/MAPI-SOF cell decreases more rapidly than those of the other cells and is in good agreement with the lower FF in this case. Adding the mesoporous layer to the *spr*-TiO₂ one has a beneficial effect since it gives rise to higher resistances in good agreement with the higher performances of these devices. We can suppose that the presence of the mesoporous layer improves the HP crystal formation and that the quality of the interface with TiO₂ is better due to less surface states.



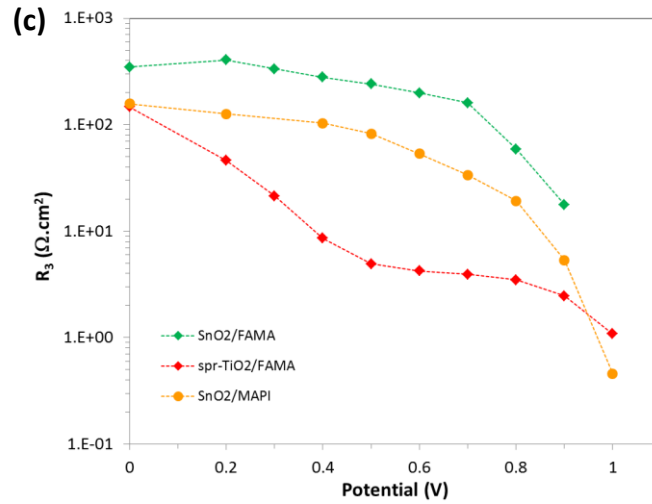


Figure 5.19. Variation of the solar cell resistance measured under light at various applied potentials. (a) R_2 ; (b) R_3+R_4 ; (c) Variation of the R_3 parameter with the applied voltage.

Based on our previous IS studies of perovskite solar cells, C_2 is assigned to the dielectric capacitance of the perovskite [1]–[3], [18], [26]. The HP absorbance curves (Figure 5.13a) were about the same for the various cells and then the equivalent HP thickness was close for the various systems. The higher C_2 of SnO₂/MAPI-SOF cell compared to SnO₂/FAMA is in good agreement with our previous results and shows a higher ϵ_r (relative permittivity) for MAPI-SOF compared to FAMA. Lower C_2 in the presence of *meso*-TiO₂ can be related to the presence of the porosity. The C_3 capacitance is clearly observed on the $C' = f(\text{Hz})$ curve (Figure 5.18g,h) for the planar SnO₂ cells. This parameter has been determined for these cells and is plotted as the function of the applied voltage in Figure 5.20b. The main feature is the low value of this capacitance in the case of SnO₂/FAMA. This observation can be correlated with the cell hysteresis results. Actually, the scan rate for the $J-V$ curve measurement corresponds to an impedance frequency in the hertz range and, at these frequencies, the SnO₂/FAMA cell has a capacitive behavior with a low capacitance value, in agreement with a small hysteresis. C_4 is the very low frequency capacitance and has large values. It is plotted in Figure 5.20c and heavily varies with the applied potential. It has been suggested that C_4 is an accumulation capacitance, controlled by ionic defects and proportional to the amount of charge, but charge accumulation must be compensated for by moving ions, which is actually the reason why its effect is detected at lower frequencies instead of a higher one, as should be expected for electronic phenomena [40].

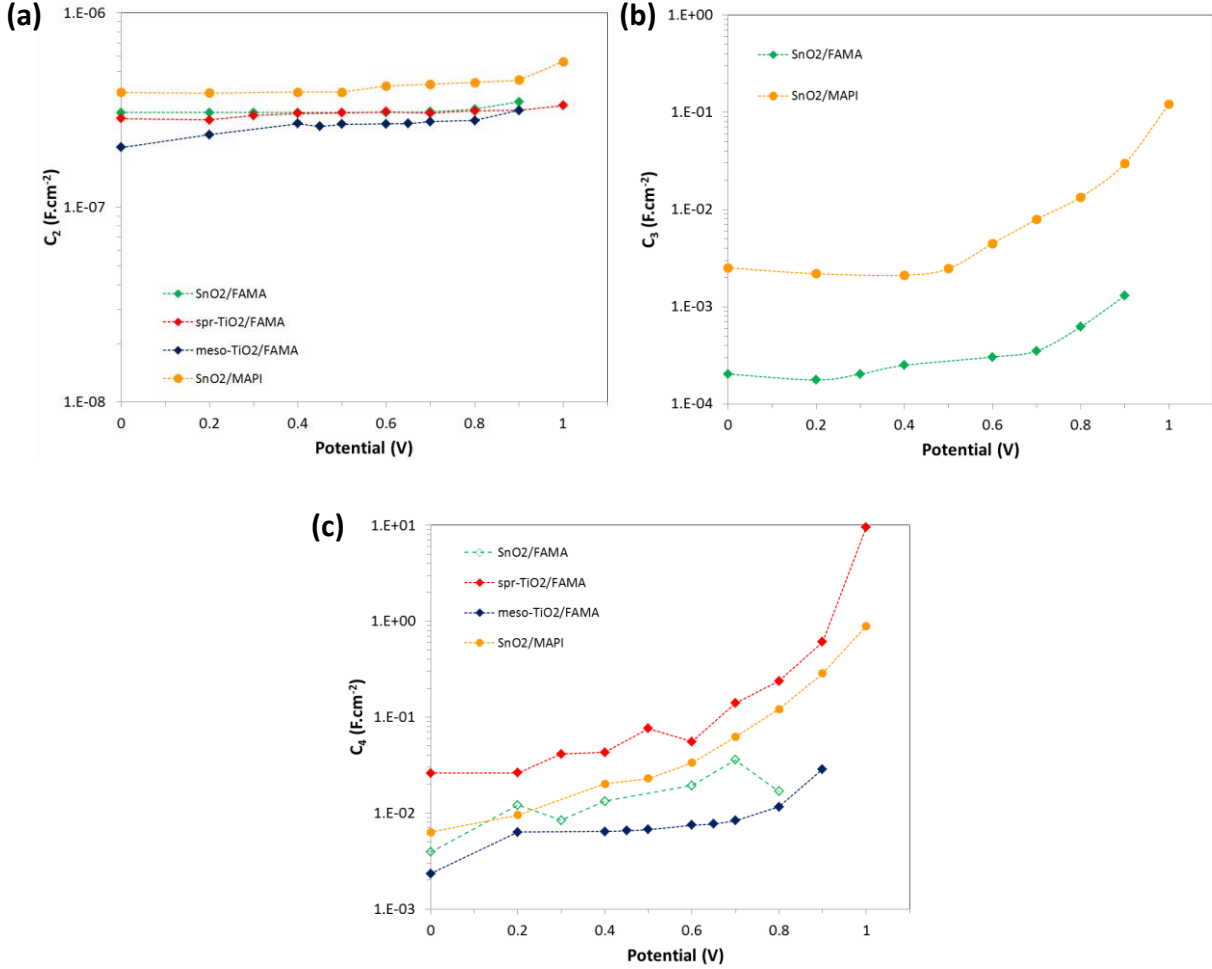


Figure 5.20. Variation of the solar cell capacitances measured under light at various applied potentials. (a) C_2 ; (b) C_3 ; (c) C_4 . Note that C_4 (green open symbol) for SnO₂/FAMA is underestimated due to a very low relaxation frequency IS feature.

V.6. Conclusion

In conclusion, we have defined a low-temperature (123°C) protocol using a colloidal solution of SnO₂ for the preparation by twofold spin-coating of an efficient ETM layer for perovskite solar cells. The layer was crack-free and correctly covered the FTO substrate. The deposition occurred preferentially at the troughs of the FTO grains and the layer was highly transparent throughout the near-UV and visible range. Planar cells have been prepared based on this layer and MAPI(1)-SOF and FAMA perovskites. With FAMA absorber, the devices were highly efficient with a maximum PCE of 18.2% and an almost hysteresis-free behavior (6.7% HI). PL spectra measurements and TCSP experiments have shown the very fast hole transfer from the perovskite layer into the Spiro-OMeTAD layer. The charge carrier injection was slower on the ETM side. Actually, TCSPC has shown that the electron transfer is highly dependent on the oxide used and its morphology. The planar SnO₂ layer permitted a fast and efficient

electron transfer, much faster than the planar TiO_2 . Moreover, the TCSPC technique also showed the less defective nature of the FAMA perovskite compared to the MAPI(1)-SOF one. Phenomena occurring at longer time scales have been investigated by the impedance spectroscopy technique. The spectra were free of inductive loop. They have been fitted with an *ad-hoc* equivalent electrical circuit, obtained from the simplification of the EEC of Figure 1.26, Chapter 1. Our results confirm that the well-working perovskite solar cells are free of significant intermediate frequency inductive loop. The R_2 resistance has been shown to be complex and to combine several phenomena. The low frequency resistances R_3 and R_4 have been assigned to the recombination phenomena occurring at the contacts with the perovskite layer. For the SnO_2/FAMA cells, the very low frequency part of the spectra was characterized by the beginning of an arc of circle at the origin of a very large R_4 over a large applied potential range which explains the very large V_{oc} achievable with SnO_2 PSCs.[27] The complex capacitance spectra of the SnO_2 -based solar cells showed the presence of intermediate C_3 and low frequency C_4 capacitances. The low-hysteresis in the J - V curves of the SnO_2/FAMA cells has been linked with the capacitive behavior of the device in the 0.5-10 Hz range (C_3 capacitance) which values were noticeably low.

References

- [1] P. Wang, Z. Shao, M. Ulfa, et T. Pauporté, « Insights into the Hole Blocking Layer Effect on the Perovskite Solar Cell Performance and Impedance Response », *J. Phys. Chem. C*, vol. 121, n° 17, p. 9131-9141, mai 2017.
- [2] M. Ulfa, T. Pauporté, T.-T. Bui, et F. Goubard, « Impact of Organic Hole Transporting Material and Doping on the Electrical Response of Perovskite Solar Cells », *J. Phys. Chem. C*, vol. 122, n° 22, p. 11651-11658, juin 2018.
- [3] M. Ulfa, T. Zhu, F. Goubard, et T. Pauporte, « Molecular versus polymeric hole transporting materials for perovskite solar cell application », *J. Mater. Chem. A*, 2018.
- [4] J. Song *et al.*, « Low-temperature SnO_2 -based electron selective contact for efficient and stable perovskite solar cells », *J Mater Chem A*, vol. 3, n° 20, p. 10837-10844, 2015.
- [5] J. P. Correa Baena *et al.*, « Highly efficient planar perovskite solar cells through band alignment engineering », *Energy Env. Sci*, vol. 8, n° 10, p. 2928-2934, 2015.
- [6] Q. Jiang *et al.*, « Enhanced electron extraction using SnO_2 for high-efficiency planar-structure $\text{HC}(\text{NH}_2)_2\text{PbI}_3$ -based perovskite solar cells », *Nat. Energy*, vol. 2, p. 16177, nov. 2016.
- [7] L. Xiong *et al.*, « Performance enhancement of high temperature SnO_2 -based planar perovskite solar cells: electrical characterization and understanding of the mechanism », *J Mater Chem A*, vol. 4, n° 21, p. 8374-8383, 2016.

- [8] M. Park, J.-Y. Kim, H. J. Son, C.-H. Lee, S. S. Jang, et M. J. Ko, « Low-temperature solution-processed Li-doped SnO₂ as an effective electron transporting layer for high-performance flexible and wearable perovskite solar cells », *Nano Energy*, vol. 26, p. 208-215, août 2016.
- [9] H. Chen *et al.*, « Enhanced Performance of Planar Perovskite Solar Cells Using Low-Temperature Solution-Processed Al-Doped SnO₂ as Electron Transport Layers », *Nanoscale Res. Lett.*, vol. 12, n° 1, p. 238, mars 2017.
- [10] G. Yang *et al.*, « Interface engineering in planar perovskite solar cells: energy level alignment, perovskite morphology control and high performance achievement », *J Mater Chem A*, vol. 5, n° 4, p. 1658-1666, 2017.
- [11] W. Ke *et al.*, « Cooperative tin oxide fullerene electron selective layers for high-performance planar perovskite solar cells », *J. Mater. Chem. A*, vol. 4, n° 37, p. 14276-14283, 2016.
- [12] E. H. Anaraki *et al.*, « Highly efficient and stable planar perovskite solar cells by solution-processed tin oxide », *Energy Env. Sci*, vol. 9, n° 10, p. 3128-3134, 2016.
- [13] J.-Y. Chen, C.-C. Chueh, Z. Zhu, W.-C. Chen, et A. K.-Y. Jen, « Low-temperature electrodeposited crystalline SnO₂ as an efficient electron-transporting layer for conventional perovskite solar cells », *Sol. Energy Mater. Sol. Cells*, vol. 164, p. 47-55, mai 2017.
- [14] S. Lin *et al.*, « Efficient and stable planar hole-transport-material-free perovskite solar cells using low temperature processed SnO₂ as electron transport material », *Org. Electron.*, vol. 53, p. 235-241, févr. 2018.
- [15] H. J. Snaith et C. Ducati, « SnO₂-Based Dye-Sensitized Hybrid Solar Cells Exhibiting Near Unity Absorbed Photon-to-Electron Conversion Efficiency », *Nano Lett.*, vol. 10, n° 4, p. 1259-1265, avr. 2010.
- [16] X. Dou, D. Sabba, N. Mathews, L. H. Wong, Y. M. Lam, et S. Mhaisalkar, « Hydrothermal Synthesis of High Electron Mobility Zn-doped SnO₂ Nanoflowers as Photoanode Material for Efficient Dye-Sensitized Solar Cells », *Chem. Mater.*, vol. 23, n° 17, p. 3938-3945, sept. 2011.
- [17] M. S. Arnold, P. Avouris, Z. W. Pan, et Z. L. Wang, « Field-Effect Transistors Based on Single Semiconducting Oxide Nanobelts », *J. Phys. Chem. B*, vol. 107, n° 3, p. 659-663, janv. 2003.
- [18] A. Guerrero *et al.*, « Properties of Contact and Bulk Impedances in Hybrid Lead Halide Perovskite Solar Cells Including Inductive Loop Elements », *J. Phys. Chem. C*, vol. 120, n° 15, p. 8023-8032, avr. 2016.
- [19] L. Kavan, L. Steier, et M. Grätzel, « Ultrathin Buffer Layers of SnO₂ by Atomic Layer Deposition: Perfect Blocking Function and Thermal Stability », *J. Phys. Chem. C*, vol. 121, n° 1, p. 342-350, janv. 2017.
- [20] T. Du, C. H. Burgess, J. Kim, J. Zhang, J. R. Durrant, et M. A. McLachlan, « Formation, location and beneficial role of PbI₂ in lead halide perovskite solar cells », *Sustain. Energy Fuels*, vol. 1, n° 1, p. 119-126, 2017.
- [21] T. J. Jacobsson *et al.*, « Unreacted PbI₂ as a Double-Edged Sword for Enhancing the Performance of Perovskite Solar Cells », *J. Am. Chem. Soc.*, vol. 138, n° 32, p. 10331-10343, août 2016.
- [22] Kim Young Chan *et al.*, « Beneficial Effects of PbI₂ Incorporated in Organo-Lead Halide Perovskite Solar Cells », *Adv. Energy Mater.*, vol. 6, n° 4, p. 1502104, déc. 2015.
- [23] D. H. Cao *et al.*, « Remnant PbI₂, an unforeseen necessity in high-efficiency hybrid perovskite-based solar cells? », *APL Mater.*, vol. 2, n° 9, p. 91101, sept. 2014.
- [24] D. Shi *et al.*, « Low trap-state density and long carrier diffusion in organolead trihalide perovskite single crystals », *Science*, vol. 347, n° 6221, p. 519, janv. 2015.
- [25] F. Staub *et al.*, « Beyond Bulk Lifetimes: Insights into Lead Halide Perovskite Films from Time-Resolved Photoluminescence », *Phys Rev Appl.*, vol. 6, n° 4, p. 44017, oct. 2016.

- [26] P. Wang, M. Ulfa, et T. Pauporté, « Effects of Perovskite Monovalent Cation Composition on the High and Low Frequency Impedance Response of Efficient Solar Cells », *J. Phys. Chem. C*, vol. 122, n° 4, p. 1973-1981, févr. 2018.
- [27] D. Pitarch-Tena, T. T. Ngo, M. Vallés-Pelarda, T. Pauporté, et I. Mora-Seró, « Impedance Spectroscopy Measurements in Perovskite Solar Cells: Device Stability and Noise Reduction », *ACS Energy Lett.*, vol. 3, n° 4, p. 1044-1048, avr. 2018.
- [28] A. R. Pascoe, N. W. Duffy, A. D. Scully, F. Huang, et Y.-B. Cheng, « Insights into Planar CH₃NH₃PbI₃ Perovskite Solar Cells Using Impedance Spectroscopy », *J. Phys. Chem. C*, vol. 119, n° 9, p. 4444-4453, mars 2015.
- [29] E. J. Juarez-Perez *et al.*, « Role of the Selective Contacts in the Performance of Lead Halide Perovskite Solar Cells », *J. Phys. Chem. Lett.*, vol. 5, n° 4, p. 680-685, févr. 2014.
- [30] E. J. Juarez-Perez *et al.*, « Photoinduced Giant Dielectric Constant in Lead Halide Perovskite Solar Cells », *J. Phys. Chem. Lett.*, vol. 5, n° 13, p. 2390-2394, juill. 2014.
- [31] A. Dualé *et al.*, « Impedance Spectroscopic Analysis of Lead Iodide Perovskite-Sensitized Solid-State Solar Cells », *ACS Nano*, vol. 8, n° 1, p. 362-373, janv. 2014.
- [32] V. Gonzalez-Pedro *et al.*, « General Working Principles of CH₃NH₃PbX₃ Perovskite Solar Cells », *Nano Lett.*, vol. 14, n° 2, p. 888-893, févr. 2014.
- [33] O. Almora, I. Zarazua, E. Mas-Marza, I. Mora-Sero, J. Bisquert, et G. Garcia-Belmonte, « Capacitive Dark Currents, Hysteresis, and Electrode Polarization in Lead Halide Perovskite Solar Cells », *J. Phys. Chem. Lett.*, vol. 6, n° 9, p. 1645-1652, mai 2015.
- [34] A. Guerrero, E. J. Juarez-Perez, J. Bisquert, I. Mora-Sero, et G. Garcia-Belmonte, « Electrical field profile and doping in planar lead halide perovskite solar cells », *Appl. Phys. Lett.*, vol. 105, n° 13, p. 133902, sept. 2014.
- [35] O. Almora, A. Guerrero, et G. Garcia-Belmonte, « Ionic charging by local imbalance at interfaces in hybrid lead halide perovskites », *Appl. Phys. Lett.*, vol. 108, n° 4, p. 43903, janv. 2016.
- [36] H.-S. Kim *et al.*, « Mechanism of carrier accumulation in perovskite thin-absorber solar cells », *Nat. Commun.*, vol. 4, p. 2242, juill. 2013.
- [37] I. Zarazua *et al.*, « Surface Recombination and Collection Efficiency in Perovskite Solar Cells from Impedance Analysis », *J. Phys. Chem. Lett.*, vol. 7, n° 24, p. 5105-5113, déc. 2016.
- [38] Yang Tae-Youl, Gregori Giuliano, Pellet Norman, Grätzel Michael, et Maier Joachim, « The Significance of Ion Conduction in a Hybrid Organic-Inorganic Lead-Iodide-Based Perovskite Photosensitizer », *Angew. Chem. Int. Ed.*, vol. 54, n° 27, p. 7905-7910, mai 2015.
- [39] H.-S. Kim *et al.*, « Control of I-V Hysteresis in CH₃NH₃PbI₃ Perovskite Solar Cell », *J. Phys. Chem. Lett.*, vol. 6, n° 22, p. 4633-4639, nov. 2015.
- [40] M. Anaya *et al.*, « Electron injection and scaffold effects in perovskite solar cells », *J. Mater. Chem. C*, vol. 5, n° 3, p. 634-644, 2017.

General conclusion and some future perspectives

Perovskite solar cell is one of the hot research topics in the world since it was first published in 2009. Since then, the research interest to perovskite materials has been extended to many types' applications. Due to the intensive study and research, a remarkable increase of the power conversion efficiency of perovskite solar cell up to $> 23\%$ has been achieved within a short period of time (10 years). This is an amazing result compared to the silicon solar cells which have needed several decades to reach such a high efficiency. The researches focus now on all the perovskite solar components: the perovskite material itself, the electron and hole transport layer as well as the structure and the device contacts.

This thesis work aimed at realizing efficient, stable, and reproducible perovskite solar cells, and to have a good understanding of the cells functioning. We started by the comparison of two different MAPI deposition techniques, called one-step and two-step. By adopting both techniques, we could achieve more than 17% PCE for $\text{CH}_3\text{NH}_3\text{PbI}_3$ PSC. Both techniques were then used to study several hole transporting materials. We investigated the role of each hole transport material in several perovskite structures and the cell electrical responses by realizing impedance spectroscopy measurements. Lastly, we focused our study on the planar structure by employing a wide bandgap semiconductor SnO_2 . A comprehensive investigation was carried out such as the SnO_2 layer thickness, the annealing time and temperature, and the perovskite to get high efficiency. Finally, the comparative study with a planar TiO_2 cell and a mesoporous TiO_2 cell was conducted to get a full understanding of the cells functioning.

In Chapter 1 we have presented the context of the research on solar cells. At first, we detailed the working mechanism of the silicon solar cells by explaining the formation of a p-n junction, the formation of a built-in-electric field, and the charge separation processes in the device. In addition, we further introduced the new comer perovskite solar cells, detailed their development and their evolution for the past few years including the various functional layers used, cells structure, deposition techniques, and others important parameters. We also explained the working mechanism of perovskite solar cells and finally we detailed the characterization techniques that are currently used for the material itself and the complete device.

In Chapter 2 we provided a comparative study of two different $\text{CH}_3\text{NH}_3\text{PbI}_3$ deposition techniques (1-step and 2-step). We fully characterized the layer and the cells prepared by both techniques. It was clear that both of them are suitable for the preparation of PSC which resulted to more than 17% PCE. We also deeply characterized the electrical responses of the cell by measuring the impedance and the lifetime of the electron by time resolved photoluminescence spectroscopy. We observed that the cells prepared by 2-step were not very stable during the impedance measurements that rendered their full study difficult.

In Chapter 3 we thoroughly studied the two main kind of hole transporting materials: molecular and polymeric. We fully characterized and compared the electrical response of PSCs prepared with the benchmark molecular Spiro-OMeTAD HTM and the conducting polymer poly(3-hexylthiophene-2,5-diyl) (P3HT) selected as a low-cost and efficient polymer HTM. We also investigated the doping effect on these HTMs. Through impedance spectroscopy measurement, we could clearly see that the doping is really important to get high efficiency in the Spiro-OMeTAD cell while the improvement was less significant in the case P3HT cell. We have shown that the Spiro-OMeTAD oxidation by the additive is important to increase the HTM layer conductivity and decrease the internal resistivity. Moreover, for both HTM, the additives improve the perovskite/HTM interface and hinders the charge recombination. Dopings improved the perovskite/hole transport material interface for P3HT cell, while they significantly helped the oxidation of Spiro-OMeTAD to increase its conductivity and improved the quality of the perovskite/Spiro-OMeTAD interface.

In Chapter 4 we investigated several new carbazole derivatives as hole transporting materials. These molecules ranged from the big dendritic core B186 to the DMs and iDMs series with lower molecular weight. Firstly, we incorporated all these new molecular HTMs into the PSCs using several kinds of perovskite structures. Among them, B186 and iDM1 showed the highest efficiency at 14.59% and 15.04%, respectively. We investigated the stability of B186 cells by following the device efficiency as well as the XRD pattern. We found that B186 has better stability than Spiro-OMeTAD. Interestingly, DM1 and DM2 from the DMs series of hole transporting materials showed a significant increase in efficiency under light irradiation soaking.

In Chapter V we studied a simple planar structure of PSC by incorporating a wide bandgap semiconductor SnO_2 as the hole blocking layer. At first, we fully investigated the optimum thickness of SnO_2 , the good temperature and annealing time, and, the substrate used, and its

combination with various perovskites. The optimum condition was found when it was prepared by two times coating of a 2.35% aqueous SnO₂ colloidal solution annealed at low temperature (123°C). The layer was crack-free and fully-covered the FTO substrate. The planar cells were then prepared using this layer combined with MAPI(1)-SOF and FAMA perovskites. With FAMA absorber, the devices were highly efficient with a maximum PCE of 18.2% and an almost hysteresis-free (6.7% HI) while with MAPI(1)-SOF the obtained efficiency was 15.2% with higher hysteresis. For the sake of comparison, we also prepared a planar perovskite solar cell using a sprayed TiO₂ layer as the electron transport layer as well as the benchmark structure combining the sprayed blocking layer and the mesoporous TiO₂ layer. This permitted us to get full information about the cell functioning.

From our studies, it is clear now that either the electron transport layer or the hole transport layer are very important for obtaining high efficiency and stable perovskite solar cells. The properties of these layers affect their abilities to transport or store carriers through the whole device. Moreover, we have illustrated the great importance of the interfaces in the devices. An optimum condition for each layer such the thickness and the morphology resulted high efficiency and stable perovskite solar cells. However, the preparation of the perovskite layer itself is also crucial to get high efficiency. The layer must contain the less defects and be of high crystallinity in order to reduce the possibility of recombination processes boost the efficiency. Through our investigation of various hole transporting materials, we can say that the classical Spiro-OMeTAD may not be the best hole transporting material for obtaining high stability and protection against moisture. We have shown that there is a wide range of possibility to find new hole transporting materials either molecular or polymeric or inorganic ones. In recent studies, we found that a carbazole based polymer showed a promising efficiency, close to 17% in our group. Interestingly, the cell's efficiency increased to 18% after 7 weeks of storage. However, the target of additive free efficient HTM is not easy to reach since we have shown the key role of additives in the perovskite/HTM interface improvement.

In term of the electron transport layer, we have shown the TiO₂ oxide layer present some drawbacks. Recently, other oxides, especially SnO₂ showed also fast electron transfer from the perovskite absorber. It is now studied intensively in many groups. The advantages of the SnO₂ ETL include the low temperature preparation, a simplified cell structure and low hysteresis. However, the performance of the prepared SnO₂ cells remained lower than that of the TiO₂ ones prepared in Pauporté's group. In addition, we also observed the interface

quality between each layer to obtain less recombination in the cells either by interface modification with a deposition of thin layer or careful examination of each layer during the cell preparation.

We started our study by using MAPI perovskite which is less stable compare to FAMA perovskite absorber. Now, in our group we studied a multiple cation perovskite with the Cs addition into the FAMA perovskite that can reach up to 21% of the PCE and has much better stability. Moreover, a lead-free perovskite is also a big opportunity for the future study in order to face the toxicity issue to the environment.

In the of the metal contact, there is a possibility to change the use of gold with other metal contact such as carbon black that can reduce the cell's fabrication cost.

Based on all our results and by following the trend of perovskite solar cells results, we believe that perovskite solar cells efficiency will continuously rise in the future and it is likely that one day it will be widely commercialized in all over the world.

Annex-I: SEM images of FAMA on various oxides and MAPI(1)-SOF on SnO₂ layer

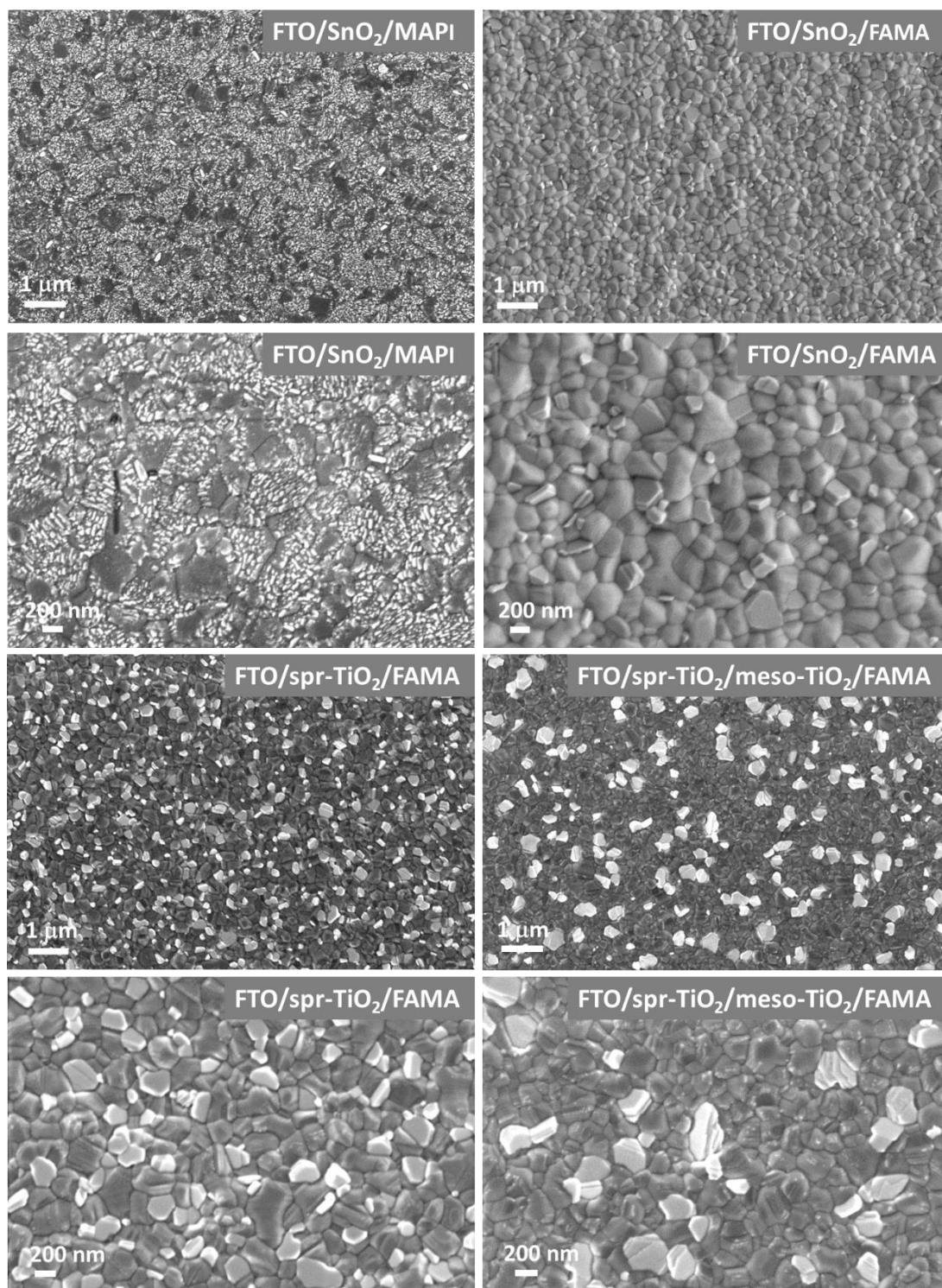


Figure AI-1. SEM-view of FAMA on various oxides layer and MAPI(1)-SOF on SnO₂ layer.

Figure AI-1 shows the SEM images of FAMA on various oxides layer and MAPI(1)-SOF on SnO₂ layer. The aspect of FAMA on various oxides layer are similar with a grain sizes ranging from 150-250 nm. However, we observed the white phase of the grain in the case of TiO₂ samples. Unfortunately, we could not clearly see the morphology of the MAPI(1)-SOF layer deposited on SnO₂. We believe that the sample started to degrade since the storage time was too long due to the technical problem of the SEM machine. However, the morphology aspect of these samples are the same with AFM results in Figure 5.15 where the largest grain was founded in these samples.

Annex-II: Cyclic voltammetry of different coating SnO₂ layer

The blocking ability and band position of the layers was evaluated by measuring the cyclic voltammogram of the samples used as a working electrode in a solution containing the $[\text{Fe}(\text{CN})_6]^{3-/4-}$ redox couple as a model of reversible redox system as described in Ref.[1]. A supporting electrolyte was employed to ensure a high conductivity of the solution. Kinetics of this redox reaction were measured at the SnO₂ layers with spin-coating numbers varying from 1 to 4 and for two different annealing times: 30 min and 3h for FTO and 30 min for ITO. They were compared to a bare TCO electrode and to a *spr*-TiO₂ layer. The curves are presented in Figure AII.1. The FTO and SnO₂ curves are characterized by Nernstian peaks-shaped voltammograms.

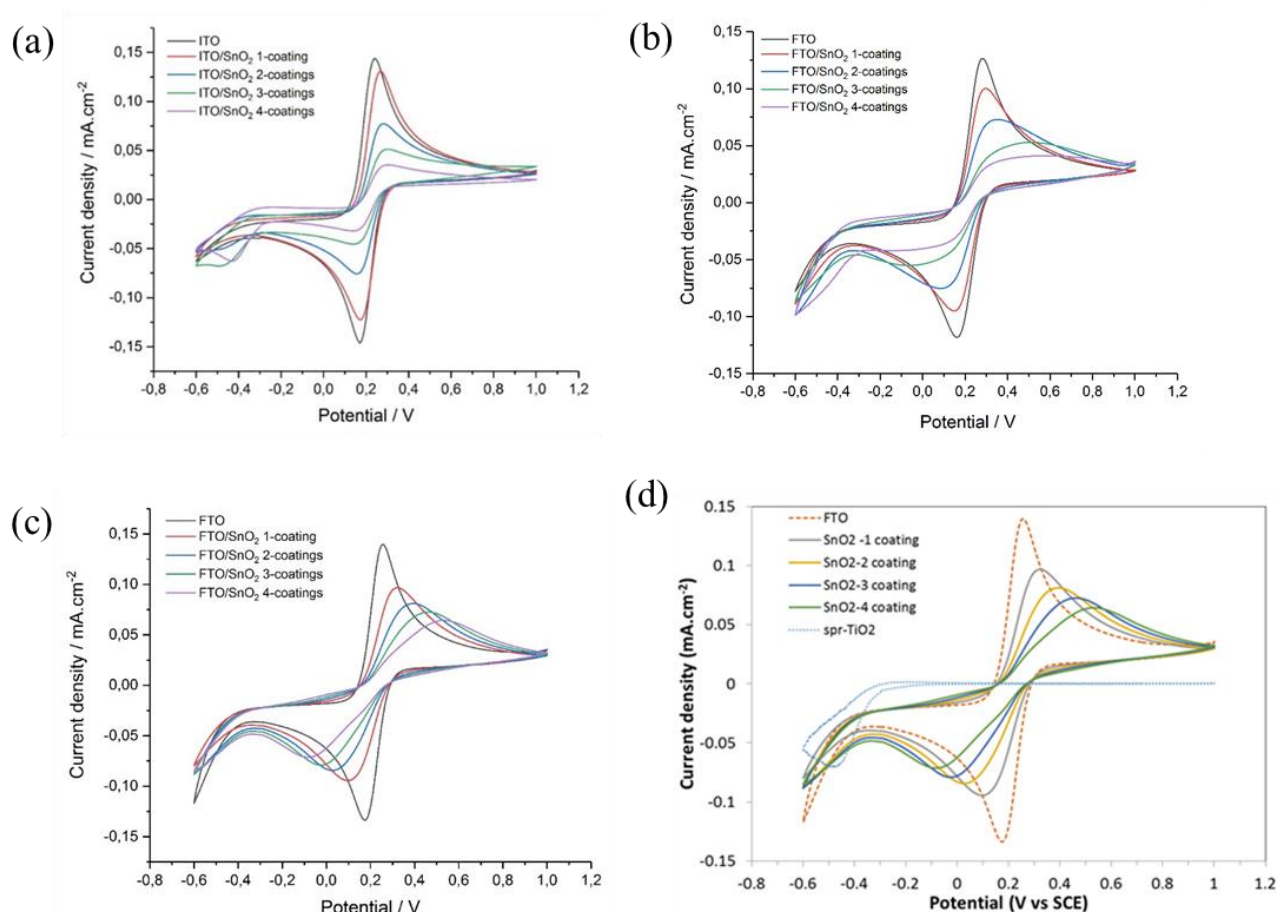


Figure AII-1. Cyclic voltammogram curves of various coating time of SnO₂ layer in an aqueous solution containing the $[\text{Fe}(\text{CN})_6]^{3-/4-}$ deposited on (a) ITO substrate- 30 min layer annealing time ; (b) FTO substrate-30 min layer annealing time; (c) FTO substrate-3h layer annealing time; (d) Curve of (c) with the CV of *spr*-TiO₂ sample.

With the number of SnO₂ coatings, the CV curves show a decrease of the anodic and cathodic peak intensities, noted j_a and j_c , respectively. Most of the decrease of j_a and j_c occurs upon the first two SnO₂ coating depositions. Figure AII.1 also shows an increasing potential difference between these two peaks, noted ΔE_p [1]. This parameter is only 78 mV and 120 mV for the FTO electrode annealed during 3h and 30 min, respectively, and the redox reaction is almost reversible. On the other hand, the first SnO₂ deposit results in a significant enlargement of this parameter. For ITO, the potential of the redox peaks did not change. In Figure AII.1(d), we have also reported the CV curve for the *spr*-TiO₂ blocking layer. In this case the two redox peaks disappeared and the redox reaction was blocked showing that TiO₂ is less electroactive than SnO₂. The different behavior between the TiO₂ and SnO₂ electrodes is due to the fact that the conduction band of SnO₂ is shifted to a more positive potential which makes possible the charge transfer from the [Fe(CN)₆]^{3-/4-} redox couple [2]. The characteristic parameters of cyclic voltammograms for ITO and FTO on various coating time are presented in Table AII.1 and Figure AII.2.

Table AII-1. CV-curve characteristics for the FTO/glass and ITO/glass substrates before and after different numbers of SnO₂ coatings.

| TCO | Duration | Number of coatings | ΔV (mV) | $i_a/i_a(\text{TCO})$ | $i_c/i_c(\text{TCO})$ |
|-----|----------|--------------------|-----------------|-----------------------|-----------------------|
| ITO | 30 min | 0 | 71 | 1 | 1 |
| | | 1 | 95 | 0.91 | 0.84 |
| | | 2 | 122 | 0.54 | 0.52 |
| | | 3 | 166 | 0.36 | 0.31 |
| | | 4 | 163 | 0.25 | 0.22 |
| FTO | 30 min | 0 | 120 | 1 | 1 |
| | | 1 | 149 | 0.79 | 0.80 |
| | | 2 | 269 | 0.58 | 0.64 |
| | | 3 | 579 | 0.42 | 0.47 |
| | | 4 | 710 | 0.33 | 0.36 |
| FTO | 3h | 0 | 78 | 1 | 1 |
| | | 1 | 310 | 0.69 | 0.71 |
| | | 2 | 368 | 0.58 | 0.63 |
| | | 3 | 491 | 0.52 | 0.59 |
| | | 4 | 608 | 0.46 | 0.53 |

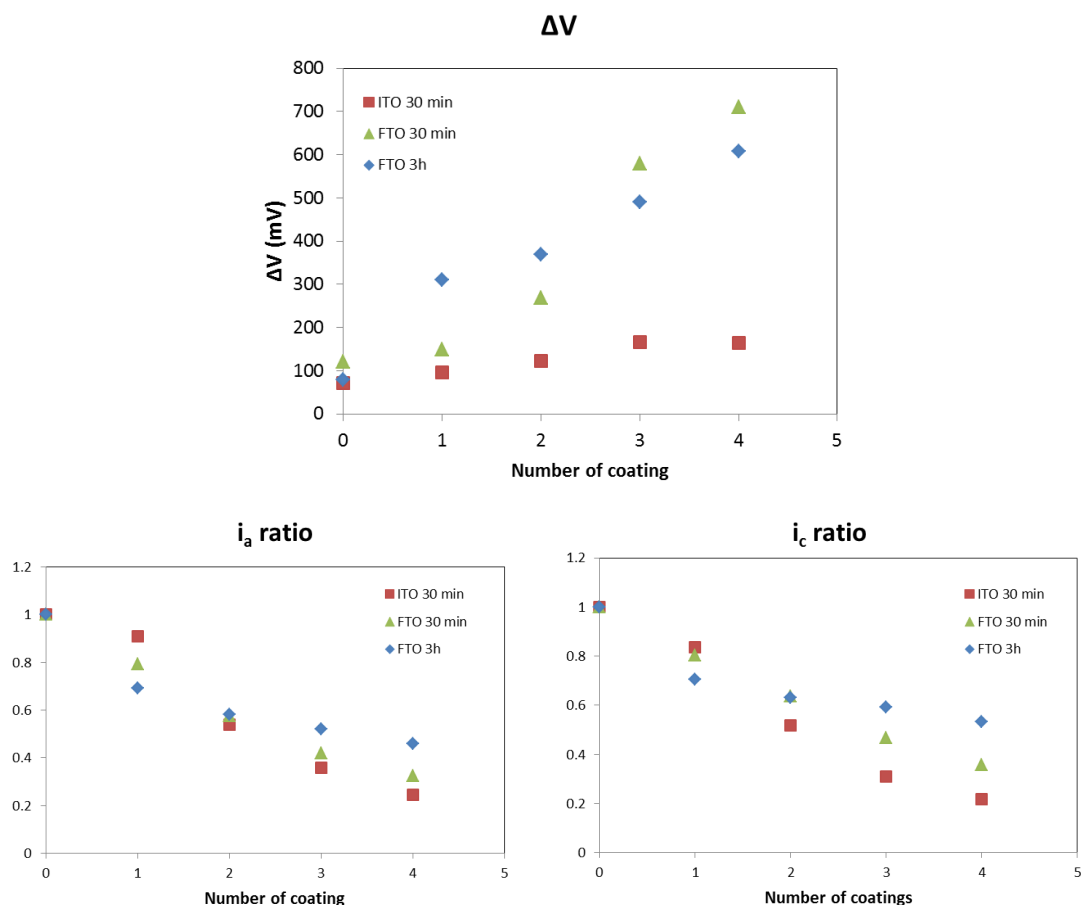


Figure AII-2. CV-curve characteristics for the FTO/glass substrate before and after different numbers of SnO_2 coatings.

References

- [1] P. Wang, Z. Shao, M. Ulfa, et T. Pauporté, « Insights into the Hole Blocking Layer Effect on the Perovskite Solar Cell Performance and Impedance Response », *J. Phys. Chem. C*, vol. 121, n° 17, p. 9131-9141, mai 2017.
- [2] L. Kavan, L. Steier, et M. Grätzel, « Ultrathin Buffer Layers of SnO_2 by Atomic Layer Deposition: Perfect Blocking Function and Thermal Stability », *J. Phys. Chem. C*, vol. 121, n° 1, p. 342-350, janv. 2017.

List of Publications and Presentations

Publications:

1. **Maria Ulfa**, Pengjiu Wang, Jie Zhang, Jiawen Liu, Willy Daney de Marcillac, Laurent Coolen, Sébastien Peralta, and Thierry Pauporté. Charge Injection and Electrical Response in Low-Temperature SnO₂-Based Efficient Perovskite Solar Cells. *ACS Appl. Mater. Interfaces*, 2018, 10 (41), pp 35118–35128.
2. **Maria Ulfa**, Tao Zhu, Fabrice Goubard, and Thierry Pauporté. Molecular versus polymeric hole transporting materials for perovskite solar cell application. *J. Mater. Chem. A*, 2018, 6, 13350-13358.
3. **Maria Ulfa**, Thierry Pauporté, Thanh-Tuan Bui, and Fabrice Goubard. Impact of Organic Hole Transporting Material and Doping on the Electrical Response of Perovskite Solar Cells. *J. Phys. Chem. C*, 2018, 122 (22), pp 11651–11658.
4. Thanh-Tuân Bui, **Maria Ulfa**, Federica Maschietto, Alistar Ottochian, Mai-Phuong Nghiem, Ilaria Ciofini, Fabrice Goubard, and Thierry Pauporté. Design of dendritic core carbazole-based hole transporting materials for efficient hybrid perovskite solar cells. *Organic Electronics*, September 2018, 60, pages 22-30.
5. Pengjiu Wang, **Maria Ulfa**, and Thierry Pauporté, Effects of perovskite monovalent cation composition on the high and low frequency impedance response of efficient solar cells. *J. Phys. Chem. C*, 2018, 122 (4), pp 1973–1981.
6. Pengjiu Wang, Zhipeng Shao, **Maria Ulfa**, Thierry Pauporté, Insights into the hole blocking layer effect on the perovskite solar cell performance and impedance response. *J. Phys. Chem. C*, 2017, 121 (17), pp 9131–9141.
7. **Maria Ulfa**, Pengjiu Wang, Zhipeng Shao, Bruno Viana, Thierry Pauporté. Oxide hole blocking selective contacts in perovskite solar cells. Proc. SPIE 10533, *Oxide-based Materials and Devices IX*, 105332R.
8. Nicolai Ababii, Mathias Hoppe, Sindu Shree, Alexander Vahl, **Maria Ulfa**, Thierry Pauporté, Bruno Viana, Vasiliu Cretu, Nicolae Magariu, Vasile Postica, Victor Sontea, Maik-Ivo Terasa, Oleksandr Polonskyi, Franz Faupel, Rainer Adelung, Oleg Lupan. Effect of film thickness and noble metal functionalization on UV and gas sensing properties of sprayed TiO₂ thin films. (Accepted in *Sensors & Actuators: A. Physical* journal).

Presentations :

1. **Maria Ulfa**, Tao Zhu, and **Thierry Pauporté**. Impedance spectroscopy study of perovskite solar cells. Spectroscopy tools for halide perovskites, 22 November 2018, Paris, France (poster presentation).
2. **Maria Ulfa**, Thierry Pauporté, Thanh-Tuan Bui, and Fabrice Goubard. Organic Hole Transporting Material for Perovskite Solar Cells: Effects of Doping and Design of New Molecules. 9th International Conference of Molecular Electronics, Paris, France, 17-20 December 2018 (oral presentation).
3. **M. Ulfa**, P. Wang, Z. Shao, **B. Viana**, Th. Pauporté "Oxide Hole Blocking Selective Contacts in Perovskite Solar Cells". SPIE Photonics West 2018, 27 January-1 February 2018, San Francisco, USA (poster presentation)
4. **Thanh-Tuân Bui**, **Maria Ulfa**, Federica Maschietto, Alistar Ottochian, Mai-Phuong Nghiem, Ilaria Ciofini, Fabrice Goubard, and Thierry Pauporté. Dendritic core carbazole-based hole transporting materials for perovskite solar cells: molecular design, photovoltaic performance and impact of hole transporters and doping on the electrical response of the photovoltaic devices. Asia-Pacific International Conference on Perovskite, Organic Photovoltaics and Optoelectronics. Kyōto-shi, Japan, 27-29 January 2019 (oral presentation).
5. **Thierry Pauporté**, Zhipeng Shao, Pengjiu Wang, **Maria Ulfa**, "Investigation of Hole Blocking Layers for Organo-Lead and Lead-Free Perovskite Solar Cells" 3ème journée Pérovskites Hybrides, May 9-10, 2017, Angers, France (oral presentation).
6. **V. Sontea**, N. Ababii, N. Magariu, V. Postica, **M. Ulfa**, T. Pauporté, V. Trofim, S. Railean, A. Vahl, I. Pocaznoi, N. Wolff, M.-I. Teresa, O. Polonskyi, F. Faupel, L. Kienle, and R. Adelung "Localized growth and integration of semiconductor oxide nanostructures for gas and bio-sensor applications". 2018 IEEE 8th International Conference on Nanomaterials: Applications & Properties. September 9-14th, 2018, Zatoka, Ukraine (poster presentation).
7. **D. Magaldi**, T.-T. Bui, **M. Ulfa**, T. Pauporté, F. Goubard, "Comparative study between two series of isomer molecules based on 3,6-Carbazole and 2,7-Carbazole molecule and designed as hole transporting materials for inorganic-organic hybrid perovskite solar cells." Interface Properties in Organic Electronics: Key Challenges, July 10-13rd, 2017 Cergy Pontoise, France (poster presentation).

8. Ababii N., **Ulfa M.**, Hoppe M., Vahl A, Lupan O, Pauporté Th., Adelung R., Faupel F, "The effects of titanium oxide functionalization on sensory performance".
9. Magariu N., **Ulfa M.**, Sereacov A., Lupan O., Pauporté Th, "The effects of nano hetero non-plane junction for oxides of titane and zinc on sensory selectivity".

RÉSUMÉ

Ce travail de thèse porte sur la réalisation de cellules solaires photovoltaïques à pérovskites hybrides efficaces, stables et reproductibles et vise à bien comprendre le fonctionnement de ces cellules. Au chapitre 1, nous présentons le contexte de la recherche sur les cellules solaires et nous décrivons les techniques utilisées pour la caractérisation des dispositifs. Le chapitre 2 propose une étude comparative de deux techniques différentes (une étape et deux étapes) pour la préparation de couches de $\text{CH}_3\text{NH}_3\text{PbI}_3$. Il est montré que les deux conviennent à la préparation de PSC performantes. Au chapitre 3, nous étudions les deux principaux types de matériaux de transport de trous organiques: moléculaires et polymères. Nous étudions également l'effet des dopants sur ces HTM. Grâce à la spectroscopie d'impédance, nous avons pu voir clairement pourquoi le dopage est important pour obtenir une haute efficacité des cellules Spiro-OMeTAD alors que l'amélioration est plus faible dans le cas des cellules P3HT. Au chapitre 4, nous examinons plusieurs nouveaux dérivés du carbazole comme matériaux transporteurs de trous. Ces molécules allaient du gros noyau dendritique B186 aux séries DM et iDM ayant une masse moléculaire inférieure. B186 et iDM1 ont donné les meilleurs rendements à 14.59% et 15.04%, respectivement. Enfin, dans le chapitre 5, SnO_2 est étudié comme couche bloquante des trous. Des cellules planaires ont ensuite été préparées en utilisant cette couche combinée aux pérovskites MAPI (1) -SOF et FAMA. Avec le FAMA, les dispositifs étaient très efficaces avec un rendement maximum de 18,2% et une quasi-absence d'hystérésis (6,7% IH), alors qu'avec MAPI(1)-SOF, le résultat était de 15,2% avec une hystérésis plus élevée.

MOTS CLÉS

Cellules solaires à pérovskites hybrides; Matériaux transporteurs de trous; Structure planaire; Oxyde d'étain; Spectroscopie d'impédance.

ABSTRACT

This thesis work aimed at realizing efficient, stable, and reproducible photovoltaic perovskite solar cells, and to achieve a good understanding of the cells functioning. In Chapter 1, we present the context of the research on solar cells and PSC components as well as a description of the main techniques employed for the device characterizations. Chapter 2 provides a comparative study of two different $\text{CH}_3\text{NH}_3\text{PbI}_3$ deposition techniques (1-step and 2-step). It is clear that both of them are suitable for the preparation of PSC which resulted in more than 17% PCE. In Chapter 3, we have thoroughly studied the two main kinds of organic hole transporting materials: molecular and polymeric. We have also investigated the doping effect on these HTMs. Through impedance spectroscopy measurement, we could clearly see that doping is really important to get high efficiency for Spiro-OMeTAD cells, while the improvement was less significant in the case of P3HT cells. In Chapter 4, we have investigated several new carbazole derivatives as hole transporting materials. These molecules ranged from the big dendritic core B186 to the DMs and iDMs series with lower molecular weight. B186 and iDM1 showed the highest efficiency at 14.59% and 15.04%, respectively. In Chapter 5, we have studied a simple planar structure of PSC by incorporating a wide bandgap n-type semiconductor SnO_2 as the hole blocking layer. Planar cells have been prepared using this layer combined with MAPI(1)-SOF and FAMA perovskites. With FAMA absorber, the devices were highly efficient with a maximum PCE of 18.2% and were almost hysteresis-free (6.7% HI) while, with MAPI(1)-SOF, the obtained efficiency was 15.2% with higher hysteresis.

KEYWORDS

Perovskite solar cells; Hole transporting materials (HTM), Planar structure, Tin oxide, Impedance spectroscopy